SEISMIC INVESTIGATION AND ATTRIBUTE ANALYSIS OF FAULTS AND FRACTURES WITHIN A TIGHT-GAS SANDSTONE RESERVOIR: WILLIAMS FORK FORMATION, MAMM CREEK FIELD, PICEANCE BASIN, COLORADO

by

SAIT BAYTOK

B.S., Kocaeli University, Turkey, 2006

A thesis submitted to the

Faculty of the Graduate School of the

University of Colorado in partial fulfillment

of the requirement for the degree of

Master of Science

Department of Geological Sciences

2010

This thesis entitled:

Seismic investigation and attribute analysis of faults and fractures within a tight-gas sandstone reservoir: Williams Fork Formation, Mamm Creek Field, Piceance Basin, CO

written by Sait Baytok

has been approved for the Department of Geological Sciences

____

Matthew J. Pranter

____

Bruce D. Trudgill

____

Geoffrey A. Dorn

Date_______________

The final copy of this thesis has been examined by the signatories, and we find that both the content and the form meet acceptable presentation standards of scholarly work in the above mentioned discipline.

ABSTRACT

Baytok, Sait (M.S., Geology [Department of Geological Sciences]) Seismic investigation and attribute analysis of faults and fractures within a tight-gas sandstone reservoir: Williams Fork Formation, Mamm Creek Field, Piceance Basin, Colorado

Thesis directed by Associate Professor Matthew J. Pranter.

The seismic-reflection characteristics, distribution and orientation of faults, and fracture intensity of the Williams Fork Formation at Mamm Creek Field vary stratigraphically and with lithology and depositional setting. The fluvial, marsh, and shallow marine deposits of the Williams Fork Formation were deposited within alluvial-plain, coastal-plain, and shallow-marine environments. The deposits produce significant amounts of natural gas from Cretaceous-age tight-gas-sandstone reservoirs that are moderately porous but exhibit low matrix permeability. Faults and fractures provide conduits for gas migration and enhance permeability and reservoir productivity.

Key stratigraphic units, fault and fracture characteristics, fracture intensity, and the controls on fracture distribution were evaluated by using p-wave seismic data and derived seismic attributes in conjunction with well logs, borehole-image logs, and core data. Amplitude dimming, poor amplitude coherency, and offset reflections characterize the alluvial-plain and coastal-plain deposits. More continuous and moderate-to-high amplitude reflections are present in the lower Williams Fork Formation, which is characterized by coastal-plain and shallow-marine deposits.

An ant-tracking workflow and interpreted seismic-amplitude data and curvature attributes indicate that fault characteristics are complex and vary stratigraphically; the lowermost lower Williams Fork Formation is characterized by north-northwest- and east-west-trending small-scale thrust and normal faults. The uppermost lower Williams Fork Formation and the middle and upper Williams Fork formations exhibit north-northeast- and east-west-trending arrays of fault splays that terminate upward and do not appear to displace the upper Williams Fork Formation. In the uppermost Williams Fork Formation and Ohio Creek Member, north-northeast-trending discontinuities are displaced by east-west-trending events and the east-west-trending events dominate.

Fracture analysis based on ant-track and t* attenuation seismic attributes suggests a non-uniform spatial distribution of fractures. In general, higher fracture intensity occurs within the southern, southwestern, and western portions of the area, and fracture intensity is greater within the fluvial reservoirs of the middle and upper Williams Fork formations. Greater than 90% of natural fractures occur in sandstones and siltstones. In-situ stress analysis, based on induced-tensile fractures and borehole breakouts, indicates a north-northwest orientation of present-day maximum horizontal stress, an approximate 20-degree rotation in the orientation of Shmax with depth, and a sudden stress shift in the Rollins Sandstone Member.

DEDICATION

I would like to dedicate this thesis to my family for being the greatest family, for being there whenever I need, and for making me the person I am today. Without their limitless support, sacrifice, and love I would not be the person I am today. I truly thank them for all their support and help.

ACKNOWLEDGEMENTS

I would first like to acknowledge and thank my advisor Dr. Matthew J. Pranter for his limitless advice, guidance, revisions, and patience in the completion of this thesis. I was lucky to be part of his team and work. Two years at University of Colorado (CU) at Boulder working in the Reservoir Characterization and Modeling Laboratory (RCML) provided me to build up knowledge and experience that I will be using in the rest of my life. I would also like to thank my committee members Bruce D. Trudgill and Geoffrey A. Dorn. I would like to thank Bruce D. Trudgill for an excellent course in structural interpretation of seismic data, which helped me in my thesis work and made me love structural geology. I would like to thank Geoffrey A. Dorn for his comments and his precious time among his busy work.

Turkish Petroleum Corporation funded me for two years during my graduate education for all my expenses. I would like to thank them for all their financial support. I would like to thank all Schlumberger team. Carrie Laudon helped me take the Seismic Visualization and Interpretation Course in Houston, TX. Dave Phillips answered my questions patiently, generated curvature volumes, and helped me understand the Domain Conversion in Petrel. I would like to thank Bill Barrett Corp. for providing me the primary dataset (well logs, formation tops, seismic data, and borehole-image logs) that I used in this work. Thanks to Steve Cumella for his comments, time, and help. I would like thank Scott Larson for his help and time with regard to borehole-image logs. I would like to thank Stan Hammon for his help and taking time to reprocess some seismic volumes. I must also give thanks to Chris Rybowiak for helping me digitizing borehole-image (FMI) logs. I would like to thank all geoscientists who gave input during the development of this thesis. I was so grateful to be part of this institution and get to know great people during my two-year journey. I believe that I made friends that I will always remember. It was pleasure to work with Alicia Hewlett and Rachel Shaak in the lab. I would like to thank my officemates Ali

Drushal, Adel Aboktef, Chris Rybowiak, Kim Hlava, Ericka Harper, and Jeremy Ring. I would also like to thank all administrative staff and of course all my friends that I have shared classes with. Thank you all who I forgot to mention.

CONTENTS

LIST OF TABLES

Table

LIST OF FIGURES

Figure

CHAPTER ONE

INTRODUCTION AND BACKGROUND

The Piceance Basin of northwestern Colorado is one of several Rocky Mountain basins that contain large amounts of natural gas from low-permeability reservoirs of the Late Cretaceous-age Mesaverde Group (Figure 1; Johnson, 1989). Studies in the basin, conducted by many different authors, show the significance of natural fractures and their role in gas production. By the late 1980s, as a result of the U.S. Department of Energy (DOE) Multiwell Experiment (MWX) project (during 1981-88, located in the Rulison gas field, west of Rifle, CO; see Figure 1), sufficient core data, borehole-image logs, and well tests had been accumulated and clearly showed that low-permeability reservoirs of the Williams Fork Formation are extensively naturally fractured at depth (Lorenz, 2003). Since the 1980s, studies by Lorenz and Finley (1991), Grout and Verbeek (1992), Hoak and Klawitter (1997), Kuuskraa et al. (1997), Lorenz (1997), and others have all focused on gaining a better understanding of fracture characteristics and their control on gas production.

Decline in well productivity from 2.2 BCF (wells drilled from 1996 to 2000) to 1 BCF (wells drilled from 2003 to 2005) per well shows the importance of additional studies to delineate fracture characteristics, distribution, and their role in unconventional gas plays (Kuuskraa et al., 2007). In this study, structural and stratigraphic interpretation utilizes three-dimensional conventional seismic data, electrical borehole-image logs, conventional well logs, and core data. An emphasis is placed on the seismic analysis of faults and fractures and relationships between seismic attributes and fracture intensity. It is common that bulk formation (in-situ) permeability (20-100 microdarcies (μD)) is orders of magnitude greater than only matrix permeability (0.01-3.0 μD). The contribution of fracture permeability in the basin is apparent and requires attention as well as characterization (Lorenz et al. 1989; Grout and Verbeek, 1992). Within the Williams

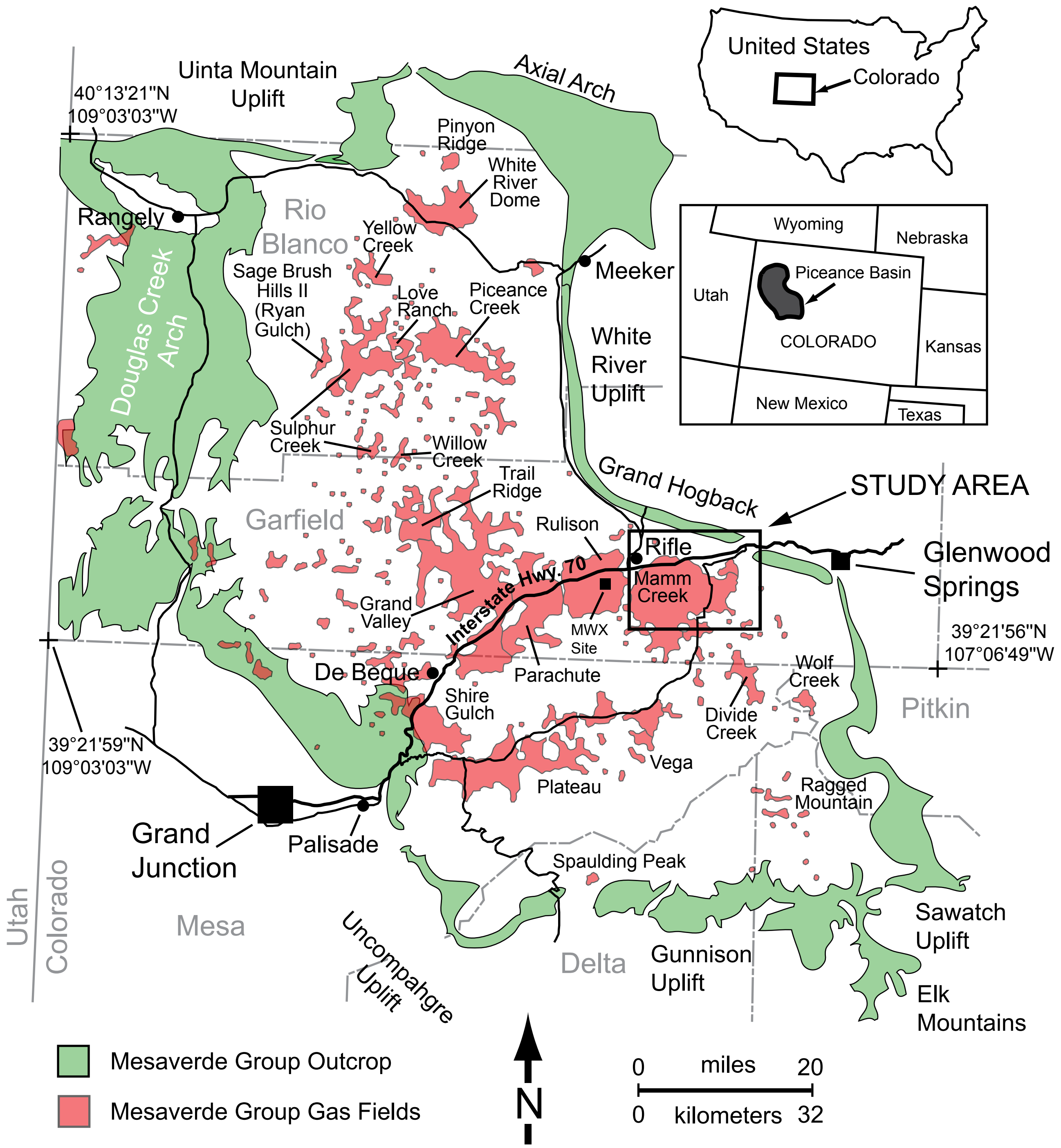

Figure 1. Map of the Piceance Basin. Map shows exposed Mesaverde outcrop along the margins of the basin (including the Williams Fork Formation) and major Mesaverde Group gas fields in the basin. The study area is outlined. The MWX site can be seen. Modified from Hoak and Klawitter (1997) and Pranter et al. (2009).

Fork Formation at Mamm Creek gas field, this study addresses the following questions: 1) How are the stratigraphic units expressed on seismic data?; 2) What is the type, distribution, and orientation of faults?; 3) What is the variability of fracture intensity?; 4) How are fractures/faults expressed on seismic data?; 5) What are the dominant controls on fracture distribution (lithology, faults, etc.)?

STUDY AREA AND DATASET

The study area is located within Mamm Creek gas field (Figures 1 and 2), ~3 mi (~4.8 km) south of Silt and ~7.5 mi (~12 km) southeast of Rifle, Colorado. The dataset used for this study contains a 3-C, 3-D seismic survey in depth and time domains, well logs and formation tops for 617 wells, ten (10) borehole-image (Formation MicroImager; FMI) logs, and core data from one well (Figure 2). The 3-D seismic survey covers an area of ~48 mi^2 (~125 km^2) with inline length of 31,790 ft (9689.5 m), crossline length of 42,350 ft (12,908 m), and 110 ft (33.5 m) inline and crossline spacing. The survey has a NW-SE orientation with a 34 degree inline rotation from north (Figure 2). Both depth and time seismic volumes have the same corner coordinates and same trace-bin geometry. Depth conversion of data was conducted using interval velocities (versus depth migration) (D. Berberick, 2009, personal communication). The depth volume has a datum of +3000 ft (+914 m) relative to sea level and base is at -2900 ft (-884 m) with a sample rate of 4 ft (1.2 m). The time volume is a two-way time (TWT) cube of the average p-wave velocity with a 0.5 ms sample rate and is datummed to a TWT of 400 ms. Both surveys have the same corner XY Universal Transverse Mercator (UTM) system coordinates (Figure 2).

Digital conventional well logs include gamma ray, neutron porosity and density porosity, for 617 wells within the seismic survey area. Most wells in the area penetrate the Rollins Sandstone Member interval with total vertical depth range from 6700-9600 ft (2042-2926 m). Formation tops for most wells include top of Mesaverde Group (also referred to as top of Ohio Creek

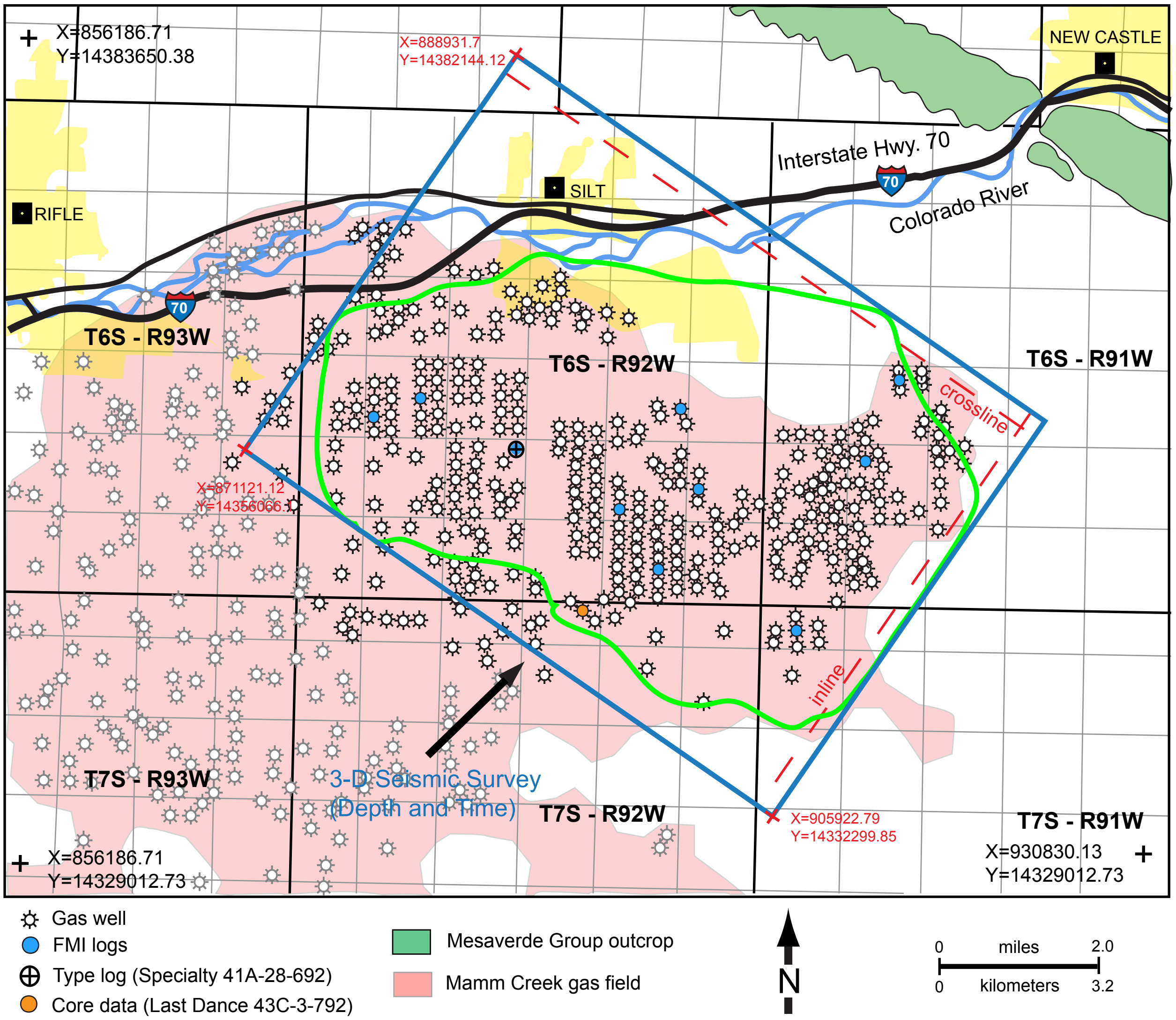

Figure 2. Study area base map. Location of the base map is shown on Figure 1. 3-D seismic survey area is outline in blue and the green outline represents the area where interpretable seismic data is available. Between green and blue outlines, no data are available for interpretation. Core data, gas wells, type log, and borehole-image log locations are also shown. Black-colored gas wells are part of the database in this study.

Member), base of Ohio Creek Member, Price Coal, Upper Sandstone base and top, Middle Sandstone, Cameo-Wheeler coal zone, and Rollins Sandstone Member. In order to interpret fracture properties, data from 10 FMI logs were used (Figure 2; Appendix A).

METHODS

Stratigraphic units were interpreted using horizon interpretation tools such as seeded 2-D/3-D autotracking, guided autotracking, and manual picking in conjunction with formation tops and well logs. Value constraints for the seismic amplitude involved setting a seed confidence, a value range, and a max value delta, and geometrical constraints involving expansion quality, vertical range, and dipping reflector optimization were set to optimize the results and to get better tracking results. The type, distribution, and orientation of faults were interpreted in the three-dimensional seismic data using an ant-tracking workflow, which generates an enhanced fault volume (ant-track attribute volume), and available fault interpretation tool and methods. Ten (10) borehole-image logs were interpreted to characterize the distribution, orientation, type of fractures, and the dominant controls on fracture distribution. Stereonets, rose diagrams, and histograms were utilized to further analyze fractures. Investigation of relationships between two different seismic attributes and fracture-intensity logs were conducted. After fracture-intensity logs were upscaled and seismic attributes were resampled to the same scale of the well logs, cross-plots were generated to examine relationships among these properties.

GEOLOGIC SETTING AND PALEOGEOGRAPHY

Regional Structural Setting

The Piceance Basin is an elongate, northwest-southeast trending basin created by Laramide tectonism from latest Cretaceous through Paleocene time, and has a highly asymmetrical profile with gently dipping western and southwestern flanks and a steeply dipping eastern flank. Exposure of strata on the eastern flank of the basin is almost vertical at the Grand

Hogback, which is a steep Laramide monocline underlain by a low-angle basement-involved thrust fault (Figures 1 and 3; Tweto, 1975; Grout et al. 1991).

The Piceance Basin is bounded by the Uinta uplift on the northwest, by the Axial basin anticline on the north, by the White River uplift and Elk Mountains on the east, by the Sawatch uplift on the southeast, by the San Juan volcanic field on the south, by the Uncompahgre uplift on the southwest, and by the Douglas Creek arch on the west (Figures 1 and 3). The structural development of the Piceance Basin began near the end of the Cretaceous and continued during the Tertiary period, and was influenced by two major tectonic events: the Sevier orogeny and the Laramide orogeny (Johnson, 1989; Grout et al., 1991; Currie, 2002). Even though both tectonic events played a role in the development of the Piceance Basin, the Laramide orogeny (Late Cretaceous – Early Tertiary time) gave the present shape and configuration of the Piceance Basin as one of a number of structural depressions in the Rocky Mountain region (Cole and Cumella, 2003).

The tectonic history of the region is related to Cordilleran orogenesis in the western United States covering a time span of at least 120 Ma from Middle Jurassic to early Eocene (DeCelles and Currie, 1996). The orogeny began its development as a result of subduction between oceanic plates of the Pacific domain beneath the North American continental plate (Monger and Price, 1979; Burchfiel et al., 1992; DeCelles, 2004). It is suggested that Cordilleran orogenesis involved thrust faulting and folding, ductile shortening, metamorphism, and igneous intrusion (Miller et al. 1988; Allmendinger, 1992; DeCelles and Currie, 1996). As a result of the growth and lateral propagation of the Cordilleran orogen, the Cordilleran foreland basin (also referred to as the Rocky Mountain foreland basin) developed, which was “a regionally elongated zone of potential sediment accommodation that develops on the forelandward side of a contractional orogen in response to flexural process associated with convergent plate boundaries” (DeCelles and Currie, 1996, p. 591; Currie, 2002, Ross et al., 2005; DeCelles et al., 2009). From Late

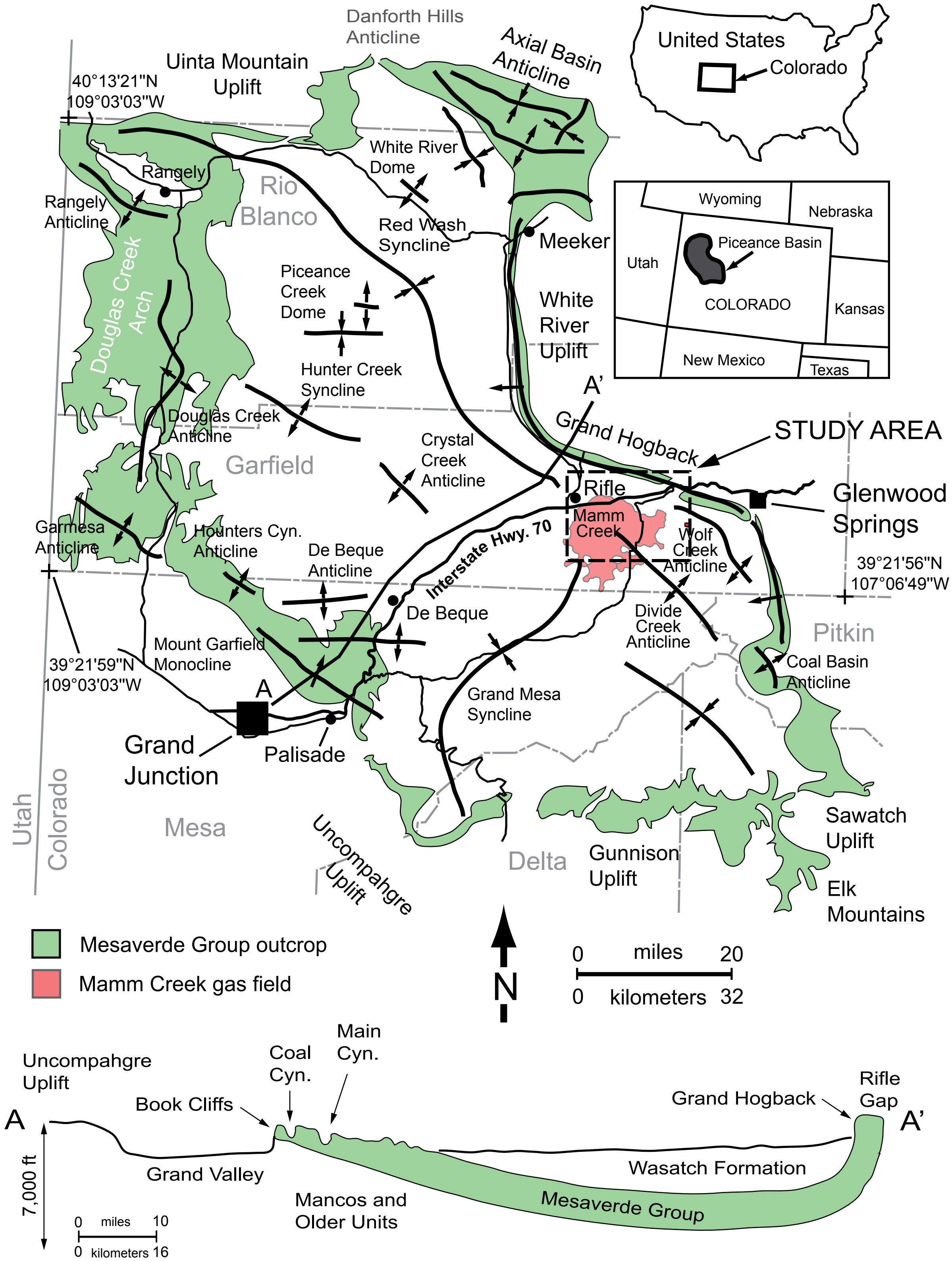

Figure 3. Main structural elements of the Picenace Basin. Location of the study area is outlined. Grand Hogback, the Divide Creek and Wolf Creek anticlines are major features in close proximity to the study area. The structural cross section is diagrammatic. Modified from Cole and Cumella (2003). Data sources: Murray and Haun, 1974; Choate et al., 1981; Tyler et al., 1996; and Johnson and Roberts, 2003.

Jurassic to Late Cretaceous time, Rocky Mountain foreland basin system comprised all four depozones (wedge-top, foredeep, forebulge, and back-bulge) of a classic foreland basin system, with the four depozones stacked into a vertical succession of deposits through time as the Cordilleran thrust belt migrated eastward (DeCelles, 2004). According to Currie (2002), the present day location of the Piceance Basin was occupied by a forebulge depozone of the Cordilleran foreland basin while central Colorado was located in a back-bulge depozone during Lower Cretaceous, defined based on thickness variations in Lower Cretaceous sediments. The deformation front of the Cordilleran orogeny moved eastward approximately 540 mi (1000 km) from Nevada to Colorado and culminated in the formation of the Laramide Rocky Mountain ranges (DeCelles and Currie, 1996; DeCelles, 2004). During the development of the Cordilleran orogeny, the retroarc region was divided into six tectonomorphic zones including, from west to east: the Luning-Fencemaker thrust belt; central Nevada (or Eureka) thrust belt; hinterland metamorphic belt; Sevier thrust belt; foreland basin system; and Laramide zone of intraforeland basement uplifts and basins (DeCelles, 2004). Oldow et al. (1989), Elison (1991), and Allmendinger (1992) suggest more than 135 mi (250 km) of horizontal shortening, based on balanced cross sections.

During the Sevier orogeny (from about 119 to 50 Ma), eastward thrusting of Paleozoic and older Mesozoic rocks formed the Sevier thrust belt to the west, which is the western boundary of the Rocky Mountain foreland basin. The Rocky Mountain foreland basin covered the area which is spanned an east-west distance of >540 mi (>1000 km) and a south-north distance of >3107 mi (>5000 km) from the Gulf of Mexico to northern Canada, and was inundated to form the Western Interior Seaway (Figure 4A; Cole and Cumella, 2003; Patterson et al., 2003; DeCelles, 2004; Mann et al., 2005). The Sevier thrust belt was first defined as entirely thin-skinned by Armstrong (1968); however, DeCelles (2004) points out that subsequent studies show large slices of Precambrian metamorphic basement rocks incorporated into the hanging wall of some

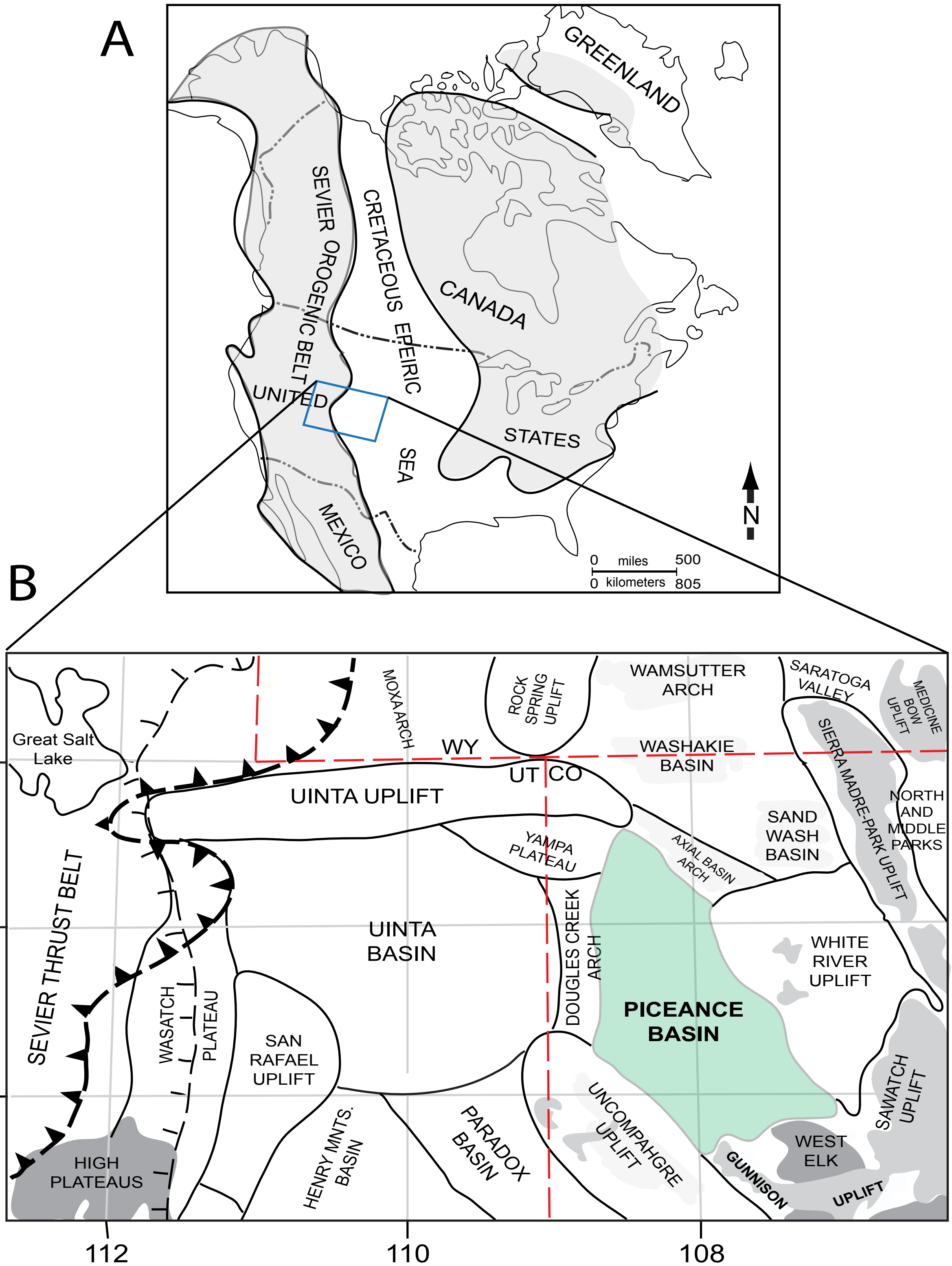

Figure 4. A) Generalized map of the Western Interior Seaway, Sevier orogenic belt, and Piceance Basin during the late Cretaceous. Modified from Johnson (1989), B) Generalized structural map of the Laramide tectonic elements in the eastern Utah and western Colorado. Modified from Patterson et al. (2003) (after Grose, 1972).

Sevier thrusts as well as westward and structurally downward merging of thrusts with ductile shear zones associated with metamorphic rocks in the hinterland. The Sevier thrust belt extends an east-west distance of ~186 mi (~300 km) in central Utah and eastern Nevada and a south-north distance of >1242 mi (>2000 km) from southern California to as far north as the Canadian portion of the Cordilleran (Monger and Price, 1979; Allmendinger, 1992). The Sevier thrust belt front continued its eastward propagation during Campanian time; however, Laramide intraforeland basement uplifts began to emerge and disrupt regional subsidence patterns (DeCelles, 2004). Maastrichtian-early Eocene is characterized by the climax of Laramide intraforeland uplift and the last major phases of the shortening in the Cordilleran thrust belt (Dickinson et al., 1988, DeCelles, 2004). During this time period, final phases of thrusting in the frontal Sevier belt continued and overlapped completely with the Laramide orogeny (Dickinson et al., 1988; Johnson 1989; DeCelles, 2004). The Laramide orogeny produced uplifts that partitioned the entire foreland province into a series of smaller basins, which allowed local sources of sediments and altered the drainage patterns; thus Laramide basins were filled with fluvial, alluvial, and lacustrine sediments (Figure 4B; Johnson, 1989; DeCelles, 2004). The relationship between the Laramide region and the Cordilleran orogenic wedge is equivocal. On the one hand, the Laramide region may be the frontal part of the Cordilleran orogenic wedge and these two were integrated (Livaccari, 1991; Erslev 1993, 2001); on the other hand, perhaps, these two were never integrated and behaved independently (Dickinson and Snyder, 1978; Bird, 1998). Regardless of the relationship, the Laramide orogeny has importance since the Piceance Basin began its development as a structural depression during the Laramide orogeny which greatly influenced the present day configuration of the Piceance Basin (Johnson, 1989; Grout et al. 1991). Grand Hogback, the Wolf Creek anticline, and the Divide Creek anticline are major structural features in close proximity to the study area (Figure 3). The original eastern margin of the basin is unknown; however, compressional deformation of the eastern margin of the Piceance Basin is suggested to have occurred during the final phases of the Laramide orogeny, which remained active in this part of Colorado (Grout et al., 1991). Tweto (1975, 1980) suggests that the Grand Hogback monocline formed in the late Eocene, even after the deposition of the Green River Formation. The monocline is suggested to be the surface expression of a basement-involved thrust wedge, which resulted from southwest- to west-southwest-directed compression and culminated within the Upper and Lower Cretaceous Mancos Shale (Perry et al., 1988; Grout and Verbeek, 1992). The monocline dies out near the eastern edge of the Elk Mountains (Tweto et al., 1978; Grout and Verbeek, 1992). The Divide Creek and Wolf Creek anticlines, which lie south of the study area with north-northwest orientation, are related to the same thrust system. Both anticlines overlie a decollement that dies out basinward as a series of imbricated splay faults in the Mancos Shale (Grout et al., 1991; Grout and Verbeek, 1992). In addition to the Grand Hogback, Divide Creek, and Wolf Creek anticlines, the Piceance Basin contains a series of west-northwest-trending anticlines, synclines, and domes in the northern Piceance Basin, such as Red Wash syncline which dies out southeastward closer to the study area, White River and Piceance Creek domes, Douglas Creek anticline, and Axial Basin anticline, as well as northwest-trending folds which characterize the southern part with the exception of Grand Mesa syncline (Figure 3; Johnson, 1983, 1989; Grout and Verbeek, 1992; Cole and Cumella, 2003).

To summarize, structural configuration of the region was complicated by Cordilleran Sevier thrusting and Laramide intraforeland uplifts. Particularly, the Laramide orogeny has exerted the major influence on the present-day structural configuration of the Piceance Basin. Four important events in the development of the Piceance Basin are summarized by Johnson (1989): 1) Original depositional patterns as a result of the Sevier orogeny; 2) Laramide uplift events that isolated the Piceance Basin, rearranged drainage patterns, and produced local sediment sources; 3) regional uplift that affected the Laramide orogenic uplifts and produced an unconformity prior to the end of the Cretaceous until sometime in the Paleocene; and 4) deposition of lower Cenozoic rocks and burial of the Mesaverde Group rocks (thermal blanket) (Johnson, 1989).

Stratigraphy

The Mesaverde Group was deposited during Campanian time which also includes Maastrichtian strata in the Piceance Basin (Hettinger and Kirschbaum, 2002, 2003). In the Piceance Basin, the Mesaverde Group contains the Iles Formation, which is named the Mount Garfield Formation in the Grand Junction area, the Williams Fork Formation, which is equivalent to the Hunter Canyon Formation in the western Piceance Basin, and the Ohio Creek Member; locally the term Mesaverde Group is considered to be equivalent to the Iles and the Williams Fork Formations, and the Ohio Creek Member (Figure 5; Johnson and Roberts, 2003; Carroll et al., 2004; Cole and Cumella, 2005). The cores that were taken as part of the Multiwell Experiment (MWX) indicate four depositional environments within the strata of the Mesaverde Group. These are, in ascending order, the marine interval (equivalent to the Iles Formation), the paludal interval (Cameo-Wheeler coal and other coal zones), the coastal interval (Lower Williams Fork), and the fluvial interval (Upper Williams Fork) (Nelson, 2003).

The stratigraphic nomenclature by Carroll et al. (2004) is followed in this study for the Mesaverde Group in the eastern and southeastern Piceance Basin (Figure 5). The Mesaverde Group is subdivided into three members in the eastern part of the Piceance Basin: the Iles Formation, the Williams Fork Formation, and the Ohio Creek Member. The Iles Formation contains the Rollins Sandstone Member, a thick, regional marine sandstone conformably overlying the Mancos Shale (Hettinger et al., 2000; Carroll, 2003; Carroll et al., 2004). The Williams Fork Formation overlies this unit. The Williams Fork Formation is locally subdivided into the Bowie Shale Member, the uncomfortably overlying Paonia Shale Member, and the informal members of the middle and upper Williams Fork Formation. The Bowie Shale Member

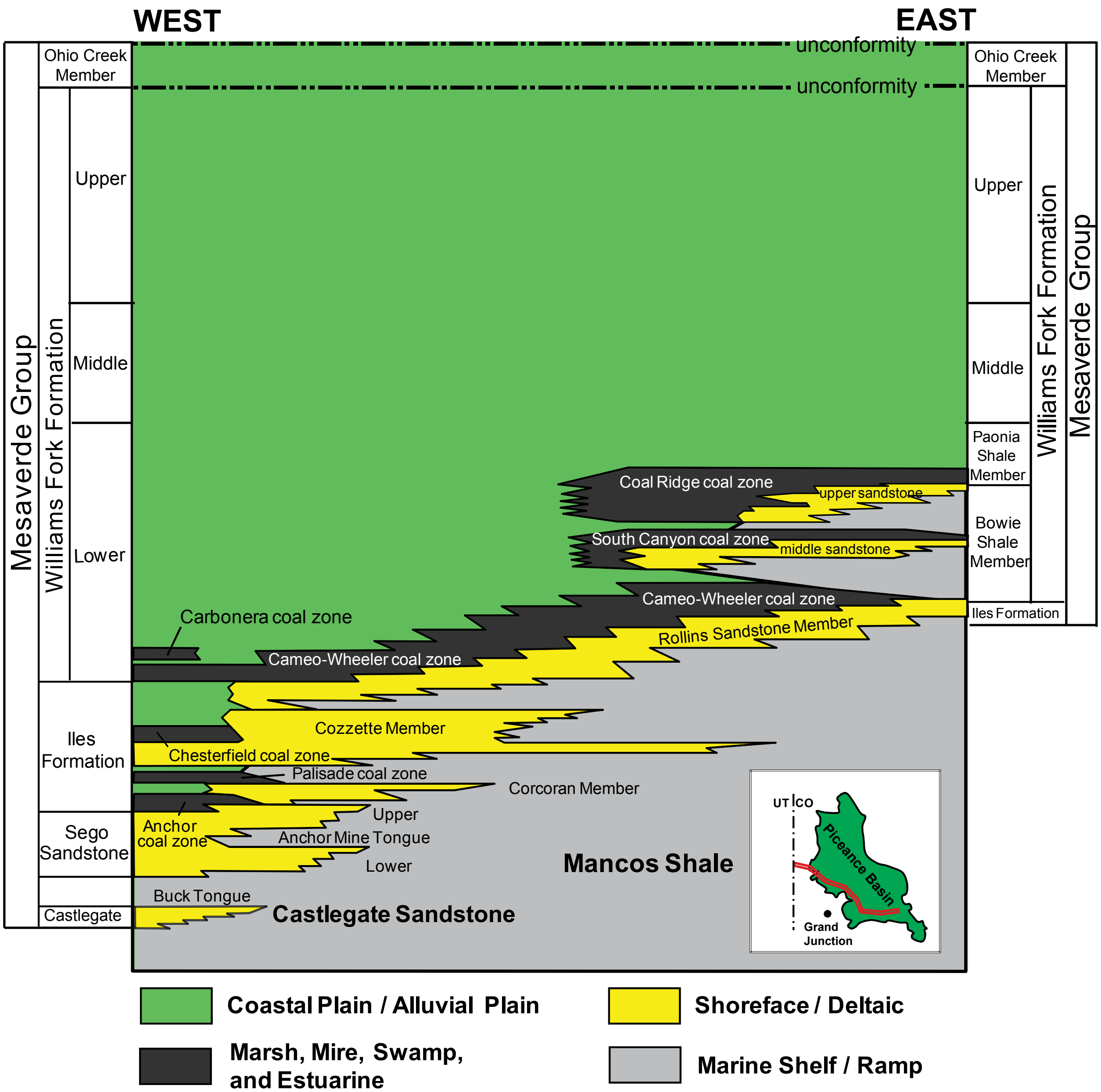

Figure 5. Stratigraphic nomenclature of Upper Cretaceous strata of the southern Piceance Basin. The Williams Fork Formation is divided into lower, middle, and upper intervals in this portion of the basin. Approximate location of transect is shown in map inset. Modified from Johnson and May (1980), Johnson and Flores (1980), Hettinger and Kirschbaum (2002, 2003), Patterson et al. (2003), Carroll et al. (2004), Burger (2007), and Cole and Pranter (2008).

consists of interbedded sandstone, mudstone, shale, siltstone, and coal. It also incorporates four coal beds, locally named “A,” “B,” “C,” and “D,” and that are grouped into two coal zones: the Cameo-Wheeler coal zone, which is the most economically important unit, and the South-Canyon coal zone, which overlies the Middle Sandstone marine unit (Figure 5; Carroll, 2003; Carroll et al., 2004). The Paonia Shale Member is composed of the South-Canyon coal zone which contains two coal beds, locally named “E” and “F” beds (Carroll, 2003; Carroll et al, 2004). Above the Paonia Shale Member, the Williams Fork Formation is subdivided into middle and upper members (informal nomenclature) that are fluvial in character and include no coal bearing strata. This interval is overlain by the Ohio Creek Member at the top (Carroll, 2003; Cole and Cumella, 2003; Patterson et al, 2003, Carroll et al., 2004).

The lowermost part of the Mesaverde Group is the Iles Formation, (also called the Mount Garfield Formation in the Grand Junction area), which comprises three regressive marine sandstone cycles separated by tongues of the underlying marine Mancos Shale. These regressive cycles are the Corcoran, the Cozzette, and the Rollins Sandstone Member, respectively (see Figure 6 for type log). Hettinger and Kirschbaum (2002, 2003) describe the three members of the Iles Formation as deposited in inner-shelf, deltaic, shoreface, estuarine, and lower coastal-plain settings. It is also suggested that the Corcoran and the Cozzette members are characterized by numerous progradations and regressions, whereas the Rollins Sandstone Member was deposited in strongly progradational and aggradational settings in the eastern part of the basin (Cole and Cumella, 2005). The Rollins Sandstone Member is characterized by fine grained to coarse-grained, cliff-forming sandstone that was deposited in a regressive nearshore marine environment. It is 0–200 ft (0-60 m) in average thickness, which changes throughout the basin (Hettinger and Kirschbaum, 2002, 2003). The Rollins Sandstone Member rests conformably on the Cozzette Member at its westward (landward) terminus, where it is separated by a tongue of Mancos Shale further southeast; and is overlain by and

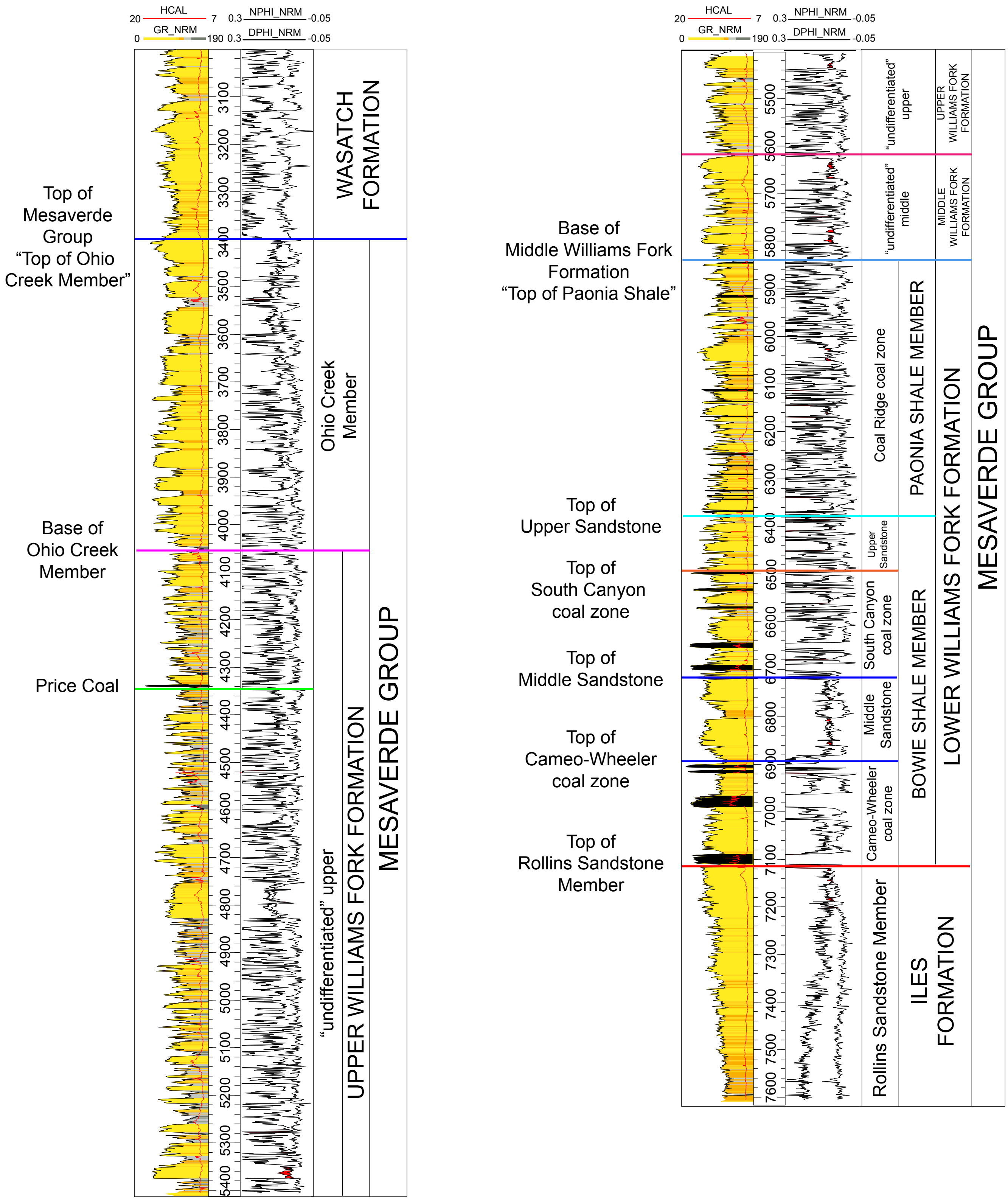

Figure 6. Type log for the Mesaverde Group at the Mamm Creek gas field (see Figure 2 for location). The interval of interest in this study comprises the Rollins Sandstone Member to the top of the Mesaverde Group. The left track shows gamma ray log, scaled from 0 to 190 API and the right track is crossover of neutron and density porosity logs. Depth units are feet.

intertongues with the Cameo-Wheeler coal zone in the Williams Fork Formation (Hettinger and Kirschbaum, 2002, 2003).

The Williams Fork Formation overlies the Iles Formation unconformably and is separated by an unconformity from the overlying Ohio Creek Member of the Mesaverde Group. The thickness of the Williams Fork Formation changes throughout the basin and thins westward towards the Colorado-Utah border from a thickness of ~5000 ft (~1524 m) to ~1200 ft (~365 m) (Cole and Cumella, 2005; Hettinger and Kirschbaum, 2002, 2003). The thickness variations are thought to be due to the combination of a regional erosional surface at the top of the Williams Fork Formation and/or subsidence during deposition (Johnson and Roberts, 2003; Cole and Cumella, 2005). The Williams Fork Formation was deposited in alluvial-plain, lower coastal-plain, and marginal-marine settings and contains interbedded sandstone, mudstone, and coal in the eastern Piceance Basin, including the study area (Cole and Cumella, 2005; Pranter et al., 2008). The Williams Fork Formation is subdivided into three members in the eastern and southeastern Piceance Basin: in ascending order, the Bowie Shale Member, the Paonia Shale Member, and an undifferentiated middle and upper (Figure 6; Hettinger and Kirschbaum, 2002, 2003; Collins, 1976, 1977). The Williams Fork Formation is not subdivided into formal members in the southwestern and western part of the basin but is recognized lithologically by the sand-poor (relatively low net-to-gross ratio) lower one-third interval (~30–60% sandstone, deposited in a coastal-plain setting), including the Cameo-Wheeler coal zone, and the sand-dominated upper two-thirds interval (50–80% sandstone, deposited in an alluvial setting) (Cole and Cumella, 2005; Pranter et al., 2008).

In the study area, the lower ~1200-1500 ft (~365-457 m) of the Williams Fork Formation consists of coal-bearing coastal-plain deposits, marine shale, and marginal-marine sandstones of the Bowie Shale and the Paonia Shale members that were deposited in inner-shelf, shoreface, and coastal-plain settings (Figure 5; Cole and Cumella, 2003; Hettinger and

Kirschbaum, 2003). The Bowie Shale Member has thicknesses of ~680-1,000 ft (~207-305 m) and consists of two superimposed coal-bearing coastal-plain strata overlain by marine shale and marginal marine sandstone (Collins 1976; Hettinger and Kirschbaum, 2002, 2003). Collins (1976) named the two marginal-marine sandstones as the middle sandstone and the upper sandstone, respectively, which are only present in the easternmost part of the basin (Figure 5). The Paonia Shale Member is 560 ft (~170 m) in thickness and is characterized by coal bearing coastal-plain deposits. The middle and upper parts of the Williams Fork Formation are undifferentiated and combined are approximately 2000-4000 ft (~610-1220 m) in thickness and are characterized by fluvial deposits, conglomeratic sandstones, conglomerate, siltstone, minor shales, and the lack of coal (Hettinger and Kirschbaum, 2002, 2003; Pranter et al., 2008). The uppermost 50-400 ft (~15-122 m) of the Mesaverde Group is occupied by the Ohio Creek Member (also referred to as the Ohio Creek Conglomerate elsewhere). The Ohio Creek Member was concluded to be a part of the Mesaverde Group by Johnson and May (1980). It is suggested that this 50-400 ft (~15-122 m) thick interval of kaolinite-rich beds of sandstone, conglomeratic sandstone, and conglomerate of fluvial origin is equivalent to the Ohio Creek Member of the Mesaverde Group (Johnson and May, 1980; Johnson and Flores, 1980; Hettinger and Kirschbaum, 2002, 2003). Subsequently, Patterson et al. (2003) place the Ohio Creek Member within the Paleocene in a sequence-stratigraphic framework for the Mesaverde Group in the Piceance Basin based on 794 ft (242 m) of core from nine wells, correlation of 280 wells, and 135 cutting samples. In addition to Patterson et al. (2003), Burger (2007) reports a fossil vertebrate fauna, which supports the late Paleocene age.

The Williams Fork Formation contains three significant coal zones in the lower interval. The lowermost Cameo-Wheeler coal zone overlies and intertongues the Rollins Sandstone Member and has economic significance due to its major role as a coalbed methane source. The Cameo-Wheeler coal zone is ~50-450 ft (~15-137 m) thick and pinches out to the south beneath the

West Elk Mountains and to the west near the Colorado border (Hettinger et al., 2000; Hettinger and Kirschbaum, 2003). It is defined by Hettinger et al. (2000) as an 87 ft (~26.5 m) interval of net coal in 1-21 beds with thicknesses of 1-44 ft (~0.3-13.5 m) (Hettinger et al., 2002; Hettinger and Kirschbaum, 2002, 2003). Other coal zones are the South Canyon coal zone, which overlies and intertongues with the middle sandstone of the Bowie Shale Member, and the Coal Ridge coal zone, which overlies and intertongues with the upper sandstone in the Bowie Shale Member of the Williams Fork Formation (Hettinger and Kirschbaum, 2003; Cole and Cumella, 2005). The South Canyon coal zone is as much as 300 ft (~91.5 m) thick and incorporates as much as 48 ft (~14.5 m) of net coal in 1-11 beds that are 1-29 ft (~0.3-9 m) thick. Likewise, the Coal Ridge coal zone comprises as much as 44 ft (~13.5 m) of net coal in 1-14 ft (~0.3-4 m) beds that are 1-23 ft (~0.3-7 m) in thickness (Hettinger et al., 2000; Hettinger and Kirschbaum, 2003).

Paleogeography

The paleogeography of the Rocky Mountain region was predominantly driven by the Cordilleran orogenic activity, which began during the late Jurassic as a consequence of Pacific oceanic plates subducting underneath the North American continental plate with the contemporaneous development of a foreland basin to the east of the orogenic belt (Monger and Price, 1979; Burchfiel et al., 1992; DeCelles and Currie, 1996; Currie, 2002 DeCelles, 2004). The Sevier fold-thrust belt was one of six tectonomorphic zones in the Cordilleran orogenic belt which extends for more than 3,730 mi (~6,000 km) from Southern Mexico to the Canadian Arctic and Alaska and became a tectonically single unit during the late Jurassic (~155 Ma) (DeCelles, 2004). The Piceance Basin of northwestern Colorado was located east of the Sevier Orogenic Belt in the western shoreline of the Western Interior Seaway within the Cretaceous Rocky Mountain Foreland Basin ~95–97 Ma years ago during Late Cretaceous time (Figures 4A and 7; Hettinger and Kirschbaum, 2002, 2003). Along the western margin of the seaway, the Sevier

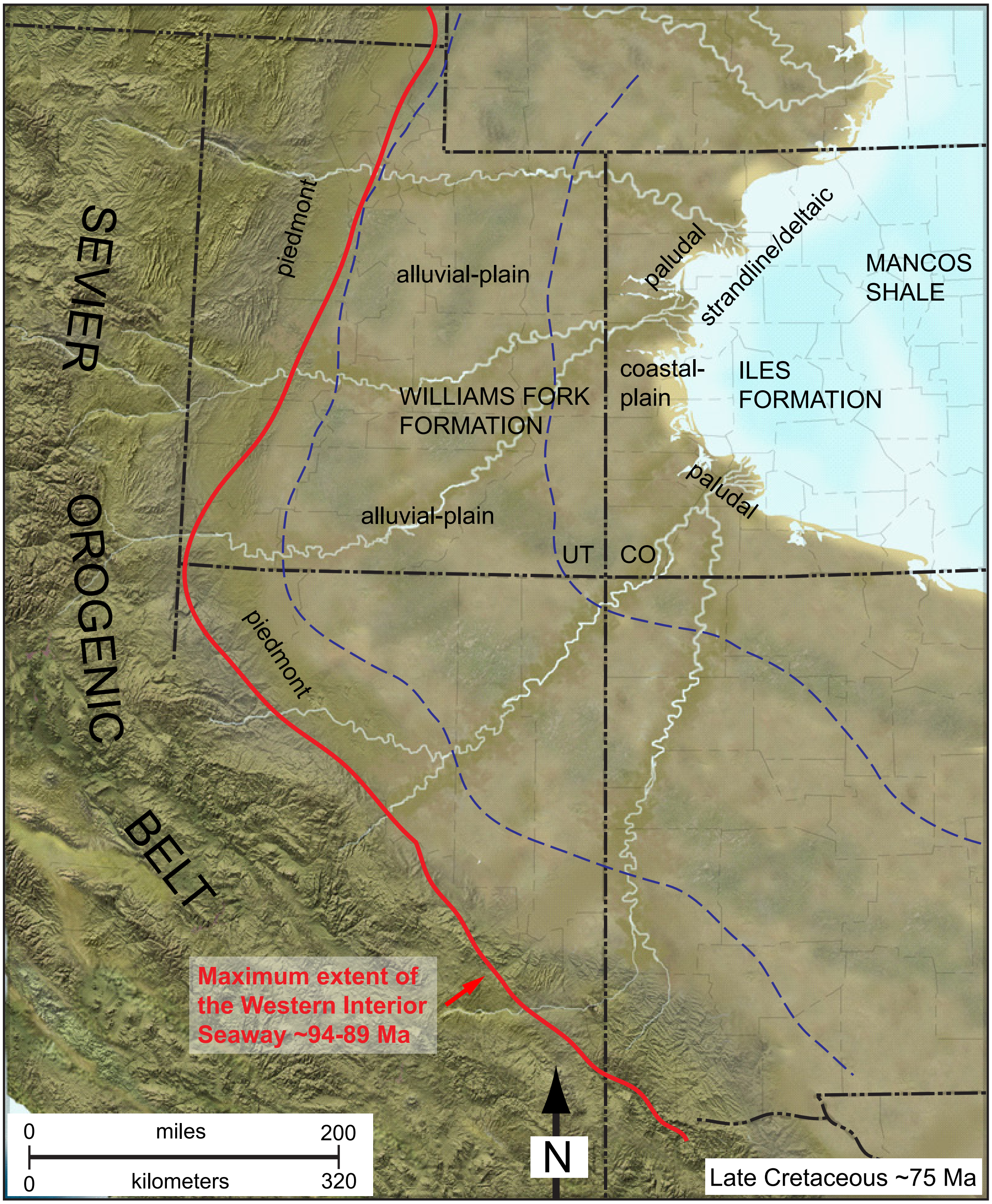

Figure 7. Late Cretaceous (~75 Ma) paleogeography of Western North America. Maximum extent of the Western Interior coastline during the early Late Cretaceous (~94-89 Ma) is shown in red. Modified from Blakey (2010).

Orogenic Belt was the major source of sediments. Sediment shed from the Sevier highlands (to the west) was transported into the Western Interior Seaway eastward on broad alluvial fans that assembled into braid-plain, coastal-plain, deltaic, shoreline, and offshore environments (Figure 7; Yurewicz et al., 2003).

The Western Interior Seaway reached its maximum extent when its western shoreline occupied a region in central Utah during the early Late Cretaceous (~94-89 Ma) as a consequence of rapid subsidence in the foreland basin (Figure 7). Another consequence of rapid subsidence was major marine incursion and deposition of the Mancos Shale in the Piceance Basin. During Late Cretaceous Campanian time, pulses of clastic sediments filled in the basin and began to push the shoreline to the east but left the region permanently during the Maastrichtian (late Cretaceous) (Johnson, 1989). Eastward migration of shorelines during the late Cretaceous with respect to variations in relative sea level and responded transgressive-regressive cycles can be seen throughout the Mesaverde Group strata (Hettinger and Kirschbaum, 2002; Cole and Cumella, 2003). By the beginning of Maastrichtian (Late Cretaceous) time, the shoreline was east of the present-day Piceance Basin, and the marginal-marine and coastal-plain sediments of the Williams Fork Formation were deposited (Johnson, 1989). From early Cretaceous through early late Cretaceous, the basin was dominated by flexural subsidence, and from Late Cretaceous through mid-Cenozoic time, it was highly partitioned by basement-involved Laramide structures (DeCelles, 2004). The Laramide Orogeny (Maastrichtian-early Eocene time, ~71.3-55 Ma) played a major role in the construction and development of the Piceance Basin. During this time interval, the final major phase of thin-skinned shortening in the Cordilleran thrust belt and the Laramide intraforeland uplift overlapped, partitioning the Rocky Mountain foreland basin into smaller basins separated by Precambrian basement-involved, high-angle reverse-fault uplifts and altering the drainage patterns (Johnson 1989; DeCelles, 2004). Laramide Basins were then filled with the thick alluvial, fluvial, and lacustrine sediments of the Eocene-Miocene age (DeCelles, 2004).

PETROLEUM SYSTEM

Magoon and Dow (1994) defined the petroleum system as “a natural system that encompasses a pod of active source rock and all related oil and gas and includes all the essential elements and processes needed for oil and gas accumulations to exist. The elements include source rock, reservoir rock, seal rock, and overburden rock and the processes include a trap and the generation-migration-accumulation of petroleum” (Magoon and Dow, 1994, p. 3). Unlike a traditional petroleum system, a basin-centered gas system (BCGS) carries all the components but it differs because some of these components interact and form a unique hydrocarbon accumulation (Spencer, 1987; Payne et al., 2000; Law, 2002; Cumella and Scheevel, 2005). BCGSs are characterized by gas saturated, abnormally pressured (high or low), low-permeability reservoirs with a lack of a down dip water contact (Law, 2002; Yurewicz et al., 2008). The petroleum system of the Piceance Basin is a BCGS that contains all of these characteristics. Like all BCGAs, the petroleum system of the Piceance Basin requires attention in drilling and completion programs since reservoir continuity and connectivity (lenticular, fluvial-dominated reservoirs of the Williams Fork Formation) are crucial aspect of these kinds of accumulations (for example: Larue and Hovadik, 2006; Pranter et al., 2007; Pranter et al., 2009). More importantly, in most BCGAs, commercial production rates are not constant over the entire basin, and fractures play a significant role in gas production (Verbeek and Grout, 1984; Pitman and Sprunt, 1986; Payne et al., 2000; Cumella and Scheevel, 2005, Kuuskraa and Bank, 2007; Kuuskraa, 2007; Warpinski and Lorenz, 2008).

In the Piceance Basin, poor correlation between net pay and the Estimated Ultimate Recovery (EUR) is evidence that fractures provide a major control on productivity.

Permeabilities calculated from core and well tests exhibit significant differences because well tests primarily measure fracture permeability. As indicated by seismic data, EUR values are higher for those wells drilled in more structurally complex areas (Cumella and Ostby, 2003). Gas production throughout the Piceance Basin mostly comes from the 1700-2400 ft (~518-731.5 m) interval of lenticular, discontinuous, low permeability sandstone reservoirs of the Williams Fork Formation. These sandstone reservoirs are 20-60 ft (6-18 m) in thickness, have porosities varying from 5% to greater than 8%, and have permeabilities ranging from 0.01 to 0.1 mD (Pitman and Spencer, 1984; Tremain, 1993; Spencer, 1996; Johnson and Roberts, 2003). Well tests show that sandstones completed within this 1700-2400 ft (~518-731.5 m) interval produce water-free gas. In the studied Mamm Creek gas field, individual wells are producing about 180 MMCFD on average, primarily from the sandstone reservoirs of the Williams Fork Formation (Cumella and Ostby, 2003). The EUR values in the Mamm Creek gas field show a wider range in comparison to the Grand Valley, Parachute, and Rulison gas fields. Older wells have EUR values that average approximately 0.6 BCF; estimated ultimate recovery is greater than 1 BCF in newer Mamm Creek wells due to improved completion techniques and more complete penetration of the Williams Fork Formation (Cumella, 2006). In the upper Williams Fork Formation, a basin-wide thin shale interval is thought to be a top seal for vertical gas migration. This thin (thickness of ~ 20 ft (~6 m) and 10 to 20 API higher Gamma Ray readings) shale is known as the upper Williams Fork shale marker (UWFSM) and has significance since it has a distinct seismic response over much of the Piceance Basin (Cole and Cumella, 2005). About 50 ft (15 m) above this shale marker, a thin coal 1–3 ft (0.3-0.9 m), informally named the Price Coal, rests. Cole and Cumella (2005) suggest that the Price Coal can be correlated from east Parachute field through the Mamm Creek field with confidence.

In the Piceance Basin, there are three kinds of source facies described by Yurewicz et al. (2003). These are: 1) marine shales within the Mancos Shale, including tongues within the

Castlegate, Sego, and Iles Formations of the Mesaverde Group; 2) coals within the Iles and the Williams Fork Formations, including the Cameo-Wheeler, South Canyon, and Coal Ridge coal zones; and 3) non-marine shales within the Iles and the Williams Fork Formations (Yurewicz et al., 2003). Certainly, coals within the Iles and the Williams Fork Formations are the main source of gas accumulation in the Piceance Basin, and have generated large amounts of natural gas (Cumella and Scheevel, 2005; Yurewicz et al., 2008; Zhang et al., 2008). In addition, Johnson and Roberts (2003) point out the up-dip migration and leakage of gas derived from Mancos Shale via some of the “blanket-like” marginal marine sandstones below the Cameo-Wheeler coal zone in the Mesaverde Group throughout the Piceance Basin. Exposure of the Rollins Sandstone Member on the margins of the Piceance Basin could have resulted in leakage and a conduit for gas migration from the deep basin to the surface since Eocene and the Rollins Sandstone Member may have prevented the gas from migrating up-dip into reservoirs higher in the Mesaverde Group (Johnson and Roberts, 2003).

Cumella and Scheevel (2005) indicate that high rates of gas generation in the Cameo-Wheeler coal zone interval (the lower Williams Fork Formation) are sufficient to provide critical pore pressure and fracturing with a combination of depth, elastic properties, and pore-pressure gradient. Furthermore, elastic strain analysis shows that high pore pressures are enough to fracture rocks within the Williams Fork Formation and open those fractures to aid in migration of gas from the deepest levels to shallower horizons (Cumella and Scheevel, 2005). During Eocene-Miocene time, following the maximum burial of coals in the lower Williams Fork Formation, large amounts of gas were generated (Johnson, 1989; Yurewicz et al., 2003). Given the low permeability and discontinuous nature of the Williams Fork Formation, gas was trapped in the low permeability sandstones and overpressuring developed as a consequence (Scheevel and Cumella, 2005; Cumella, 2006). Next was the development of pervasive natural fractures in the lower Williams Fork Formation and vertical gas migration through the fracture systems

(Scheevel and Cumella, 2005; Cumella, 2006). According to Cumella (2006) there is an interval of continuous gas saturation in the lower Williams Fork Formation. Above this interval, a transition zone is present which contains both gas- and water-bearing sandstones that have better porosity and permeability than those in the continuously gas-saturated interval. In the Piceance Basin, it is important to indicate that the test and production data show the absence of long distance lateral migration, which is evident from wells drilled on the eastern flank of the Piceance Basin. Only a few of these wells have successful economic production rates from the Williams Fork Formation (Yurewicz et al., 2003). Therefore, Yurewicz et al. (2003) conclude that significant gas production does not exceed the limits of the Mesaverde and Mancos source kitchens.

Thermal history of the Piceance Basin is complicated by igneous activity during Tertiary time in the southern part of the basin. The effect of Tertiary igneous activity on regional heating patterns is not clear. Johnson and Nuccio (1986) argue that the igneous activity had no or little effect. Yurewicz et al. (2003) maintain that the Tertiary igneous activity had a measurable effect on the thermal history of the Piceance Basin in the southern part of the basin, with minor effect in the northern part of the basin. Thermal maturities based on vitrinite reflectance (R_o) values of coal zones in the Mesaverde Group have R_o values of 0.60% or less in outcrops and exceed 1.35% in deeper areas. In the deep trough of the Piceance Basin R_o values are 2.1%. Given that R_o values of 0.73-0.75% are required for thermogenic gas generation, coal-bearing intervals in the Mesaverde Group are mature enough to generate gas throughout much of the Piceance Basin (Johnson and Roberts, 2003).

CHAPTER TWO

STRATIGRAPHIC INTERPRETATION OF THREE-DIMENSIONAL SEISMIC DATA

INTRODUCTION

The Piceance Basin of northwestern Colorado has long been the focus of research on fracture characterization, structure, and stratigraphy using geophysical and geological concepts and techniques. During the Department of Energy's (DOE) Multiwell Experiment (MWX) Project at the Rulison gas field in Colorado, extensive testing, measurement, and data collection facilitated understanding of the fracture characteristics and stratigraphy of the Mesaverde Group (including the Williams Fork Formation) in the Piceance Basin (Warpinski and Lorenz, 2008). A great deal of research in these areas has been conducted at Colorado School of Mines (CSM) by the Reservoir Characterization Project (RCP). RCP has conducted research related to time-lapse Vp/Vs analysis, reservoir prediction from multicomponent seismic data, fracture analysis using amplitude variations with offset (AVO) technique, and interpretation of P-wave time-lapse seismic data (discussed in later sections). Furthermore, structural research on the Wolf Creek and Divide Creek anticlines involving analysis of outcrop and subsurface data is ongoing (B. D. Trudgill, 2010, personal communication).

This study expands on these previous studies and integrates three-dimensional seismic data, ten (10) borehole-image (FMI) logs, conventional well logs, and formation tops at 617 wells to build a structural and stratigraphic interpretation of the Williams Fork Formation in the Mamm Creek gas field, Piceance Basin, Colorado.

The seismic horizon interpretation was conducted using a depth seismic volume for the most part, whereas structural interpretation was performed in conjunction with time and depth volumes. Looking at data in both time and depth domains rules out the artifacts that may be

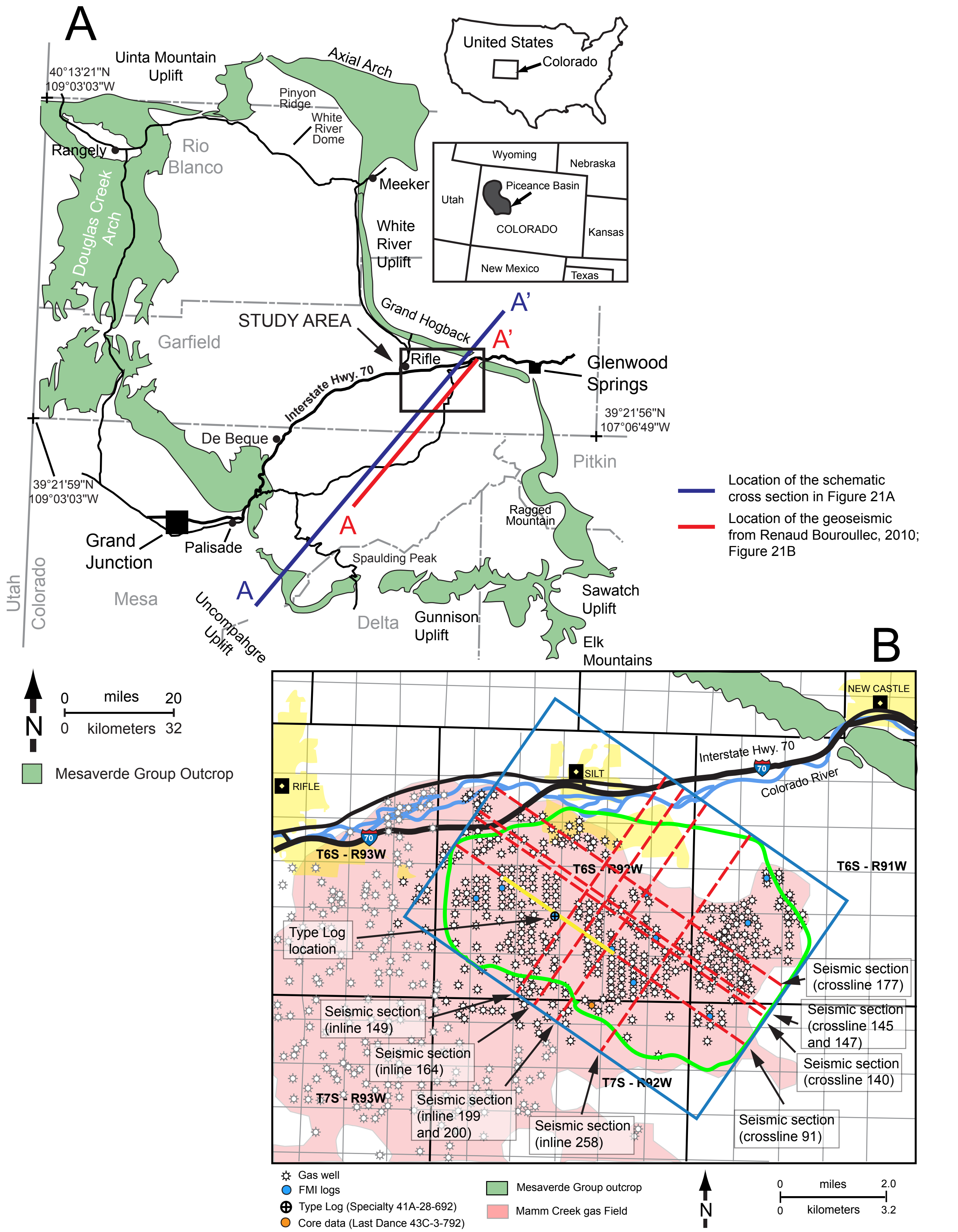

Figure 8. A) Location of the schematic cross section and geoseismic profile in Figures 21A and 21B. B) Location of the seismic sections given in chapters 2 and 3.

caused by depth conversion, and the more extensive depth coverage provided by the time volume clarifies deeper events in the seismic data. The time migrated seismic volume has been scaled to depth using a vertical velocity multiplication derived by correlating well tops against their respective reflections on the seismic volume (Figure 9). It is important to note that this is not a depth migration process, but a simple velocity/time multiplication scaling, where the velocity is calculated via well ties to the seismic data (D. Berberick, 2009, personal communication).

SEISMIC INTERPRETATION OF STRATIGRAPHIC SURFACES

The interpretation of key stratigraphic surfaces in the study area has been performed by conducting a three-dimensional horizon interpretation using several different methods and tools: 1) seeded 2-D/3-D auto-tracking; 2) guided auto-tracking; 3) paintbrush auto-tracking; 4) active box auto-tracking; and 5) manual interpretation, where it is necessary, especially in areas where auto-tracker fails to trace the events. Another tool used to constrain stratigraphic interpretation was “seed confidence”, where the user sets a value of percentage that determines whether auto-tracker accepts or rejects expansion. In addition to a value constraint, a geometrical constraint was applied as necessary, allowing the user to specify the number of samples per trace by increasing and decreasing inline and crossline directions. In areas where reflections were weak and disrupted, every fifth or tenth inlines and crosslines were interpreted first using “2-D auto-tracking”, “guided auto-tracking”, and manual interpretation tools. After interpreting horizons on every fifth and tenth line, the gap between manually picked horizons was filled out by using a 3-D track feature to interpolate between the interpreted lines.

The interpretation of some key seismic horizons are problematic due to dimming of reflections and reflection offset (weak and disrupted reflections). The 10-acre (435600 ft^2 and 40468.5 m^2) well spacing provides effective use of formation tops as a constraint to determine

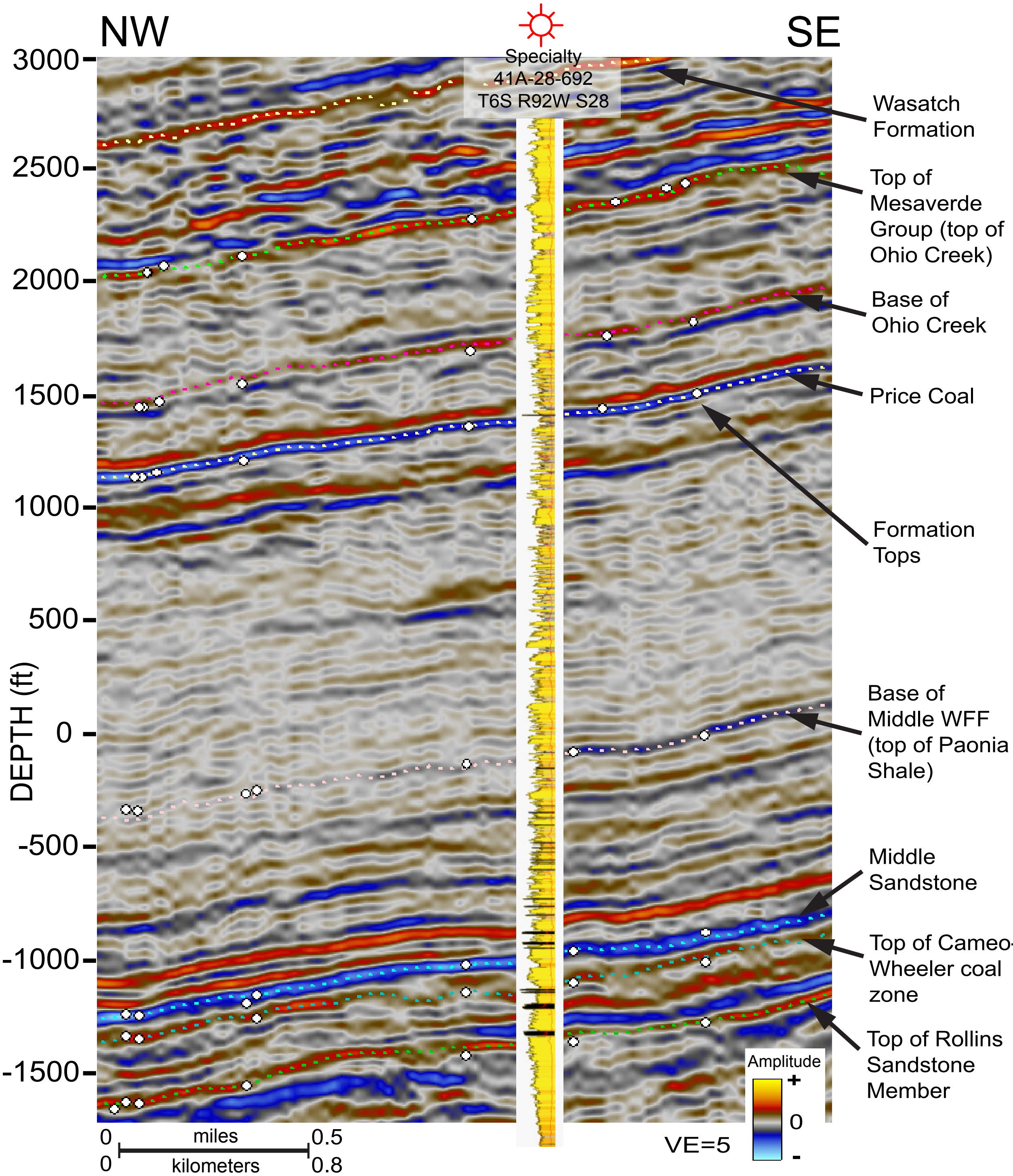

Figure 9. Vertical seismic section (crossline 91) through seismic amplitude data (in depth) with Speciality type log displayed. Interpreted horizons, formations tops, and reflection configurations can be seen. Location of the vertical seismic section is shown in Figure 8. Only formation tops in 200 ft (~61 m) vicinity of this seismic section are displayed. The time-migrated volume scaled to depth using a vertical/multiplication derived by correlating well tops against their respective reflections.

seismic horizons associated with key stratigraphic surfaces in areas where dimming of reflections and reflection offset are present. Displaying formation tops on 3D window and 2D interpretation windows assisted in the determination of seismic response (peak or trough, S-crossing, Z-crossing, etc.) related to a stratigraphic surface.

In this study, seven key stratigraphic surfaces have been interpreted in the study area. These surfaces are (from stratigraphic top to base): 1) Top of Mesaverde Group (also referred to as the top of Ohio Creek Member); 2) base of Ohio Creek Member (also referred to as top of the Williams Fork Formation; 3) Price Coal; 4) base of middle Williams Fork Formation (also referred to as the top of Paonia Shale Member); 5) Middle Sandstone; 6) Cameo-Wheeler coal zone; and 5) Rollins Sandstone Member of the Iles Formation (Figures 9 and 10). Each stratigraphic surface and interval differs in reflection parameters such as reflection configuration, reflection strength, and reflection continuity. Mitchum et al. (1977) define seismic facies units as “groups of seismic reflections whose parameters (configuration, amplitude, continuity, frequency, and interval velocity) differ from adjacent units” (Mitchum et al., 1977, p. 117). Because certain lithology, stratification, and depositional features generate seismic reflections, seismic facies units define different deposits (Mitchum et al., 1977). This study utilizes the terminology from Mitchum et al. (1977) (see Table 1), but focuses on reflection configuration, reflection continuity, and reflection amplitude to describe the key stratigraphic units.

Ohio Creek Member of the Mesaverde Group

The Ohio Creek Member occupies the uppermost Mesaverde Group and is separated from the overlying Wasatch Formation and underlying Williams Fork Formation by unconformities at the top and the base, which are evident from onlapping reflections in seismic data (Figures 11A and 11B). The top and the base of the Ohio Creek Member are both expressed by positive amplitude (peak); however, they are different in reflection strength. The unconformity at the top

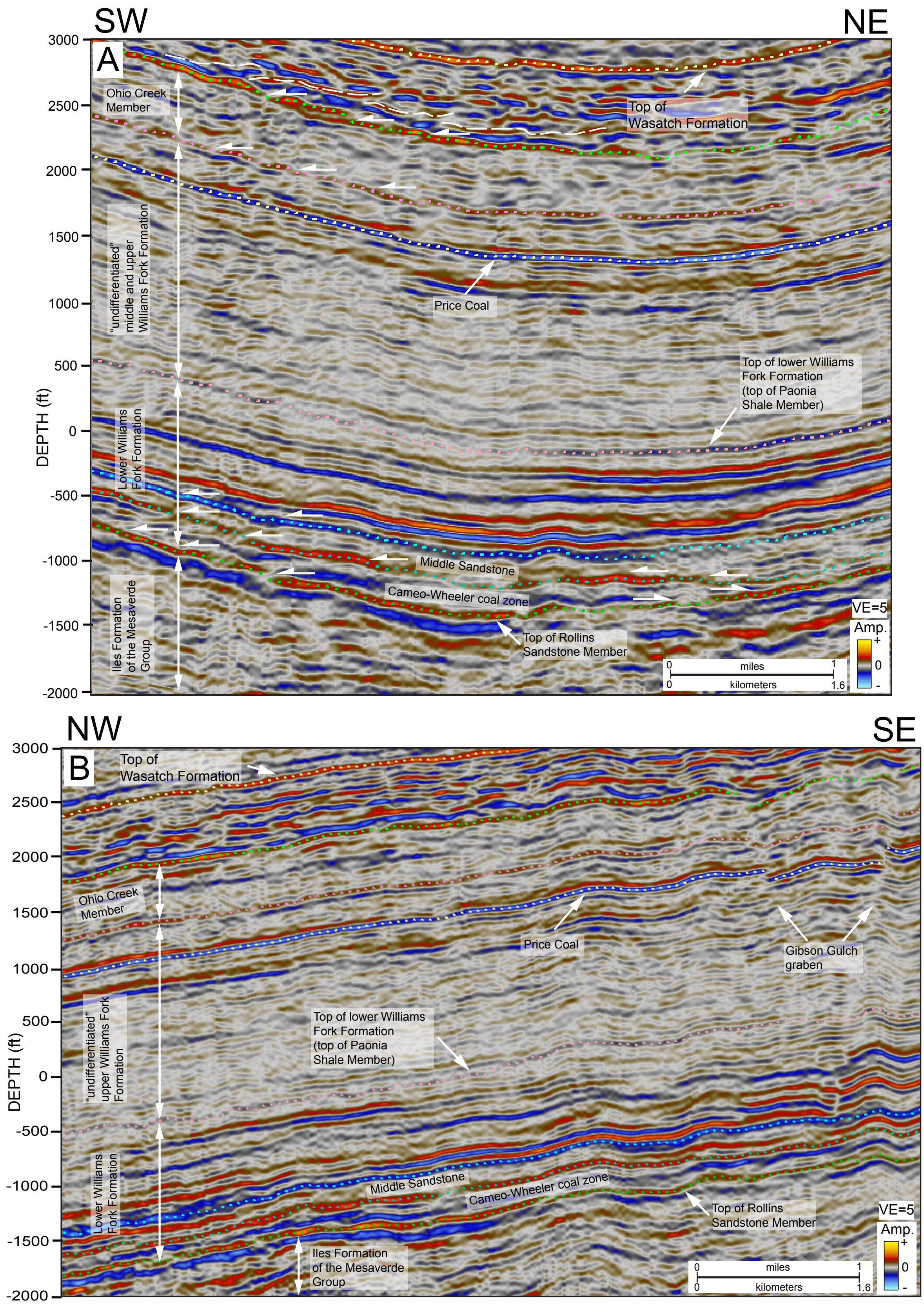

Figure 10. A) Vertical seismic inline (inline 199) and B) Vertical seismic crossline (crossline 140) through the seismic amplitude data showing reflection parameters such as reflection strength, reflection continuity, and reflection configuration for each stratigraphic unit within the Williams Fork Formation interval in the study area. Locations of the seismic sections are given in Figure 8B.

Seismic Facies Parameters	Geologic Interpretation
Reflection Configuration (parallel, subparallel, divergent, prograding clinoform, chaotic, reflection-free) (modifying terms: even, wavy, regular, irregular, uniform,variable, hummocky, lenticular, disrupted, contorted)	- bedding patterns - depositional processes - erosion and paleotapography - fluid contacts
Reflection Continuity (good, moderate, fair, poor)	- bedding continuity - depositional processes
Reflection Amplitude (high, moderate, fair, low)	- velocity-density contrast - bed spacing - fluid content
Reflection Frequency	- bed thickness - fluid content
Interval Velocity	- estimation of lithology - estimation of porosity - fluid content
External form and areal association of seismic facies units	- gross depositional environment - sediment source - geologic setting

Table 1. Terminology used in this study from Mitchum et al. (1977) listing the seismic reflection parameters used in seismic stratigraphy and their geologic significance. Each key stratigraphic interval was examined in terms of reflection configuration, reflection continuity, and reflection amplitude (modified from Mitchum et al., 1977).

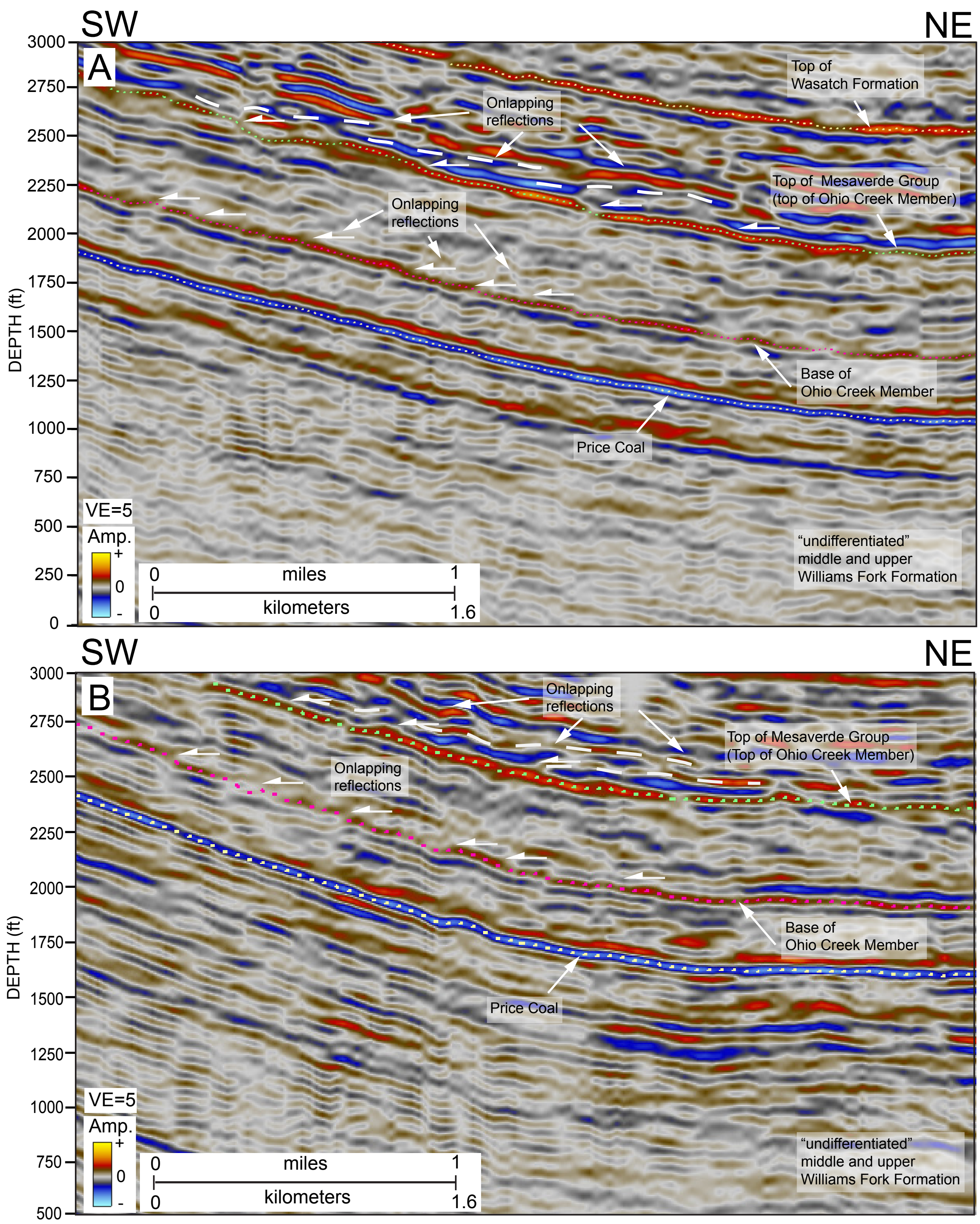

Figure 11. A) Vertical seismic inline (inline 149) and B) Vertical seismic inline (inline 258) showing reflection strength, reflection continuity, and reflection configuration of Ohio Creek Member of the Mesaverde Group and "undifferentiated" middle and upper Williams Fork Formation intervals. Price coal reflection and onlapping reflections can be seen. Locations of the seismic sections are given in Figure 8B.

of the Ohio Creek Member (also referred to as the top of the Mesaverde Group) is expressed by a moderate-to-high positive amplitude (peak) in comparison to the unconformity at the base of the Ohio Creek Member, which is fair-to-moderate in strength. This difference may indicate a different velocity-density contrast within the beds above and below the unconformities. In terms of reflection continuity, the top horizon exhibits moderate reflection continuity, whereas the base horizon exhibits moderate reflection continuity that is problematic to trace in some areas; however, interpretation was done in such areas manually by using formation tops. Internal reflection configuration of the Ohio Creek Member is expressed by parallel to sub-parallel reflections which have variable reflection strength and continuity (Figure 11A and 11B). This variety may be a result of the type of deposition which is interpreted as lowstand deposits formed by braided-fluvial streams (Patterson et al., 2003). The Ohio Creek Member is a maximum thickness of ~621 ft (~189 m) and an average thickness of ~488 ft (~149 m) in the study area. The isopach map of this interval shows thinning of the strata in the southeastern part of the study area (Figure 12).

The Williams Fork Formation

The Williams Fork Formation of the Mesaverde Group overlies the Rollins Sandstone Member of the Iles Formation and is overlain by the Ohio Creek Member of the Mesaverde Group in the study area. The Williams Fork Formation comprises (from stratigraphic base to top): 1) the Bowie Shale Member which includes (from base to top) the Cameo-Wheeler coal zone, the South-Canyon coal zone, the Middle Sandstone, and the Upper Sandstone; 2) the Paonia Shale Member which includes the Coal-Ridge coal zone; and 3) the undifferentiated middle and upper Williams Fork Formation (Figure 5; Carroll et al., 2004). The Williams Fork Formation is overlain by the Ohio Creek Member and is separated from this interval by an unconformity (Johnson and May, 1980; Hettinger and Kirschbaum, 2003, 2004; Johnson and Roberts 2003; Patterson et al., 2003). In the study area, this unconformity is evident from

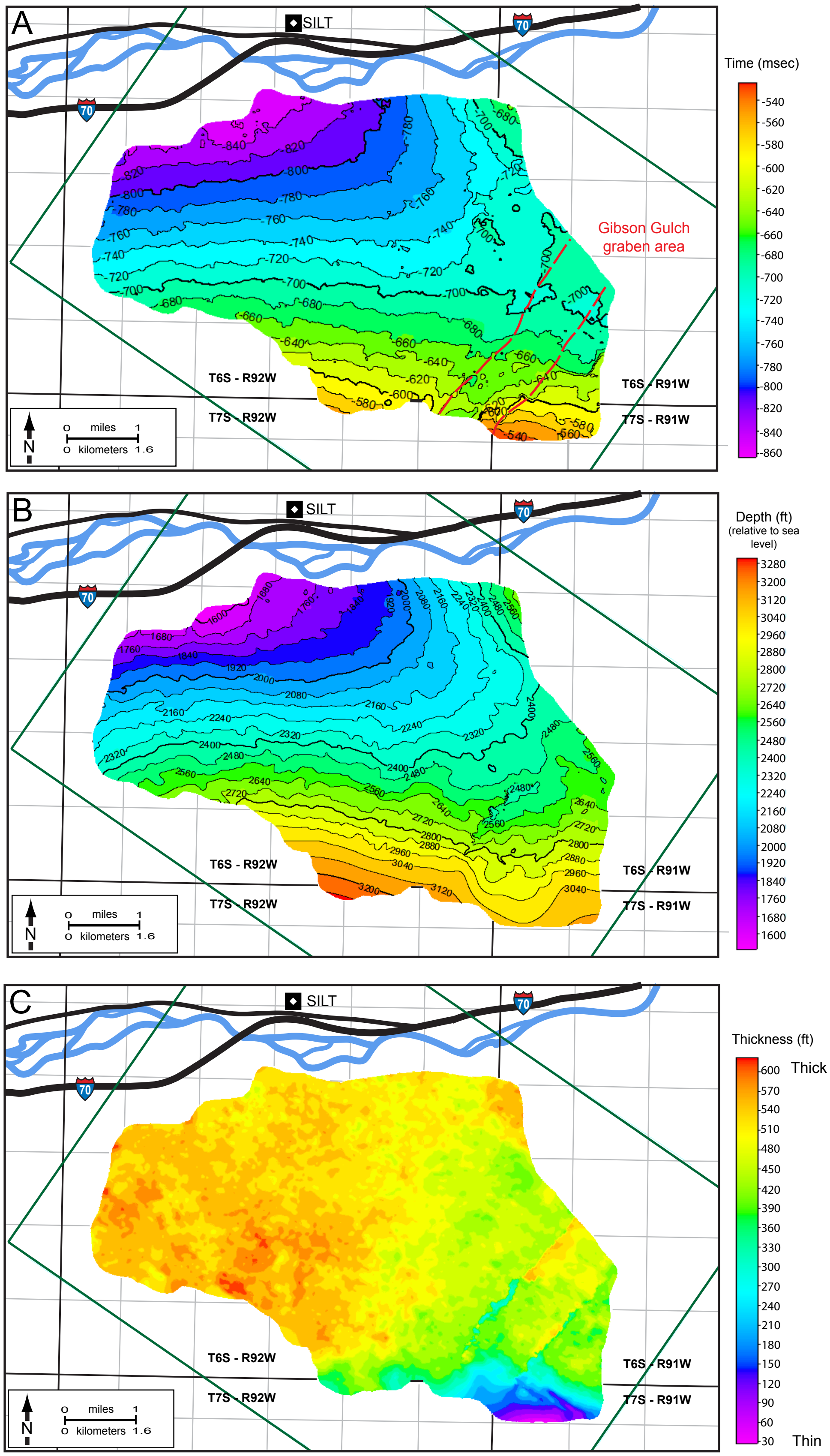

Figure 12. A) Time structure contour map, B) Depth structure contour map, and C) Isopach map of the Ohio Creek Member interval interpreted from three dimensional seismic data. Time and depth structure maps are same as the top of Mesaverde Group. Isopach map indicates thickness variations across the area. Irregular shape of the maps are due to uninterpreted area where data either is poor or not available.

disrupted reflections of the top of the Williams Fork Formation horizon and from onlapping reflections (Figure 11A and 11B). The top of the Williams Fork Formation horizon (also referred as to the base of the Ohio Creek Member) is expressed as a positive amplitude (peak) that has fair-to-moderate amplitude strength and moderate continuity. Reflections are especially interrupted in the Gibson Gulch graben area because of the displacement caused by graben. Reflection configuration of the Williams Fork Formation varies with depth and depositional environment (Figure 10). Distinct differences in reflection configuration exist between the undifferentiated middle and upper Williams Fork Formation that were deposited in alluvial plain and fluvial settings and the lower Williams Fork Formation that is characterized by lower-coastal plain and marine settings (Figure 10). The reflection configuration of each interval is described in individual sections below. In the study area, the Williams Fork Formation has a maximum thickness of ~3460 ft (~1055 m) and an average thickness of ~3067 ft (~935 m) (Figure 13). The isopach map shows thinning of the Williams Fork Formation toward the Grand Hogback monocline and abrupt thickness changes in the graben area (Figure 13).

“Undifferentiated” Middle and Upper Williams Fork Formation

From the base of the Ohio Creek Formation through the base of the middle Williams Fork Formation (also referred to as the top of the Paonia Shale Member) lie the “undifferentiated” middle and upper Williams Fork Formation dominated by fluvial deposits that include sandstone, siltstone, and shale lithologies. The horizon bounded at the top of this interval is the base of the Ohio Creek Member horizon which is a moderately continuous positive amplitude (peak) that has fair-to-moderate amplitude strength, while the base of this interval is expressed as poorly continuous, low negative amplitude (trough) that is very challenging to trace through some areas because of the dimming of the amplitudes (Figures 10 and 14). The fair-to-moderate amplitude strength at the top and the base of the whole interval indicates a low velocity-density contrast between this interval and the overlying Ohio Creek Member and the underlying

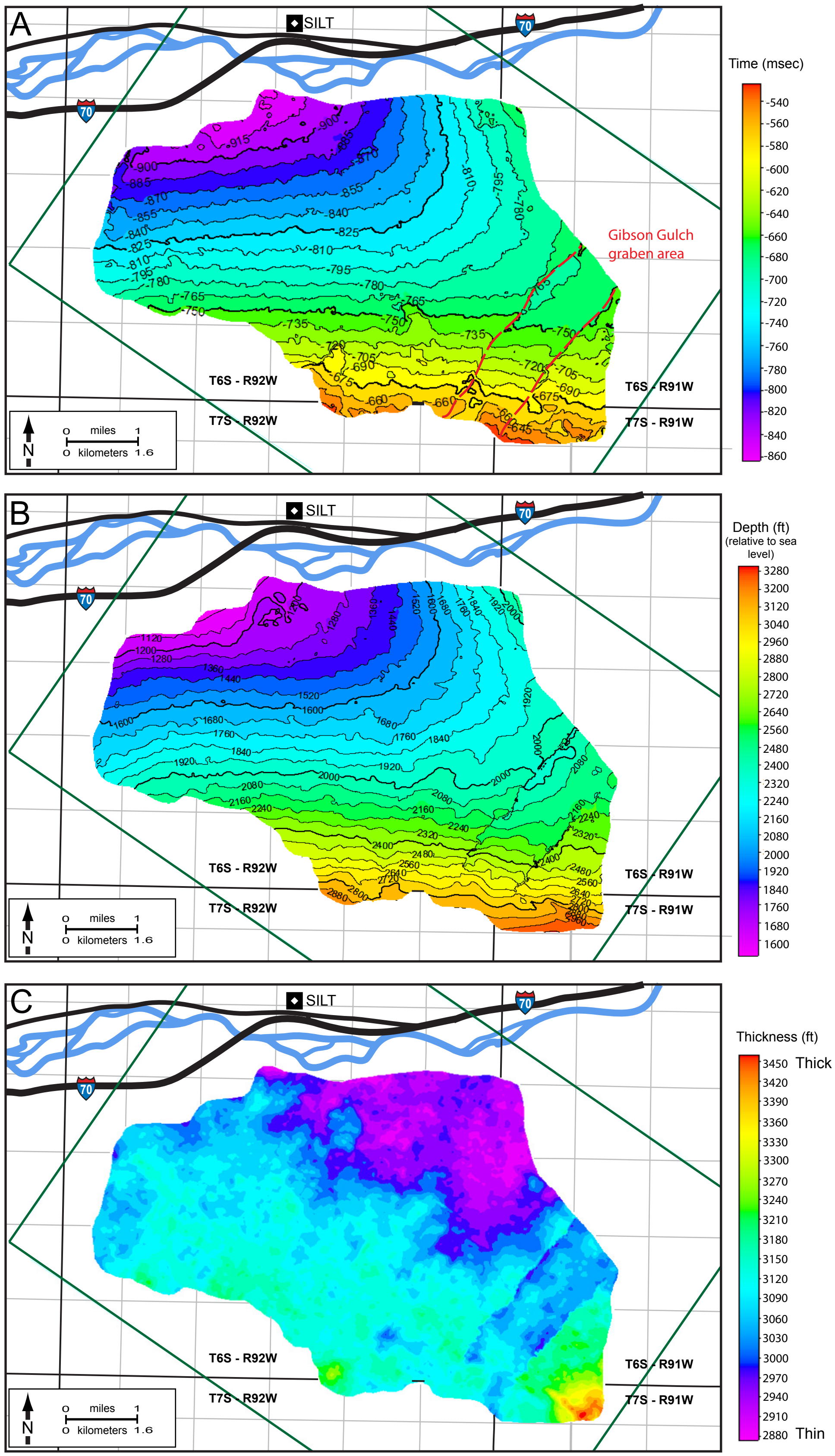

Figure 13. A) Time structure contour map, B) Depth structure contour map, and C) Isopach map of the Williams Fork Formation interval interpreted from three dimensional seismic data. Gibson Gulch Graben area is present on structure contour maps both in time and depth. Isopach map shows thickness variation of this interval. Irregular shape is due to uninterpreted area where data either is poor or not available.

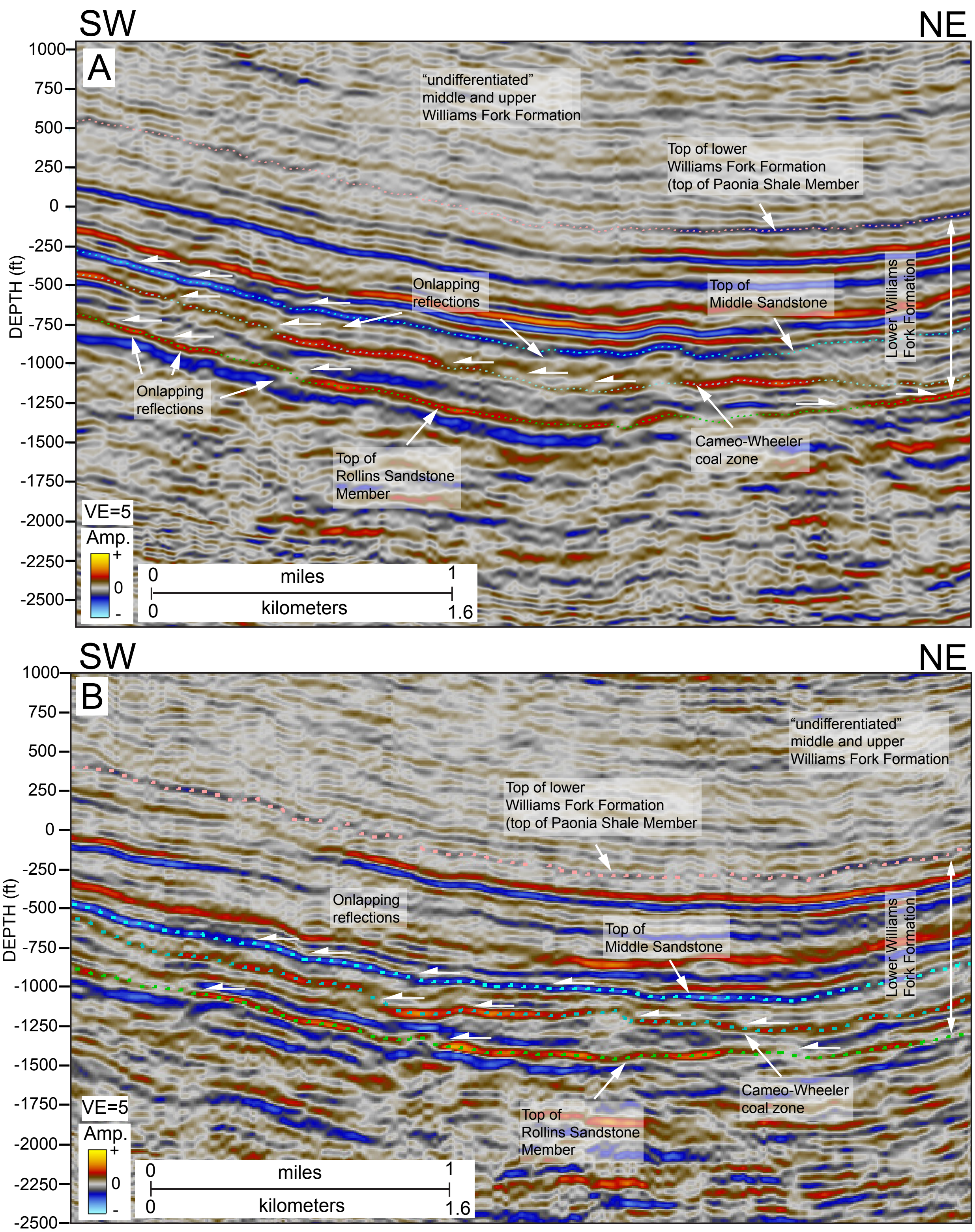

Figure 14. A) Vertical seismic inline (inline 164). B) Vertical seismic inline (inline 200) through the seismic amplitude volume showing reflection strength, reflection continuity, and reflection configuration for lower Williams Fork Formation interval including Middle Sandstone, Cameo-Wheeler coal zone, and Rollins Sandstone Member of the Iles Formation. Onlapping reflections are present. Locations of the seismic sections are given in Figure 8B.

uppermost part of lower Williams Fork Formation (Figure 10 and 14). The most distinct feature within this interval is Price coal which is a thin coal 1-3 ft (0.3-0.9 m) in thickness and informally named. Price coal is an important seismic marker across the study area, which has highly continuous negative amplitude (trough) and high reflection amplitude strength (Figures 9, 10, and 11). Price coal is identified easily using 3-D auto-tracker. Cole and Cumella (2005) suggest that the Price coal reflector can be confidently correlated from the east Parachute field through the Mamm Creek field. Price coal reflections are disrupted in the Gibson Gulch graben area by tens of feet of displacement caused by the graben. The Price coal horizon surface map clearly reveals the lateral extent of the Gibson Gulch graben area (Figure 15). Reflection configuration of the “undifferentiated” middle and upper Williams Fork Formation interval shows depositional characteristics similar to those in the Ohio Creek Member (Figures 10 and 11), including parallel-to-subparallel reflections, reflector offset, poor amplitude coherency, and dimming of amplitudes (Figures 10 and 11). The distinction between middle and upper Williams Fork Formation is difficult to establish on the basis of seismic data only and there was no formation top available to aid in interpretation of this horizon. The entire “undifferentiated” interval of the middle and upper Williams Fork Formation has a maximum thickness of 2100 ft (640 m) and an average thickness of 1813 ft (552 m) in the study area (Figure 16).

Lower Williams Fork Formation (including the Paonia Shale Member and the Bowie Shale Members)

The lowermost Williams Fork Formation is divided into the Bowie Shale Member and the overlying Paonia Shale Member. This entire interval is bounded at the top by the base of the Middle Williams Fork Formation (also referred to as the top of the Paonia Shale and the top of the lower Williams Fork Formation) and at the bottom by the top of the Rollins Sandstone Member of the Iles Formation (sees Figure 5 for stratigraphic column). Within the lower Williams Fork Formation, the Middle Sandstone and the Cameo-Wheeler coal zone of the Bowie

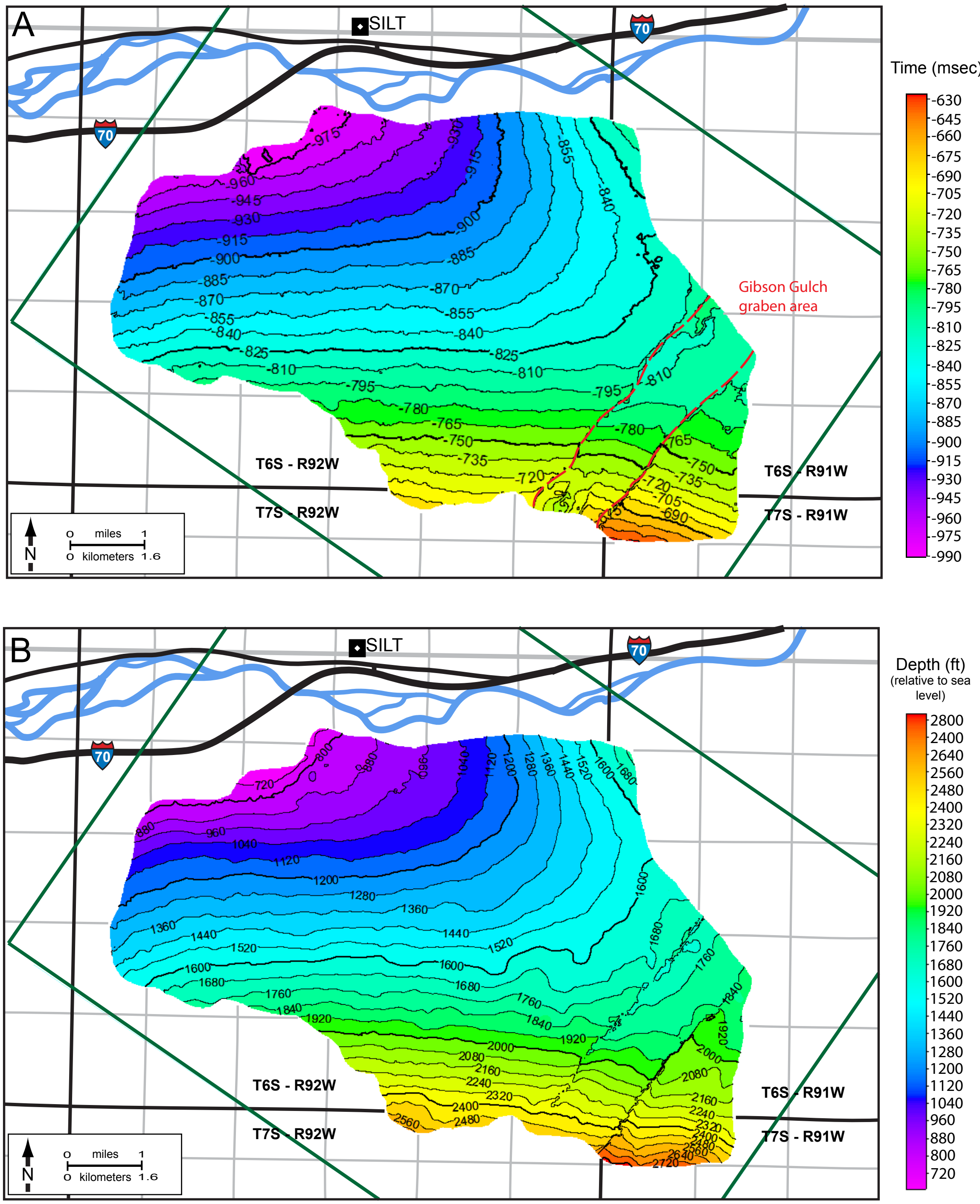

Figure 15. A) Time structure contour map, B) Depth structure contour map of the Price Coal. Structure contour maps reveals the extent of the Gibson Gulch graben area.

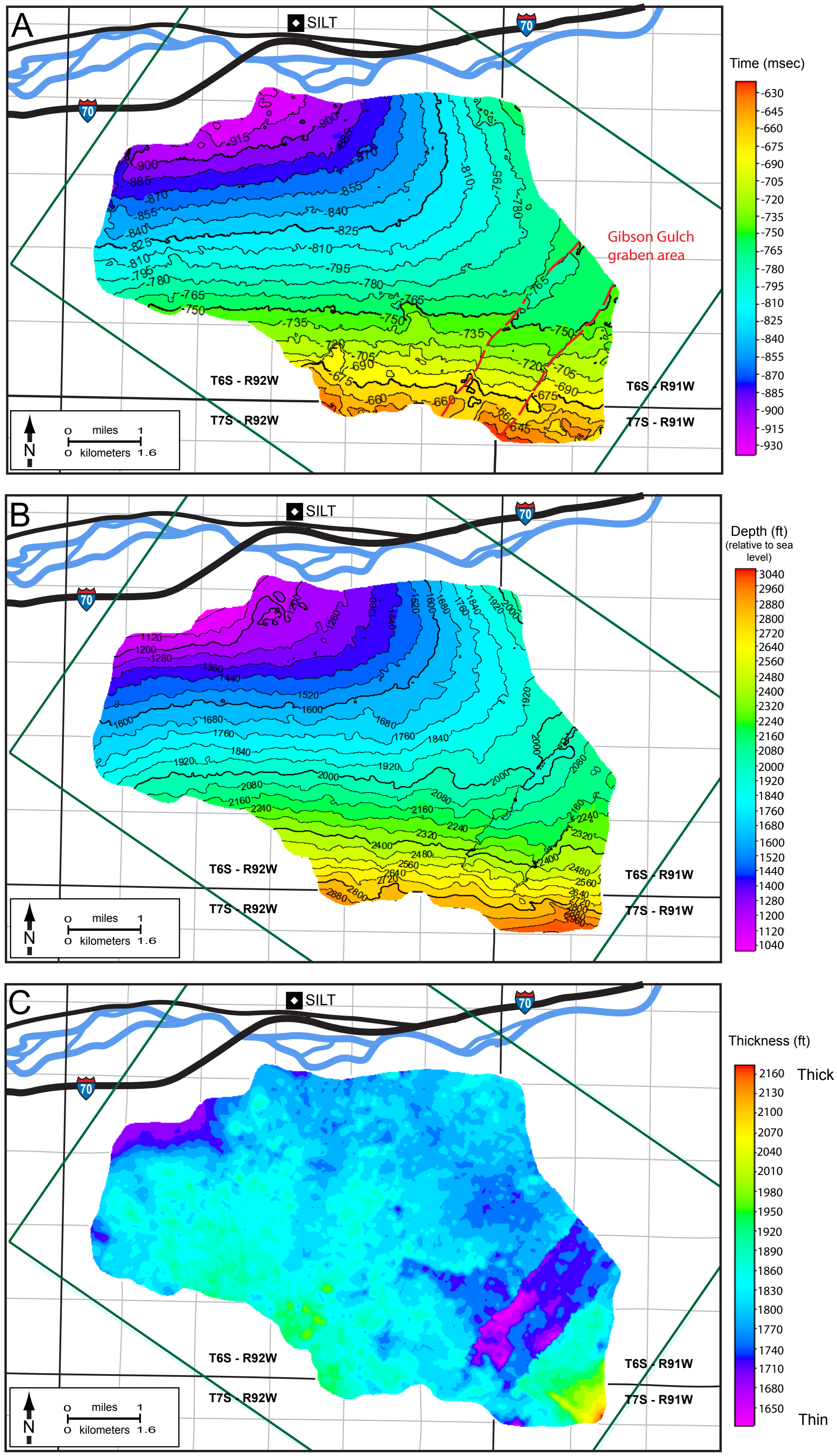

Figure 16. A) Time structure contour map, B) Depth structure contour map, and C) Isopach map of “undifferentiated” middle and upper Williams Fork Formation interpreted from three dimensional seismic data. Isopach map indicates thickness variations across the area. Irregular shape of the maps are due to uninterpreted area where data either is poor or not available.

Shale Member are seismically expressed; however, the South-Canyon coal zone and the Upper Sandstone of the Bowie Shale Member and the Coal-Ridge coal zone of the Paonia Shale Member appear not to be resolved by seismic data (Figure 14). Although these intervals are expressed in seismic data, interpretation is complex and reflections are difficult to trace. The lower Williams Fork Formation in the study area has a maximum thickness of 1491 ft (454.5 m) and an average thickness of 1254 ft (382 m), thinning to the northeast of the study area toward the Grand Hogback (Figure 17).

Middle Sandstone of the Bowie Shale Member

The Middle Sandstone of the Bowie Shale Member is a transgressive marine sandstone unit which is only present in the easternmost part of the Piceance Basin. In the study area, the Middle Sandstone is expressed as moderate-to-high negative amplitude (trough) which has moderate-to-good continuity and can be comfortably traced across the seismic data (Figure 14). The presence of an unconformity surface (sequence boundary) at the top of this marine unit is evident from onlapping seismic reflections, which suggest that the South Canyon coal zone overlies this marine unit uncomfortably (Figure 14). The Middle Sandstone has a maximum thickness of 395 ft (120 m) and an average thickness of 170 ft (51 m), thickening to the east in the study area (Figure 18).

Cameo-Wheeler Coal Zone of the Bowie Shale Member

The Cameo-Wheeler coal zone is the most important coal zone among the other coal zones within the lower Williams Fork Formation (Johnson, 1989; Johnson and Roberts, 2003). In the study area, onlapping reflection patterns at the top and the base of this interval suggest that this economically significant coal zone overlies the Rollins Sandstone Member uncomfortably and is divided from overlying strata by an unconformity surface (Figure 10; Patterson et al., 2003). In seismic data, the top of this interval is expressed by low-to-moderate

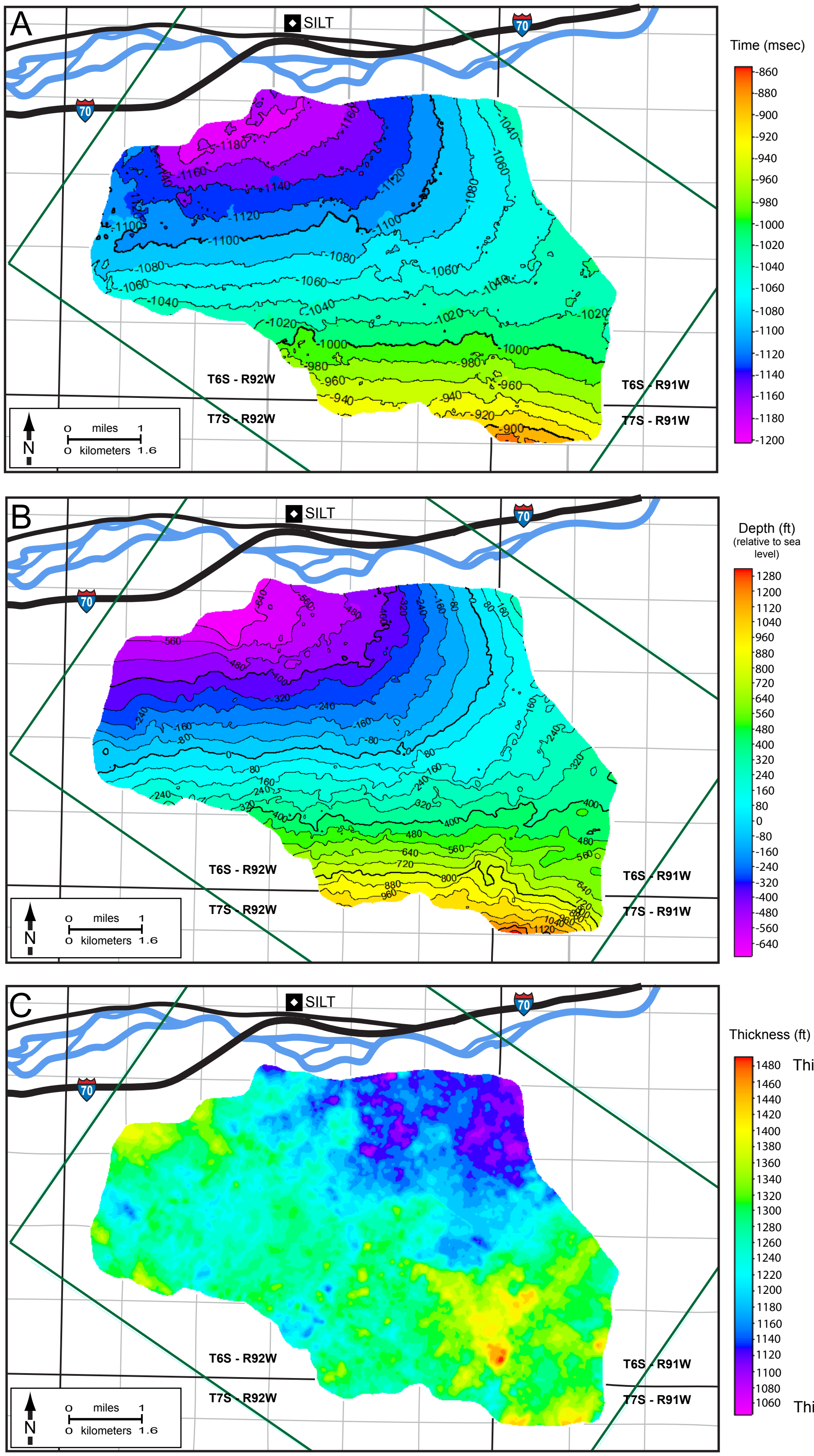

Figure 17. A) Time structure contour map, B) Depth structure contour map, and C) Isopach map of the lower Williams Fork Formation interpreted from three dimensional seismic data. Isopach map indicates that interval thins northeast and thickens southeast. Irregular shape of the maps are due to uninterpreted area where data either is poor or not available.

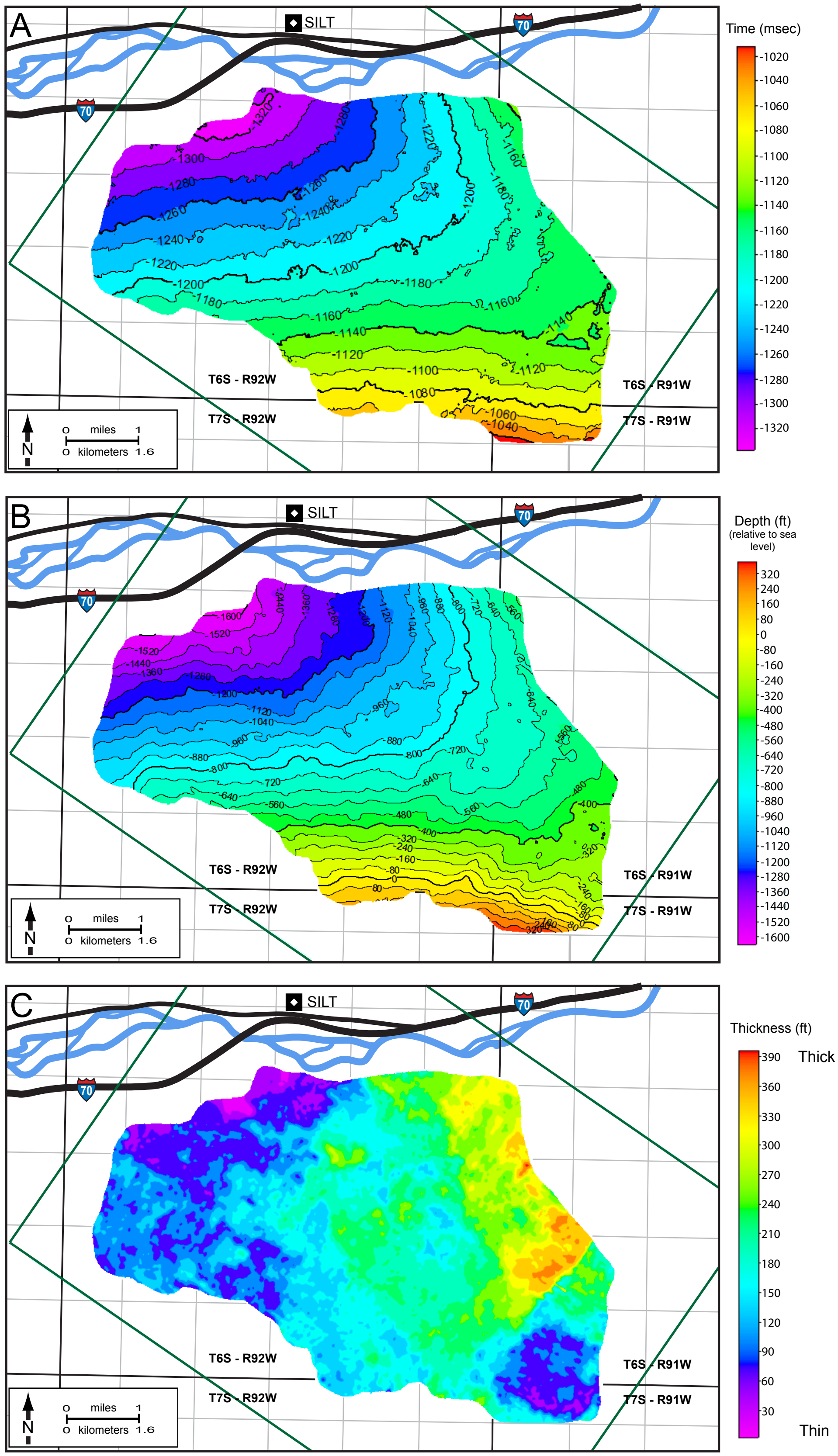

Figure 18. A) Time structure contour map, B) Depth structure contour map, and C) Isopach map of the Middle Sandstone interpreted from three dimensional seismic data. Isopach map shows abrupt thickness changes which is consistent with faults. Irregular shape of the maps are due to uninterpreted area where data either is poor or not available.

positive amplitude (peak) which is moderately continuous across the study area. In terms of interval reflection configuration, although the whole interval is mostly expressed by negative amplitude (trough), positive amplitudes are still present and interrupt negative amplitudes, suggesting that there is change in impedance within the interval (Figure 14). This entire interval has a maximum thickness of 416 ft (127 m) and an average thickness of 233 ft (71 m) based on the isopach map generated using interpreted horizons. The whole interval thins to the northeastern part of the study area (Figure 19).

Rollins Sandstone Member of the Iles Formation

The Rollins Sandstone Member of the Iles Formation underlies the Cameo-Wheeler coal zone and marks the lower boundary of the Williams Fork Formation. In seismic data, the top of the Rollins Sandstone Member is expressed by moderate-to-high positive amplitude (peak), which suggests an increase in acoustic impedance into this interval (Figure 14). Reflections are moderately continuous except where they are interrupted by the offset which causes the dimming of the reflections. Seismic data suggests that the Cameo-Wheeler coal zone overlies the Rollins Sandstone Member uncomfortably, shown by onlapping reflection patterns onto the Rollins Sandstone Member horizon (Figure 14). The Rollins Sandstone Member structure contour map can be seen in Figure 20.

DISCUSSION

In the Piceance Basin, 10-acre (435600 ft^2 and 40468.5 m^2) well spacing provides abundant control to interpret stratigraphic units, and well-log data provide a reliable and fine-scale input for comparison to the lower resolution seismic data. However, correlating the discontinuous, lenticular-shape sandstone bodies and highly variable coals of the Williams Fork Formation has always been a challenge because of the small scale variations caused by the fluvial depositional characteristic of this interval. Structure contour maps and isopach maps

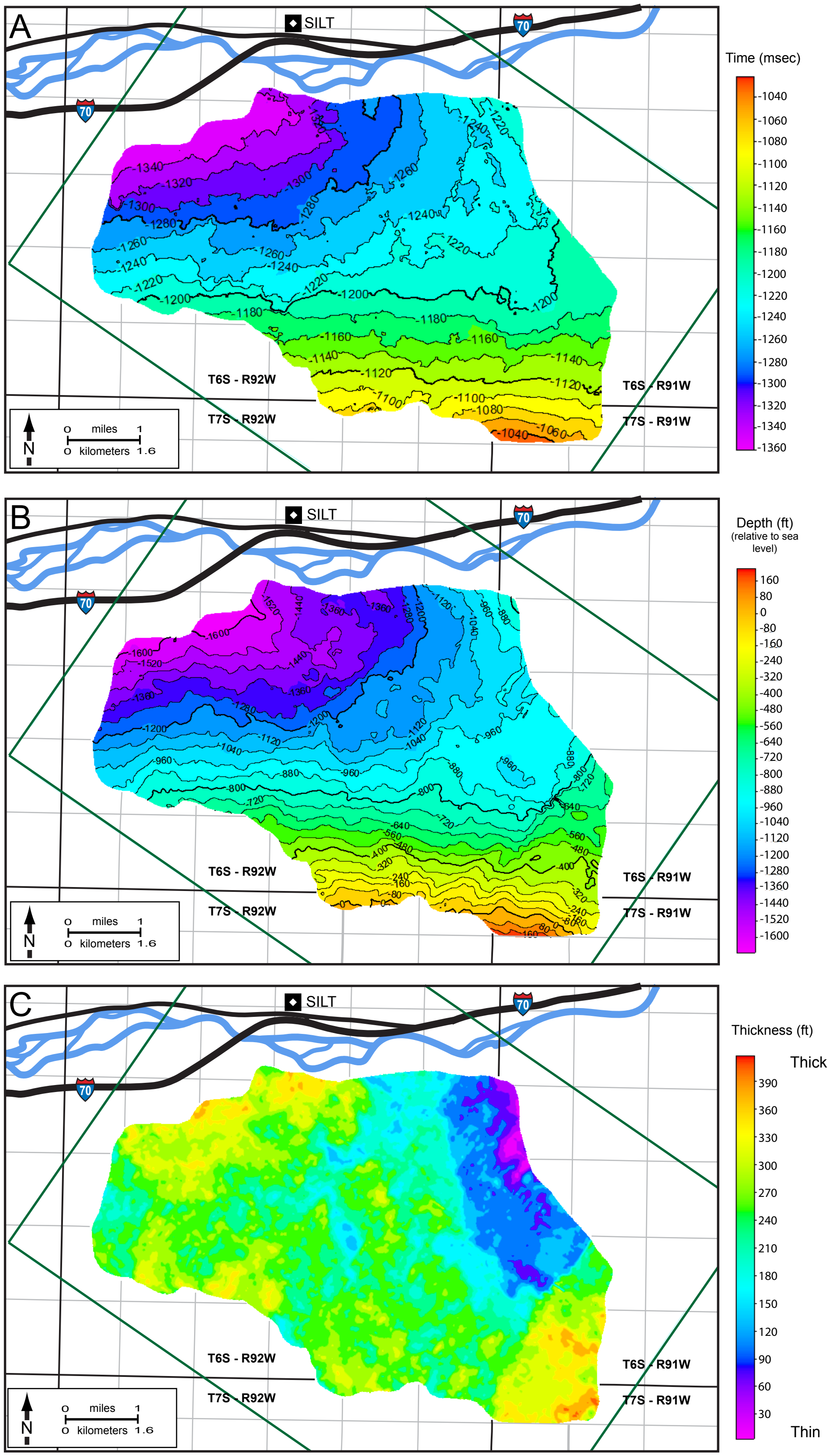

Figure 19. A) Time structure contour map, B) Depth structure contour map, and C) Isopach map of the Cameo-Wheeler coal zone interpreted from three dimensional seismic data. Abrupt thickness chnages are present. Irregular shape of the maps are due to uninterpreted area where data either is poor or not available.

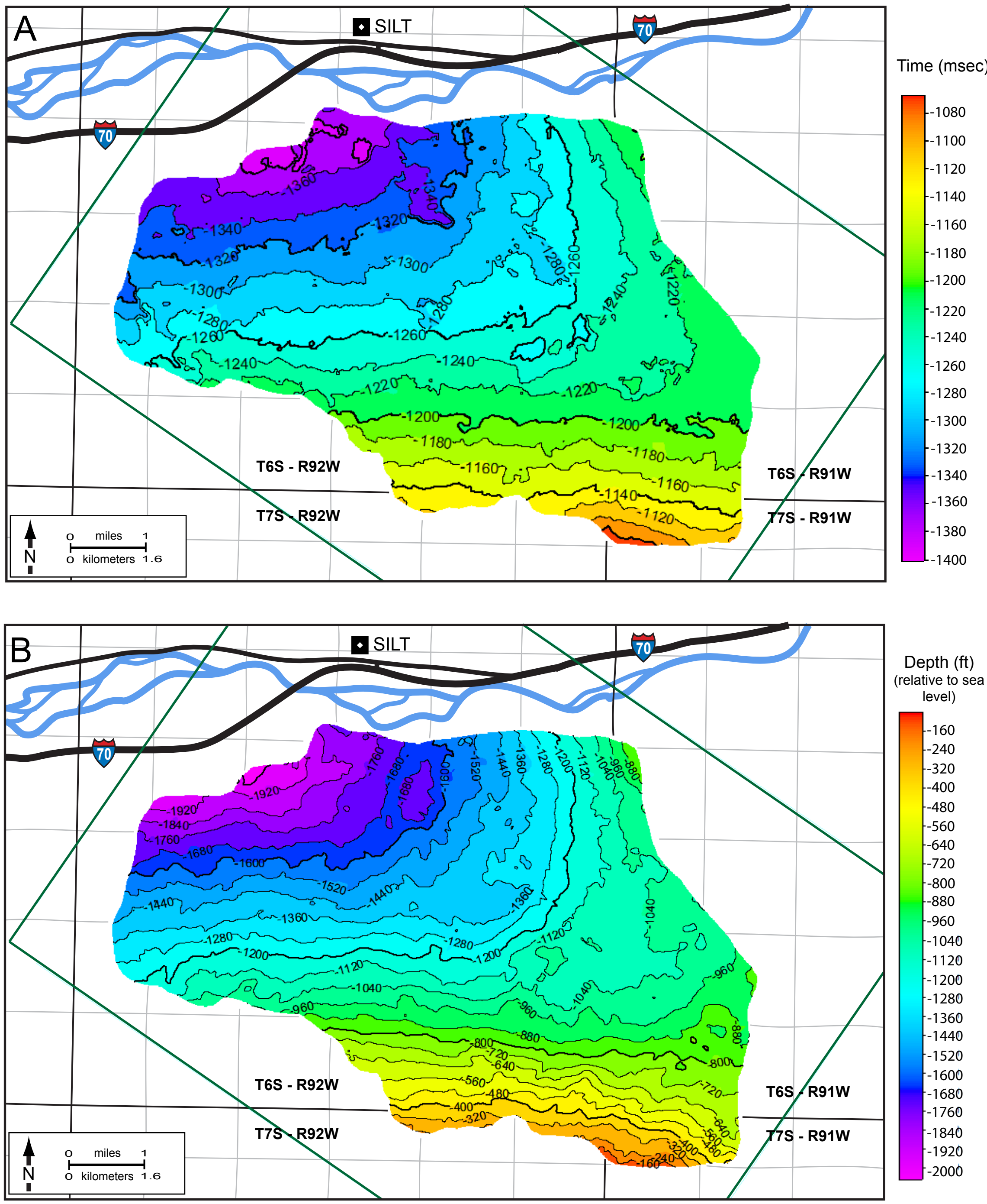

Figure 20. A) Time structure contour map, B) Depth structure contour map of the Rollins Sandstone Member.

generated using interpreted well tops as an input show the structure and thickness variations within the Williams Fork Formation; however, well-log data is limited to wellbores and data gaps between wells are interpolated. Three-dimensional seismic interpretations of key stratigraphic units in the study area reveal that thickness and structure vary considerably between wells and that stratigraphic variations are complex. Based on seismic interpretation, thicknesses derived from isopach maps and structure contour maps of key stratigraphic surfaces are consistent with previous observations in the eastern and southeastern Piceance Basin (Johnson and May, 1980; Johnson and Flores, 1980; Hoak and Klawitter, 1997; Hettinger and Kirschbaum, 2002, 2003).

CHAPTER THREE

STRUCTURAL INTERPRETATION OF THREE DIMENSIONAL SEISMIC DATA

PREVIOUS STUDIES

Numerous studies completed by multiple groups of workers in the central and eastern Piceance Basin relate natural fractures, regional structure, and fault characteristics to gas production in the Williams Fork Formation.

Lorenz and Finley (1991) identify a regional set of west-northwest extension fractures as an example of load-parallel extension fracturing and basinwide dilatancy at depth, under conditions of high pore pressure and anisotropic horizontal stress. Grout and Verbeek (1992), in a study of the Divide Creek and Wolf Creek anticlines in the southern Piceance Basin (south of the study area), related three or possibly four fracture sets to a basement-involved thrusting wedge underneath those structures. Thus, they conclude that the presence of these fractures is responsible for enhanced fracture permeability at least in this part of the basin. Hoak and Klawitter (1997) investigate the control of subsurface structures on production trends and the relationship to deeper basement fault trends. They suggest that basement thrust faults terminate up-section in the coals and fluvial sands of the Mesaverde Group, thus enhancing fracture permeability at the tip line termination. Figure 21 shows two schematic cross-sections, which are generated by Hoak and Klawitter (1997) and Wilson et al. (1998) and a geoseismic profile, which is interpreted by R. Bouroullec (2009) as part of an ongoing research, illustrating the relationships in basement-involved thrusting and their relevance to the Mesaverde Group and the Mancos shale. They also suggest more intense thrusting in the eastern basin with strong influence of Mancos–level detachment on Mesaverde Group reservoirs. Verbeek and Grout (1998) study relations between basement structures in Precambrian crystalline rocks and fracture systems in overlying rocks in three parts of the Colorado Plateau. They give examples

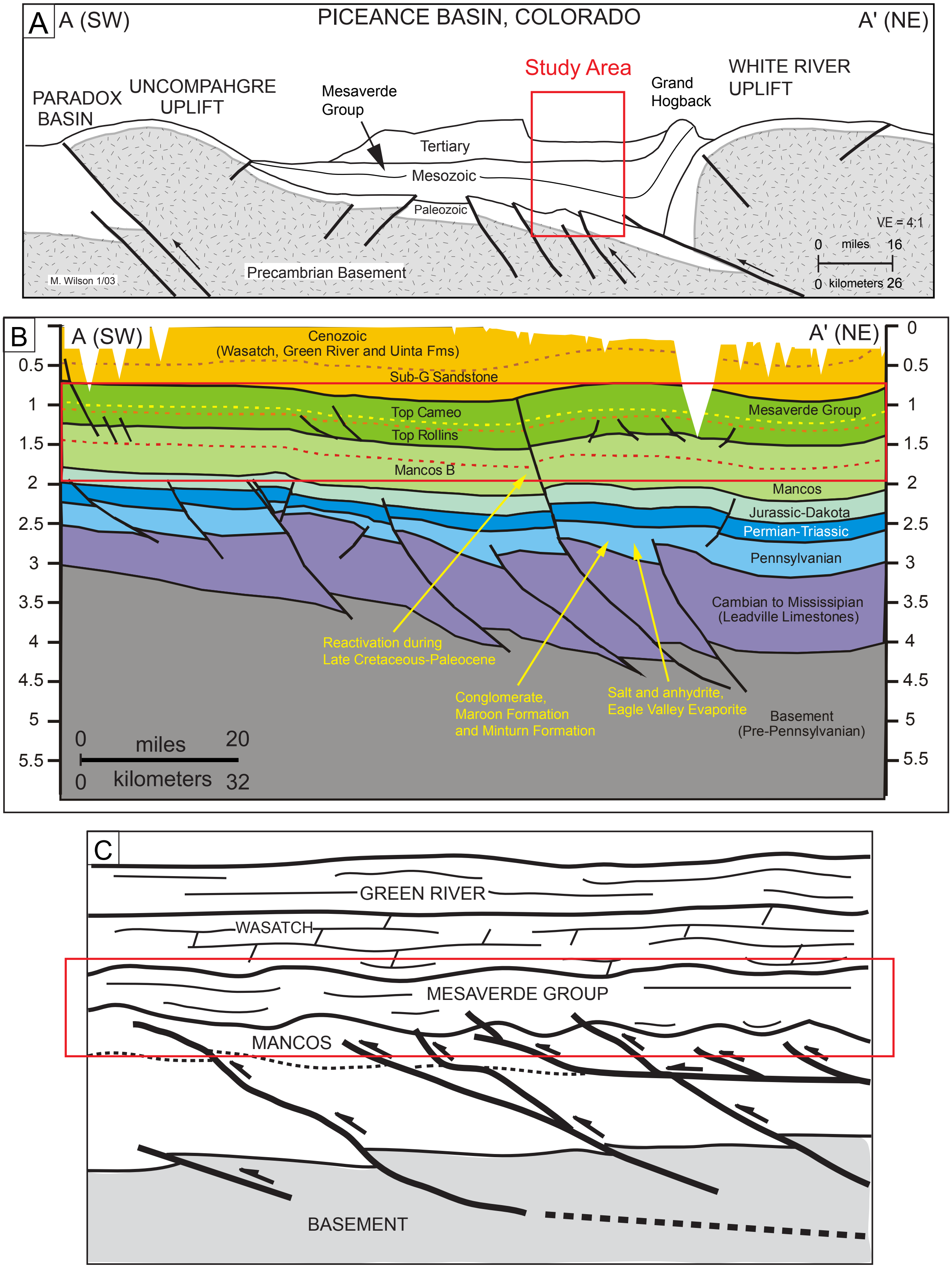

Figure 21. A) Schematic cross sections illustrating the structural style in the southern Piceance Basin. See Figure 8A for the location of the cross section. B) Geoseismic profile provided by Renaud Bouroullec shows some of the structure at deeper levels, location of the profile shown in Figure 8A. C) Schematic illustration of the multiple detachment surfaces interpreted from regional seismic, typical of the eastern and central Piceance Basin. The interval and the area of study is shown in red outline. Modified from Hoak and Klawitter (1997) and Wilson et al. (1998).

from the Grand Hogback and the Divide Creek and Wolf Creek anticlines area in the Piceance Basin section of their study. Cumella and Ostby (2003) suggest a left-lateral transpressional structural style based on seismic data in Parachute and the Rulison gas field. They show left-lateral, near vertical faults trending ~N45°W on seismic data. Some of their observations include the eastward rise of the Williams Fork Formation toward the Mamm Creek field; abrupt thickness changes in the Cameo-Wheeler coal zone interval near faults, which indicates structural growth of faults during the time of Cameo deposition; and major fault zones in the Mesaverde Group and their relationship to deep-seated fault zones.

Jansen (2005) uses seismic attributes to characterize a complex wrench fault network and its relations to enhanced natural fracture zones. He links the occurrence of natural fractures to fault geometry and tectonic fracturing to gas production at the Rulison gas field within the Mesaverde Group interval. Jackson (2007) presents a structural model that incorporates well data, three-dimensional seismic data, geomechanical analysis, and well production data to characterize the Mesaverde Group tight gas sandstone reservoirs. His model highlights compartmentalization within key reservoir intervals, confirms that the fault zones are pathways for fluid migration, and correlates to areas of known fracture production. Matesic (2007) characterizes structural and stratigraphic features in the lower Williams Fork Formation at the Rulison gas field using three image logs. He suggests that faulted zones of enhanced permeability are accompanied by fractures of the same orientation. He also analyzes fractures and the orientation of maximum horizontal in-situ stress (Sh_{max}) based on borehole-image logs. LaBarre (2008), in a study of the Late Cretaceous Williams Fork Formation interval at the Rulison gas field, suggests the presence of north-northwest oriented faults in the Cameo coal interval based on compressional and shear wave data. LaBarre (2008) notes the upward propagation of these faults into the main reservoir interval, arguing that wrench faults splay as flower structures that control the fracturing in the Williams Fork Formation.

SEISMIC ANALYSIS OF FAULTS

Introduction

Evaluation of the types, distributions, and orientations of faults completed using 3-D seismic p-wave data, including curvature and ant-track attributes. Interpretation of structural features using different seismic attributes and the original 3-D seismic p-wave data increases confidence, reduces the time spent interpreting discontinuities, and decreases subjectivity and user bias in interpretation; hence it leads to a more reliable interpretation including the interpretation of small-scale faults. The ant-track filter is used to create an enhanced fault volume by taking all spatial discontinuities into account in three dimensions, allowing the interpreter to better characterize subtle or complex features in the seismic data. Using the ant-track results, a combination of both manual interpretation and auto-track interpretation were used. This workflow merged visualization of the ant-track attribute volume with the seismic-amplitude volume, resulting in a more accurate interpretation. Vertical and horizontal seismic sections (depth and time slices from the seismic volumes) were commonly used to step through the seismic data in order to evaluate seismic discontinuities by using reflection dip and other characteristics.

METHODS

Ant-Tracking Workflow (Ant-track Attribute Generation)

The ant-tracking algorithm is based on the idea of ant colony systems to capture trends in noisy data. Intelligent agents, also referred as “ants”, trace or extract discontinuous features on an edge-detection volume, such as chaos, variance, or coherence. This approach enhances the discontinuities on edge-detection volume because it only captures features that are continuous and likely to be faults. Non structural features such as noise and channels are less likely to be captured by the ant-tracking algorithm because these features usually have internally chaotic texture, which is not continuous, that prevents the ant-tracker from extracting these non-surface-shaped features (Jansen, 2005). The ant-tracker uses the principles of swarm intelligence, which describes the collective behavior of a group of social insects; for example, how ants find the shortest path between the nest and a food by communicating via a chemical substance (Pedersen et al., 2002).

The ant-track workflow consists of four main activities: 1) seismic conditioning; 2) edge detection; 3) edge enhancement (ant tracking); and 4) interactive interpretation (Figure 22). Seismic conditioning improves the data signal-to-noise ratio and leads an improved edge-detection volume. The second step, edge detection, involves running one of any available edge-detection methods to enhance spatial discontinuities in the seismic data. In this study, variance is preferred rather than chaos, because the chaos attribute enhances not only faults but also chaotic textures within the seismic data (carbonate reefs, channels, gas chimneys, etc.), as indicated by Randen et al. (2001). Results from the Gibson Gulch graben area show that chaos creates more chaotic results and it allows too many chaotic textures within the seismic data (Figure 23). The third step in ant-tracking workflow, edge enhancement, generates the ant-track volume. This step significantly improves the fault attributes by suppressing noise and the remains of non-fault events. The fourth step, interactive interpretation, involves traditional 3-D seismic interpretation using manual or auto-tracking methods or automatic-fault extraction. This step provides the interpreter with functionality to validate extracted surfaces because surfaces that are not faults may still be extracted (Pedersen et al., 2002). As indicated before, non structural features such as noise and channels have internally chaotic texture and are discontinuous; therefore they are less likely to be traced by the ant-tracker (Jansen, 2005). Traditional or conventional 3-D seismic interpretation methods were used in this study.

Seismic Conditioning

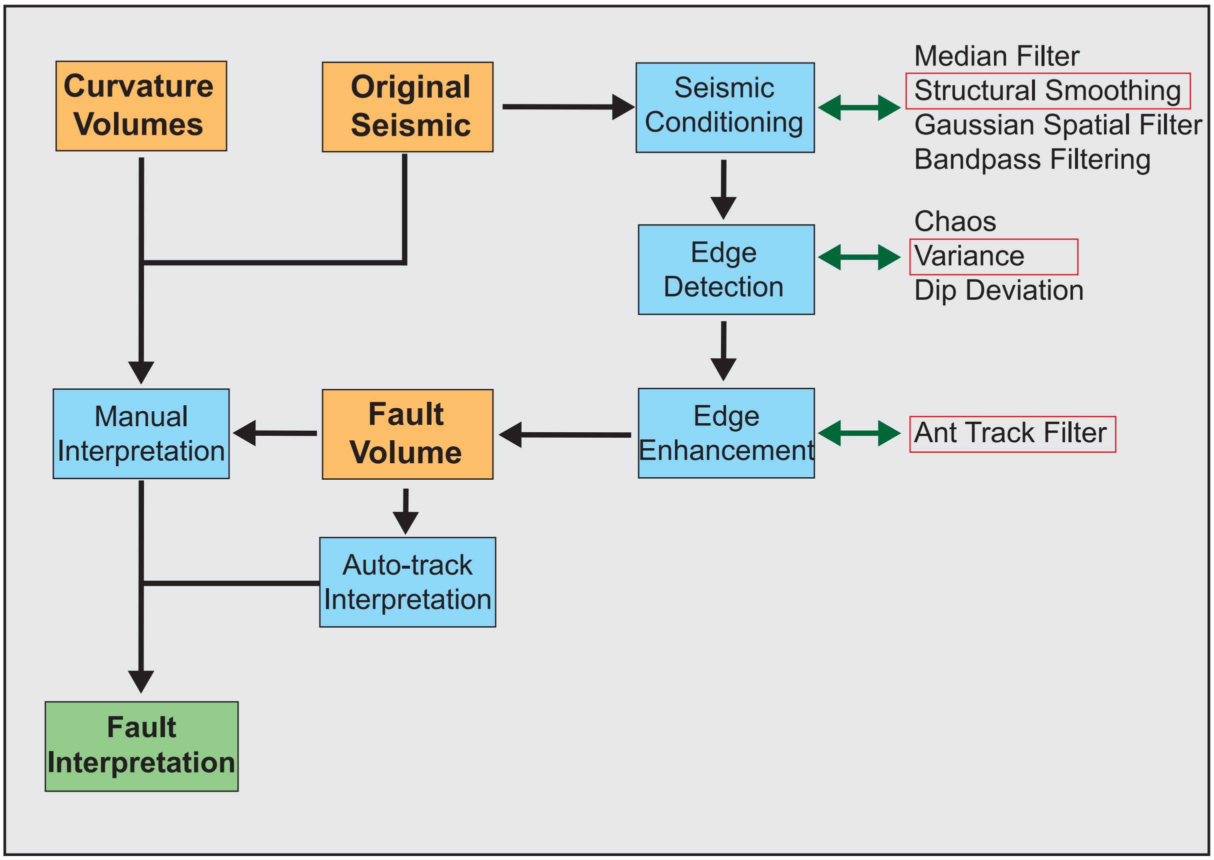

Figure 22. Ant-tracking Workflow. Fault interpretation is done using a fault volume, original seismic data, and curvature volumes. Ant-tracking workflow consists of four steps: 1) seismic conditioning; 2) edge detection; 3) edge enhancement; and 4) interactive interpretation using original seismic, curvature attributes, and fault volume (ant-track attribute volume). Modified from Petrel Workflow Tools, 2009.

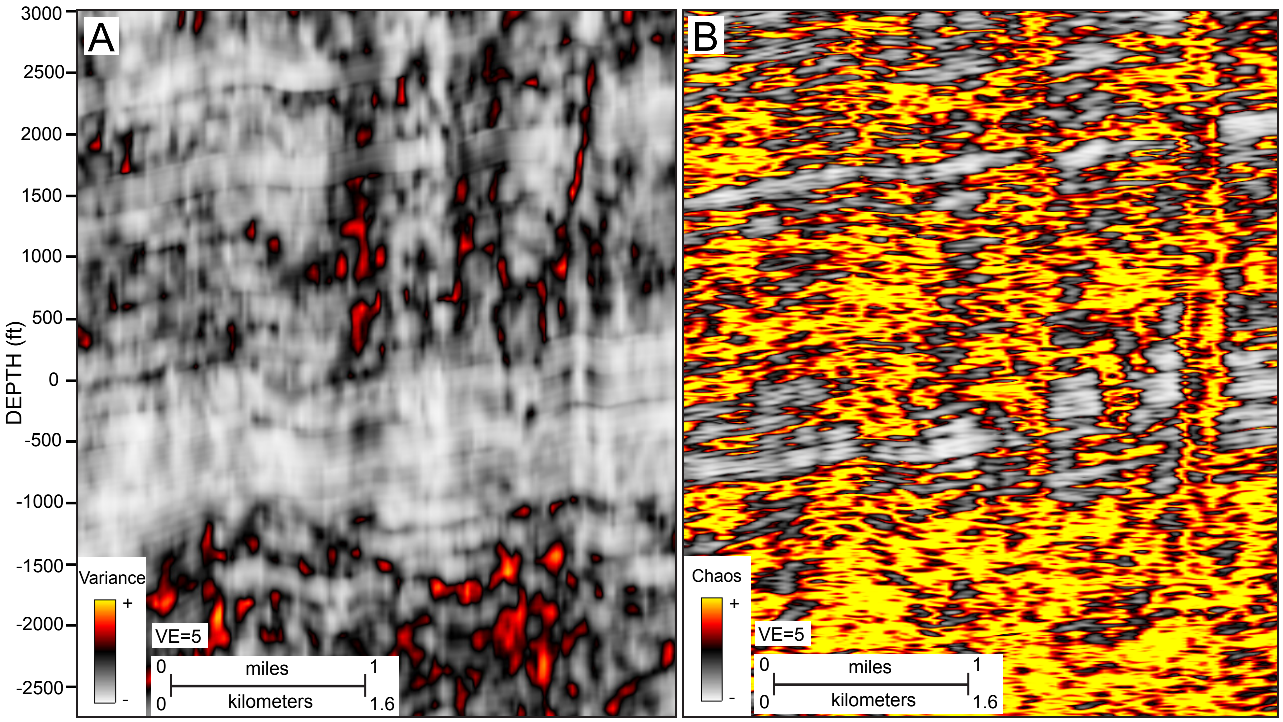

Figure 23. Vertical seismic sections (crossline 145) through the variance (on the left) and chaos (on the right) attribute volumes. The difference between the products of two edge detection methods can be seen. Variance is the preferred attribute. Chaos will not only enhance faults but also allows too much chaotic texture within this seismic data.

Seismic conditioning was conducted using structural smoothing, which uses principal component dip/azimuth computation to determine the local structure; following that, it applies Gaussian smoothing parallel to the orientation of the local structure to reduce the noise and improve results for seismic edge detection. Randen et al. (2003) indicates that “the traditional approach of extracting attributes along vertical traces, irrespective of any dipping nature of the data, imposes a risk of enclosing artifacts” (Randen et al., 2003, p. 1). In order to avoid such artifacts, Randen et al. (2003) introduces a dip/azimuth estimation approach that also enables layer-consisting smoothing (also referred to as “structure oriented filter” elsewhere) both with and without edge enhancement. The dip/azimuth estimation approach consists of three steps: 1) gradient vector estimation $\nabla x(t1,t2,t3)$; 2) local gradient covariance matrix estimation $C(t1,t2,t3)$; and 3) principal component analysis (Randen et al., 2000; Randen et al., 2003). This approach applies smoothing parallel to the local structure, while not applying orthogonally; therefore, it preserves the vertical resolution and enhances the lateral continuity. Then Gaussian smoothing is applied (Randen et al., 2003). Structural smoothing was used in this study because layer-parallel smoothing with edge enhancement is a powerful noise suppressing technique proven by practical experiments (Pedersen et al., 2002; Randen et al., 2003). Structural smoothing allows the user to define a filter size for inline, crossline, and vertical directions to control the number of horizontal traces and vertical samples to use for estimating structural smoothing. The filter size value represents the standard deviation for the Gaussian filter. Three different filter sizes of 1.0, 1.5, and 2.0 were tested before running edge detection (Figure 24). A standard deviation of 1.0 smoothes seismic data reasonably in this study (Figure 24). The large smoothing enhances the lateral continuity greatly while preserving major features (Randen et al., 2003). In contrast, a standard deviation of 1.5 or 2.0 is not desirable because it may cause the destruction of the features of interest. No benefit was seen in using a standard deviation value greater than 1.0, based on practical experience with the seismic data.

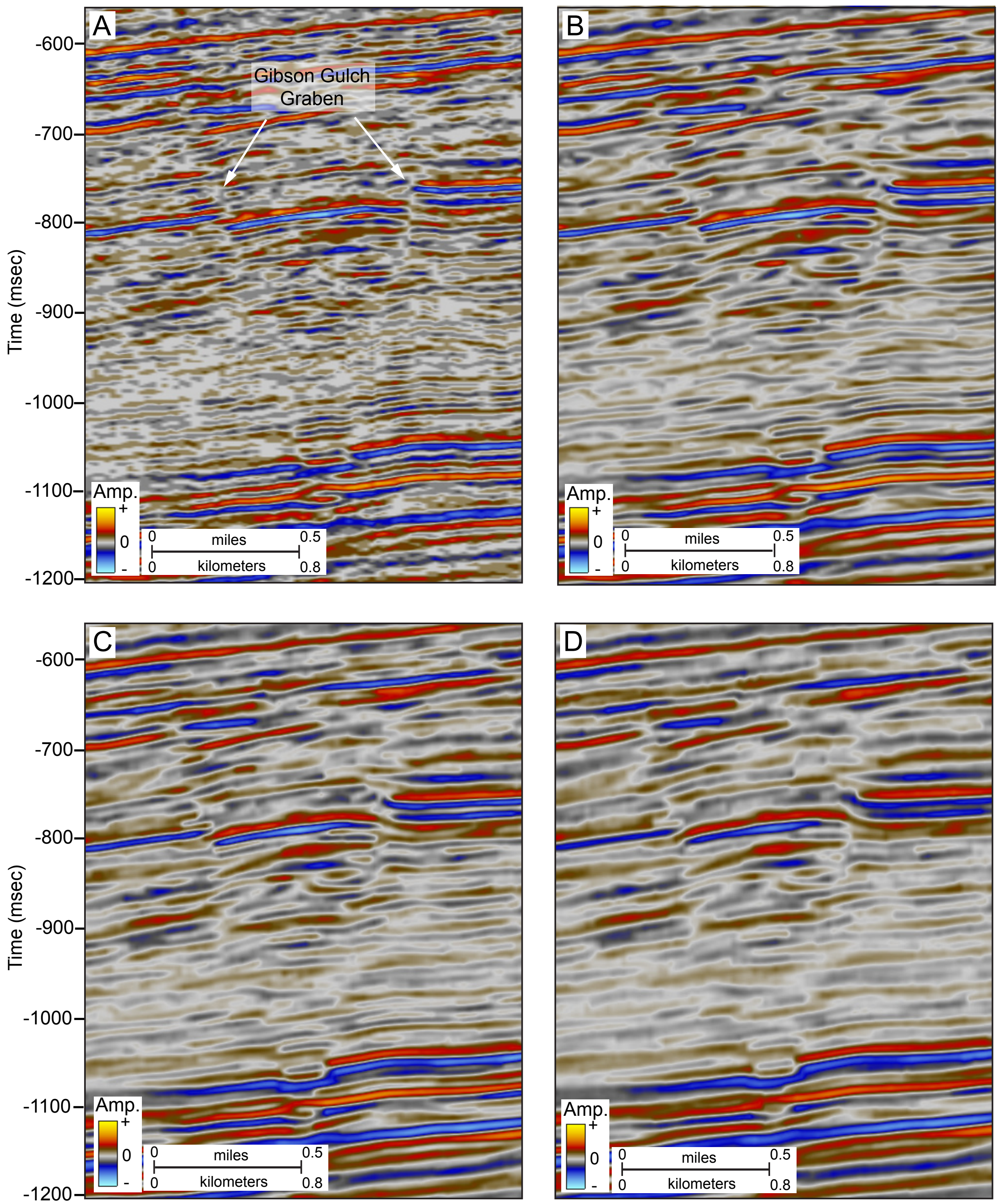

Figure 24. Vertical seismic section (crossline 147) through seismic volumes that have had structural smoothing. A) Original seismic data, notice graben, B) structural smoothing with standard deviation 1.0, C)structural smoothing with standard deviation 1.5, D) structural smoothing with standard deviation 2.0. A standard deviation of 1.0 smoothes seismic data reasonably in this study. A standard deviation of 1.5 and 2.0 is not desirable because larger smoothing enhances the lateral continuity greatly, so it may cause the destruction of the features of interest.

Edge Detection (Fault Attributes)

Seismic edge-detection methods may have the broadest and most common usage in the industry to conduct stratigraphic and structural interpretation of geologic features in seismic data (Marfurt and Chopra, 2007). Seismic edge-detection methods commonly measure the similarity between waveforms or traces to bring out stratigraphic and structural features expressed in seismic data (Marfurt and Chopra, 2007). Such information provides valuable input for reservoir modeling (Marfurt and Chopra, 2007). The most commonly used edge-detection methods are chaos, variance, and coherence. A range of chaos and variance attributes was created and evaluated for use in this study. Chaos and variance attributes show drastically different results using the same seismic data, as a result of the algorithm used by each method. The following is a concise review of chaos and variance attributes.

Chaos attribute is defined as a measure of the “lack of organization” in the dip and azimuth estimation method (Petrel Workflow Tools, 2009). In other words, it searches the chaotic signal pattern contained within seismic data; therefore, chaos in the signal can be used to help clarify faults and discontinuities and to facilitate seismic classification of chaotic texture (Petrel Seismic Vis. and Int. Course Notes, 2009). The Chaos algorithm uses the dip/azimuth estimation approach (also referred to as the dominating orientation analysis) to extract areas of discontinuities (Randen et al., 2003). Based on the dip/azimuth estimation approach introduced by Randen et al. (2001), “the dominating orientation is computed by the principal component analysis, which is found by aggregating the gradients (estimated during gradient estimation in the first step) into a covariance matrix, which is then decomposed into its corresponding eigenvectors and eigenvalues” (Randen et al., 2001, p. 552). The Chaos attribute follows directly from the dominating orientation analysis. It studies the value of the sorted eigenvalues (λ_{max}, λ_{mid}, λ_{min}) and calculates the ratio between λ_{max}, λ_{mid}, and λ_{min} to detect discontinuities in the seismic data (Randen et al., 2001). Randen et al. (2001) suggest that “the chaos attribute will not only enhance faults but also chaotic texture within the seismic" (Randen et al., 2001, p.552). This was experienced firsthand given the seismic data used in this study and is the main reason why the variance attribute was preferred.

Variance attribute measures the signal unconformity using the local variance and is used to isolate discontinuities in the horizontal continuity of amplitudes (Randen et al., 2001). Randen et al. (2001) indicate that "for each voxel, the local variance is computed from horizontal sub-slices" (Randen et al., 2001, p. 553). The variance of a slice within an unbroken reflection layer is small, whereas faults cause amplitude changes and this result in a larger variance (Randen et al., 2001). Furthermore, variance allows the user to apply an optional vertical smoothing for noise reduction and filter length to determine the number of traces horizontally for estimating horizontal variance (Petrel Seismic Vis. and Int. Course Notes, 2009). Filter lengths of 3, 5, and 7 traces are tested with vertical window size of 32-48-64-81 milliseconds (Figure 25). It is suggested that 32-64 milliseconds is a reasonable starting point, but the optimum length is data and objective dependent and also suggested that larger values (greater than 81 ms) reduce the noise effectively but "smear" the sharpness of the detected edges (Petrel Workflow Tools, 2009). Considering filter length and vertical window size, different variance attribute volumes are generated using 32-48-64-81 millisecond vertical window sizes and different filter lengths (Figure 25). Window sizes of 48 ms and smaller allow lateral events in output variance attribute volume which are related to reflection interfaces and structural dip; therefore, filter values below 48 ms were not used. A better input variance attribute for ant tracking was a volume generated using a 64 ms vertical window size, which suppresses noise and does not allow lateral events caused by reflection interfaces and structural dip (Figure 25). In addition to vertical window size, filter length significantly improves the results of edge detection because larger values lead to a larger number of traces to be taken into consideration. A filter length of five traces was found to be very beneficial, whereas there is no benefit in using a filter length greater than five traces.

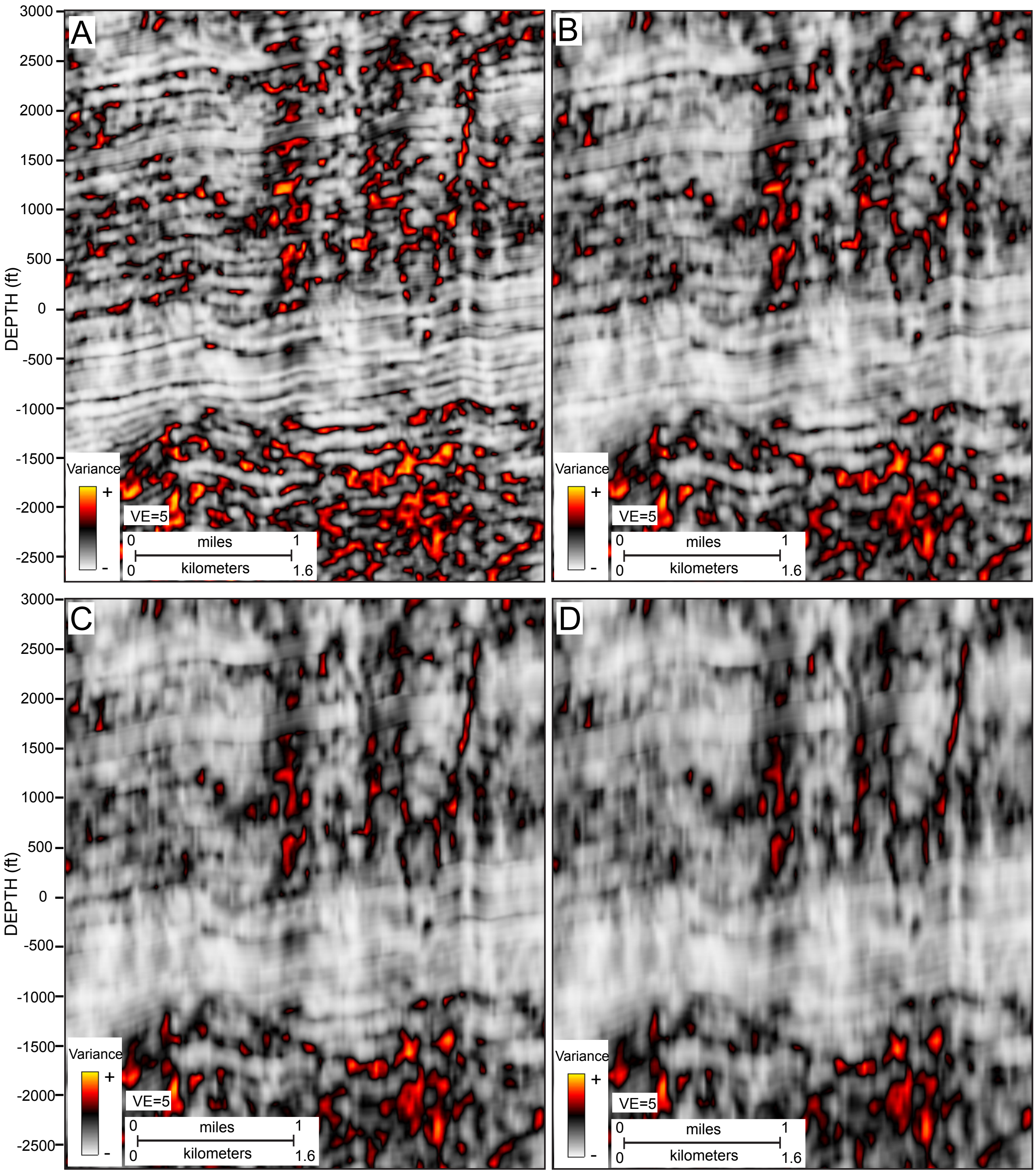

Figure 25. Vertical cross sections (crossline 145) through variance (edge detection) attribute volumes, A) Vertical window 32 ms, B) Vertical window 48 ms, c) Vertical window 64 ms (preferred), and D) Vertical window 81 ms. As filter size increases, lateral events caused by reflection interfaces disappear and noise is reduced. 32 ms and 48 ms vertical window allows lateral events to be present, whereas 64 ms suppresses noise and does not allow lateral events. 81 ms smears the sharpness of the edges too much.

Consequently, variance (edge detection) attribute generates a reasonable input attribute volume for ant tracking, as it is run on a structural smoothed volume using standard deviation of 1.0 with variance parameters: 64 ms of vertical window size and filter length value of five traces.

Ant-track Filter (Ant-tracking Attribute Generation and Parameters)

Ant tracking works similar to how ant colonies behave to optimize their path in search of food. Predefined “artificial ants” are placed as seeds on a seismic discontinuity volume to track and capture seismic discontinuities (Figure 26). Ant tracking allows the user to define six different parameters that determine how intelligent agents, “artificial ants”, will behave in order to capture the events/discontinuities in seismic data. These parameters are also used to discriminate between more regional events, such as large faults, and small scale (local) events, such as fractures.

The initial ant boundary (number of voxels) defines the initial distribution of agents by putting a territorial radius around each agent; therefore, no agent is placed within the radius of another agent. For extracting large regional faults, the distribution can be coarse, such as 5-7 voxels; for detailed work and the mapping of small faults and fractures (sweet spots), the distribution can be set to 3-4 voxels. As a first step in the ant-track algorithm, each agent makes an initial estimate of the orientation for the identified local maximum within the agent’s territory.

The ant-track deviation (number of voxels) controls the maximum allowed deviation of each agent from a local maximum as it tracks. Each ant agent is restricted to a maximum of 15% deviation from the initial orientation. The method allows the agent to accept a local maximum of one voxel on either side of the predicted position as legal. If the maximum is outside this ant-track step range, the track deviation parameter comes into play. For instance, a value of one would allow the agent to deviate by one voxel in either direction from the legal positions to search for a local maximum. If a maximum is not found, that step is recorded as an illegal step.

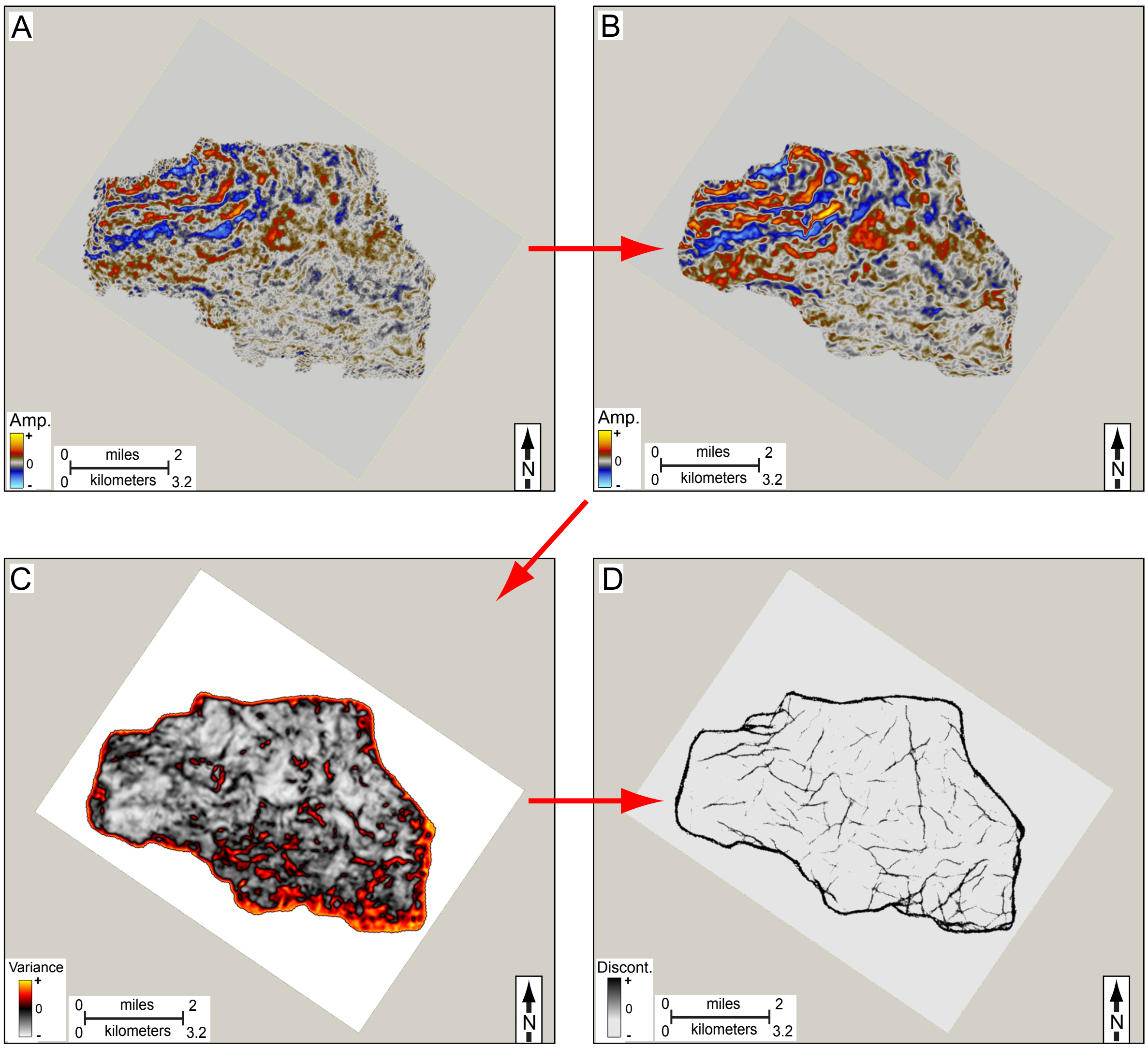

Figure 26. Illustration of depth slices from seismic data step through ant-tracking workflow. A) Original seismic, B) Structural smoothing with standard deviation of 1.0, C) Variance (edge detection) with vertical window size of 64 ms, D) Final product, ant-tracked attribute volume. Structural smoothing enhances the lateral continuity of reflections and improve edge detection results. Notice ant-track algorithm only tracks and captures events that are likely to be faults on variance attribute volume.

The ant step size (number of voxels) defines the number of voxels an ant agent advances for each increment within its searching step. Increasing this value allows an ant agent to search further, but it lowers the resolution of results.

The illegal steps allowed (number of voxels) parameter defines how far an agent's track can continue without finding an acceptable edge value (a local maximum).

The legal steps required (number of voxels) parameter controls how "connected" a detected edge must be to help distinguish an edge from unoriented noise. It is also expressed as the number of steps that must contain a valid edge value for the agent to continue.

Illegal steps allowed and legal steps required are used in combination with each other. For instance, if "Illegal Steps Allowed" is set to 1, that agent is only allowed to do one illegal step without finding a local maximum. Likewise, as the agent advances and encounters a valid edge, this means one legal step. If the ant advances again and finds another valid edge, this is considered second legal step. If "Legal Steps Required" is set to 2, the track is considered legitimate and recorded. If the parameter is set to 3, and on the next advance of the agent an edge is not encountered, this track will not be considered legitimate and will not be recorded. Illegal steps are only counted after legal steps have been recorded.

The stop criteria refer to the percentage of illegal steps allowed throughout a single agent's life. When the accumulation of illegal steps becomes a significant portion of the agent's search area (when this value becomes too large), the search can no longer be considered legitimate fault geometry based on the stop criteria set by the user, and therefore the track is terminated.

The stereonet tab is a graphic device where the user restricts which azimuth and dips the agents will be allowed to work. This parameter allows the user to filter unwanted events in seismic data such as events originated by dipping reflection interfaces.

(Petrel Workflow Tools, 2009)

RESULTS

Type, Distribution, and Orientation of Faults

Before the discussion of faults and fault interpretation in the study area, it is important to point out a few challenges resulting from data quality. Those challenges are:

1) Poor data quality and low signal-to-noise ratio make attribute analysis and structural interpretation a challenge. Events are so subtle that interpretation requires integration of different seismic attributes and does not allow using “Automatic Fault Extraction”; hence, manual interpretation is necessary.

2) Artifacts resulting from structural dip are another challenge due to the presence of regional dip in reflections. Edge-detection methods such as chaos and variance pick reflection interface (S- and Z- crossings) as a seismic discontinuity; therefore, ant-track filter also tracks these events and contains artifacts. These events are excluded throughout variance volume generation by setting certain parameters as well as using stereonet function in the ant-tracking process.

3) Due to poor data quality, the ant-track filter selects some events that may be faults or may not be; however, it should be noted that ant-track filter increases confidence in fault interpretation even in poor quality data.

In this study, seismic analysis of faults has been performed on an ant-track attribute volume generated using an initial ant boundary of 5, ant-track deviation of 2, ant step size of 4, illegal steps allowed of 2, legal steps required of 3, and stop criteria of 15%. These parameters were determined after running many realizations and examining the results of each. In order to prevent seismic artifacts in the output ant-track attribute volume, the ant-track filter was run on a variance attribute volume constrained by a 64 ms vertical window size and filter length of five traces. The 64 ms vertical window reduces the level of noise and removes events caused by reflection interface due to structural dip. The stereonet tab in the ant-track filter is also used as a constraint to filter events caused by the acquisition footprint and reflection interfaces. This tool is powerful since it restricts which azimuths and dips the agents will be allowed to search. Therefore, ant agents are only allowed to search dips greater than 20 degrees and azimuths +/- 4 degrees greater than inline and crossline orientation (Figure 27). Despite the poor data quality, the ant-track filter captured discontinuities successfully.

Seismic analysis of faults reveals that fault type, distribution, and orientation exhibit different characteristics with respect to depth. The upper and middle Williams Fork Formation interval has a highly complex ant-track attribute expression of discontinuities that makes interpretation of individual faults difficult. Deeper in the study area, below the Middle Sandstone, small thrust faults and normal faults are evident by dip changes in reflections, which becomes horizontal and differs from regional structural dip (Figures 28 and 31). These small thrust faults terminate up-section in the Rollins Sandstone Member, Cameo-Wheeler coal zone, and the Middle Sandstone intervals by causing small offset or no offset of these stratigraphic surfaces (Figure 28). Dip change in reflections demonstrates the rotation of blocks as a consequence of thrusting (Figures 28 and 31). The number of small thrust faults is subjective, and two thrust faults are interpreted; one with confidence, another one with less confidence because data quality becomes very poor near the edges of the seismic survey. A depth slice through the ant-track attribute volume shows N-NW- and E/W-trending discontinuities; however, N-NW-trending strike of deep thrusts and normal faults appears to be dominant (Figures 29 and 30). These small thrust and normal faults can be traced back to Mancos Shale in the time volume, but it is difficult to relate these thrusts to a basement fault or a detachment surface due to the limited extent of seismic data (Figures 21B and 31). The interpretation of a 2-D line in the study area

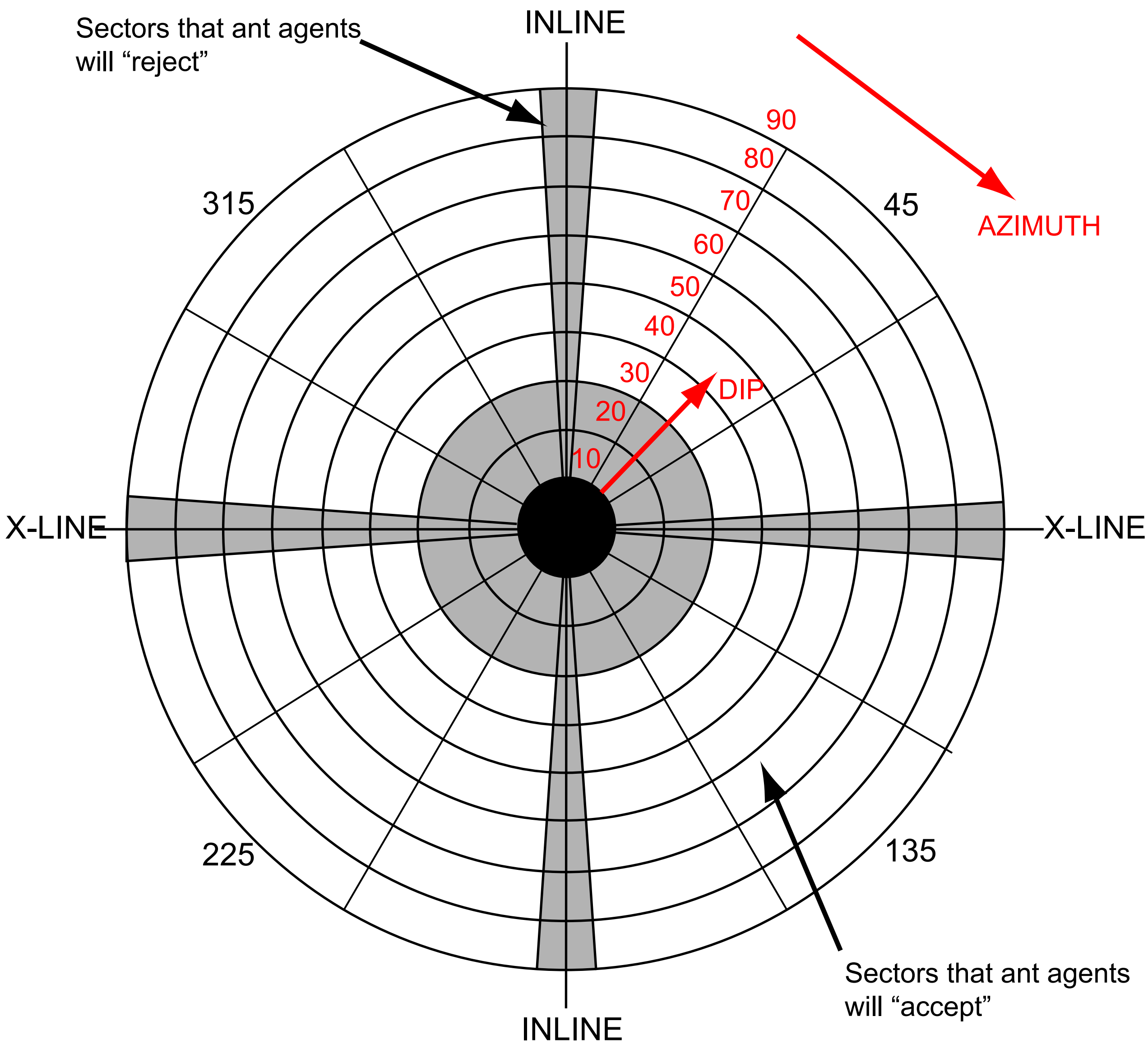

Figure 27. Stereonet tab constrained in ant-tracking workflow, figure shows open and restricted sectors for ant-track agents. Grey colored areas are restricted areas that ant-track agents will avoid. In order to prevent acquisition footprint, sectors that have +/- 4 degrees azimuths to inline and crosslines were restricted to search of ant-track agents. Ant-agents were also restricted to search dips of less than 20 degrees to prevent events caused by structural dip. Modified from Petrel Workflow Tools, 2009.

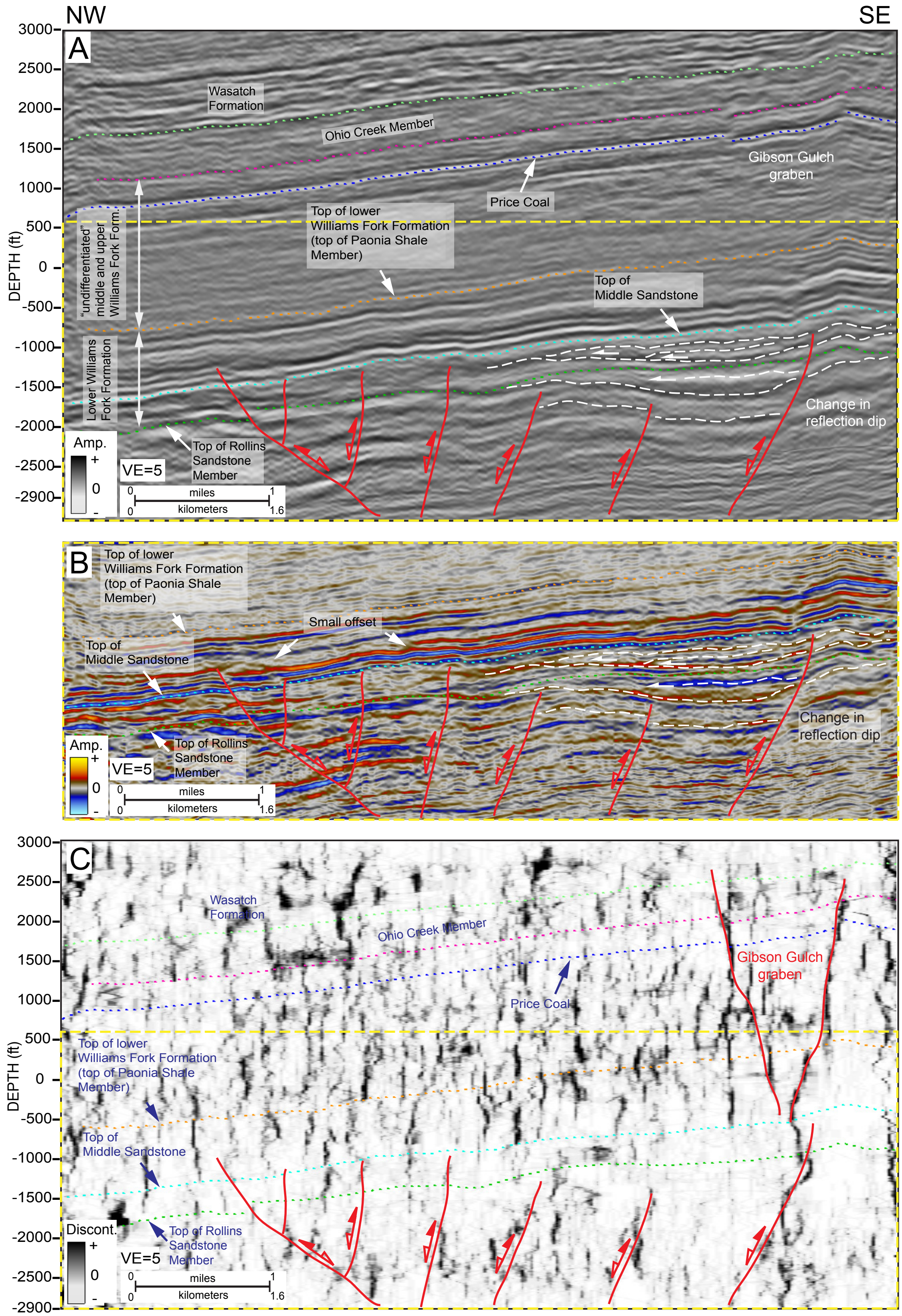

Figure 28. Vertical seismic section (crossline 177) through the seismic amplitude and ant-track attribute volumes, A and B) Interpreted thrust and normal faults on two different color scheme, notice small offset caused by thrust and normal faults, C) Ant-track expression of discontinuities. Notice the events captured by ant tracking continue upwards from the tip line of the thrust and normal faults. Location of the seismic section (crossline 177) is given in Figure 8B.

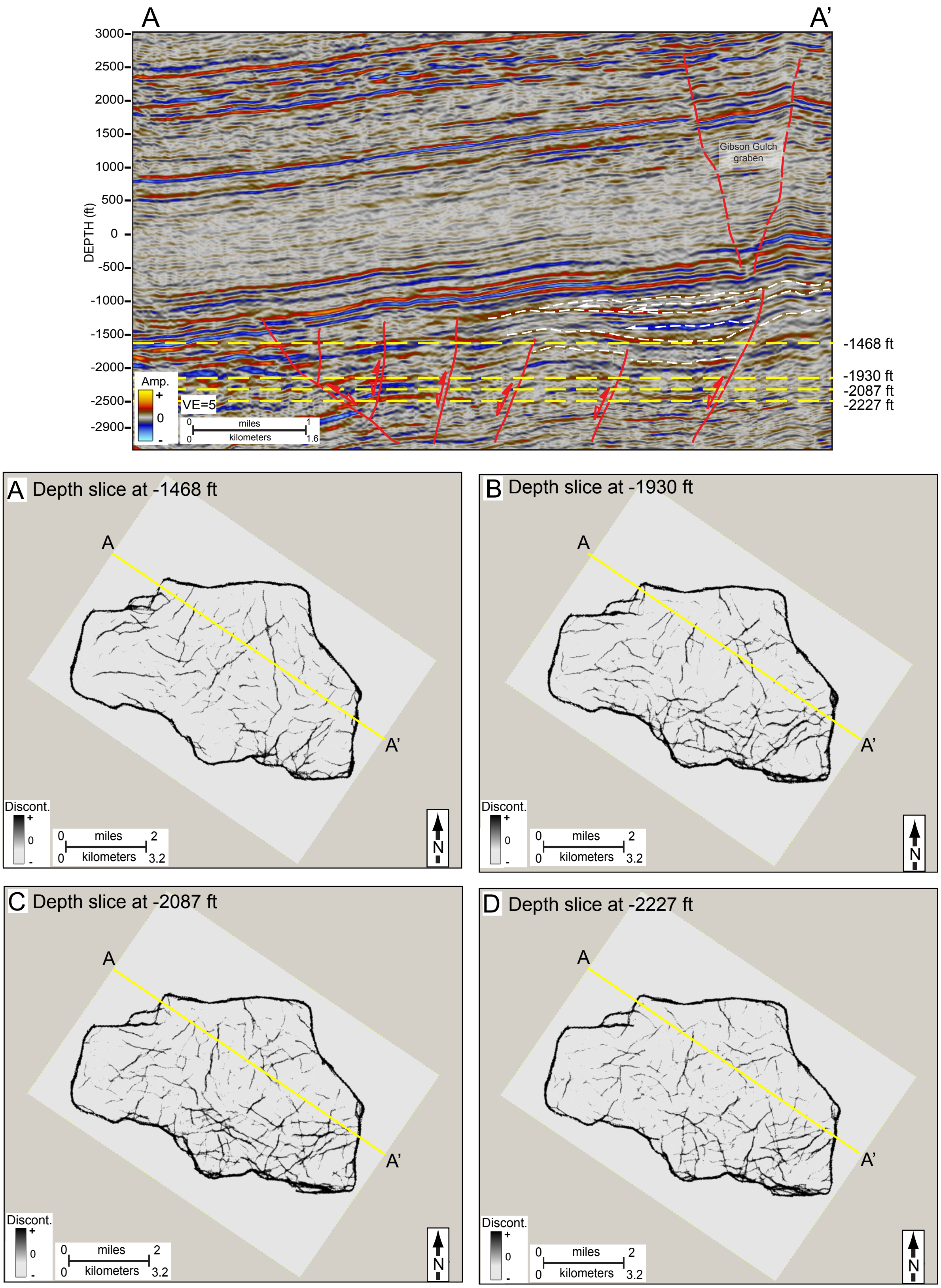

Figure 29. Depth slices through ant-track attrribute volume showing discontinuities captured by ant-track filter in lower levels in the study area. NW- and E/W-trending discontinuities are present; however, interpretation requires careful evaluation of discontinuities in collaboration with original seismic data and curvature attributes. Location of the vertical seismic section (crossline 177) is given in Figure 8B.

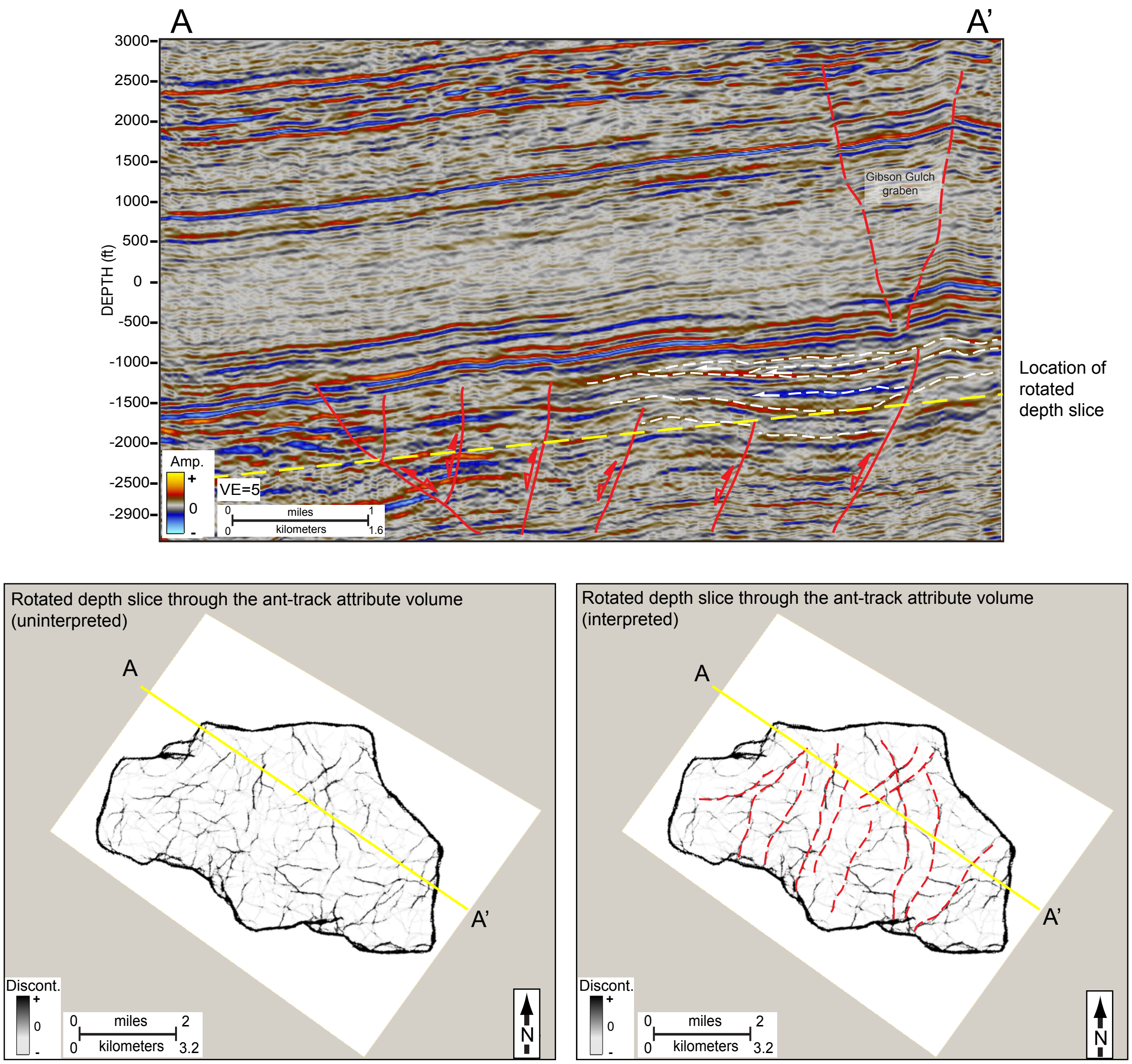

Figure 30. Rotated depth slice through the ant-track attribute volume showing discontinuities captured by ant-track filter in lower levels in the study area. Interpretation of faults requires careful evaluation of discontinuities in collaboration with original seismic data and curvature attributes. Depth slice is rotated to follow the stratigraphy. Location of the vertical seismic section (crossline 177) is given in Figure 8B.

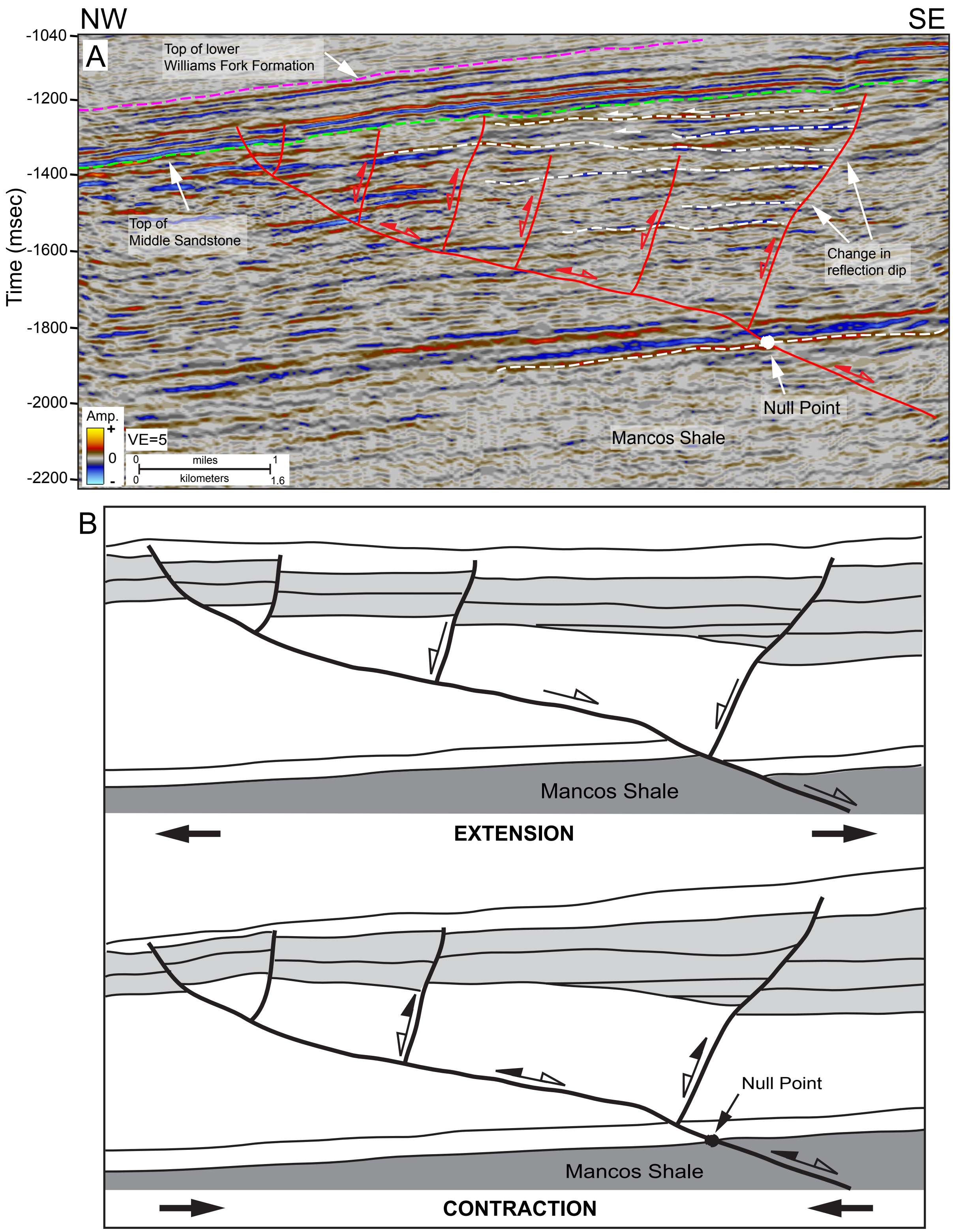

Figure 31. A) Vertical sseismic section (crossline 177) through the seismic data in time domain. Interpreted thrust fault can be traced back to the Mancos-Shale level. The lack of observable slip on the faults is explained by a null point as a consequence of positive inversion, which is resulted from a change from extension to contraction in the study area. B) Inversion type model to explain the lack of observable slip on faults in the study area. Location of the vertical seismic section (crossline 177) is given in Figure 8B.

shows no apparent relationship between basement fault or a detachment surface and Mancos-Shale level thrust faults (Figure 21B).

Coward (1994) describes the term “inversion” as “regions which have experienced a reversal in uplift or subsidence, that is, areas which have changed from being regions of subsidence to regions of uplift, or vice versa” (Coward, 1994, p. 289). When structural inversion occurs, the change from subsidence to uplift is considered positive inversion, and the change from uplift to subsidence is considered negative inversion (Harding, 1985; Coward, 1994; Williams et al., 1989). Positive inversion results in each fault to retain displacement caused by extension and an anticline growth in the upper portion of faults caused by contraction (Figure 32A; Williams et al., 1989). Three distinct stratigraphic sequences are present during and after extensional fault movement: 1) prerift sequence, which includes strata deposited before extension; 2) synrift sequence, which includes strata deposited coeval to extensional faulting; and 3) postrift sequence, which includes strata deposited after the extensional faulting (Figure 32A; Williams et al., 1989). During the contractional fault movement, the top and base synrift sequence markers move upward and retain their positions and exhibit no displacement, or appear unfaulted (Figure 32B; Williams et al., 1989). This point is defined as the null point and it shifts downward during the progressive movement of an extensional synrift sequence causing by contraction (Figure 32B; Williams et al., 1989). In the study area, the lack of observable slip on thrust and normal faults can be explained by positive inversion, meaning that extensional faults have reversed their movement during contractional movement, following the extension (Figure 31). During Late Cretaceous-Paleocene time, reactivation of structural features occurred in the Piceance Basin, based on the interpretation of 2-D regional seismic lines (Figure 21B; R. Bouroullec, 2009, personal communication). Following the extensional movement in the area, contraction caused individual faults to retain net extension at depth, which explains the lack of

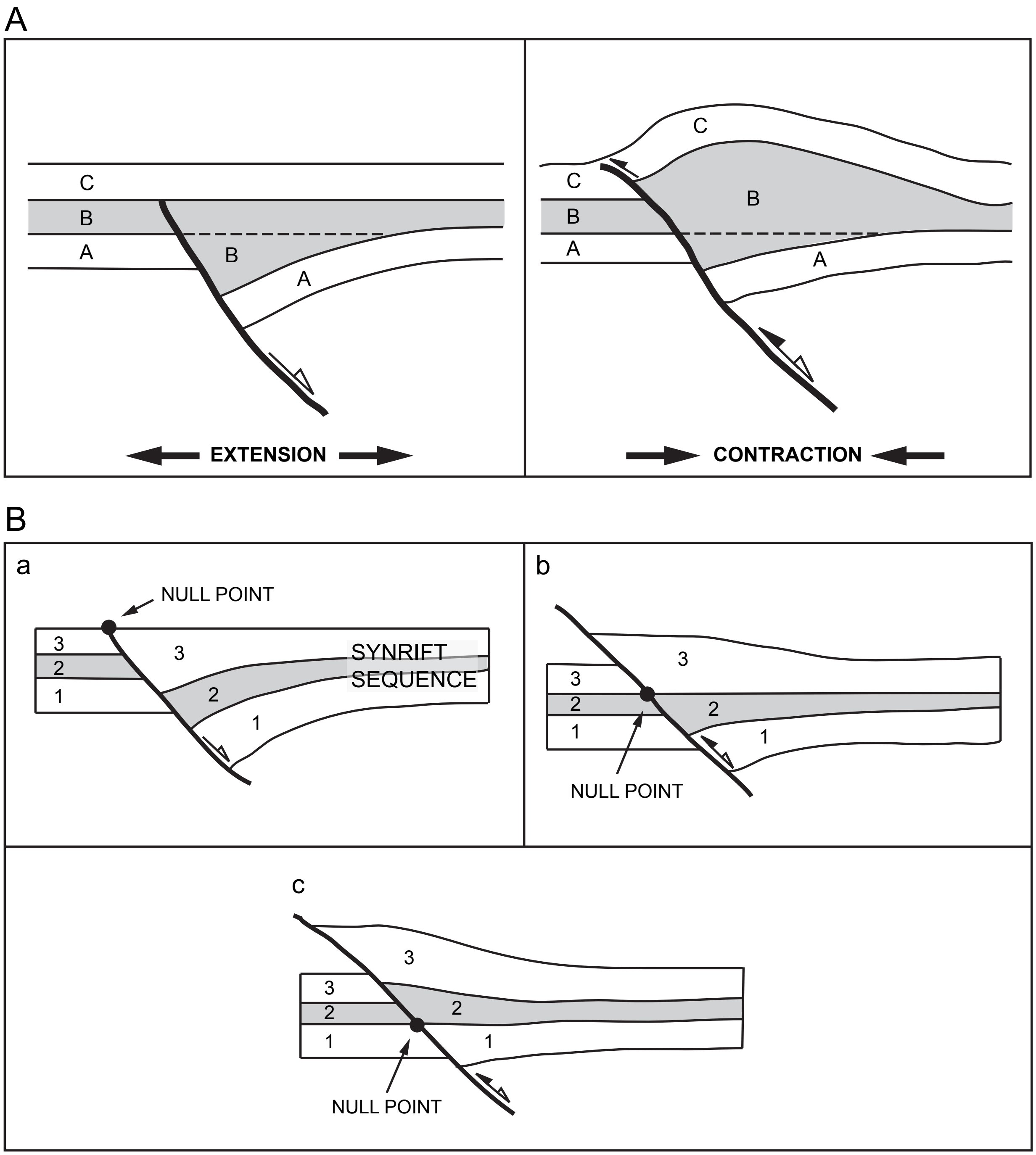

Figure 32. A) Schematic diagram of a classical positive inversion structure. A, B, and C are stratigraphic sequences. A, prerift; B, synrift; C, postrift sequence (modified from Williams et al., 1989). B) Sequential diagrams to show the contractional inversion of an extensional fault. The null point shifts down the synrift sequence with increased contractional inversion (modified from Williams et al., 1989).

observable slip on seismic reflections and causes a null point in Mancos-shale level (Figure 31; Williams et al., 1989).

Basement features and their relation to shallower structures have long been discussed in the Piceance Basin. Particularly, Hoak and Klawitter (1997) and Kuuskraa et al. (1997) suggest a basement-controlled thrusting that causes faulting and fracturing in the Mesaverde Group. In the study area, this relationship is problematic due to limited and poor quality data. Despite the difficulties, vertical sections through the ant-track attribute volume indicate discontinuities at the tip line of the thrust and normal faults (Figure 28). A small amount of offset on shallow reflections and high ant-track attribute values appears to continue up-section from the tip line of thrust and normal faults (Figure 28). This relationship may have been complicated by over-pressuring because over-pressuring plays a role in fracture occurrence as well. As produced in laboratory experiments, faults create perturbations in the regional stress field at their terminations; thus, a fault tip creates zones of increased tension and compression (Logan et al, 1979; Kuuskraa et al, 1997). As a result, fracture density and permeability can be expected to be influenced by thrusting and faulting.

In intermediate levels in the study area, reflectors exhibit amplitude dimming, poor amplitude coherency, and reflector offset, so interpretation mostly relies on ant-track attributes. Depth slices through the ant-track attribute volume indicate E/W- and N-NE-trending discontinuities. It appears that E/W trending discontinuities become N-NE-trending further north closer to the Grand Hogback. NE-trending Gibson Gulch graben is also evident in the ant-track attribute volume (Figures 33 and 34). In shallow levels, E/W-trending faults become dominant (Figures 35 and 36). Within the upper and middle Williams Fork Formation, subsurface structure is complicated due to fracturing caused by over-pressuring and fault and fracturing related to basement structures. The complex interplay of ant-track attribute anomalies may indicate fracture and fault enhancement due to thrusting deeper in the Cameo-Wheeler coal zone and

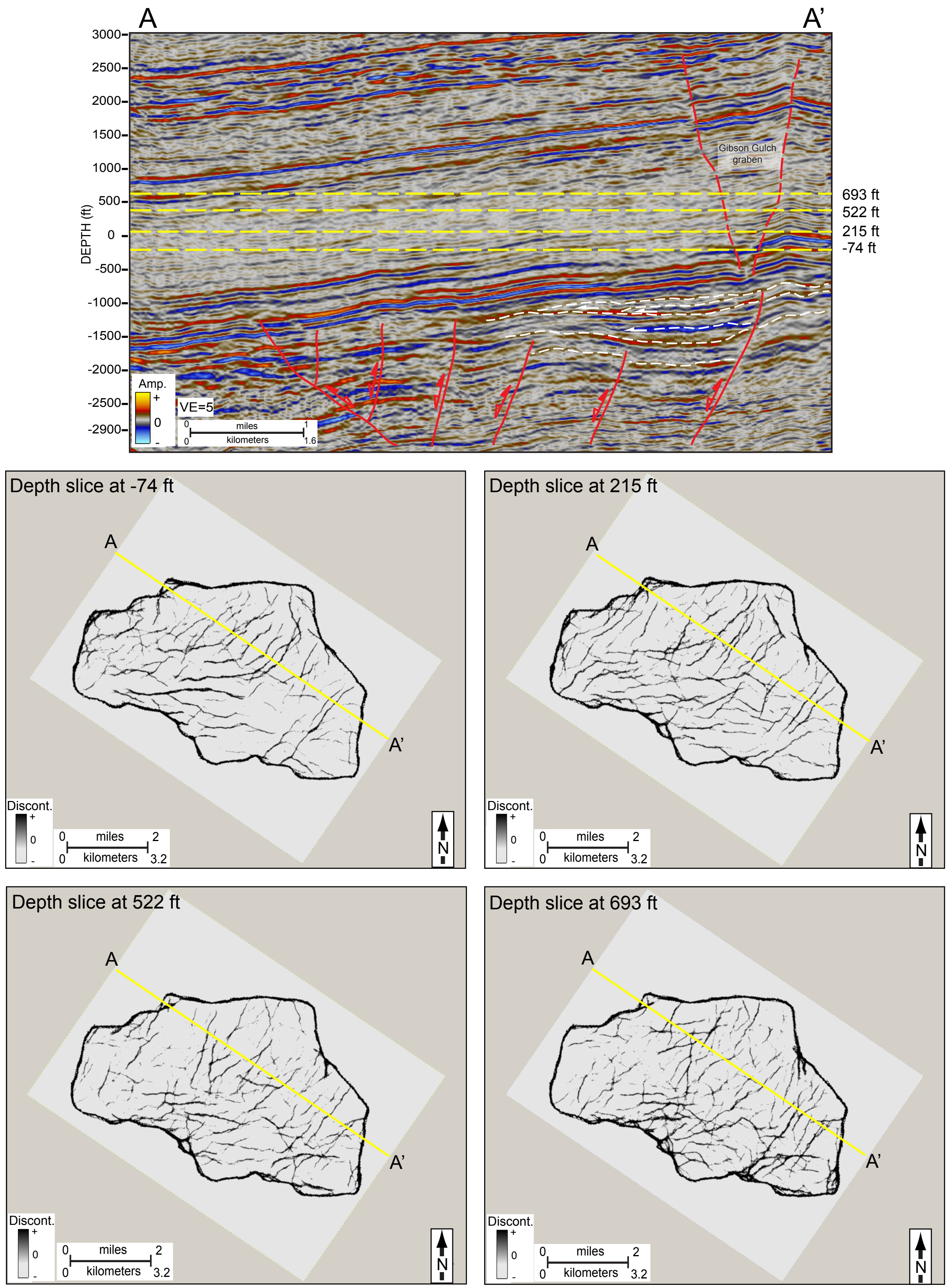

Figure 33. Depth slices through the ant-track attribute volume showing the intermediate level discontinuities captured by ant-track filter. NNE- and E/W-trending events dominate this level. It appears that E/W-trending discontinuities become NNE-trending further north closer to the Grand Hogback monocline. Location of the vertical seismic section (crossline 177) is given in Figure 8B.

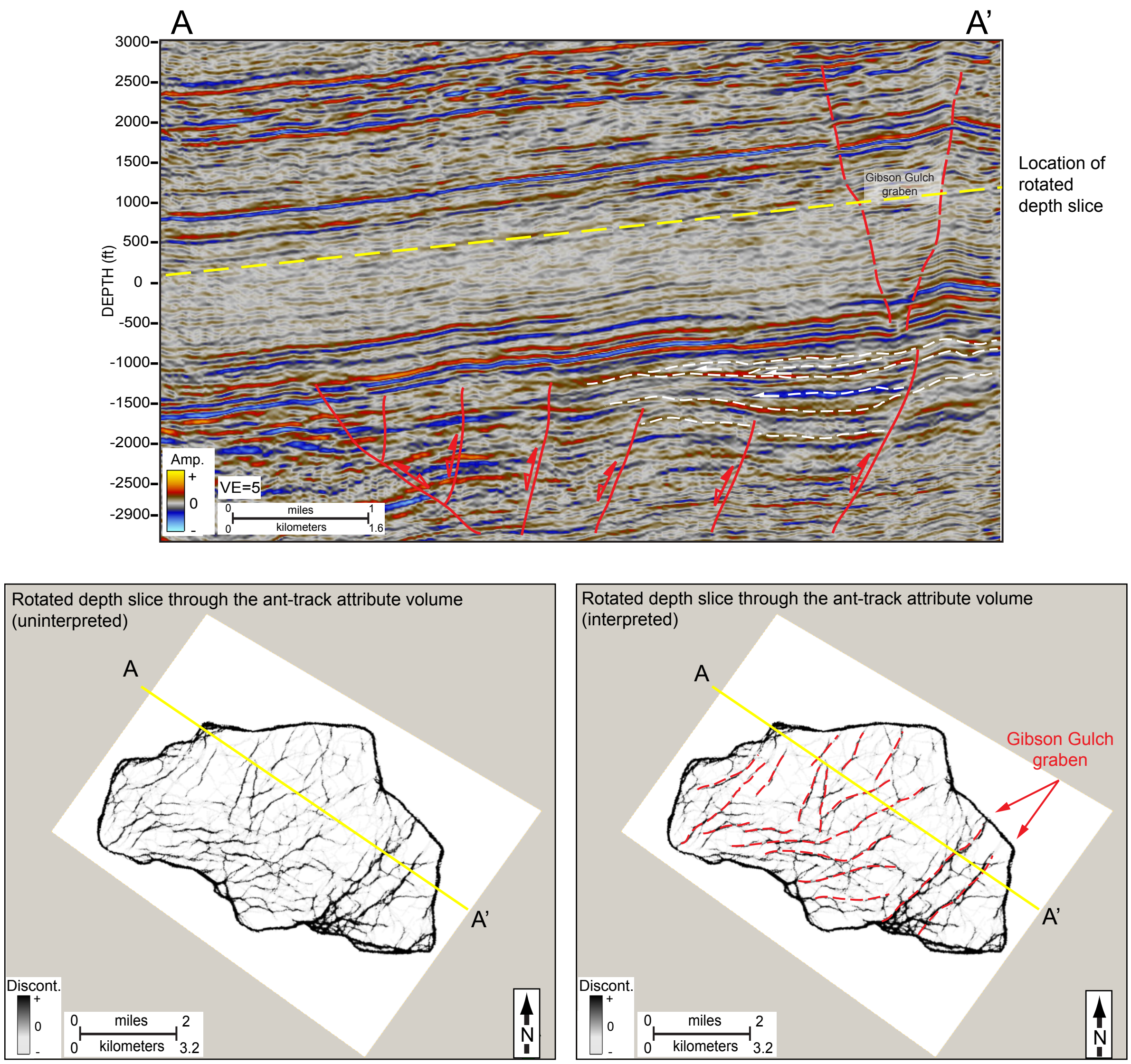

Figure 34. Rotated depth slice through the ant-track attrribute volume showing discontinuities captured by ant-track filter in reservoir level in the study area. NW- and E/W-trending discontinuities are present; however, interpretation requires careful evaluation of discontinuities in collaboration with original seismic data and curvature attributes. Depth slice is rotated to follow the stratigraphy. Location of the vertical seismic section (crossline 177) is given in Figure 8B.

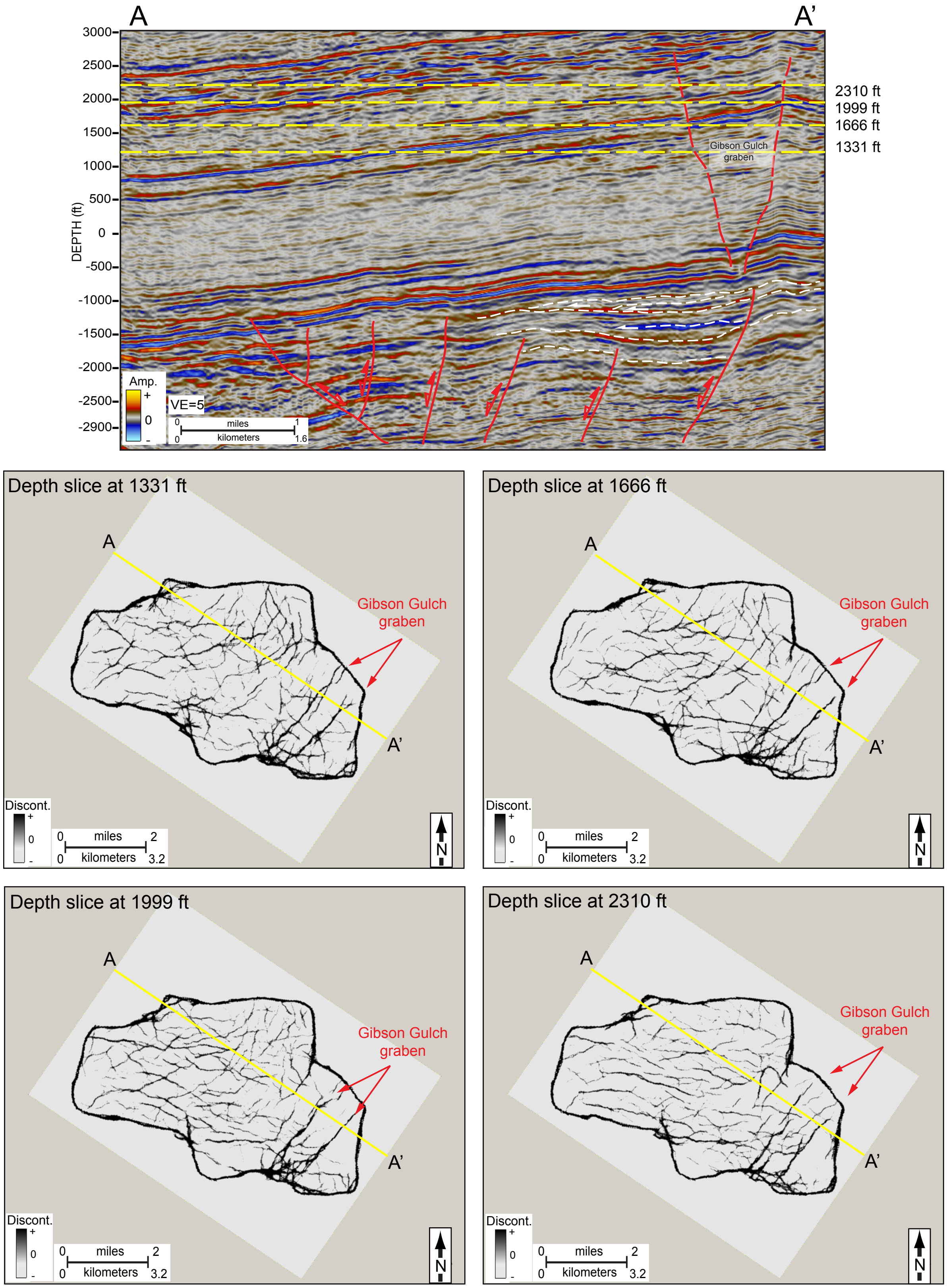

Figure 35. Depth slices through the ant-track attribute volume showing the shallow level discontinuities captured by ant-track filter. E/W-trending faults dominate this level. Ant-track filter captures the Gibson Gulch graben and reveals the extent of it. Location of the vertical seismic section (crossline 177) is given in Figure 8B.

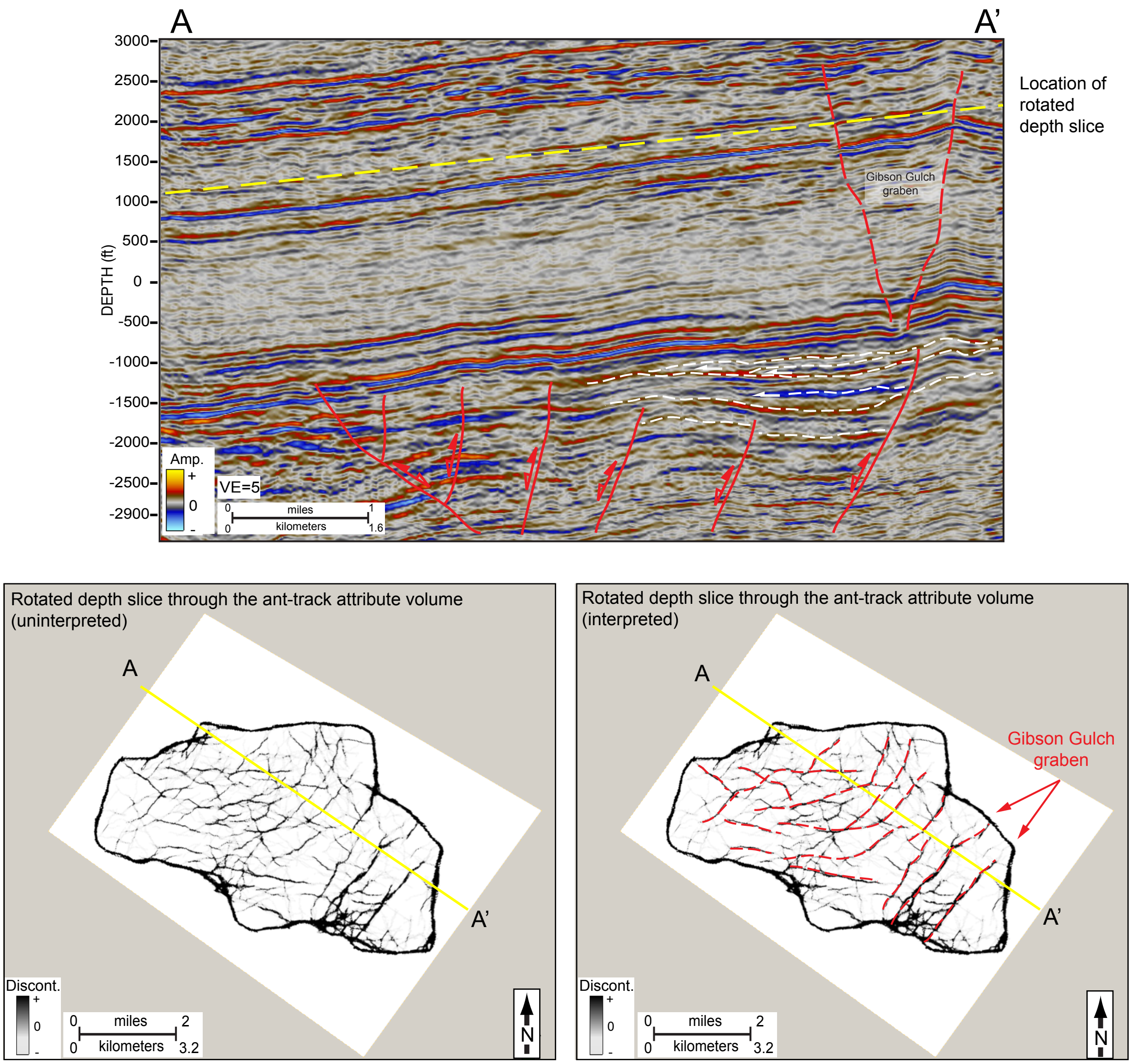

Figure 36. Depth slices through ant-track attrribute volume showing discontinuities captured by ant-track filter in lower levels in the study area. NW- and E/W-trending discontinuities are present; however, interpretation requires careful evaluation of discontinuities in collaboration with original seismic data and curvature attributes. Location of the vertical seismic section (crossline 177) is given in Figure 8B.

Rollins Sandstone Member levels. It is very likely that thrust and normal faults may penetrate through this section and terminate into a series of faults in a broad area of fracture clusters.

DISCUSSION

This study reveals the existence of thrust and normal faults in the study area which are evident based on three-dimensional seismic interpretation. Thrust faults can be traced back to the Mancos-Shale level using the seismic time volume; however, data coverage is limited to confirm the existence of a possible Mancos-level detachment and relations of these thrust faults to basement faults. Hoak and Klawitter (1997) emphasize the importance of a Mancos-level detachment in the central and eastern Basin based on detailed aeromagnetic data calibrated with published and proprietary seismic data. Moreover, Grout and Verbeek (1992) relate the development of the Divide Creek and Wolf Creek anticlines to a decollement on the basinward side of a large, basement-involved thrust wedge whose surface expression is the Grand Hogback monocline. The study area lies in the vicinity of the Grand Hogback monocline and N-NW-trending intrabasin folds of the Wolf Creek and Divide Creek anticlines; therefore, interpreted thrust faults may be related to this basement-involved wedge. However, this relationship is not proved due to limited areal extent of seismic data and it requires interpretation of 2-D regional seismic lines. Normal faults related to thrust faulting were also observed in the study area. Thrust faults and normal faults cause small-scale and no offsets in the Rollins Sandstone Member, Cameo-Wheeler coal zone, and Middle Sandstone level seismic reflections. The lack of observable slip on seismic reflections in this level is explained by positive inversion, which resulted in the reactivation of faults. Isopach maps show abrupt thickness changes in the Cameo-Wheeler coal and Middle Sandstone intervals that are consistent with interpreted thrust and normal faults and previous observations by Cumella and Ostby (2003).

Thrust faults and their relation to shallow structures and production in the Mesaverde Group have already been discussed before. Thrust faults in the study area appear to terminate up-section in the Rollins Sandstone Member, Cameo-Wheeler coal zone, and Middle Sandstone intervals. There is no apparent offset on the reflections above the Middle Sandstone. This results in ambiguous fault interpretation; however, the ant-track filter captures discontinuities successfully and reduces the ambiguities and user's bias. Discontinuities traced by the ant-track filter appear to continue up-section into the Williams Fork Formation from the tip line of the thrust faults. Jansen (2005) investigated the wrench faulting in the Rulison gas field. His observations are similar to that observed in the central Mamm Creek gas field in this study, meaning that wrench faulting could be present in the Mesaverde Group level, which may have been caused by left-lateral strike slip suggested by Cumella and Ostby (2003). In the study area, faults in the Mesaverde Group show structural complexity and arrays of upward-diverging fault splays, which are characteristic of wrench faulting. Production data including Estimated Ultimate Recovery (EUR) values for each well in the central Mamm Creek field are available and show a wide range of EUR values (see Appendix E-1 for production data). EUR data show cumulative production rates as low as 390 MMCF (0.39 BCF) and as high as 2630 MMCF (2.6 BCF); however, it is difficult to relate high production rates to structure due to complexity and closely spaced wells (Figure 37).

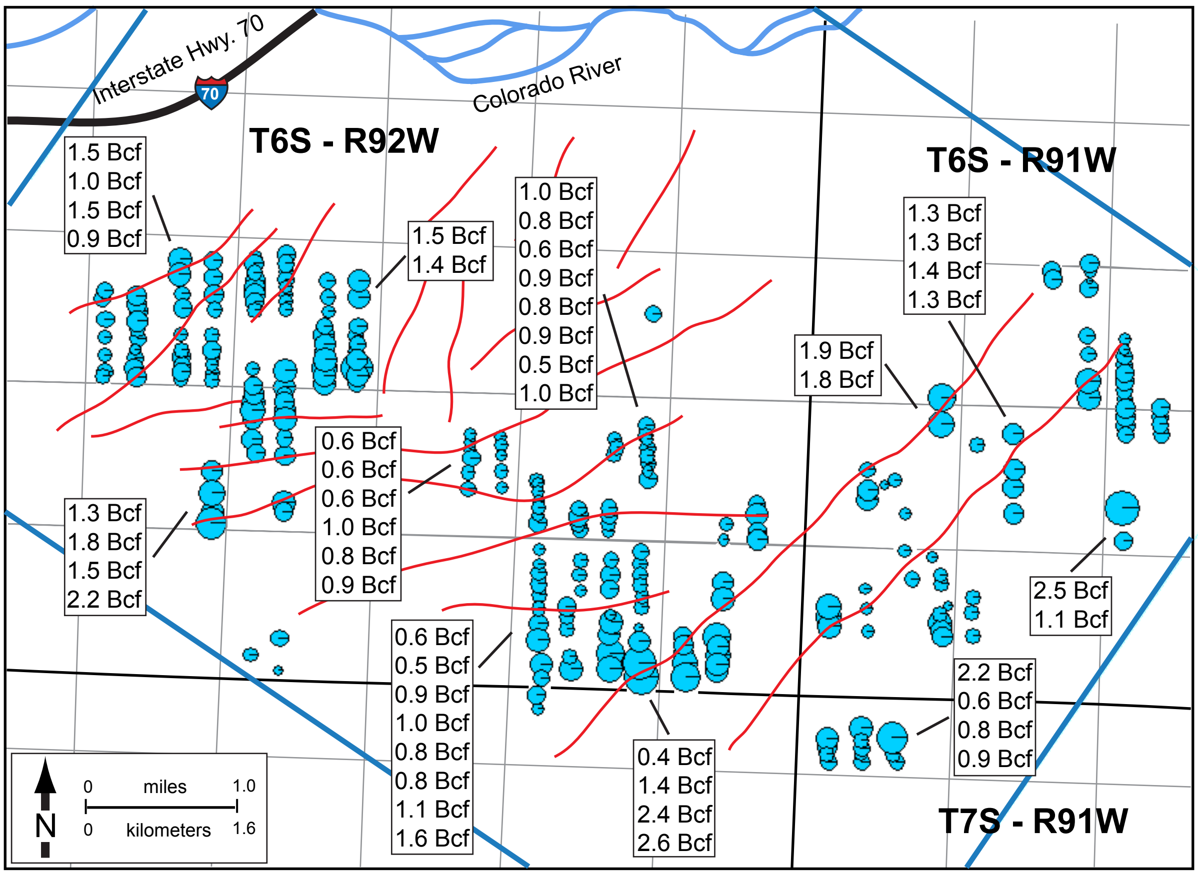

Figure 37. Production bubble map in the study area created using estimated ultimate recovery (EUR) data. Cumulative production values range from 0.3 BCF to 2.6 BCF. Even though it is difficult to relate high production rates to structure due to complexity, high EURs (>2.0 Bcf) are present in the southern and soutwesrtern portion of the study area. Some of interpreted faults in reservoir level can also be seen.

CHAPTER FOUR

FRACTURE ANALYSIS

INTRODUCTION

A reservoir fracture is defined as “a naturally occurring macroscopic planar discontinuity in rock due to deformation or physical diagenesis” (Nelson, 2001, p. 3). Fractures can be initially open, but may have been subsequently altered or mineralized, if they are caused by brittle failure; or if related to ductile failure, they can occur as a band of highly deformed country rock (Nelson, 2001). As a consequence of fracture type, density, and processes that form fractures, fractures may have either a positive or negative effect on reservoir fluid flow. Because fractures have different origins, characterization of fractured reservoirs is often complicated and requires integration of different types of data. The presence of fractures and their effect on production in the Piceance Basin has been documented through well tests, core samples, and outcrop studies. Therefore, the tight-gas sandstone reservoirs of the Piceance Basin can be defined as fractured reservoirs.

Fracture studies of the Williams Fork Formation were initiated as early as 1979 by the U.S. Geological Survey and involved collection of outcrop data (more than 900 outcrops) and core samples in the Piceance Basin. In the 1980s, the government-sponsored Multiwell Experiment (MWX) at Rulison gas field conducted extensive research to characterize the Mesaverde Group sandstone reservoirs. This field experiment entailed extensive testing, measurement, and data collection, resulting in numerous reports and papers published by independent researchers and the investigators of the MWX. Pitman and Sprunt (1986) relate the formation of fractures to high pore-fluid pressure that developed during hydrocarbon generation and to tectonic stress associated with uplift and erosion. Their observations include fractures either open or nonmineralized or partly to completely filled by calcite, with a range of fracture strike orientations from N60°W to N80°W and from N5° to N35°E. Lorenz and Finley (1989, 1991), in their observations on a dataset obtained during MWX, suggest a regional set of W-NW extension fractures which formed at ~36-49 Ma during a phase of increased W-NW Laramide compression, based on time-depth relations, fracture orientation, and fluid inclusion analyses. Lorenz and Finley (1989, 1991) report a high variability of fracture height and spacing and primary fracture occurrences in sandstone and siltstone (more than 95% in core). Northrop and Frohne (1990), in a summary paper that highlights some insights from MWX, describe fractures as unidirectional and subparallel with infrequent, low-angle, echelon intersections, which occur in a wide spectrum of lengths, widths, and spacing. Northrop and Frohne (1990) also indicate that fractures occur principally in the sandstone and siltstone and terminate vertically at lithologic boundaries. Verbeek and Grout (1984) and Grout and Verbeek (1992) describe two systems of fractures in the Upper Cretaceous through Middle Eocene rocks of the Piceance Basin and the Grand Hogback area. The older system is termed the Hogback system and contains two sets of joints assigned the MV_1 and MV_2 sets. The younger system is termed the Piceance system and comprises five regional sets of joints assigned F_1 (oldest) through F_5 (youngest). The joints of each set are steeply dipping vertical extension fractures which strike N-NW and N-NE and show different relative abundance across the basin (Grout and Verbeek, 1992). Joints are fractures that are described as "planar discontinuities show opening displacements with no apparent shear displacement" (Badgley, 1965; Bankwitz, 1966; Engelder, 1987; Nelson, 2001). Joints are also referred to as extension fractures (Griggs and Handin, 1960) or veins (Ramsay, 1980). Joints are often observed on outcrops and can be correlated from outcrop to outcrop (Nickelsen and Hough, 1967; Engelder, 1987). Hoak and Klawitter (1997) relate surficial features to the subsurface using satellite and airborne imagery analysis and core data. They demonstrate that the reservoir level is dominated by W-NW-trending fractures and lacks NE-trending fractures, whereas NE- and E-NE-trending fractures are present on the surface in the vicinity of the MWX site but do not continue into the reservoir interval. Recent observations are similar to ones which were made earlier. Nelson (2003) indicates N-NW orientation of maximum horizontal stress which is the same as that of natural fractures, based on Warpinski's (1988, 1989, and 1990) observations indicating maximum horizontal stress orientation ranging from N52°W to N80°W in the paludal interval, from N58°W to N88°W in the coastal interval, and from N55°E to N103°E in the fluvial interval.

Today, ongoing research still continues in the basin to better characterize fractured reservoirs of the Mesaverde Group and understand fracture controls on production. The fracture analysis section of this study aims to characterize fractures in the Williams Fork Formation based on borehole-image logs (Formation MicroImager (FMI)), available core (Last Dance), and seismic attributes.

METHODS

Fracture Analysis Workflow

In this study, analysis of fractures was based on borehole-image logs (10 FMI image logs), 3-D seismic data (seismic-attribute analysis), and core data from one well (Last Dance 43C-3-792) (Figure 38). Ten (10) Formation MicroImager (FMI) logs were the main source of fracture information. The borehole-image log data were obtained by Schlumberger Technologies and those fracture interpretations were used to conduct further analysis. FMI logs provide fracture type, class, description (open, sealed, etc.), apparent dip, apparent azimuth, and depth information. For each well, spreadsheets were created of the necessary information from FMI logs. For the seismic analysis of fractures, relationships between ant-track and t* attenuation attributes and fracture-intensity logs were examined. In addition, core data was used to evaluate the reliability of FMI logs in comparison to core data.

FMI Logs (Formation MicroImager) Background

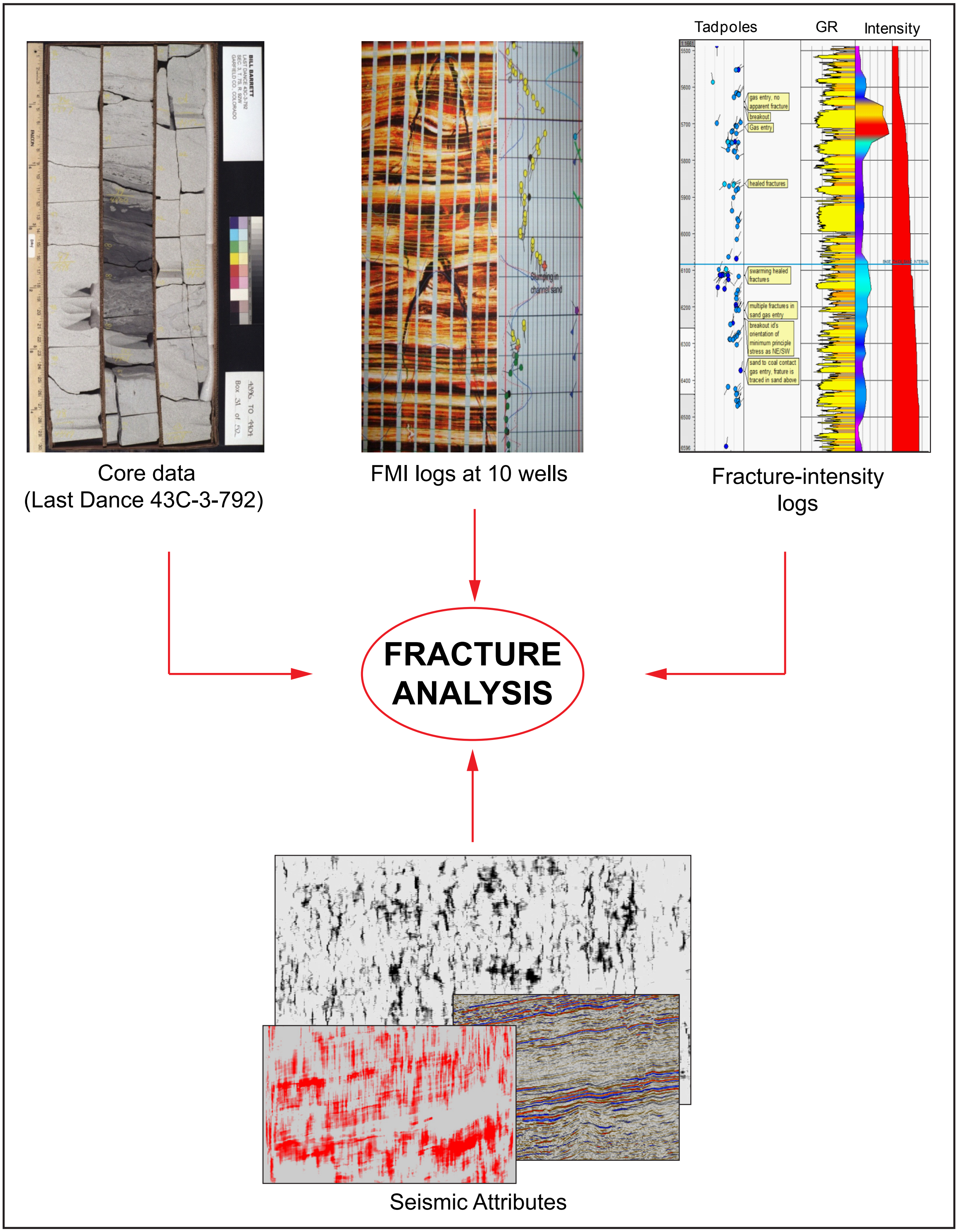

Figure 38. Fracture-analysis workflow. Seismic attributes, core data at one well, FMI logs at 10 wells, and fracture-intensity logs were used to conduct fracture analysis. Relationships between seismic attributes of ant-tracking and t* attenuation and fracture-intensity logs are investigated. A core data is used to compare FMI log data with rocks to test the reliability of FMI log data.

Borehole images provide unique and critical information about the rocks and fluids encountered by a wellbore. This critical information could be bedding dip, fractures, faults, unconformities, paleocurrent data, vuggy and fracture porosity, and other geological features obtained by electrical, acoustic, or video devices that have been lowered down into the well (Hurley, 2004). Using borehole images in conjunction with other available data such as well logs, cores, production data, and seismic data is an effective method to evaluate fractured reservoir characteristics and behavior.

Electrical borehole-image logs were developed using dipmeter technology, which has been available since the 1950s (Hurley, 2004). Basically, a borehole-image log tool consists of microresistivity electrodes on pads that force electrical current into the formation of rocks around the wellbore (Hurley, 2004). After an electrical current is sent into the rocks, measurement is done by remote sensors. Data acquisition involves multiple-electrode, caliper, accelerometer, and magnetometer readings which determine the borehole deviation and pad one orientation (Hurley, 2004).

After data acquisition is complete, borehole-image logs are interpreted by log interpreter. The interpreter steps through the image data and picks bed boundaries, fractures, faults, and other geologic features of interest. Because a wellbore is circular in shape, those features are represented by sine waves. Borehole-image logs contain important information related to fracture dip angle, dip azimuth, type, class, description, and aperture. Analysis of fractures is mostly done by using rose diagrams, tadpole plots, stereonets, and fracture-intensity logs that are generated to show these types of data.

Another useful aspect of borehole-image logs is that they allow the user to distinguish open fractures from healed ones, based on appearance. On borehole-image logs, an open fracture appears as a dark trace because it fills with conductive drilling mud; if the fracture is filled with cement such as quartz, calcite, or anhydrite then it is resistive and appears as a white trace (Hurley, 2004). Borehole-image logs also allow the interpreter to determine the orientation of in-situ stress by using borehole breakouts and induced-tensile fractures. This information is important because it is used in planning well stimulation, optimizing the orientation of horizontal wells, and configuring injection patterns (Heffer and Lean, 1993; Barton et al., 1997; Hurley, 2004).

RESULTS

Fracture Types

Based on 10 FMI logs, approximately 1634 natural fractures are categorized into 1) conductive and 2) non-conductive (resistive) fractures (Figure 39). Conductive fractures appear as dark and exhibit low resistivity because they are considered to be open and filled with a low resistivity fluid of drilling mud within the aperture. Hurley (2004) indicates that shale-filled fractures also appear as dark traces, so discrimination between shale-filled versus open fractures can be done utilizing the gamma ray log. Conductive fractures are sub-categorized into the following sets by Schlumberger:

1) Continuous Fractures: These can be considered to have large apparent aperture on the electrical borehole-image logs. They are open and appear thick in visual size. Continuous fractures may be a swarm of extremely close spaced parallel fractures. Production could have a relationship with the number of continuous fractures present at the wellbore, connections between fractures, and the fracture aperture (Schlumberger, 2008).

2) Lithologically Bound Fractures: These terminate at lithologic bed boundaries. Apparent traces of these fractures are limited and often do not extend around the wellbore. Lithologically bound fractures may relate to production if they are connected with other continuous fracture paths in

the well. Because they terminate at bed boundaries, their vertical extent may limit the reservoir drainage (Schlumberger, 2008).

3) Partially healed/open fractures: These appear as a cemented portion of the fracture. Extreme care should be taken since they may be completely cemented and opened due to the drilling process (Schlumberger, 2008).

Non-conductive (resistive) fractures appear as light or white traces on electrical borehole-image logs and can be considered to be open even if they are completely filled/cemented by calcite, anhydrite, or quartz (Hurley, 2004). Resistive fractures can act as permeability barriers within the reservoir and have a minimum contribution to production. Because resistive fractures exhibit different characteristics in comparison to conductive (open) fractures, they should be modeled and analyzed separately (Schlumberger, 2008).

Interpretation of FMI logs at 10 wells indicates that conductive fractures (N=1148) occur almost three times more than resistive fractures (N=486) (Figure 39).

Fracture Intensity

Fracture-intensity logs show the density of fractures per unit length, and are used in this study for seismic analysis of fractures and investigating the relationships between lithology, architectural elements, and fracture intensity. Fracture-intensity logs are created by determining a window length and sample interval, correcting for borehole deviation. Borehole correction is often done by assigning a weight based on the angle between a normal to the fracture and the inclination of the borehole; thus, fractures perpendicular to borehole are assigned a value of 1 and fractures parallel to the borehole are assigned a value approaching infinity (Petrel Workflow Tools, 2009). Borehole correction is an important aspect while creating a fracture intensity log because possibility of a well crossing a fracture depends on the angle between fracture and the borehole. For investigation of the relationships between seismic attributes and fracture intensity,

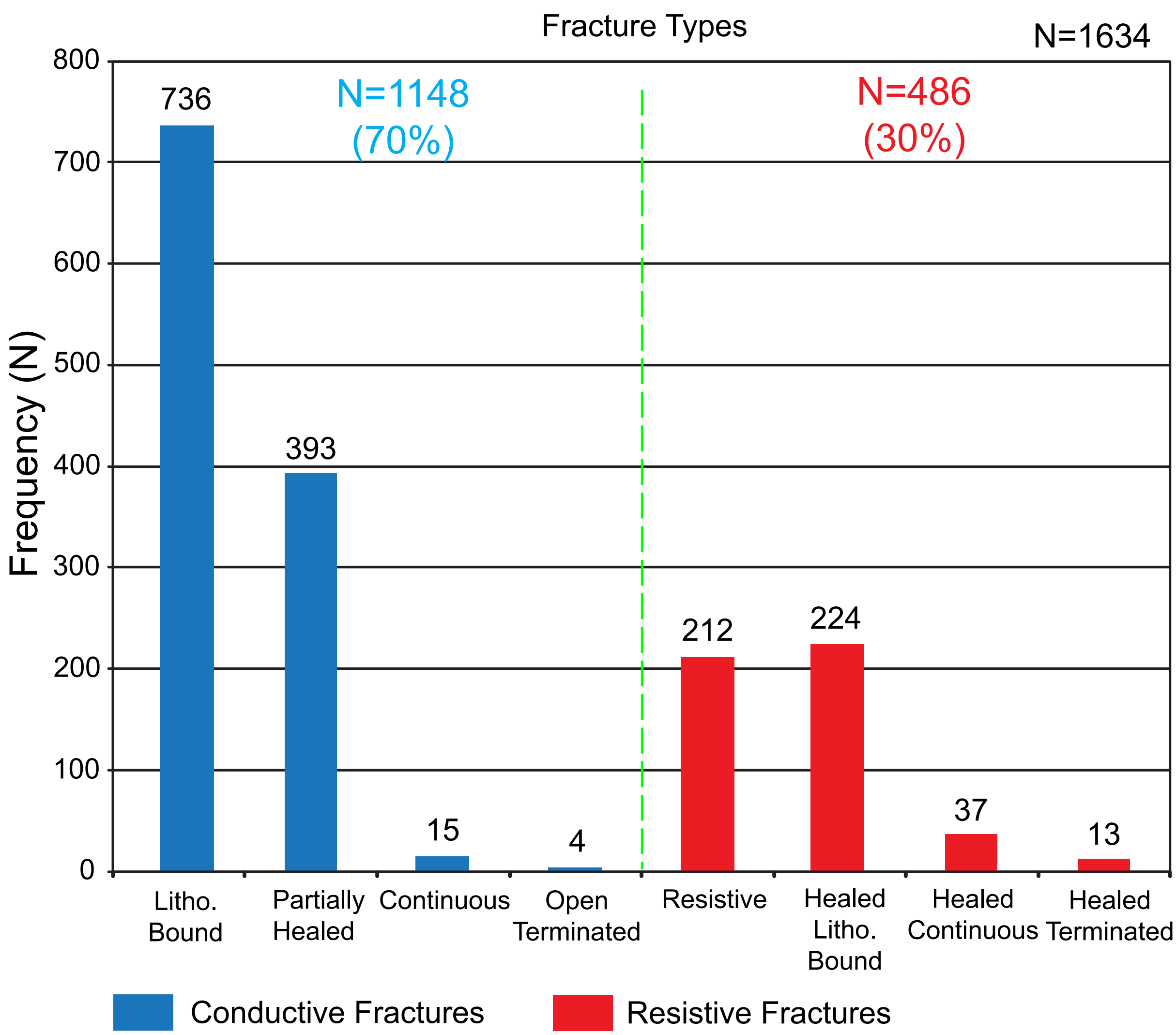

Figure 39. Histogram shows the number of fractures per fracture type. Conductive fractures are shown in blue and resistive fratures are in red. The interpretation of 10 FMI logs indicates that 70% of natural fractures is conductive while 30% of them is resistive. Sub-categories are also given.

the window length was set to a larger value of 100 ft (30 m), which resulted in a coarser scale fracture-intensity log because seismic resolution is lower than the well-log scale. For investigation of the relationships between lithology, architectural elements, and fracture intensity, this value (window length) was set to a smaller value of 5 ft (1.5 m). In practice, intensity logs are created by sliding a triangular window along the borehole. Intensity values are calculated at each point, then summed and divided by the area of the window to give the number of fractures per unit length (P11). The window is used in the following way below:

Intensity (measured depth) = (cumulative (measured depth + window length/2) – cumulative (measured depth – window length/2)) / window length

In addition to fracture intensity logs, cumulative intensity logs were created using fracture point data. Cumulative fracture intensity logs are useful to divide the reservoir into mechanical zones.

Based on 10 wells fracture-intensity logs generated for each fracture type indicate that fracture intensity varies spatially (with depth and aerially) (Figures 40 and 41A). Fracture-intensity logs indicate a non-uniform distribution of fractures throughout the study area. The number of fractures per well differs as much as by one order of magnitude from one well to another (Figures 41B and 42). A simple count of natural fractures at 10 wells indicates a low of 30 and a high of 338 natural fractures with an average number of 163 (Figures 41B and 42). Distributions of conductive fractures versus resistive fractures show no apparent relationship in terms of depositional characteristics (fluvial vs. marine) and depth. It appears that resistive and conductive fractures can form in any interval regardless of depositional environment. The data suggest that the fracture intensity is higher in the cemented sandstones of the fluvial interval; however, fracture intensities between fluvial and marine sandstones overlap to a small degree.

Fracture Orientations

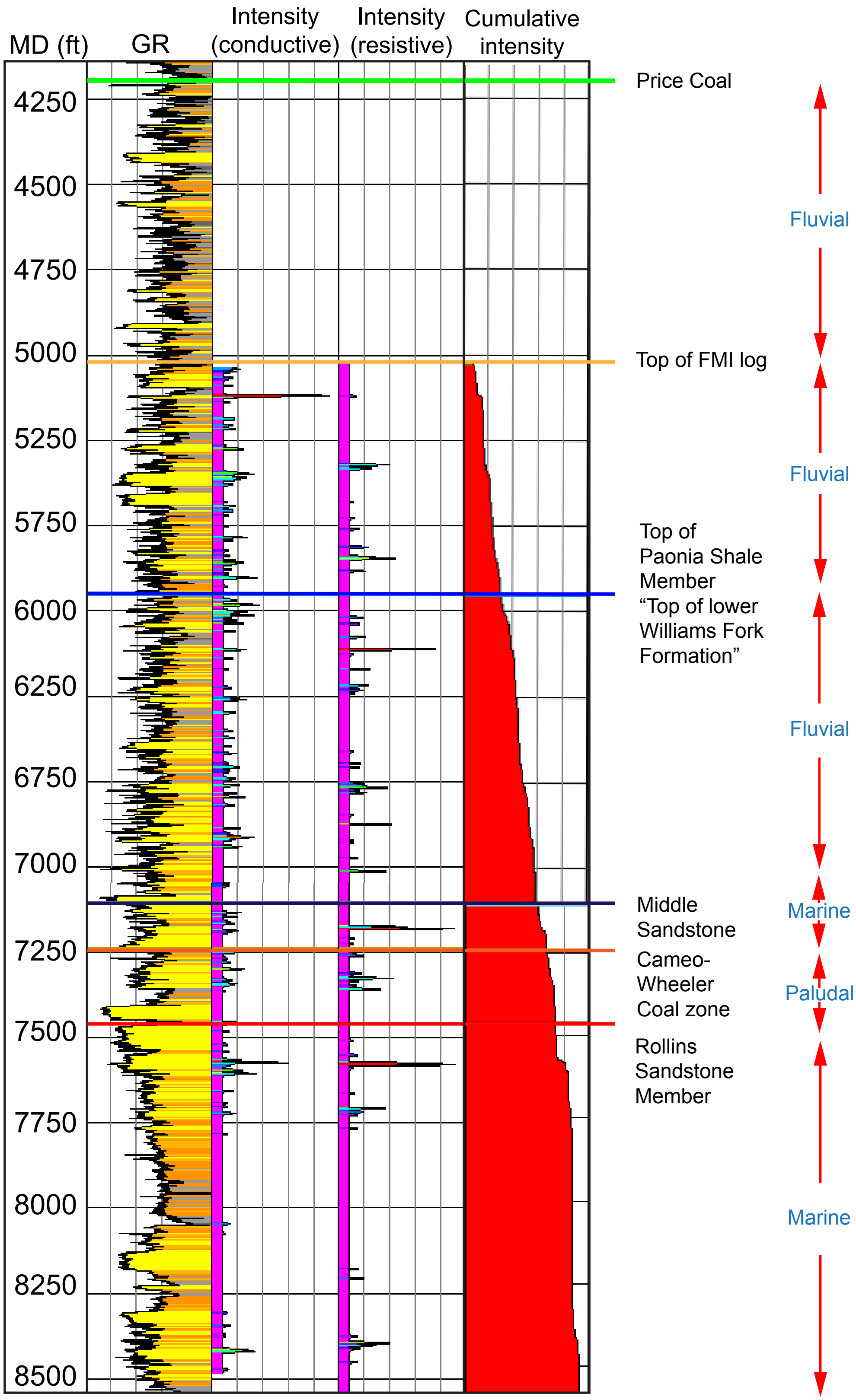

Figure 40. Fracture-intensity type log. Fracture-intensity logs were generated for conductive and resistive fractures at 10 wells using a 5 ft (1.5 m) window. Fracture-intensity logs indicate a non-uniform distribution of natural fractures. It appears that conductive and resistive fractures occur in any depositional settings.

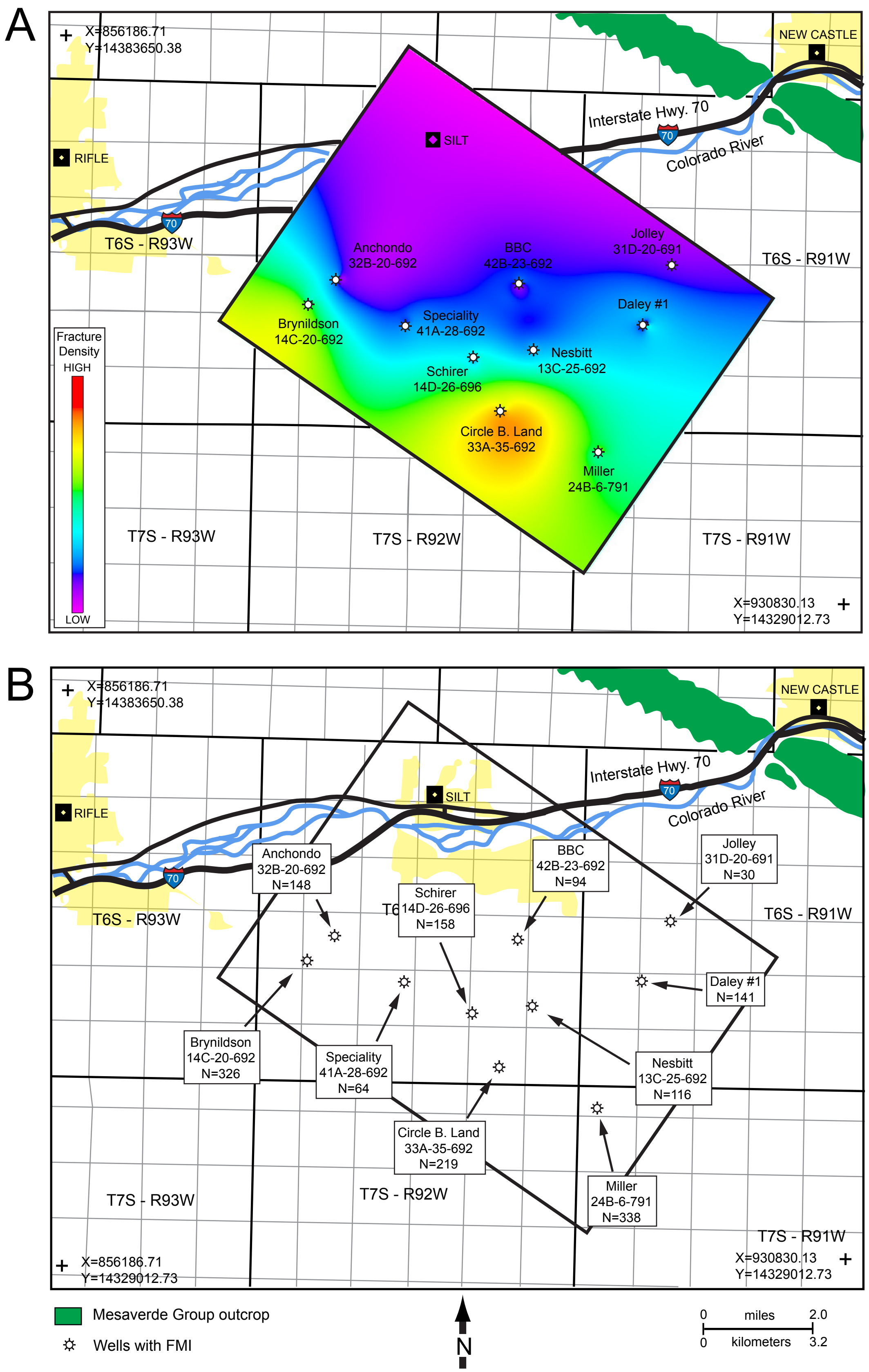

Figure 41. A) Fracture-density map for the Williams Fork Formation generated using fracture-intensity logs for 10 wells. Fracture density map shows higher fracture intensity in the southern and southwestern portion of the study area. B) Map view of the number of fractures per well in the study area.

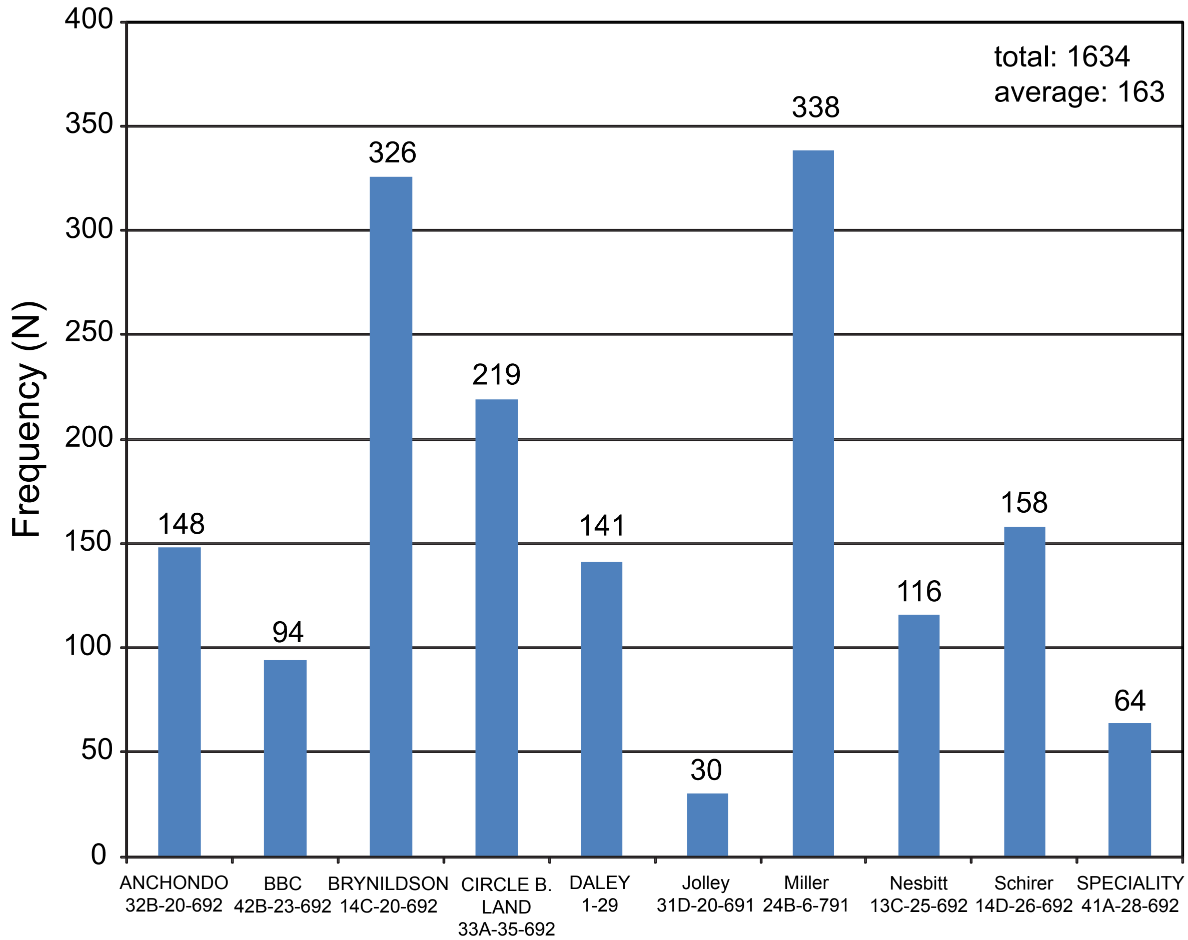

Figure 42. Histogram of the number of fracture per well. Fracture distribution varies greatly from one well to another indicating that the distribution of fractures in the study area is non-uniform and differs as much as by one order of magnitude from one well to another.

An important part of fracture analysis is to analyze the dip and strike orientation of fractures to evaluate the data for preferred orientations. Fracture orientations of conductive and non-conductive (resistive) fractures, as well as measured dip angle and dip azimuth values from electrical borehole-image logs, are displayed on equal-angle (Schmidt) stereographic net projections and rose diagrams (dip azimuth and strike azimuth) for the 10 wells. Interpretation of electrical borehole-image logs indicates a consistent N45°W strike of conductive fractures, which is parallel to present-day in-situ maximum horizontal stress (S_{hmax}), and a mean dip value of 74° (Figure 43). Resistive fracture strike ranges from N45°W to N80°W and N-NE striking resistive fractures are present as well (Figure 44).

In-situ Stress Analyses

Borehole breakouts are commonly good indicators of present-day in-situ stress. When a well is first drilled, the wellbore has a circular shape, which becomes more elliptical with time under tectonic stress. Under tectonic stress, wellbore deformation (from circular to elliptical) creates induced-tensile fractures and borehole breakouts. If one thinks of an elliptical wellbore deformed under the tectonic stress, this wellbore can be divided by two orthogonal coordinate axes into quadrants. Each quadrant is either extensional or compressional; the extensional quadrant forms along the Maximum Horizontal Stress (S_{hmax}) and the compressional quadrant forms along the Minimum Horizontal Stress (S_{hmin}) (Figure 45). When the wellbore deforms due to tectonic stress, tensile fractures form along the extensional quadrants of the wellbore, parallel to the Maximum Horizontal Stress (S_{hmax}), and borehole breakouts form within the compressional quadrants, parallel to the Minimum Horizontal Stress (S_{hmin}). Borehole breakouts when combined with the orientation of inferred natural and induced fracture sets may be related to directional permeability in the subsurface (Haws and Hurley, 1992; Heffer and Lean, 1993; Hurley, 2004). This information can also be used to optimize the orientation of horizontal wells and to configure injection patterns in secondary and tertiary recovery schemes (Hurley, 2004).

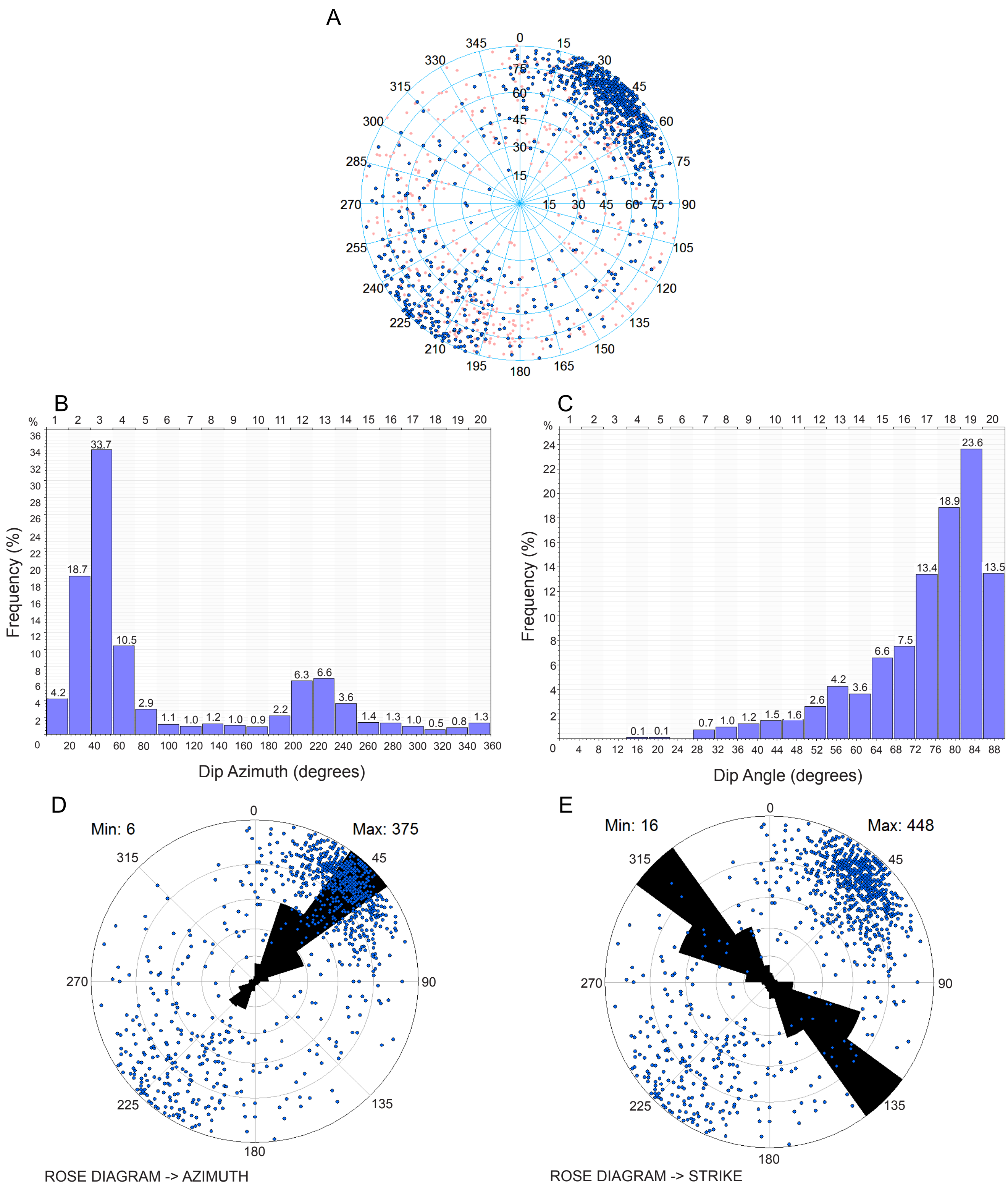

Figure 43. Stereonet, rose diagrams, and histograms of conductive fratures. A) The stereonet displays conductive fracture dip azimuth and dip angle data. B and C) the histograms of dip angle and dip azimuth data. 33.7% of conductive fractures dip N45°E. The histogram of dip angles indicate that conductive fracture are near-vertical. D and E) rose diagrams display dip azimuth and strike azimuth of conductive fractures. Conductuve fracture dip azimuth accumulates around N45°E, so conductive fractures strike N45°W in the direction of the Maximum Horizontal Stress (S_{hmax}).

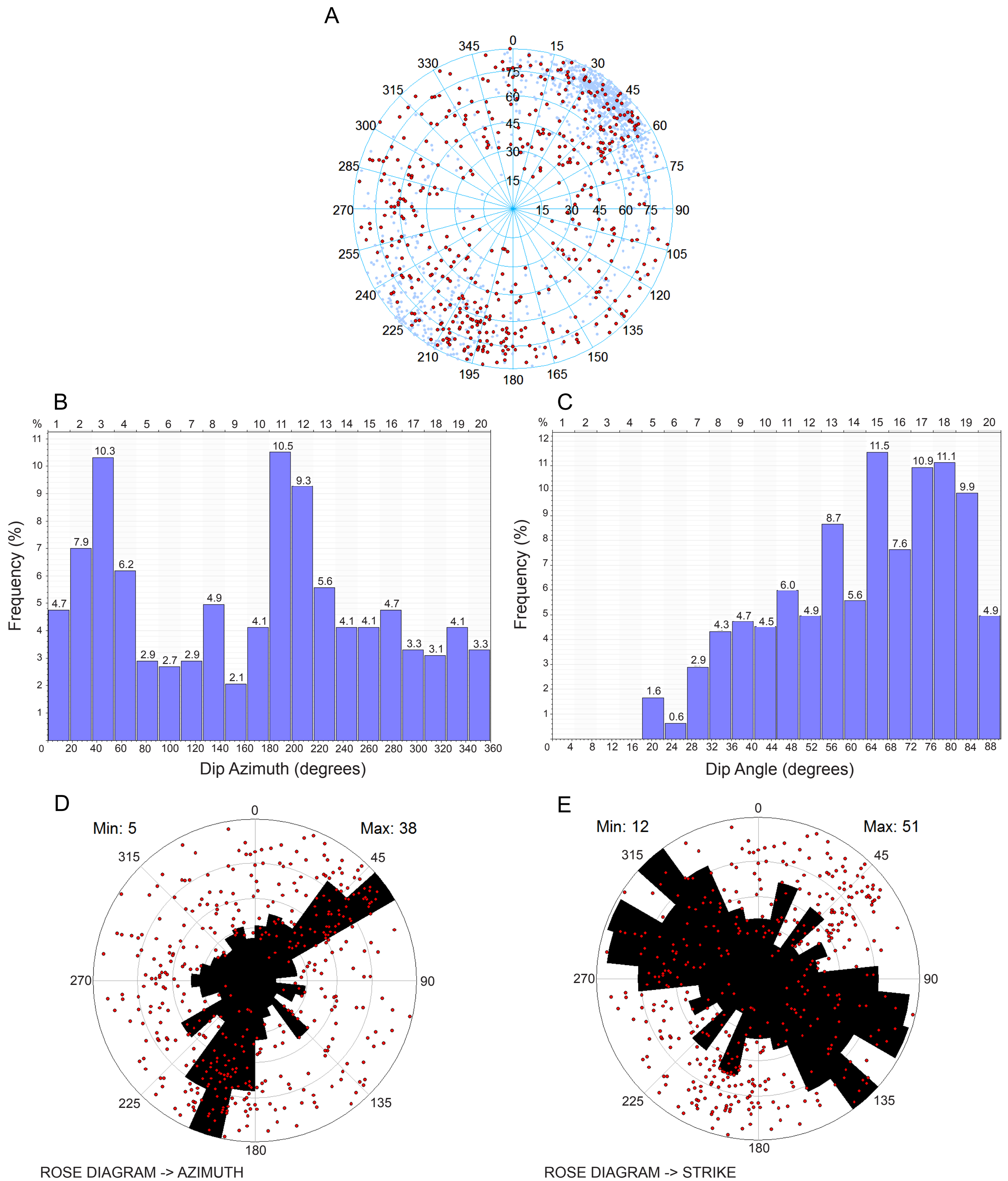

Figure 44. Stereonet, rose diagrams, and histograms of resistive fratures. A) Stereonet displays resistive fracture dip azimuth and dip angle data. B and C) the histograms of dip angle and dip azimuth data. Unlike conductive fractures, dip azimuth values of resistive fractures vary. Resistive fractures dip in lower angles. D and E) rose diagrams display dip azimuth and strike azimuth of resistive fractures. Dip azimuth values of resistive fractures cluster around N65°E and S25°W. Resistive fracture strikes scatter. It appears that resistive fractures strike N45°W to N80°W.

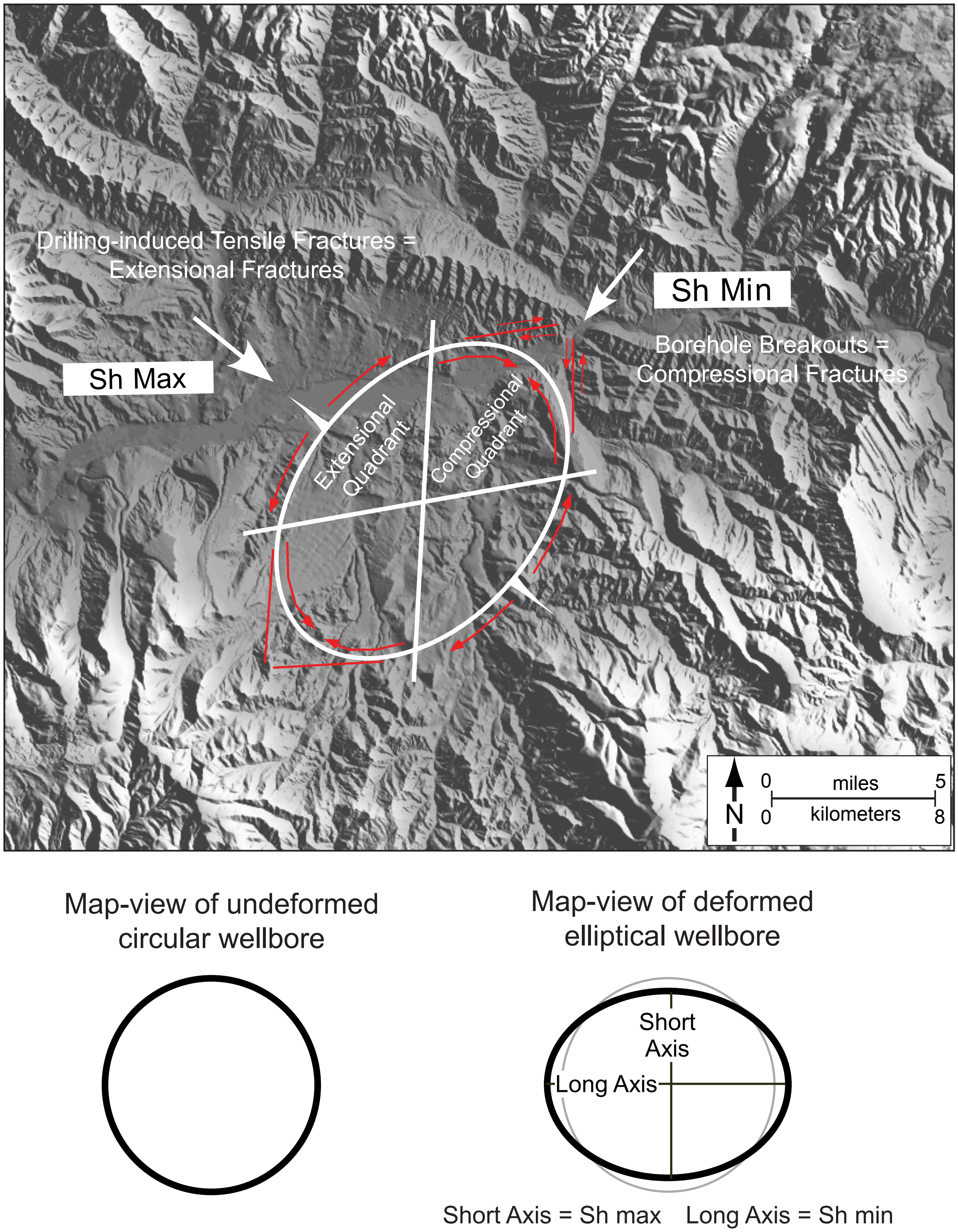

Figure 45. Wellbore before and after the deformation caused by regional stress. Figure shows the compressional and the extensional quadrants of a wellbore after deformation, which is illustrated in a study area map. Borehole breakouts form along the compressional quadrants, whereas drillind-induced fractures form along the extensional quadrants (DEM data from http://seamless.usgs.gov/).

Electrical borehole-image logs were also used to evaluate present-day in-situ stress direction on the basis of wellbore failures, which comprises both borehole breakouts as compressive failures and drilling-induced tensile fractures as tensile failures (Moos and Zoback, 1990; Tezuka et al., 2002). A consistent N-NW oriented present-day in-situ maximum horizontal compressive stress (S_{hmax}) state is evident both from N-NW oriented induced-tensile fracture strike orientation and from borehole breakout strike orientation which is perpendicular to this direction and is an indicator of minimum horizontal compressive stress (S_{hmin}) (Figures 46 and 47). Induced-tensile fractures and breakouts are observed along the entire interval from 4000 to 8400 ft (1220 to 2560 m) of the image data for all 10 wells. Furthermore, a dip azimuth versus depth cross-plot reveals rotation of the axes of horizontal stresses along the well trajectory with increasing depth. The axis of maximum horizontal stress from 4000 to 7200 ft (1220 to 2195 m) exhibits about 20 degrees of rotation in a clockwise direction; however, the cross-plot indicates about a 20-degree sudden counterclockwise shift in the rotation of stresses at about 7200 ft (2195 m), where Rollins Sandstone Member of the Iles Formation rests (Figure 48). Below a depth of 7200 ft (2195 m), a similar clockwise rotation change is observed.

SEISMIC ANALYSIS OF FRACTURES

Introduction

The detection of subsurface fractures and the estimation of fracture parameters from seismic data are of great importance in hydrocarbon recovery because significant amounts of hydrocarbons are trapped in tight reservoirs, where natural fractures have great impact on production (Sava and Mavko, 2007). Although FMI logs, cores, outcrops, and conventional well logs provide direct observations of fractures and fracture properties, they do not provide enough information about how the fracture orientation, intensity, and distribution change spatially with respect to distance from the wellbore; in other words, this information is localized to the well

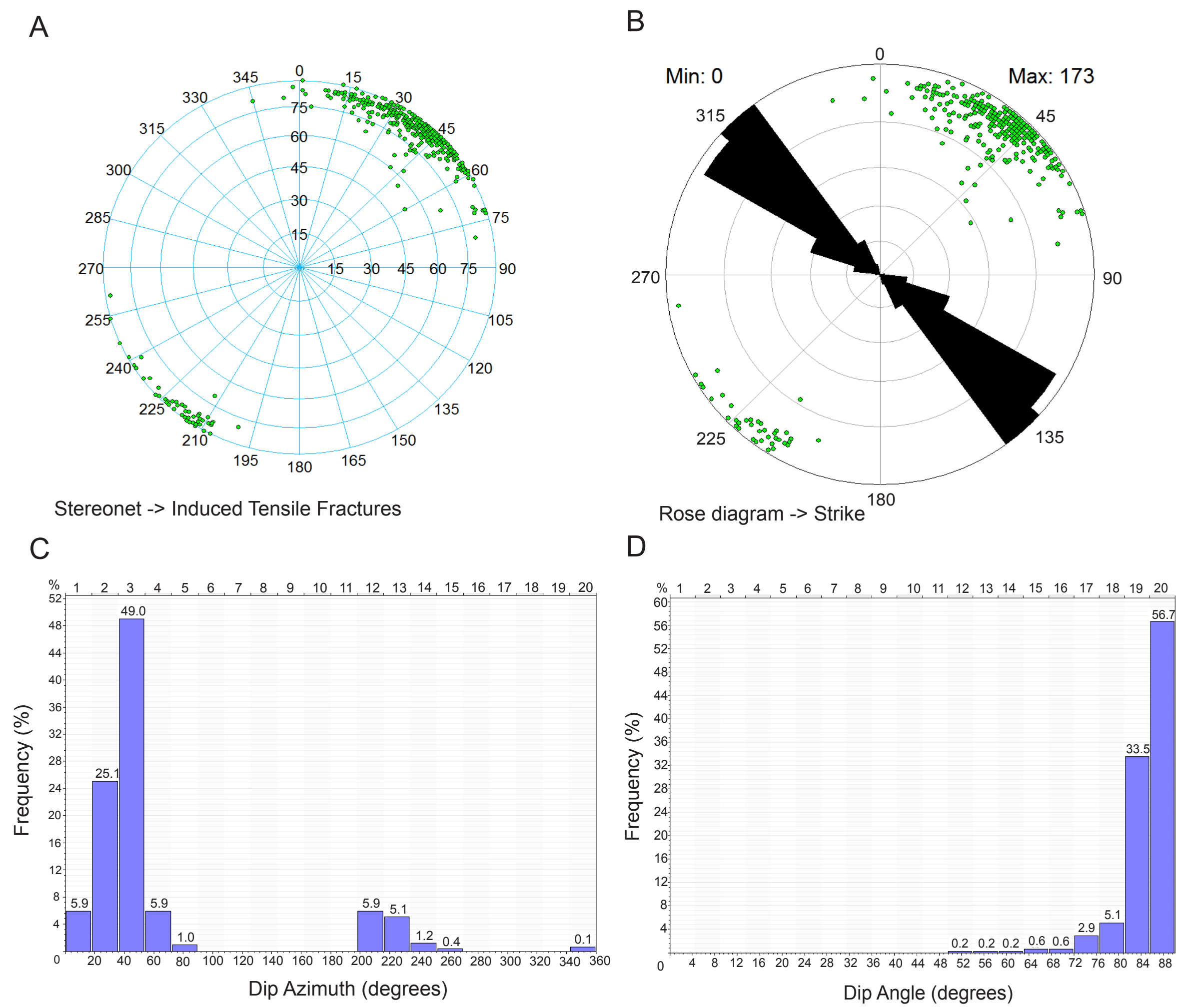

Figure 46. Stereonet, rose diagram, and histograms of drilling-induced fractures interpreted at 10 wells. In-situ stress orientation analysis indicate a N-NW orientation of maximum horizontal stress (Shmax). A and B) Induced-tensile fractures strike along the maximum horizontal stress (Shmax). C and D) 49% of induced-tensile fractures dip N45°E, which is perpendicular strike orientation of N45°W.

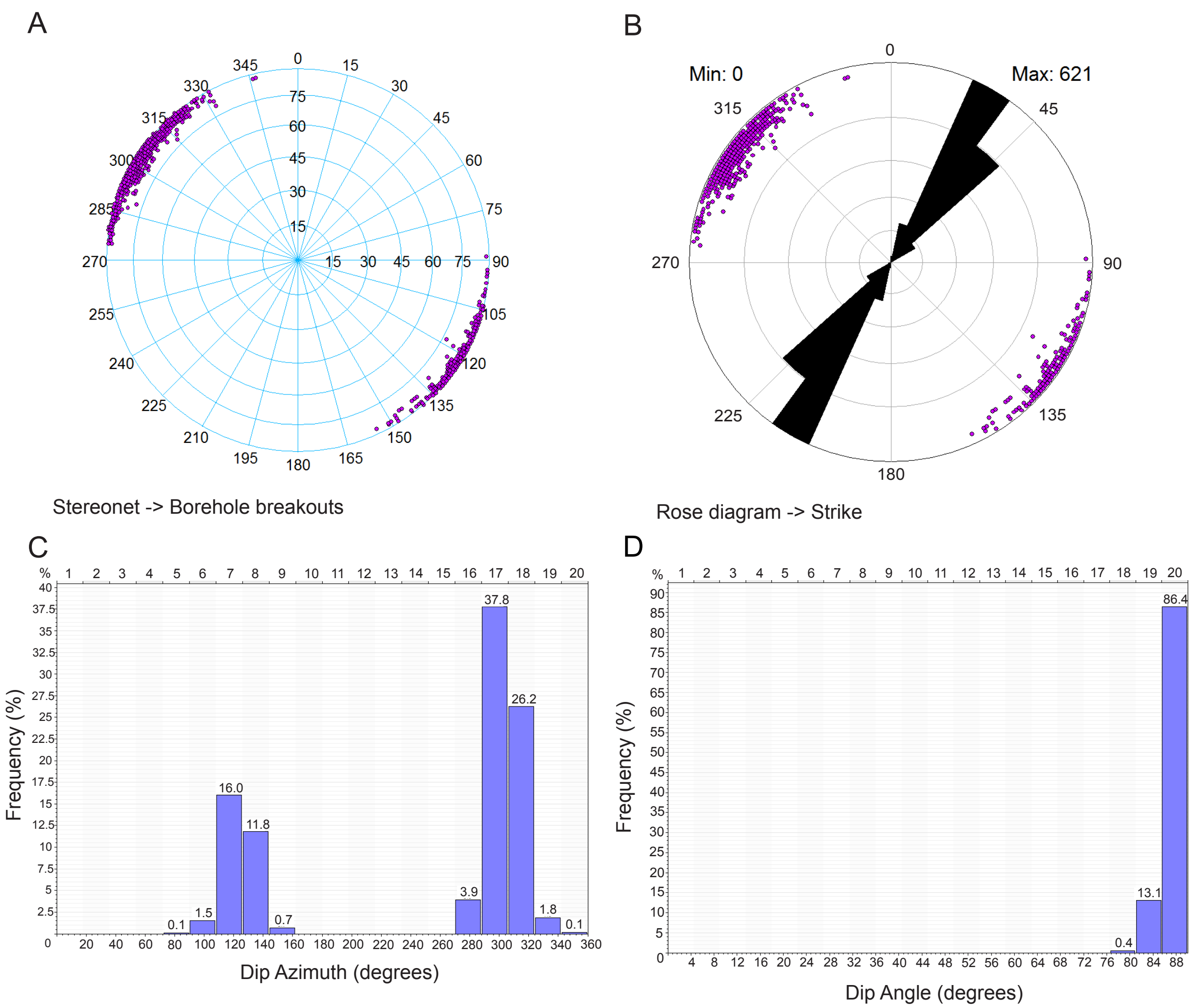

Figure 47. Stereonet, rose diagram, and histograms of borehole breakouts interpreted at 10 wells. A and B) Stereonet and rose diagram show a N-NE orientation of the minimum horizontal compressive stress (Shmin), which is consistent with induced-tensile fractures. Borehole breakouts form within the compressional quadrants alont the Shmin. C and D) Histograms show frequency of dip azimuth and dip angle values. Dip azimuth of borehole breakouts cluster around N60°W and S60°E and they dip vertical.

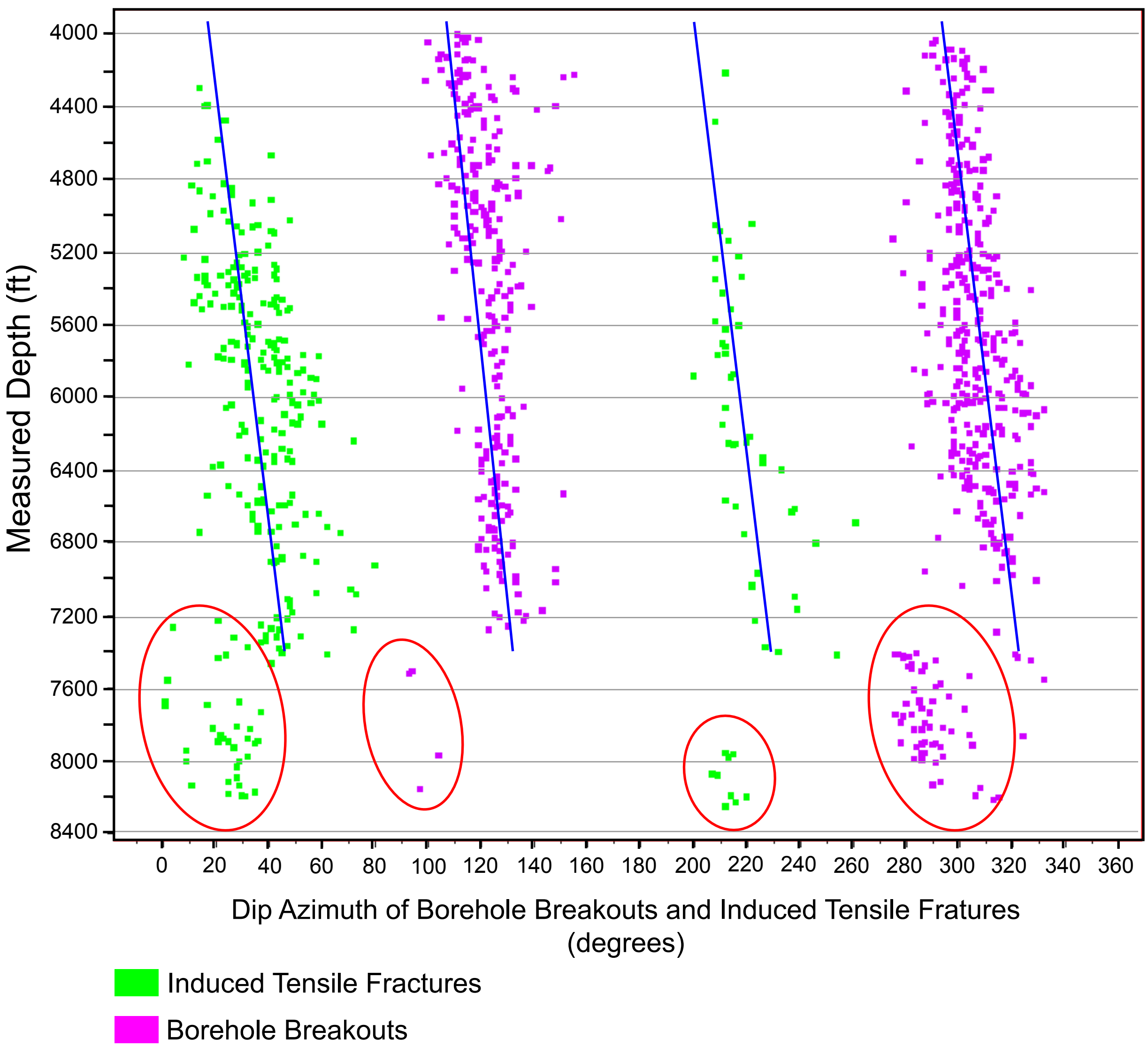

Figure 48. Cross-plot of measured depth versus dip azimuth of borehole breakouts and induced tensile fractures. Induced-tensile fracture and borehole breakout dip azimuth values show ~20 degrees of rotation in the direction of the maximum horizontal present-day stress in the Piceance Basin. Abrupt 20-degree counterclockwise shift is shown at 7200 ft (2195 m).

bore. In order to fill the gap between wells, three-dimensional seismic data is a powerful tool, as the relationship between seismic and fracture properties is established. Even though seismic reflection data itself may not be the indicator of fracture properties alone, seismic attributes extracted from seismic data are useful to identify fracture properties such as fracture intensity and orientation. This study identifies highly fractured areas (intensity) indirectly by measuring certain seismic attributes such as ant-track and t* attenuation. Characterization of fractures using seismic attributes is a scale-dependent process, and the seismic resolution is lower than the scale of the features of interest to characterize. The resolution of seismic data is determined by seismic wavelength, which is given by the ratio between seismic velocity and frequency (seismic wavelength (λ)=Velocity (V)/Frequency (F)). The seismic wavelength is expected to increase with depth and causes poor resolution due to change in seismic velocity and frequency with respect to depth. On the one hand, seismic velocity increases with increasing depth because of the compaction of rocks due to their age, older rocks are expected to be more compact (Sheriff, 1985; Brown, 2004). On the other hand, increasing depth causes a decrease in the predominant seismic frequency because higher frequencies are attenuated with increasing depth (Sheriff, 1985; Brown, 2004). The changes in seismic velocity and frequency result in poor seismic resolution, therefore seismic imaging of fractures becomes a challenge given the size of features of interest (fractures) in comparison to seismic wavelength (Maerten et al., 2006; Lines et al., 2007; Lohr et al., 2008; Ameen et al., 2010). Migration is known to improve seismic resolution significantly by repositioning reflections, collapsing diffractions, and focusing energy spread over a Fresnel zone (Lindsey, 1989; Brown, 2004).

Methods

The method used to analyze relationships between seismic attributes (ant-track and t* attenuation attributes) and fracture-intensity logs allows investigation of such relationships along a wellbore using a 3-D grid (Figure 49). The advantages of using a 3-D grid for seismic analysis

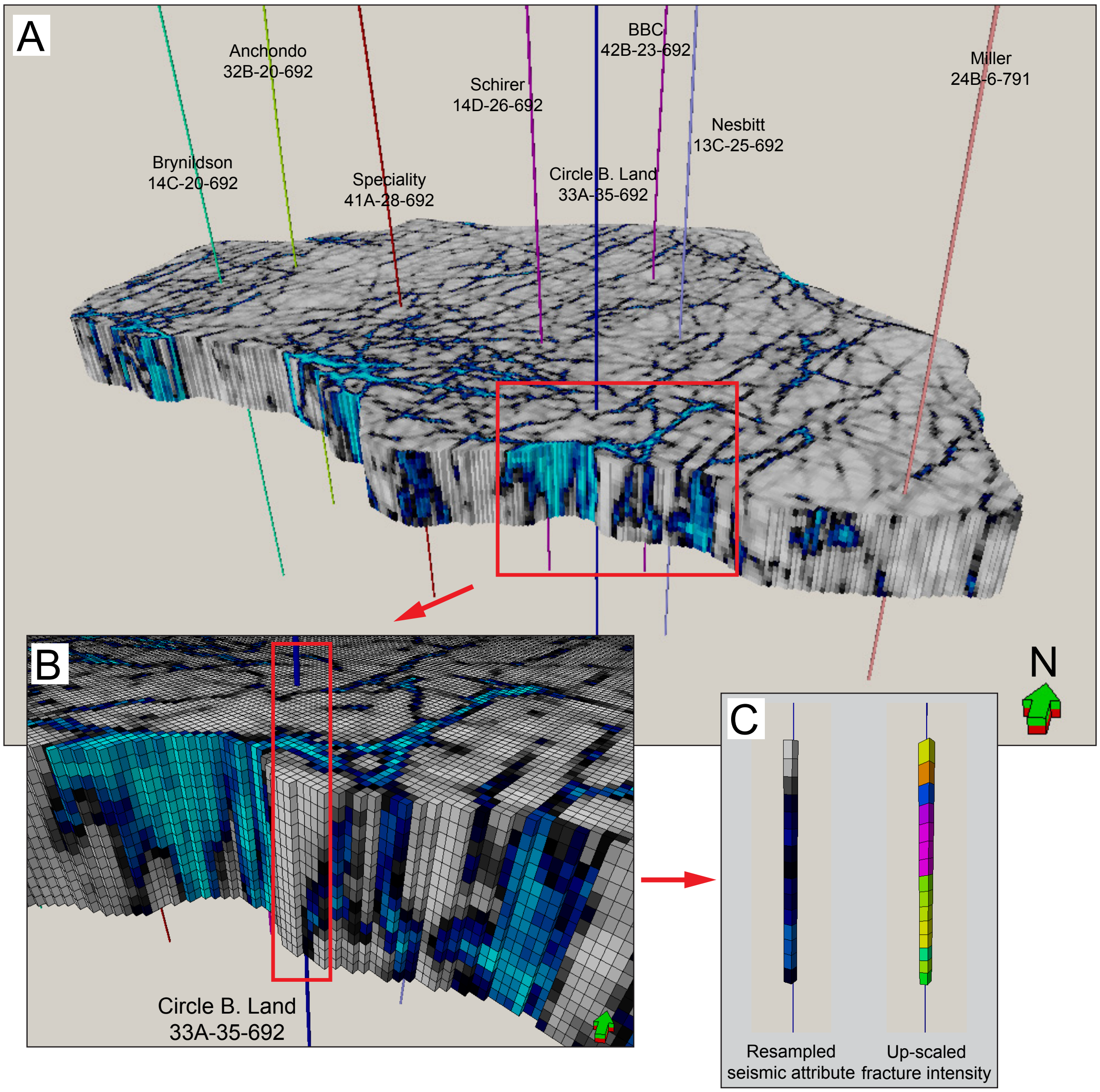

Figure 49. Example of a 3-D grid used in this study to investigate relationships between resampled seismic attributes and up-scaled fracture-intensity logs. A) General view of the 3-D grid in the study area with wells which has FMI log data available displayed. B) Zoom-in box shows Circle B. Land and each grid cell in more details. C) Resampled seismic attributes and up-scaled fracture intensity log along the wellbore can be seen.

of fractures are: first, it makes it possible to investigate the relationship in different scales (different layering of 5-10-25-50-100 ft (1.5-3-7.5-15-30 m)), and second, it allows cross-plotting of seismic attributes versus fracture intensity to see the correlation between the two parameters. In order to generate cross-plots from seismic attribute and fracture-intensity logs, the user must sample seismic attributes into the 3-D grid and scale-up fracture intensity logs. The seismic attribute is sampled into the 3-D grid by assigning an attribute value to each cell, using an intersecting method with arithmetic averaging in which all seismic cells intersecting the property contribute to the average calculations (Figure 49). This method produces accurate results as seismic attributes are sampled into a 3-D grid. In scaling up the fracture-intensity logs, each grid cell that the well penetrates is assigned a log value based on all log values that fall within the cell and the algorithm (average method) used (Figure 49). Fracture-intensity logs were up-scaled using an arithmetic mean averaging method.

RESULTS

Ant-track Attribute Fracture Intensity Relationships

Different ant-track volumes were created to analyze fracture-intensity and seismic-attribute relationships. The ant-track workflow was adopted again to generate ant-track attribute cubes, except that the structural smoothing step was omitted because in this part of the study, small discontinuities are significant and structural smoothing reduces small discontinuities. Therefore, variance edge-detection method was applied to original seismic data with a vertical window size of 64 ms and filter length value of three traces. These values were set to vertical window size of 64 ms and filter length value of five traces in the fault analysis part of this study.

After generating different ant-track attribute cubes, investigation was conducted by following the steps below. Each generated ant-track attribute volume was sampled into a 3-D grid and cross-plots were generated between up-scaled fracture intensity logs and resampled attribute volumes. 20 different ant-tract attributes were generated by adjusting “initial ant boundary,” “ant-track deviation,” “ant step size,” “illegal steps allowed,” “legal steps required,” and “stop criteria.” Explanations and how these parameters work are provided in the Ant-tracking Workflow section (please see Chapter 2 for more information). Some of the observations made are below:

1) The initial ant boundary parameter determines how closely the initial ant-track agents can be placed within the volume. For a fracture related study, this parameter should be kept small enough to capture smaller details. When this value is set to a larger number, fewer initial ants are placed and less detail is captured. Comparison between 5 and 3 voxels has been made and no difference observed. It is worth noting that there is no benefit using a radius smaller than 3 voxels, as the agents will follow the same events and no new information will be added.

2) Observations did not show any benefit of changing the ant-track deviation parameter; thus a default value of 2 was used.

3) Observations showed that “ant step size,” “illegal steps allowed,” and “legal steps required” parameters affected the output. Ant step size was set and limited to 4 since increasing this value allowed ant agents to search further, finding more connections but at a coarser resolution.

4) Finally, it was observed that stop criteria of 10% to 15% allowed a reasonable number of illegal steps. Larger stop criteria allow more illegal steps, creating illegitimate fault geometry. This was also observed in the seismic data by practical experience.

Based on 20 different realizations, a reasonable relationship was found using the parameters below:

Initial Ant Boundary: 5

Ant-track deviation: 2

Ant step size: 4

Illegal step allowed: 2

Legal steps required: 3

Stop criteria: 15%

Seismic attribute/fracture relationships were examined for eight different zones throughout the seismic survey area. A type log showing an up-scaled fracture-intensity log and re-sampled ant-track attributes for two zones are shown in Figure 50. Cross-plots between ant-track attribute and fracture-intensity logs give reasonable values of correlation coefficient from 0.55 to 0.75 in five zones (Figure 51). Moreover, ant-track attributes are extracted along the wellbore and visual examination is done (Figure 50). Ant-track attribute appears to give higher values in response to high fracture intensity along the wellbore (Figure 50). However, it should be noted that there may be fractured intervals in the wellbore which has no or weak ant-track attribute expression where ant track is expected to give higher values. At this point, it should be stressed that the wellbore may not be the true expression of how fractures exist beyond the wellbore. The wellbore may or may not cross all the fractures around the wellbore, thus some fractures may be part of a bigger swarm of fractures extended beyond the wellbore. Consequently, ambiguities may exist not only related to seismic data but also related to FMI log data. Figure 52 shows a vertical seismic section (crossline 177) through the ant-track attribute volume, which is the volume that reasonable correlation coefficient values were obtained from after the examination of relationships between seismic attributes and fracture-intensity logs. In addition, Figure 53 contains rotated depth slices through this volume showing the areas of higher ant-track attributes values, so it indicates areas of higher fracture intensity.

t* Attenuation Fracture Intensity Relationships

Frequency dependent attenuation of amplitudes was first introduced as a fracture indicator by Najmuddin (2001). Before Najmuddin (2001), Haugen and Schoenberg (2000) discuss

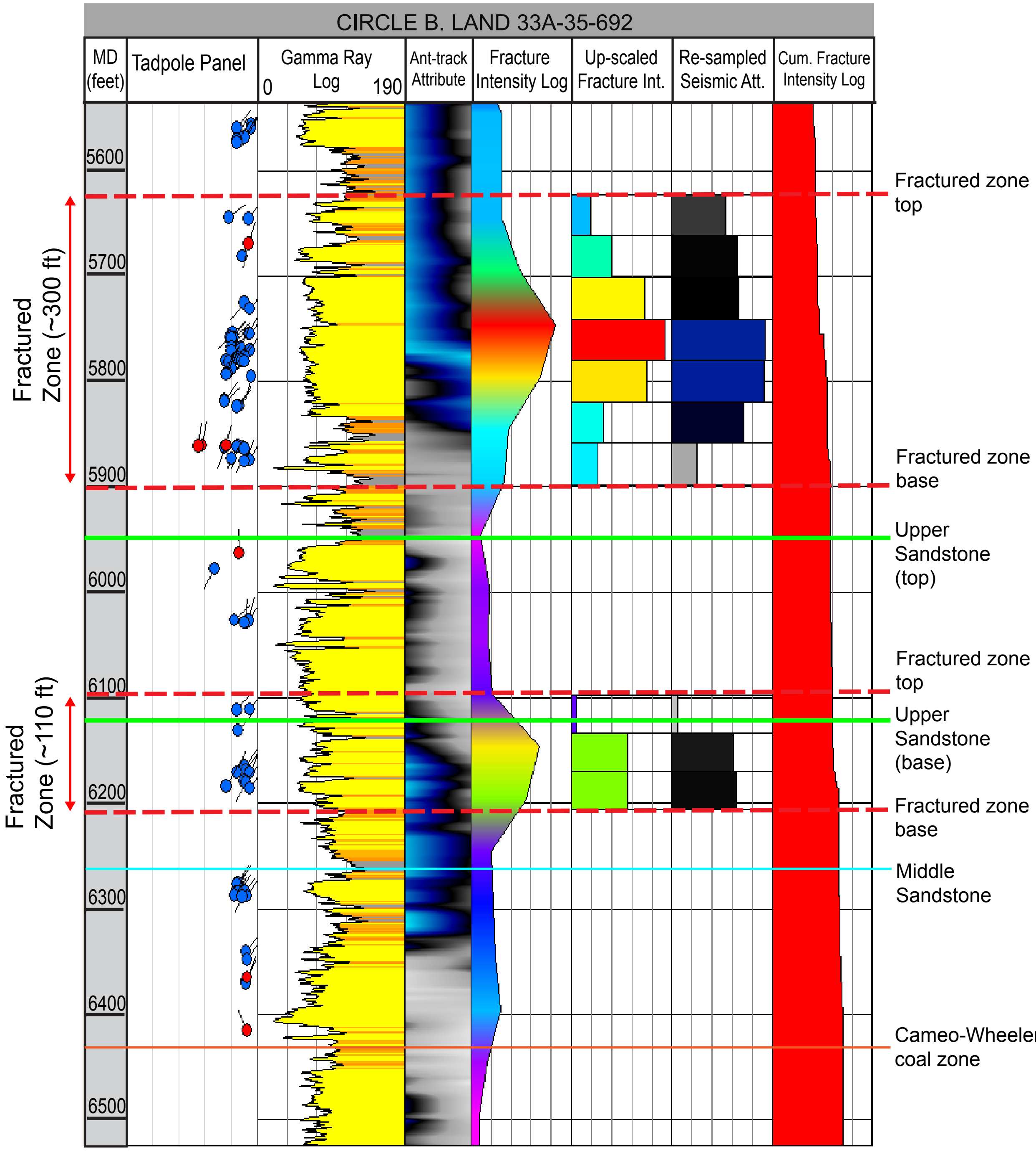

Figure 50. Circle B. Land type log shows tadpole panel of natural fractures, gamma ray log, ant-track attributes extracted along the wellbore, fracture-intensity log generated, and up-scaled fracture-intensity log and re-sampled ant-track attributes for two fractured zones. Cumulative intensity log is also given on the last track. Ant-track attribute values are higher in areas where fracture intensities are higher.

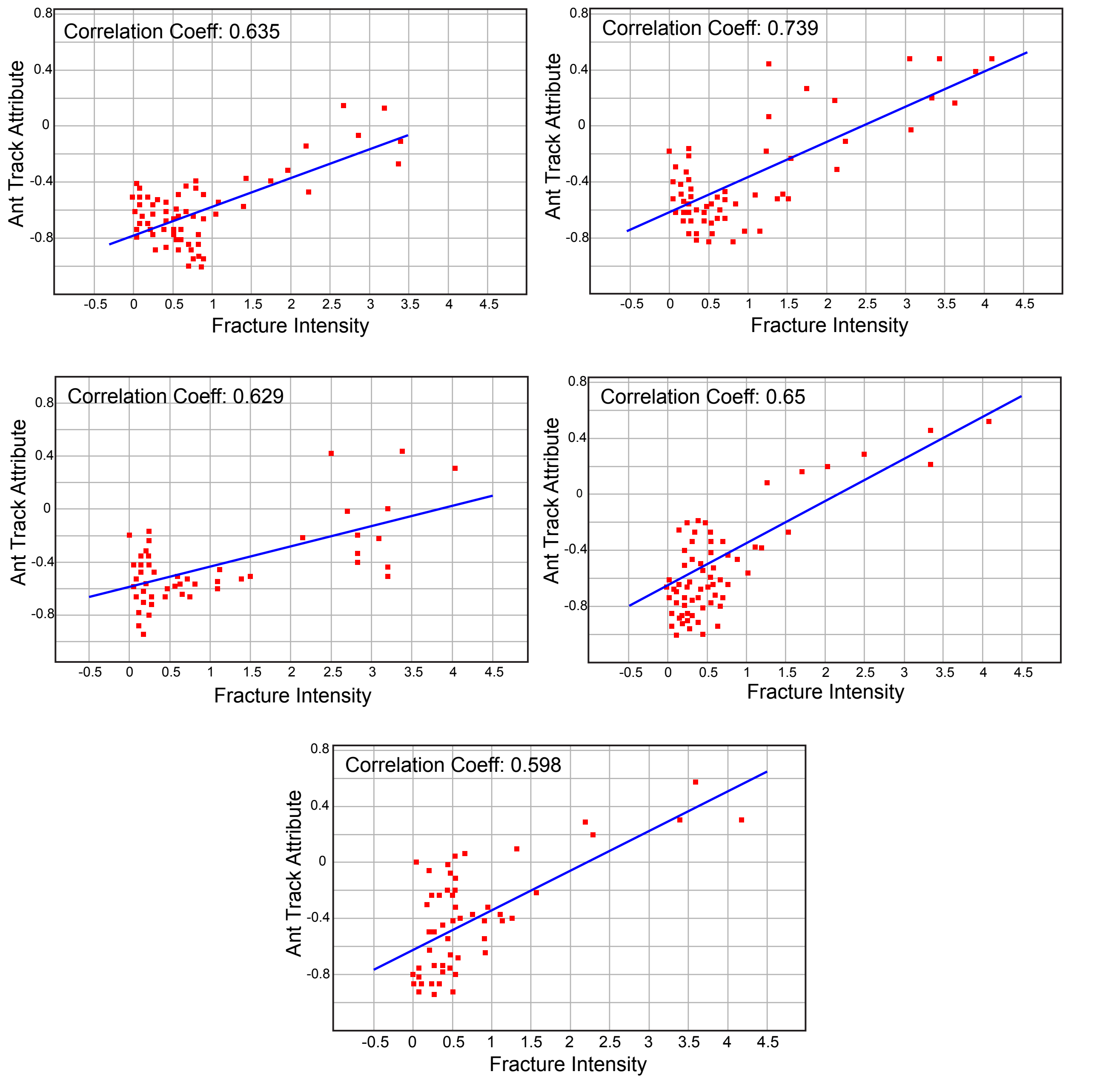

Figure 51. Cross-plots of resampled ant-track attributes versus up-scaled fracture-intensity logs at 10 wells show a reasonable relationship within the fractured zones. Correlation coefficient values range from 0.598 to 0.739, showing the relationship.

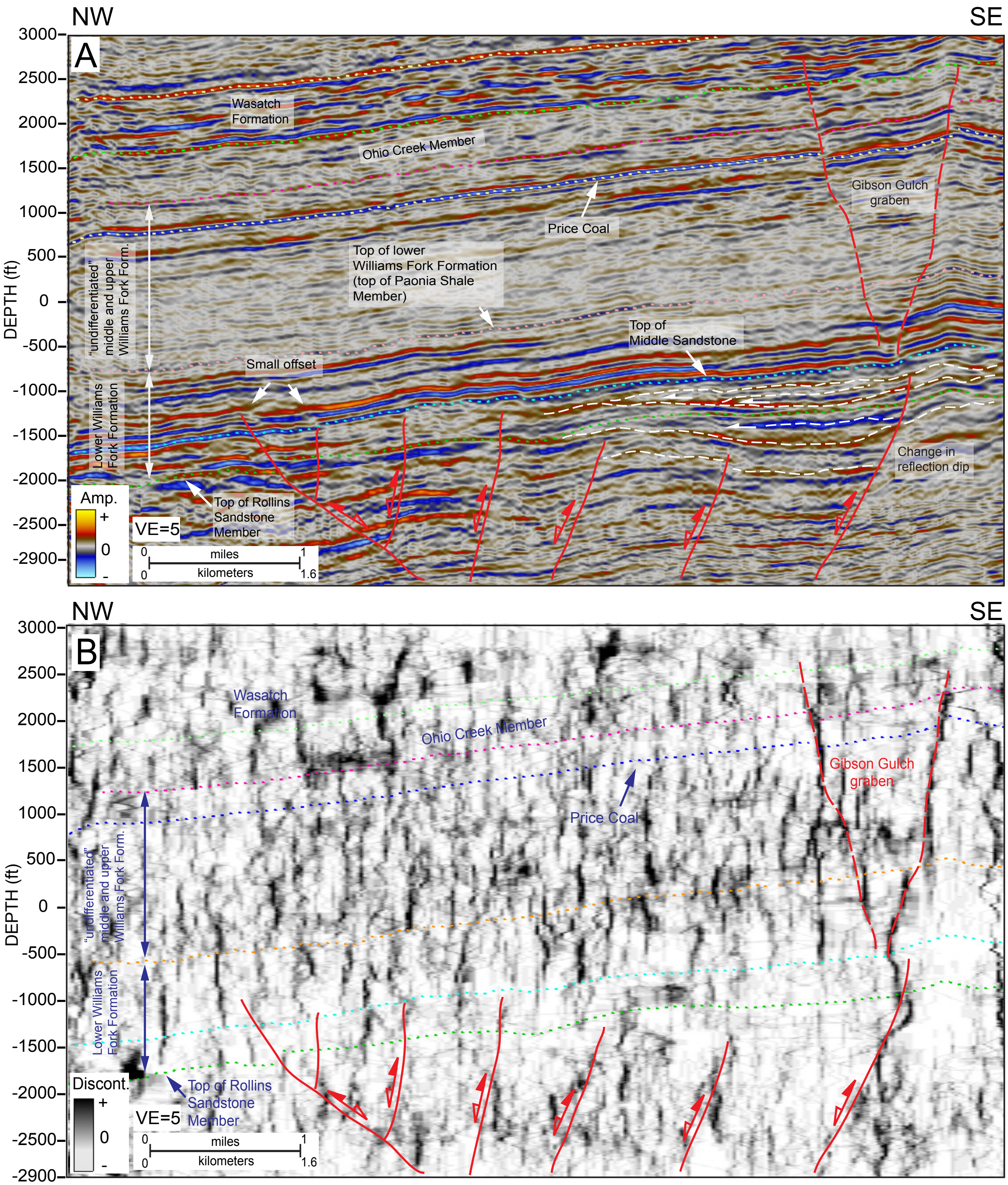

Figure 52. A) Vertical seismic section (crossline 177) through the seismic amplitude volume showing stratigraphic units and interpreted thrust and normal faults. B) Same seismic section (crossline 177) throught the ant-track attribute volume, which has reasonable correlation coefficient values (0.598-0.739), showing ant-track expression of fractures. Location of the seismic section is given in Figure 8B.

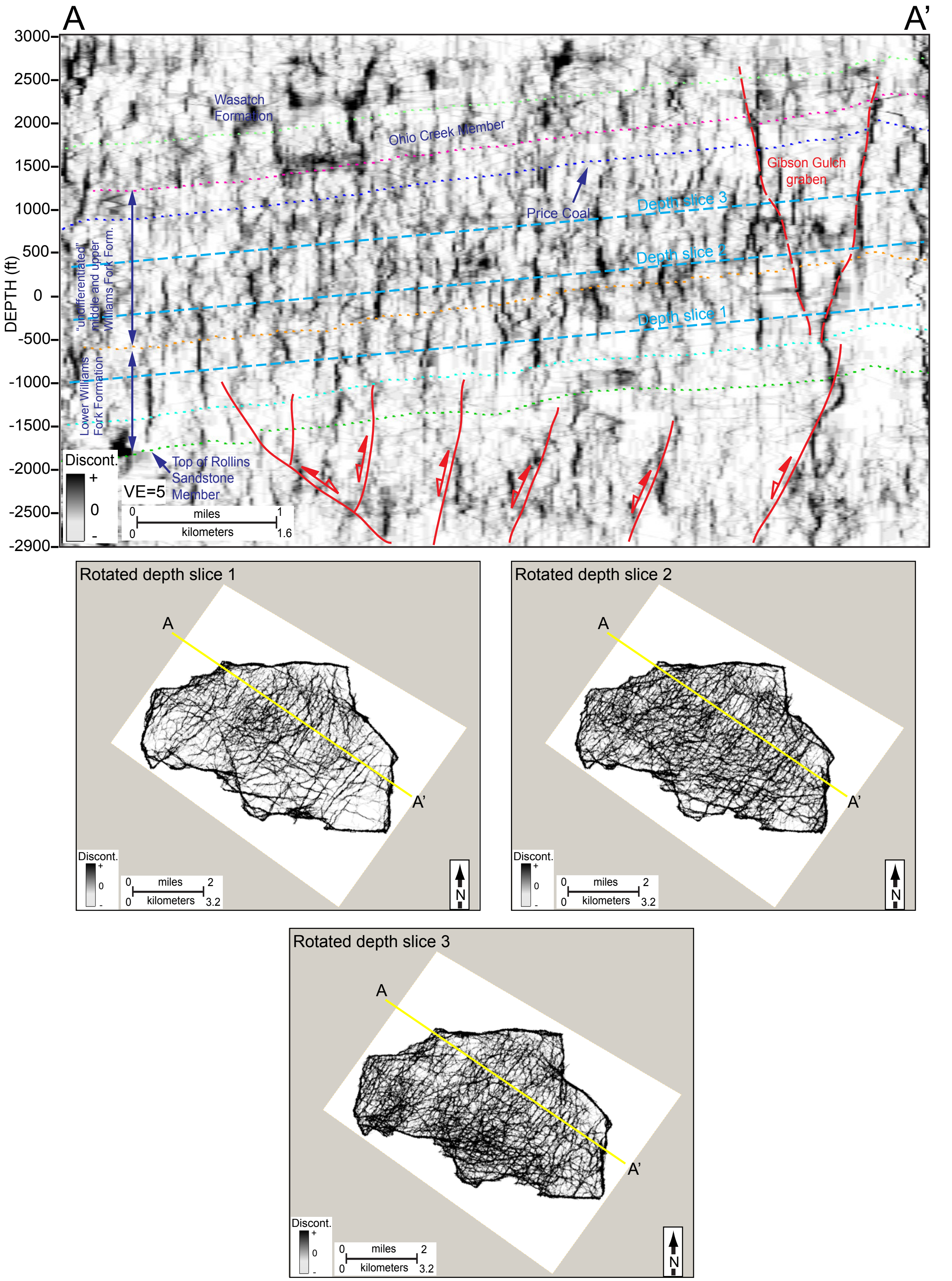

Figure 53. Vertical seismic section (crossline 177) through the ant-track attribute volume, which has reasonable correlation coefficient values (0.598-0.739). Rotated depth slices show ant-track attribute expression of fractures in the study area. Ant-track attribute indicates areas of high disturbance in reflections, so does areas where fracture intensity is higher.

scattering caused by fractures and its relationship to wavelength. Moreover, Schoenberg (1988) discusses the preferential attenuation of higher frequency amplitudes from seismic data and Liu et al. (1997) and Gibson et al. (2000) indicate the diffraction of fracturing using synthetic data derived from theoretical and physical models. The t* attenuation attribute is intended to use frequency data derived from P-wave data to delineate fractures, which attenuates higher frequencies. The product is an attribute volume that includes attribute values called “t*”; therefore, it can be said that larger t* values result from greater attenuation of higher frequencies and the shift of the spectra towards lower frequencies (Najmuddin, 2001). It is suggested by Najmuddin (2003) that higher t* values indicate higher fracture intensity, larger thickness of the fractured layer, or a combination of the two.

This fracture indicator produces a qualitative attribute to indicate intensely fractured areas (sweet spots). However, it doesn’t give a quantitative measure of the number of fractures (Najmuddin, 2001).

Data in this study are expected to be noisy; therefore, it can be expected that the frequency content of the traces may contain noise. As a result, there may be some attenuation of frequencies not related to fracturing. In addition to noise related attenuation, there may be some attenuation of frequencies due to layering, interference, multiples, etc. Therefore, t* values may contain some errors related to factors indicated above (Najmuddin, 2003).

In order to examine the relationship between t* attributes and fracture-intensity logs, different t* attenuation attribute cubes were generated and cross-plotted with up-scaled fracture-intensity logs for eight zones. An example zone is shown in Figure 54. Results showed correlation coefficient values from 0.546 to 0.753 (Figure 55); nevertheless, a discrepancy arose in the interval below the base of the middle Williams Fork Formation. Although ant-track attribute values presented a reasonable relationship, t* attribute values exhibited a poor

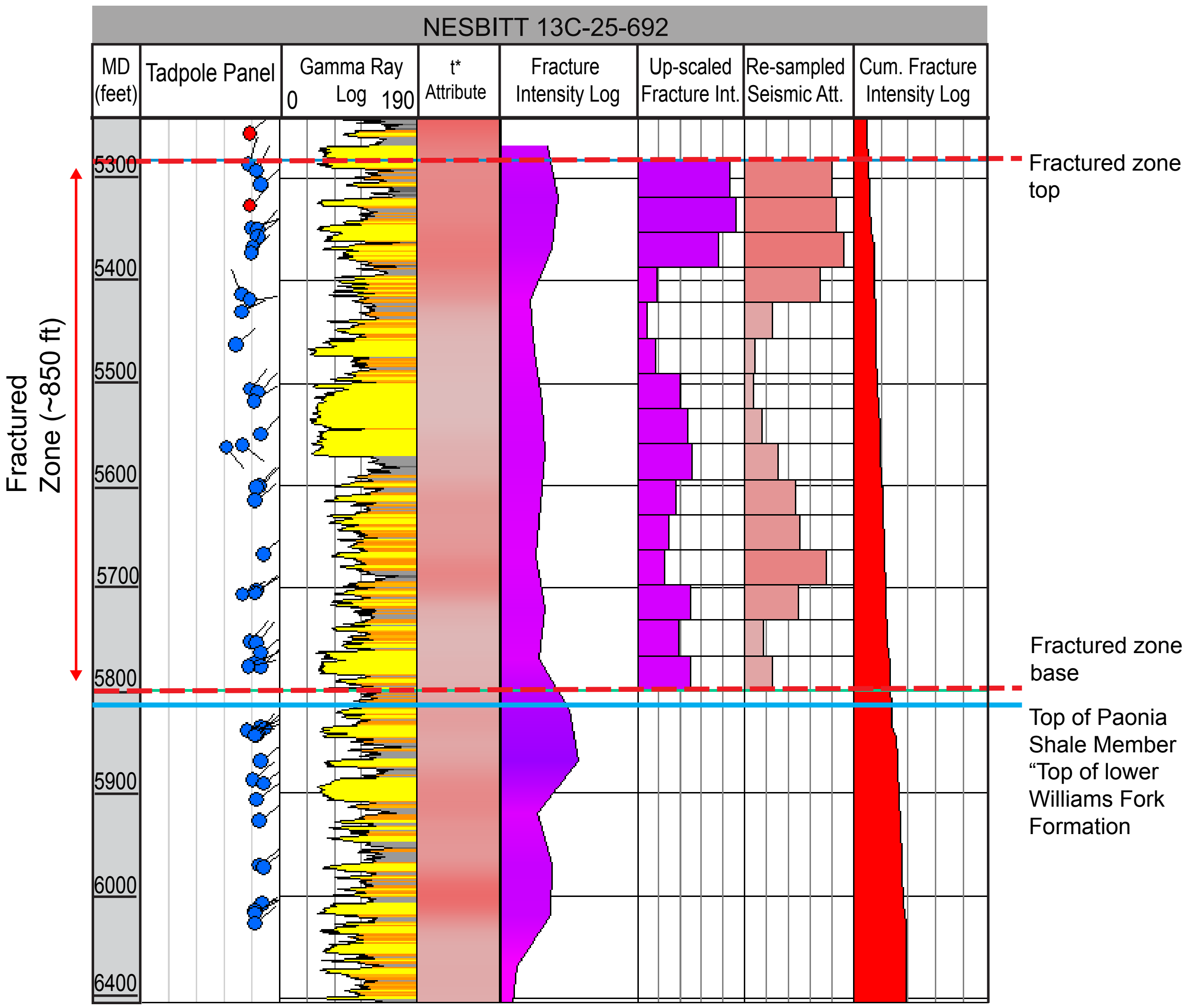

Figure 54. Nesbitt type log shows tadpole panel of natural fractures, gamma ray log, t* attenuation attributes extracted along the wellbore, fracture-intensity log generated, and up-scaled fracture-intensity log and re-sampled t* attenuation attributes for a 850 ft (259 m) thick fractured zone. Cumulative intensity log is also given on the last track. t* attenuation has a reasonable relationship with fracture intensity.

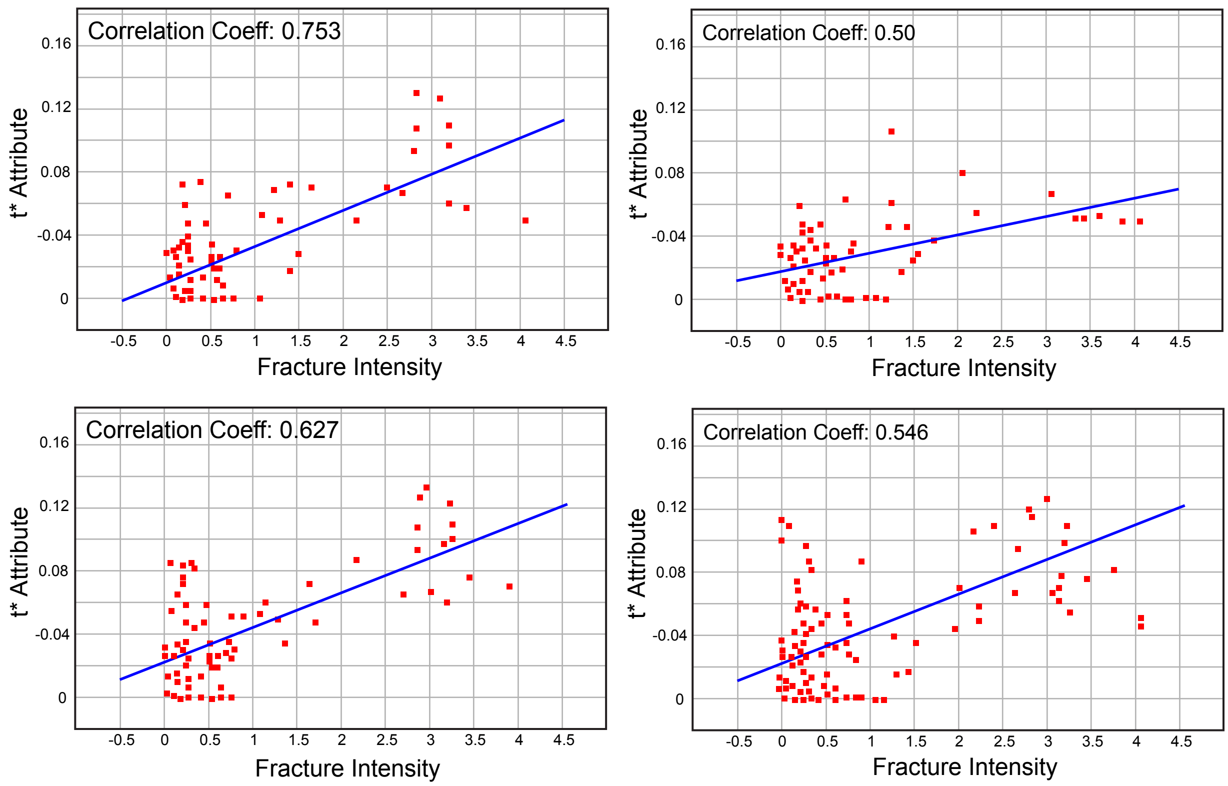

Figure 55. Cross-plots of resampled t* attenuation attributes versus up-scaled fracture-intensity logs show a reasonable relationship within fractured zones. Correlation coefficient values ranges from 0.50 to o.753 in the middle and upper Williams Fork Formation intervals; however, as indicated the relationship is poor within the lower Williams Fork Formation.

(correlation coefficient values from 0.2 to0.35) relationship with fracture intensity in this interval. In contrast, in the middle and upper Williams Fork Formation interval, reasonable results were obtained when t* attribute values were cross-plotted with fracture intensity logs. This discrepancy is assumed to be caused by different seismic properties in lower and upper intervals. Parameters for t* attribute generation allow the user to set a lower and higher frequency comparison point and an analysis window length. Because frequencies are attenuated by increasing depth, parameters allowing a relationship in the upper interval are not applicable to lower interval. Figure 56 shows a vertical seismic section (crossline 177) through the t* attenuation attribute volume and a rotated depth slice through this volume for the interval where reasonable correlation coefficient values (from 0.546 to 0.753) were obtained. Red color indicates areas of high t* values in the study area, so it indicates areas of higher fracture intensity. The interval which gives poor correlation coefficient values (from 0.2 to 0.35) is also shown in Figure 56.

CONTROLS ON FRACTURE DISTRIBUTION

In order to examine the controls on fracture distribution, lithology and architectural element logs were created for the 10 wells with borehole-image logs. Four distinct lithologies were determined based on gamma ray, density porosity, and neutron porosity logs: 1) Clean sandstone is defined by the criteria of < 70 API gamma-ray cut-off; 2) shaley sandstone is ≥ 70 API and ≤ 96 API gamma-ray cut-off; 3) mudstone is >96 API gamma-ray response; and 4) coal is ≤ 96 API gamma-ray cut-off and > 0.25 for density porosity and neutron porosity readings. After creating lithology logs, further analysis was carried out using histograms to investigate the amount of fracturing in a certain type of lithology. Fractures (N=1634) are nearly vertical and dominantly strike W-NW, parallel to the Maximum Horizontal Stress. 60% of natural fractures were interpreted as lithologically bound, terminating against minor lithologic boundaries within the reservoir sandstones and against mudstone contacts bounding the reservoir. More than

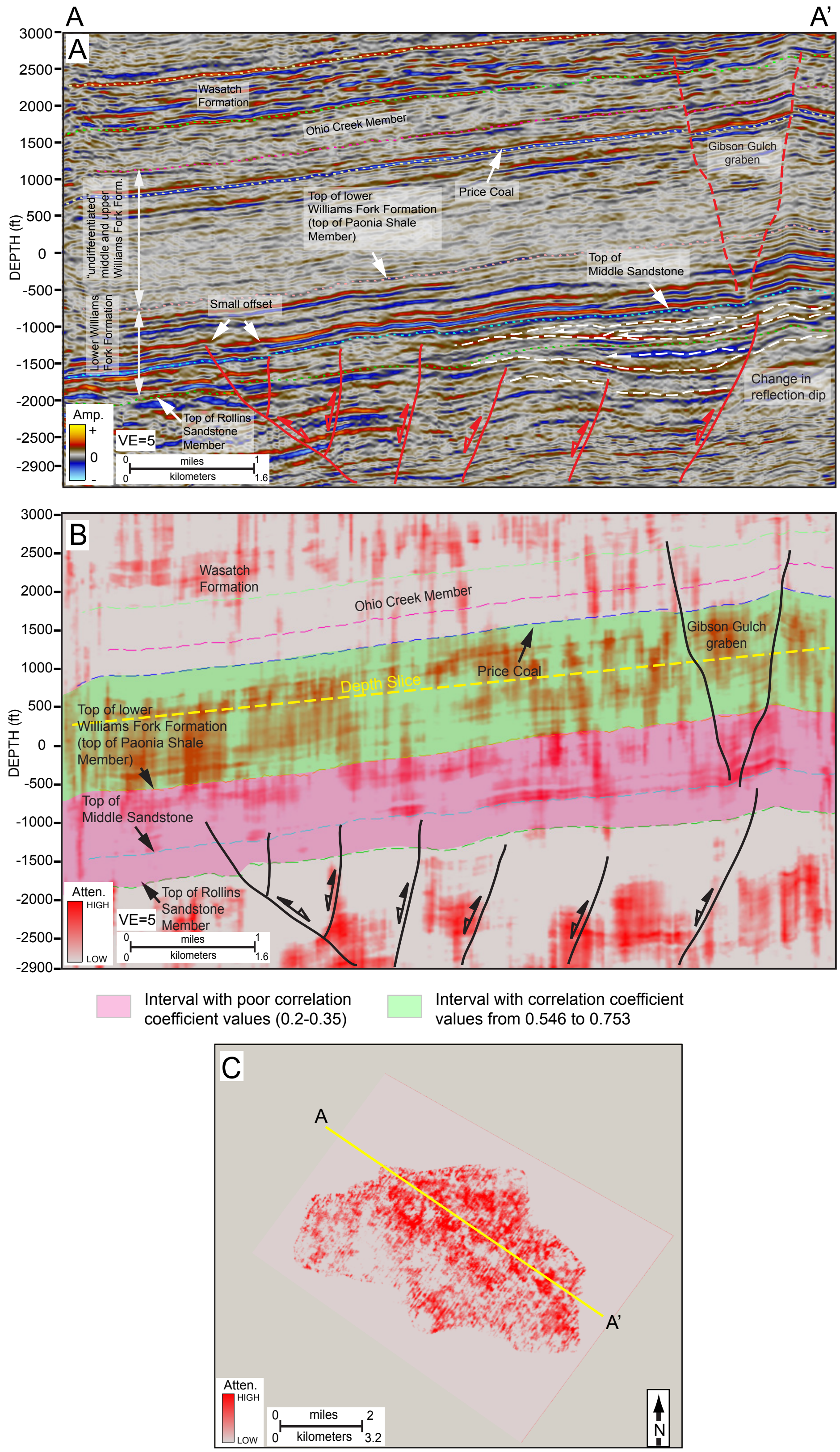

Figure 56. A) Vertical seismic section (crossline 177) through the seismic amplitude volume showing stratigraphic units and interpreted faults. B) Same vertical seismic section (crossline 177) through the t* attenuation attribute volume, which has reasonable correlation coefficient values (0.50-0.753). Interval with poor correlation coefficient values can also be seen. C) Rotated depth slice through the t* attenuation attribute volume. Red areas indicate high t* values, so does areas of high fracture intensity (sweet spots).

90% of natural fractures occur in sandstone and siltstone (Figure 57). However, a few natural fractures are seen in mudstone; those are mostly low-angle resistive fractures and some of them strike in a different orientation than S_{hmax} (S. D. Sturm, 2010, personal communication). The origin of this set is hard to determine and may have been related to a different stress field.

Marine sandstone reservoirs of the Mesaverde Group are more laterally continuous and have more uniform internal characteristics, reflecting few internal discontinuities (Lorenz and Finley, 1989). Conductive fractures within marine intervals of the Rollins Sandstone Member of the Iles Formation, the Upper Sandstone, and the Middle Sandstone, commonly strike W-NW. The distribution of these fractures is irregular, showing swarms of fractures in some wells along with unfractured and/or less fractured intervals. Resistive fractures also occur within these marine intervals, whereas both quantity and occurrence of resistive fractures are visibly small in comparison to conductive fractures. Contrary to conductive fractures, resistive fracture strike orientation varies, and distribution is irregular. Regardless of whether a fracture is conductive or not, fractures occur in two sets, one set belonging to the regional system and striking W-NW, and the other less common set striking N-NE. Typically, conductive fractures strike N-NW, lie parallel to the Maximum Horizontal Stress, and are considerably more important, greater in quantity, and possibly more permeable (open, larger aperture, etc.) than resistive fractures.

Fluvial sandstone reservoirs of the Mesaverde Group differ significantly from marine sandstone reservoirs. Fluvial reservoirs are lenticular in shape, are often discontinuous ways, and contain internal lithologic heterogeneities in terms of grain size, sedimentary structure, and permeability. Because connectivity and internal heterogeneity of the Mesaverde fluvial sandstone reservoirs vary, poor communication among fractures may exist; however, fractures might be interconnected by continuous fractures. Fractures within fluvial sandstone reservoirs provide considerable enhancement in permeability, thus, higher fracture related productivity. Conductive fractures within these reservoirs exhibit dominant W-NW fracture orientation;

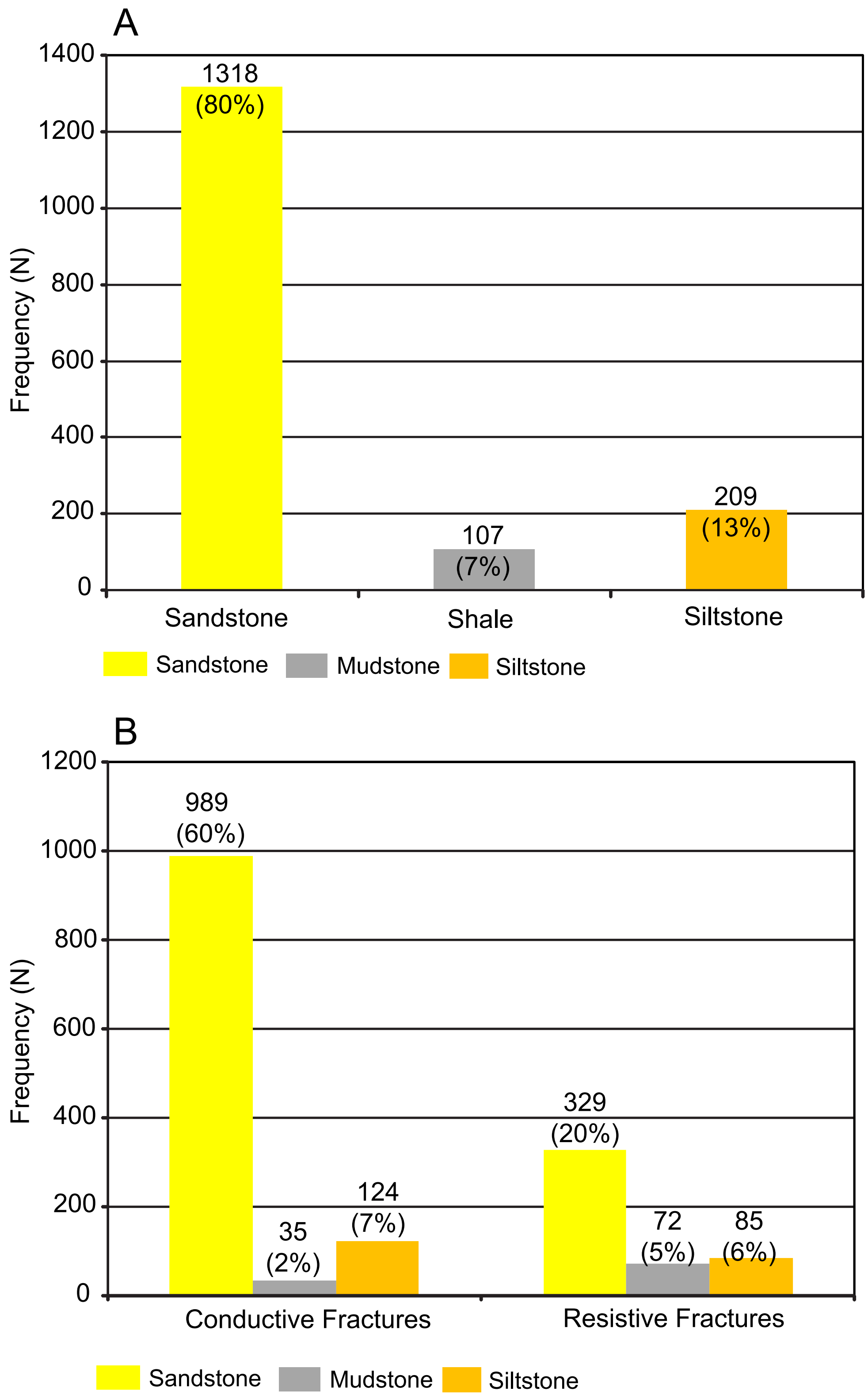

Figure 57. Histograms show the distribution of fractures with respect to lithology. A) the percentages of fractures are observed in sandstone, mudstone, and shale at 10 wells. More than 90% of natural fractures occur in sandstone and siltstone. B) the percentages of the distribution of natural fractures with respect to fracture type as well as lithology. Three-fourths of natural fractures in sandstone are conductive fractures.

however, resistive fracture strike still varies within this interval as in the marine interval. The Cameo-Wheeler coal zone interval exhibits similar kinds of reservoirs as in the fluvial interval, except that this interval differs with the presence of thick coal layers. Lorenz and Finley (1989) suggest the effects of coal-derived fluids and gases on the diagenetic processes within the paludal interval, contending that these processes produced compaction, secondary porosity, and tertiary carbonate and quartz cement in this interval (Lorenz and Finley, 1989). Electrical borehole-image logs indicate a higher number of resistive (healed/cemented) fractures in this interval in comparison to the number of conductive fractures in fluvial and marine intervals.

Because depositional settings in the Mesaverde Group vary extensively, relationships between fractures and architectural elements may have significance because fractures may occur preferentially within certain types of architectural elements and/or be distributed indiscriminately. In order to reveal the relationships between architectural elements and fractures, the generation and interpretation of architectural element logs is required. The criteria used to interpret architectural element logs are: 1) channel and point bars meet the criteria of ≤ 96 API gamma ray signature, fining upward log signature, 0.05-0.25 density porosity log signature, sharp base, and thicknesses of 2-30 ft (~0.5-9 m); 2) crevasse splay meets the criteria of ≤ 96 API gamma ray cut-off, coarsening upward log signature, <0.05 density porosity log response, and thickness of ~1’-15’ ft (~0.3-4.5 m); 3) floodplain meets > 96 API gamma ray cut-off; and 4) coal meets ≤ 96 API gamma ray cut-off and > 0.25 density and neutron porosity log signature. It should be noted that even though channel and point bars meet the same criteria, they are named differently based on the interval. The term point bar is used for the lower Williams Fork Formation interval, which includes isolated point-bar sand-bodies and was deposited in a coastal-plain setting with meandering streams, swamps, and floodplains; and the term channel bar is used for middle and upper Williams Fork Formation intervals, which was deposited in an alluvial-plain setting with braided streams. After creating architectural element logs, histograms were generated to examine the distribution of fractures with respect to architectural elements. Interpretations of histograms indicate that nearly 70% of natural fractures occur in fluvial deposits versus 30% in marine deposits (Figure 58). It should be noted that the interval of electrical borehole-image log data only contains the marine units of Upper Sandstone, Middle Sandstone, and Rollins Sandstone Member of the Iles Formation. Only one well penetrates deep enough to have fracture data in the Cozzette and Corcoran marine sandstone intervals. Histograms also indicate that fractures can occur in any amount regardless of the type of architectural element. The percentage of fracturing in point bar, channel bar, and crevasse splay does not present any distinct differences that may have revealed the controls on fracture distribution with respect to architectural elements (Figure 58). It appears that resistive fracture occurrence is lower in channel bars than point bars and crevasse splays, indicating that resistive fractures occur less in the middle and upper Williams Fork Formation on the basis of electrical borehole-image logs at 10 wells (Figure 58).

DISCUSSION

Ten (10) borehole-image logs provide a reliable dataset for fracture analysis part of this study. 1634 natural fractures are interpreted on ten (10) borehole-image logs. Analysis of fractures reveals that 70% of natural fractures are conductive, whereas only 30% of natural fractures are resistive. Conductive fractures of the Williams Fork Formation have a dominant strike orientation of N45°W and resistive fractures have a strike orientation of ranging from N40°W to N80°W. N-NE strike orientation was also observed on small number of resistive fractures. The reason of scatter in resistive fracture strike orientation is hard to determine; however, it may have been caused by change in stress orientation by time in the Piceance Basin. The origin of fractures in the Piceance Basin has long been discussed. Pitman and Sprunt (1986) suggest that the formation of fractures may be associated with high pore pressures that developed as a consequence of burial and periods of regional uplift and erosion.

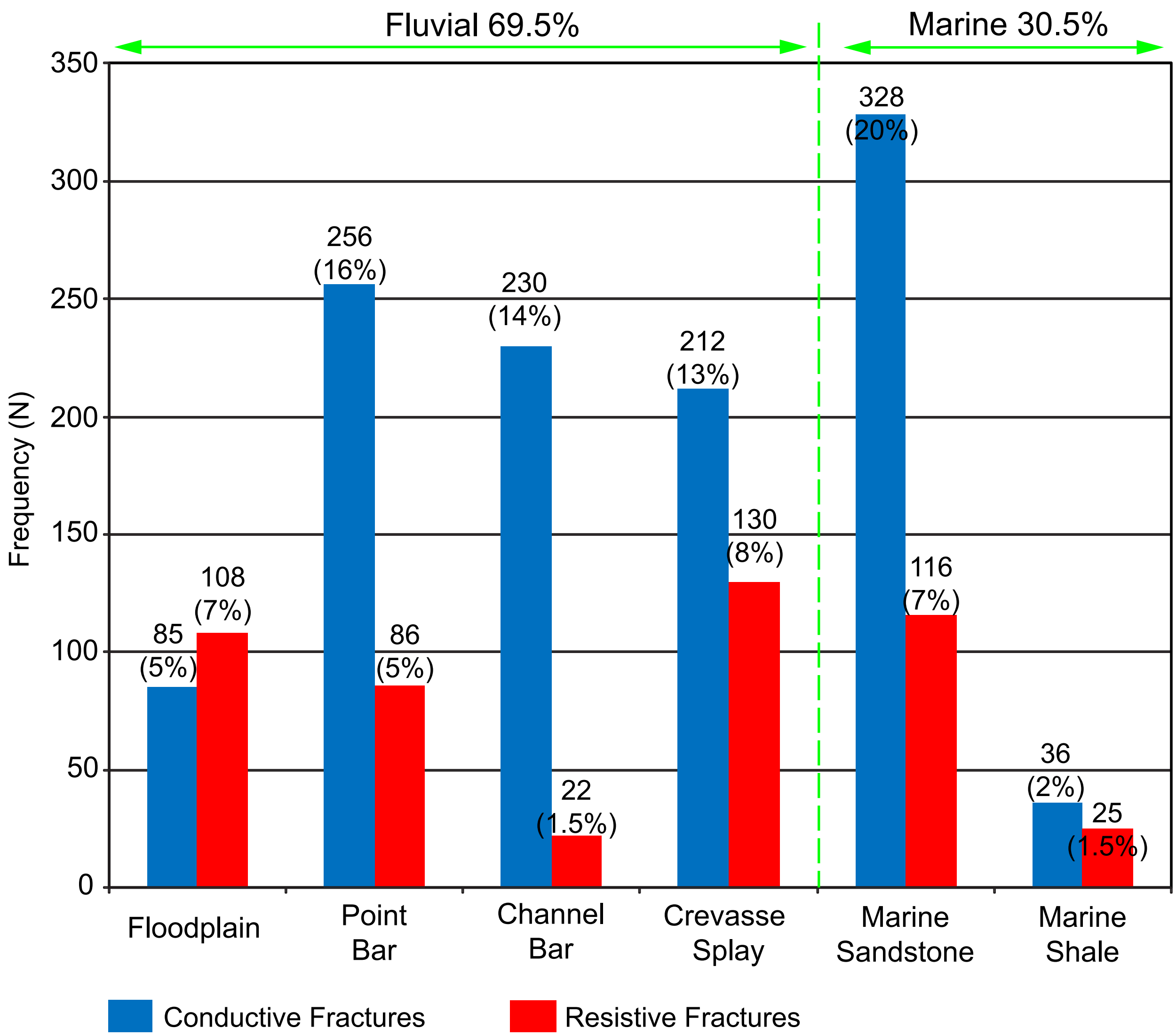

Figure 58. The distribution of fractures with respect to architectural elements as well as fracture type and depositional settings. Based on FMI logs at 10 wells, 69.5% of natural fractures were observed in fluvial interval, whereas 30.5% observed in marine intervals of the Upper Sandstone, Middle Sandstone, and Rollins Sandstone Member. It appers that resistive fracture occurrence in channel bars is lower than point bars.

Lorenz and Finley (1989) relate the occurrence of natural fractures in the Piceance Basin to local faulting and folding (structural deformation) and regional stresses in conjunction with high pore pressures. Cumella and Scheevel (2008) indicate that the orientation of fractures are related to the orientation of tectonic stresses at the time that fractures form, whereas Cumella and Scheevel (2008) relate the distribution and intensity of fracturing to the history and magnitude of overpressuring. Because there may be multiple causes of fracturing in the Mesaverde Group sandstone reservoirs, it is difficult to determine the real origin of each fracture sets in the study area. In-situ stress analysis based on induced-tensile fractures and borehole breakouts reveals N-NW orientation of present-day maximum horizontal stress, which is consistent with the orientation of conductive fractures in the area. In-situ stress analysis also indicates a ~20 degrees of rotation in the orientation of stress state. Such information may be useful in designing reservoir stimulation and fluid-flow simulation of sandstone reservoirs of the Williams Fork Formation. Fracture strike and in-situ stress orientations derived from borehole-image logs are consistent with previous interpretations done by Pitman and Sprunt (1986), Lorenz and Finley (1989,1991), Verbeek and Grout (1984), Grout and Verbeek (1992), Hoak and Klawitter (1997), and Nelson(2003). The Mesaverde Group (including the Williams Fork Formation) is exposed along the Grand Hogback, which allows the comparison of subsurface fracture data to outcrop. Therefore, the fracture analysis part of this study may expand by conducting an outcrop study.

Fracture density map for the Williams Fork Formation shows higher densities of fracturing in the southern and southwestern portion of the study area. Higher fracture density values are consistent with the EURs. All six wells which have production rates of >2 BCF fall into the area where fracture density map indicates high fracture densities. EUR values show wide variety of production rates in the study area, ranging from 0.3 BCF to 2.6 BCF. Fracture density map yields general insights; however, it lacks information to explain abrupt production changes between closely spaced wells. A reasonable relationship between seismic attributes and fracture-intensity logs exist in the study area. The ant-track and t* attenuation attribute cubes may allow the inference of information on the fracture distribution. A discrete fracture network (DFN) model generated using all the information in the fracture analysis part of this study may lead a reasonable DFN model. After running many realizations, fracture properties can be upscaled and fracture permeability, porosity, and sigma (defining the connectivity between fractures and matrix) can be obtained. Then, comparison between cumulative production data and fracture properties can be done and flow simulations can be run.

The investigation of controls on fracture distribution was done by creating lithology and architectural element logs for 10 wells. Results indicate that 60% of natural fractures terminate against minor lithologic boundaries and 90% of natural fractures occur in sandstone and siltstone. This is consistent with the interpretations done by Lorenz and Finley (1989, 1991) and Northrop and Frohne (1990). Based on architectural element logs, 70% of natural fractures occur in fluvial deposits and only 30% occur in marine deposits. Lorenz and Finley (1989) state that depositional environment may control the distribution of fractures because it controls the lithologic variability in a reservoir.

CHAPTER FIVE

CONCLUSIONS AND RECOMMENDATIONS

CONCLUSIONS

The Piceance Basin of northwestern Colorado is one of several Rocky Mountain basins that produce large amount of gas from the lenticular, discontinuous, low-permeability sandstone reservoirs of the Williams Fork Formation. These reservoirs are proven to be extensively fractured at depth and fractures play a significant role in gas production.

In the study area, each stratigraphic surface and interval differs in reflection continuity, reflection strength, and reflection configuration. Seismic expression of the “undifferentiated” middle and upper Williams Fork Formation shows differences in comparison to the lower Williams Fork Formation reflecting the different depositional characteristics of the intervals. Poor amplitude coherency, dimming of amplitudes, and parallel-to-subparallel reflections are present in the “undifferentiated” middle and upper Williams Fork Formation interval. Within the lower Williams Fork Formation, the Middle Sandstone, Cameo-Wheeler coal zone, and Rollins Sandstone Member, which bounds the Williams Fork Formation at the bottom, are seismically resolved. The reflection coefficient of the lower Williams Fork Formation interval is higher, indicating a velocity-density contrast between the lower and upper Williams Fork Formations.

The ant-tracking workflow was used to generate an enhanced fault volume to interpret the type, distribution, and orientation of faults in collaboration with the seismic amplitude and curvature volumes. Results reveal the presence of small thrust and normal faults deeper in the study area. Dip changes in reflections suggest a rotation of blocks as a consequence of thrusting and reflections become almost horizontal and differ from regional structural dip. The lack of observable slip on the faults at this level is explained with positive inversion, which caused the reactivation of faults and resulted in each fault to retain displacement, during a contraction following an extension. Depth slices through the ant-track attribute volume show N-NW- and E/W-trending discontinuities; however, N-NW-trending strike orientation of thrust and normal faults appears to be dominant. The amplitude dimming, poor amplitude coherency, and reflector offset in the “undifferentiated” middle and upper Williams Fork Formation interval results in a highly complex ant-track attribute expression of discontinuities that makes interpretation of individual faults difficult. Within this interval, arrays of upward-diverging fault splays suggest the discontinuities might reflect wrench faults that spread upward into the reservoir interval and die out. Depth slices through the ant-track attribute volume indicate the E/W- and N-NE-trending discontinuities and N-NE-trending discontinuities are more prevalent toward the Grand Hogback monocline. The shallow levels in the study area (Price coal, Ohio Creek Member, and above) only exhibit E/W-trending discontinuities.

The seismic attribute analysis of fractures reveals reasonable values of correlation coefficient (0.55 to 0.75 for ant-track attribute and from 0.546 to 0.753 for t* attenuation attribute) between seismic attributes and fracture intensity in fractured zones. The interpretation of borehole-image logs indicates that conductive fracture occurrence in sandstone reservoirs of the Williams Fork Formation is twice more likely than resistive fractures (70% (N=1148) of natural fractures were interpreted as conductive and 30% (N=486) as resistive). Fracture-intensity logs for 10 wells indicate a nonuniform distribution of fractures and distribution varies spatially (with depth and aerially). The fracture intensity map for the Williams Fork Formation interval shows higher intensity of fracturing on the southern and western portion of the study area, which decreases toward the Grand Hogback. A simple count of fractures at the 10 wells indicates as a low of 30 and as a high of 338 natural fractures with an average number of 163. A N-NW oriented present-day maximum horizontal stress (S_{hmax}) is present in the area, which is determined based on borehole breakouts and induced-tensile fractures This orientation is consistent with the conductive fracture strike, which is N45°W. A crossplot of measured depth versus dip azimuth of induced tensile fractures and borehole breakouts shows ~20 degrees of clockwise rotation in the orientation of Shmax and a 20-degree sudden shift at 7200 ft (2195 m) in Rollins Sandstone Member level. Fracture analysis indicates that natural fractures (more than 90%) occur in sandstone and siltstone and terminate against minor lithologic boundaries and against mudstone contacts bounding the reservoir indicating that the distribution of natural fractures is controlled by the stress differences in different lithologies. Only a minor number of natural fractures occur in mudstone and these are low-angle resistive fractures. The fracture analysis also reveals that 70% of natural fractures occur in fluvial deposits versus 30% in marine deposits. This suggests that the depositional environment, which controls the lithologic variety in the reservoir, controls the distribution of natural fractures. The magnitude of fracturing in point bars, channel bars, and crevasse splays does not show distinct differences; however resistive fractures were observed less in channel bars (middle and upper Williams Fork Formation) than point bars (lower Williams Fork Formation) and crevasse splays.

RECOMMENDATIONS

Seismic studies almost always contain some degree of uncertainty and ambiguity due to acquisition, processing, level of noise, etc. The level of uncertainty and ambiguity may be reduced by the application of different methods and workflows. Based on the foregoing interpretation, analysis, and conclusions following recommendations are made:

1) Obtain 2-D regional seismic lines in and around the study area to get a better regional tectonic understanding. Thus, interpreted small thrust faults can be tracked down to a detachment level and related to a subsurface structure.

2) Reprocess or reacquire seismic data to reduce the level of noise for better results in interpretation.

3) Apply other seismic conditioning methods such as median filter, Gaussian spatial filter, and bandpass filtering to examine whether or not any better conditioning is possible as an alternative to structural smoothing.

4) Incorporate all information gained from this study into a discrete-fracture-network model that may be helpful to predict areas of high fracture intensity and fracture related porosity and permeability. Generating several different discrete-fracture-network models can aid in designing reservoir stimulation (hydraulic fracturing).

5) Acquire s-wave data in the area, not p-wave converted s-wave. Share wave anisotropy could be corresponded to high fracture intensity proven by previous studies. Share-wave anisotropy can be correlated with results gained in seismic analysis part of this study.

REFERENCES

Allmendinger, R. W., 1992, Fold and thrust tectonics of the western United States exclusive of the accreted terranes, in Burchfiel, B. C., et al., eds., The Cordilleran orogen: Conterminous U.S.: Boulder, Colorado, Geological Society of America, Geology of North America, v. G-3, p. 583–607.

Ameen, M. S., I. M. Buhidma, and Z. Rahim, 2010, The function of fractures and in-situ stresses in the Khuff reservoir performance, onshore fields, Saudi Arabia, AAPG Bulletin, vol. 94, no. 1, p. 27-60.

Armstrong, R. L., 1968, Sevier orogenic belt in Nevada and Utah: Geological Society of America Bulletin, v. 79, p. 429–458.

Badgley, P. C., 1965, Structural and tectonic principles, Harper and Row, New York.

Bankwitz, P., 1966, Ueber Kluefte; II, Die Bildung der Kluftflaeche und eine Systematik ihrer Strukturen, Geologie, vol. 15, no. 8, p. 896-941.

Barton, C. A., D. Moos, P. Peska, and M.D. Zoback, 1997, Utulizing wellbore image data to determine the complete stress tensor: Application to permeability anisotrophy and wellbore stability: The Log Analyst, v. 38, p. 21-33.

Bird, P., 1998, Kinematic history of the Laramide orogeny, in latitudes 35°49°N, western United States: Tectonics, v. 17, p. 780–801.

Blakey, R. C., 2010, Paleogeographic and Paleotectonic Maps-Use, Construction, Interpretation, and Example, RMAG Short Course CD, January 28, 2010.

Brown, A. R., 2004, Interpretation of three-dimensional seismic data, AAPG Memoir, vol. 42, p. 541.

Burchfiel, B. C., D.S. Cowan, and G.A. Davis, 1992, Tectonic overview of the Cordilleran orogen in the western United States, in Burchfiel, B. C., Lipman, P. W., and Zoback, M. L., editors., The Cordilleran Orogen: Conterminous U. S.: Geological Society of America, The Geology of North America, v. G-3, p. 407–480.

Carroll, C. J., 2003, Fractures in the Mesaverde Group at Somerset Coal Field, Delta and Gunnison counties, Colorado, in K. M. Peterson, T. M. Olson, and D. S. Anderson eds., Piceance Basin 2003 guidebook: RMAG, p. 194-207.

Carroll, C. J., E. Robeck, G. Hunt, and W. Koontz, 2004, Structural implications of underground coal mining in the Mesaverde Group in the Somerset coal field, Delta and Gunnison counties, Colorado; field trips in the southern Rocky Mountains, USA. GSA Field Guide*, 5*, 41-58.

Choate, R., D. Jurich, and G. J. Saulnier, Jr., 1981, Geologic overview, coal deposits, and potential for methane recovery from coalbeds, Piceance Basin, Colorado: TRW, Energy Engineering Division, 184 p.

Cole, R.D., and S.P. Cumella, 2003, Stratigraphic architecture and reservoir characteristics of the Mesaverde Group, southern Piceance Basin, Colorado, in K. M. Peterson, T. M. Olson, and D. S. Anderson eds., Piceance Basin 2003 guidebook: RMAG, p. 385-442.

Cole, R.D., and S.P. Cumella, 2005, Sand-body architecture in the lower Williams Fork Formation (Upper Cretaceous), Coal Canyon, Colorado, with comparison to the Piceance Basin subsurface; Cretaceous sand body geometries in the Piceance Basin area of northwest Colorado: The Mountain Geologist, v. 42, p. 85-107.

Collins, B. A., 1976, Coal deposits of the Carbondale, Grand Hogback, and southern Danforth Hills coal fields, eastern Piceance basin, Colorado: Quarterly of the Colorado School of Mines, v. 71, no. 1, 138 p.

Coward, M., 1994, Inversion tectonics, in Hancock, P. L., ed., Continental deformation, Pergamon Press, Tarrytown, NY, p. 289-304.

Cumella, S.P. and D.B. Ostby, 2003, Geology of the basin-centered gas accumulation, Piceance Basin, Colorado, in K. M. Peterson, T. M. Olson, and D. S. Anderson eds., Piceance Basin 2003 Guidebook: RMAG, p. 171-193.

Cumella, S.P., J. Scheevel, and L. George, 2005, Geology and mechanics of the basin-centered gas accumulation, Piceance Basin, Colorado; AAPG Rocky Mountain Section, abstracts: Abstracts - AAPG Meeting, Rocky Mountain Section, v. 2005.

Cumella, S.P., 2006, Overview of a giant basin-centered gas accumulation, Mesaverde Group, Piceance Basin, Colorado; Rocky Mountain gas reservoirs revisited; extended abstracts [modified]: The Mountain Geologist, v. 43, p. 219-224.

DeCelles, P. G., and B.S. Currie, 1996, Long-term sediment accumulation in the middle Jurassic-early Eocene cordilleran retroarc foreland-basin system: Geology (Boulder), 24(7), p. 591-594.

DeCelles, P. G., 2004, Late Jurassic to Eocene evolution of the Cordilleran thrust belt and foreland basin system, western U.S.A.: American Journal of Science, 304(2), p. 105-168.

DeCelles, P. G., M. N. Ducea, P. Kapp, and G. Zandt, 2009, Cyclicity in Cordilleran orogenic systems, Nature Geoscience, vol. 2, no. 4, p. 251-257.

Dickinson, W. R., and W.S. Snyder, 1978, Plate tectonics of the Laramide orogeny, in Matthews, V., editor, Laramide folding associated with block faulting in the western United States: Geological Society of America Memoir 151, p. 355–366.

Dickinson, W. R., M.A. Klute, M.J. Hayes, S.U. Janecke, E.R. Lundin, M.A. McKittrick, et al., 1988, Paleogeographic and paleotectonic setting of Laramide sedimentary basins in the central Rocky Mountain region: Geological Society of America Bulletin, 100(7), p. 1023-1039.

Elison, M. W., 1991, Intracontinental contraction in western North America: Continuity and episodicity: Geological Society of America Bulletin, v. 103, p. 1226–1238.

Engelder, T., 1987, Joints and shear fractures in rock, in Atkinson, B. K., ed., Fracture mechanics of rock, United Kingdom (GBR), Acad. Press, London, United Kingdom (GBR).

Erslev, E. A., 1993, Thrusts, back-thrusts and detachment of Rocky Mountain foreland arches, in Schmidt, C. J., Chase, R. B., and Erslev, E. A., editors, Laramide basement deformation in the Rocky Mountain foreland of the western United States: Geological Society of America Special Paper 280, p. 339–358.

Erslev, E. A., 2001, Multistage, multidirectional Tertiary shortening and compression in north-central New Mexico: Geological Society of America Bulletin, v. 113, p. 63–74.

Finley, S. J. and J. C. Lorenz, 1989, Characterization and significance of natural fractures in Mesaverde reservoirs at the Multiwell Experiment site, , p. 721-728 19007.

Gibson, R.L., S. Theophanis, and M.N. Toksoz, 2000, Physical and numerical modeling of tuning and diffraction in azimuthally anisotropic media: Geophysics, 65, 1613-1621.

Gries, R., 1983, Oil and Gas prospecting beneath Precambrian of Foreland thrust plates in Rocky Mountains: American Association of Petroleum Geologists Bulletin, v. 67, no. 1, p. 1-28.

Griggs, D. T., J. W. Handin, and D. T. e. Griggs, 1960, Observations on fracture and a hypothesis of earthquakes, Chapter 13; Rock deformation--A symposium, Memoir - Geological Society of America, p. 347-364.

Gregson, J. D., and E.A. Erslev, 1997, Heterogeneous laramide deformation in the uinta mountains, colorado and Utah, in T. E. Hoak, A. L. Klawitter & P. K. Blomquist (Eds.), Fractured reservoirs; characterization and modeling, United States (USA): Rocky Mountain Association of Geologists, Denver, CO, United States (USA).

Grout, M. A., G.A. Abrams, R.L. Tang, T.J. Hainsworth, and E.R. Verbeek, 1991, Late Laramide thrust related and evaporite-domed anticlines in the southern Piceance Basin, northeastern Colorado Plateau. AAPG Bulletin, 75(2), p. 205-218.

Grout, M. A., and E.R. Verbeek, 1992, Fracture history of the divide creek and wolf creek anticlines and its relation to Laramide basin-margin tectonism, southern piceance basin, northwestern Colorado (16 Structural geology; 29A Economic geology, geology of energy sources No. B 1787-Z). United States (USA): U. S. Geological Survey, Reston, VA, United States (USA).

Grose, L. T., 1972, Tectonics: Geologic Atlas of the Rocky Mountain Region: RMAG, p. 35-44.

Harding, T. P., 1985, Seismic characteristics and identification of negative flower structures, positive flower structures, and positive structural inversion, AAPG Bulletin, vol. 69, no. 4, p. 582-600.

Haugen, G.U., and M.A. Schoenberg, 2000, The echo of a fault or fracture, Geophysics, 65, 176-189.

Haws, G.W., and N.F. Hurley, 1992, Applications of pressure-interference data in reservoir characterization studies, Big Horn basin, Wayoming: Society of Petroleum Engineers, Annual Conference and Exhebition, p. 53-62, paper SPE 24668.

Heffer, K.J., and J.C. Lean, 1993, Earth stress orientation-a control on, and guide to, flooding directionality in a majority of reservoirs: in W. Linville (ed.), Reservoir Characterization III, Tulsa, Oklahoma, Penn Well, p.799-822.

Hettinger, R.D., L.N.R. Roberts, and T.A. Gognat, 2000, Investigations of the distribution and resources of coal in the southern part of the Piceance Basin, Colorado, Chapter O of Kirschbaum, M.A., Roberts, L.N.R., and Biewick, L.R.H., eds., Geologic assessment of coal in the Colorado Plateau—Arizona, Colorado, New Mexico, and Utah: U.S. Geological Survey Professional Paper 1625–B, 61 p, [available only on CD-ROM].

Hettinger, R.D., and M.A. Kirschbaum, 2002, Stratigraphy of the Upper Cretaceous Mancos Shale (upper part) and Mesaverde Group in the southern part of the Uinta and Piceance basins, Utah and Colorado: Report I-2764, 21 p.

Hettinger, R.D., M.A. Kirschbaum, and U. S. Geological Survey, Uinta- Piceance Assessment Team, United States, compiler (USA), 2003, Stratigraphy of the Upper Cretaceous Mancos Shale (upper part) and Mesaverde Group in the southern part of the Uinta and Piceance Basins, Utah and Colorado; Petroleum systems and geologic assessment of oil and gas in the Uinta-Piceance Province, Utah and Colorado: Report DDS-0069-B, 21 p.

Hoak, T. E., and A.L. Klawitter, 1997, Prediction of fractured reservoir production trends and compartmentalization using an integrated analysis of basement structures in the Piceance basin, western Colorado, in T. E. Hoak, A. L. Klawitter, and P. K. Blomquist, eds., fractured reservoirs: characterization and modeling: Rocky Mountain Association of Geologists Guidebook, p. 67 -102.

Hurley, N., 2004, Borehole Images, in G. Asquith and D. Krygowski, Basic Well Log Analysis: AAPG Methods in Exploration 16, p. 151-163.

Jackson, J. W., 2007, Fracture Modeling and fault zone characteristics applied to reservoir characterization of the Rulison gas field, Garfield County, Colorado, Master's thesis, Colorado School of Mines, Golden, Colorado, 143 p.

Jansen, K., 2005, Seismic Investigation of wrench faulting and fracturing at Rulison field, Colorado, Master's thesis, Colorado School of Mines, Golden, Colorado, 139 p.

Johnson, R. C., and R. M. Flores, 2003, History of the Piceance Basin from latest Cretaceous through early Eocene and the characterization of lower Tertiary sandstone reservoirs, in

K.M. Peterson, T.M. Olson, and D.S. Anderson, eds., Piceance Basin 2003 Guidebook: RMAG, Denver, p. 21-61.

Johnson, R.C., and F. May, 1980, A study of the Cretaceous-Tertiary unconformity in the Piceance Basin, Colorado—The underlying Ohio Creek Formation (Upper Cretaceous) redefined as a member of the Hunter Canyon or Mesaverde Formation: U.S. Geological Survey Bulletin 1482–B, 27 p.

Johnson, R. C., and V. F. Nuccio, 1986, Structural and thermal history of the Piceance Creek basin, western Colorado, in relation to hydrocarbon occurrence in the Mesaverde Group, in Spencer, Mast, eds., Geology of tight gas reservoirs: AAPG Studies in Geology, 24, p. 165-205.

Johnson, R. C., 1989, Geologic history and hydrocarbon potential of late cretaceous-age, low-permeability reservoirs, piceance basin, western colorado (29A Economic geology, geology of energy sources; 06A Sedimentary petrology; 12 Stratigraphy No. B 1787-E). United States (USA): U. S. Geological Survey, Reston, VA, United States (USA).

Johnson, R. C., and S. B. Roberts, 2003, The Mesaverde total petroleum system, Uinta-Piceance province, Utah and Colorado (Chapter 7), in Petroleum Systems and geologic assessment of oil and gas in the Uinta-Piceance province, Utah and Colorado: USGS Digital Data Series DDS-69-B, 68 p.

Kuuskraa, V.A., D. Decker, and H.B. Lynn, 1997, Optimizing technologies for detecting natural fractures in the tight sands of the Rulison Field, Piceance Basin: Proceedings of the Natural Gas Conference Emerging Technologies for the Natural Gas Industry, paper NG6-3, 29 p.

Kuuskraa, V. A., D. Campagna, and D. Decker, 1997, Application of high fold, multi-azimuth 3-D P-wave seismic to characterize natural fractures in the rulison field, piceance basin. In E. B. Coalson, J. C. Osmond & E. T. Williams (Eds.), Innovative applications of petroleum technology in the rocky mountain area (). United States (USA): Rocky Mountain Association of Geologists, Denver, CO, United States (USA).

Kuuskraa, V.A., and G.C. Bank, 2007, The unconventional gas resource base: Advanced Resources International, Inc. White Paper, No. 1 of 6, July, 2007: http://www.adv-res.com/pdf/Unconventional-Gas-Whitepaper-1-ResourceBase.pdf, p. 10.

LaBarre, E. A., 2008, Reservoir prediction from multicomponent seismic data, Rulison field, Piceance Basin, Colorado, Master;s thesis, Colorado School of Mines, Golden, Colorado, 86 p.

Larue, D. K. and J. Hovadik, 2006, Connectivity of channelized reservoirs; a modelling approach, Petroleum Geoscience, vol. 12, no. 4, p. 291-308.

Law, B. E. 2002. Basin-centered gas systems; unconventional petroleum systems. AAPG Bulletin, 86(11), 1891-1919.

Law, B.E., G.F. Ulmishek, and V.I. Slavin eds., Abnormal pressures in hydrocarbon environments: AAPG Memoir 70, p. 195–214.

Lindsey, J.P., 1989, The Fresnel zone and its interpretive significance, The Leading Edge, v. 10, 33-39.

Lines. L., P.F. Daley, and R.P. Bording, Seismic Imaging of Fractures-A Feasibility Study, Let it Flow-2007CSPG CSEG Convention, p. 240-242.

Liu E., S. Crampin, and J.A. Hudson, 1997, Diffraction of seismic waves by cracks with application to hydraulic fracturing, Geophysics, 62, 253-265.

Livaccari, R. F., 1991, Role of crustal thickening and extensional collapse in the tectonic evolution of the Sevier-Laramide orogeny, western United States: Geology, v. 19, p. 1104–1107.

Logan, J.M., M. Friedman, and M.T. Stearns, 1979, Experimental folding of rocks under confining pressure: Part VI. Further studies of faulted drape folds: Geological Society of America, Memoir 151, p. 79.

Lohr, T., C. M. Krawczyk, D. C. Tanner, R. Samiee, H. Endres, P. O. Thierer, O. Oncken, H. Trappe, R. Bachmann, and P. A. Kukla, 2008, Prediction of subseismic faults and fractures; integration of three-dimensional seismic data, three-dimensional retrodeformation, and well data on an example of deformation around an inverted fault, AAPG Bulletin, vol. 92, no. 4, p. 473-485.

Lorenz, J. C. and S. J. Finley, 1989, Differences in fracture characteristics and related production; Mesaverde Formation, northwestern Colorado, SPE Formation Evaluation, vol. 4, no. 1, p. 11-16.

Lorenz, J. C., and S. J. Finley, 1991, Regional fractures II: fracturing of Mesaverde reservoirs in the Piceance basin, Colorado: AAPG Bulletin, v. 75, p. 1738 – 1757.

Lorenz, J. C., 1997, Heartburn in predicting natural fractures; the effects of differential fracture susceptibility in heterogeneous lithologies. In T. E. Hoak, A. L. Klawitter & P. K. Blomquist (Eds.), Fractured reservoirs; characterization and modeling (). United States (USA): Rocky Mountain Association of Geologists, Denver, CO, United States (USA).

Lorenz, J.C., 2003, Fracture systems in the Piceance Basin, overview and comparison with fractures in the San Juan and Green River basins, in K.M. Peterson, T.M. Olsen, and D.S. Anderson, eds., Piceance Basin 2003 guidebook: Rocky Mountain Association of Geologist, p. 75-94.

Lorenz, J.C., N.R. Warpinski, P. Branagan, and A.R. Sattler, 1989, Fracture characteristics and reservoir behavior of stress-sensitive fracture systems in flat-lying lenticular formations: Journal of Petroleum Technology, v.4, no. 1, p. 11-16.

Maerten, L., P. Gillespie, and J. Daniel, 2006, Three-dimensional geomechanical modeling for constraint of subseismic fault simulation, AAPG Bulletin, vol. 90, no. 9, p. 1337-1358.

Magoon, L. B., and W. G. Dow, eds., 1994, The petroleum system - from source to trap: AAPG Memoir 60, 655 p.

Mann, P., L. Gahagan, and M. B. Gordon, 2003, Tectonic setting of the world's giant oil and gas fields, in M. T. Halbouty, ed., Giant oil and gas fields of the decade 1990–1999, AAPG Memoir 78, p. 15–105.

Marfurt, K., and S. Chopra, 2007, Seismic Attributes for Prospect Identification and Reservoir Characterization, United States (USA): SEG/EAGE Publication.

Matesic, M., 2007, Structural and stratigraphic controls on Mesaverde reservoir performance, Rulison field, Garfield County, Colorado, Master's thesis, Colorado School of Mines, Golden, Colorado, 187 p.

Miller, E. L., P.B. Gans, J.E. Wright, and J.F. Sutter, 1988, Metamorphic history of the east-central Basin and Range province: Tectonic setting and relationship to magmatism, in Ernst, W. G., ed., Metamorphism and crustal evolution of the western United States: Englewood Cliffs, New Jersey, Prentice-Hall, p. 649–682.

Mitchum, R. M., Jr, P. R. Vail, and J. B. Sangree, 1977, Seismic stratigraphy and global changes of sea level; Part 6, Stratigraphic interpretation of seismic reflection patterns in depositional sequences; Seismic stratigraphy; applications to hydrocarbon exploration, Memoir - American Association of Petroleum Geologists, no. 26, p. 117-133.

Monger, J. W. H., and R.A. Price, 1979, Geodynamic evolution of the Canadian Cordillera–progress and problems: Canadian Journal of Earth Science, v. 16, p. 770–791.

Moos, D., and M. D. Zoback, 1990, Utilization of observations of wellbore failure to constrain the orientation and magnitude of crustal stresses: Application to continental, Deep Sea Drilling Project and Ocean Drilling Project boreholes: Journal of Geophysical Research, v. 95, p. 9305–9325.

Murray, D.K., and J.D. Haun, 1974, Introduction to the geology of the Piceance Creek Basin and vicinity, northwestern Colorado, in D.K. Murray, (ed.), Energy resources of the Piceance Creek basin, Colorado: RMAG, p. 29-39.

Najmuddin, I., 2001, Detecting fracture zones in the austin chalk using seismic P-wave data. The Bulletin of the Houston Geological Society, 44(1), 22-27.

Najmuddin, I., 2003, Austin Chalk fracture mapping using frequency data derived from seismic data, dissertation, Texas A&M University.

Nelson, R. A. 1985, In Chilingarian G. V. (Ed.), Geologic analysis of naturally fractured reservoirs. United States (USA): Gulf Publ. Co., Houston, TX, United States (USA).

Nelson, P.H., 2003, A review of the multiwell experiment, Williams Fork and Iles Formations, Garfield County, Colorado: Petroleum systems and geologic assessment of oil and gas in the Uinta-Piceance Province, Utah and Colorado: Report DDS-0069-B, p. 24.

Nickelsen, R. P. and V. N. D. Hough, 1967, Jointing in the Appalachian Plateau of Pennsylvania, Geological Society of America Bulletin, vol. 78, no. 5, p. 609-629.

Oldow, J., A. Bally, H. Ave Lallemant, and W. Leeman, 1989, Phanerozoic evolution of the North American Cordillera; United States and Canada, in A. Bally and A. Palmer, eds., The geology of North America—An overview: Geological Society of America, v. A, p. 139–232.

Patterson, P.E., K. Kronmueller, and T.D. Davies, 2003, Sequence stratigraphy of the Mesaverde Group and Ohio Creek Conglomerate, northern Piceance Basin, Colorado, in K. M. Peterson, T. M. Olson, and D. S. Anderson eds., Piceance Basin 2003 guidebook: RMAG, p. 115-129.

Payne, D.F., K. Tuncay, A. Park, J.B. Comer, and P. Ortoleva, 2000, A reaction-transport-mechanical approach to modeling the interrelationships among gas generation, overpressuring, and fracturing; implications for the Upper Cretaceous natural gas reservoirs of the Piceance Basin, Colorado: AAPG Bulletin, vol. 84, no. 4, p. 545-565.

Pedersen, S. I., T. Randen, L. Sonneland, and O. Steen, 2002, Automatic fault extraction using artificial ants; Society of Exploration Geophysicists, international exposition and 72nd annual meeting; technical program, expanded abstracts with authors' biographies, SEG Annual Meeting Expanded Technical Program Abstracts with Biographies, vol. 72, p. 512-515.

Perry, W. J.,Jr, M.A. Grout, T.J. Hainsworth, and R.L. Tang, 1988, Wedge model for late Laramide basement-involved thrusting, Grand Hogback monocline and White River uplift, western Colorado: Geological Society of America 1988 centennial celebration. Abstracts with Programs - Geological Society of America, 20(7), p. 384-385.

Petrel Workflow Tools. (Version 2009.2) [Computer Software Manual], Schlumberger Information Solutions, Houston, TX, U.S.A.

Petrel Fracture Modeling Course notes, 2007, [Computer Software Course Manual], Schlumberger Information Solutions, Houston, TX, U.S.A.

Petrel Seismic Visualization and Interpretation Course notes, 2009, [Computer Software Course Manual], Schlumberger Information Solutions, Houston, TX, USA.

Pitman, J.K., and C.W. Spencer, 1984, Petrology of selected sand-stones in the MWX wells, (northwest Colorado) and its relationship to borehole geophysical-log analysis and reservoir quality, in Spencer, C.W., and Keighin, C.W., eds., Geologic studies in support of the U.S. Department of Energy Multiwell Experiment, Garfield County, Colorado: U.S. Geological Survey Open-File Report 84–757, p. 33–66.

Pitman, J. K. and E. S. Sprunt, 1986, Origin and distribution of fractures in lower Tertiary and Upper Cretaceous rocks, Piceance Basin, Colorado, and their relation to the occurrence of hydrocarbons; Geology of tight gas reservoirs, AAPG Studies in Geology, vol. 24, p. 221-233.

Pranter, M.J., A. I. Ellison, R.D. Cole, and P.E. Patterson, 2007, Analysis and modeling of intermediate-scale reservoir heterogeneity based on a fluvial point-bar outcrop analog, Williams Fork Formation, Piceance Basin, Colorado: AAPG Bulletin, v. 91, p. 1025-1051.

Pranter, M.J., M.F. Vargas, and T.L. Davis, 2008, Characterization and 3-D reservoir modeling of fluvial sandstones of the Williams Fork Formation, Rulison Field, Piceance Basin, Colorado: Journal of Geophysics and Engineering 5, p. 158-172.

Pranter, M. J., R. D. Cole, H. Panjaitan, and N. K. Sommer, 2009, Sandstone-body dimensions in a lower coastal-plain depositional setting; lower Williams Fork Formation, Coal Canyon, Piceance Basin, Colorado, AAPG Bulletin, vol. 93, no. 10, p. 1379-1401.

Ramsay, J. G., 1980, The crack-seal mechanism of rock deformation, Nature (London), vol. 284, no. 5752, p. 135-139.

Randen, T., E. Monsen, C. Signer, A. Abrahamsen, J. Hansen, T. Saeter, J. Schlaf, and L. Sønneland, 2000, Three-Dimensional Texture Attributes for Seismic Data Analysis: Ann. Int. Mtg., Soc. Expl. Geophys., Exp. Abstr.

Randen, T., S.I. Pedersen, and L. Sønneland, 2001, Automatic extraction of fault surfaces from three-dimensional seismic data: Expanded Abstracts, Int. Mtg., Soc. Exploration Geophys., 551–554.

Randen, T., L. Sønneland, A. Carrillat, T.S. Valen, T. Skov, S.I. Pedersen, B. Rafaelsen, and G. Elvebakk, 2003, Preconditioning for optimal 3-D stratigraphical and structural inversion: Extended Abstracts, European Association of Exploration Geophysicsts, p. 1-4.

Ross, G. M., P. J. Patchett, M. Hamilton, L. Heaman, P. G. DeCelles, E. Rosenberg, and M. K. Giovanni, 2005, Evolution of the Cordilleran Orogen (southwestern Alberta, Canada) inferred from detrital mineral geochronology, geochemistry, and Nd isotopes in the foreland basin, Geological Society of America Bulletin, vol. 117, no. 5-6, p. 747-763.

Sava, D., G. Mavko, and C.M. Sayers, 2007, Rock physics-based integration of geologic and geophysical data for fracture characterization; fractures. Leading Edge (Tulsa, OK), 26(9), 1140-1146.

Schlumberger, 2008, Formation Microimager Geologic Interpretation Report Overview by Randy Koepsell, Schlumberger-Data Consulting Services, 6501 S. Fiddlers Green Cir. Ste. 400, Greenwood Village, CO, 80111

Schoenberg, M.S., and J. Douma, 1988, Elastic wave propagation in media with parallel fractures and aligned cracks, Geophysical Prospecting, 36, 571-590.

Sheriff, R. E., 1985, Aspects of seismic resolution; Seismic stratigraphy II; an integrated approach to hydrocarbon exploration, AAPG Memoir, vol. 39, p. 1-10.

Spencer, C. W., 1987, Hydrocarbon generation as a mechanism for overpressuring in Rocky Mountain Region: AAPG Bulletin, 71(4), p. 368-388.

Spencer, C.W., 1996, Uinta-Piceance Province (020), in Gautier, D.L., Dolton, G.L., Takahashi, K.I., and Varnes, K.L., eds., 1995 National assess-ment of United States oil and gas resources—Results, methodol-ogy, and supporting data: U.S. Geological Survey Digital Data Series DDS–30, Release 2, 1 CD-ROM.

Tezuka, K., T. Namikawa, T. Tamagawa, A. Day-Lewis, and C. A. Barton, 2002, Roles of the fracture system and state of stress for gas production from the basement reservoir in Hokkaido, Japan: Society of Petroleum Engineers Gas Technology Symposium, Calgary, Canada, SPE Paper 75704, 11 p.

Tremain, C.M., 1993, Chapter PC-2—Mesaverde Group, in Hjellming, C.A., ed., Atlas of major Rocky Mountain gas reservoirs: Socorro, N.Mex., New Mexico Bureau of Mines and Mineral Resources, p. 97–98.

Tweto, O., 1975, Laramide (Late Cretaceous-early Tertiary) orogeny in the southern Rocky mountains, in Curtis, B. F., ed., Cenozoic history of the Southern Rocky Mountains: Geological Society of America Memoir 144, p. 1-44.

Tweto, O., 1980, Tectonic history of Colorado, in H. C. Kent and K.W. Porter, eds., Colorado Geology: Denver, Colorado, Rocky Mountain Association of Geologist, p. 5-9.

Twiss, R. J., and E.M. Moores, 1992, Structural geology. United States (USA): W.H. Freeman and Company, New York, NY, United States (USA).

Tyler, R., A.R. Scott, W.R. Kaiser, H.S. Nance, R.G. McMurry, C.M. Tremain, and M.J. Mavor, 1996, Geologic and hydrologic controls critical to coalbed methane producibility and resource assessment: Williams Fork Formation, Piceance basin, Northwest Colorado: Gas Research Institute Report GRI-95/0532, 397 p.

Waechter, N. B., and W.E. Johnson, 1986, Pennsylvanian-permian paleostructure and stratigraphy as interpreted from seismic data in the piceance basin, northwest colorado. In D. S. Stone, & K. S. Johnson (Eds.), New interpretations of northwest colorado geology, United States (USA): Rocky Mt. Assoc. Geol., Denver, CO, United States (USA).

Warpinski, N. R., and J. C. Lorenz, 2008, Analysis of the multiwell experiment data and results: Implications for the basin-centered gas model, in S. P. Cumella, K.W. Shanley, andW. K. Camp, eds., Understanding, exploring, and developing tight-gas sands-2005 Vail Hedberg Conference: AAPG Hedberg Series, no. 3, p. 157–176.

Williams, G. D., C. M. Powell, and M. A. Cooper, 1989, Geometry and kinematics of inversion tectonics; Inversion tectonics meeting, Geological Society Special Publications, vol. 44, p. 3-15.

Wilson, M.S., B.G. Gunneson, K. Peterson, R. Honore, and M.M. Laughland, 1998, Abnormal pressures encountered in a deep wildcat well, southern Piceance Basin, Colorado, in Law, B.E., G.F. Ulmishek, and V.I. Slavin eds., Abnormal pressures in hydrocarbon environments: AAPG Memoir 70, p. 195–214.

Yurewicz, D.A., K.M. Bohacs, J.D. Yeakel, and A. Kronmueller, 2003, Source rock analysis and hydrocarbon generation, Mesaverde Group and Mancos Shale, Northern Piceance Basin, Colorado, in K. M. Peterson, T. M. Olson, and D. S. Anderson eds., Piceance Basin 2003 guidebook: RMAG, p. 130-153.

Yurewicz, D., 2008, Controls on gas and water distribution, Mesaverde Basin-center gas play, Piceance Basin, Colorado; Conventional and unconventional hydrocarbon resources; abstracts book, Earth Sciences Research Journal, vol. 2008, ABST., p. 206.

Verbeek, E. R., and M. A. Grout, 1984, Fracture studies in Cretaceous and Paleocene strata in and around the Piceance Basin, Colorado; preliminary results and their bearing on a fracture-controlled natural-gas reservoir at the MWX site, Open-File Report - U.S. Geological Survey, vol. OF 84-0156, p. 32.

Verbeek, E. R., M. A. Grout, J. D. Friedman, and A. C. Huffman Jr, 1998, Relation between basement structures and fracture systems in cover rocks, northeastern and southwestern Colorado Plateau; Laccolith complexes of southeastern Utah; time of emplacement and tectonic setting; workshop proceedings, , vol. B 2158, p. 111-149.

Zhang, E., R. J. Hill, B. J. Katz, and Y. Tang, 2008, Modeling of gas generation from the Cameo coal zone in the Piceance Basin, Colorado, AAPG Bulletin, vol. 92, no. 8, p. 1077-1106.

APPENDIX A

Appendix A contains spreadsheets of natural fracture data derived from borehole-image logs (FMI) for 10 wells. For each well, fracture depth, dip azimuth, dip angle, fracture type, lithology code, and architectural element code are given.

List of FMI logs				
UWI	**WELL NAME**	**TOWNSHIP #**	**SEC. #**	**FIELD**
05045106810000	ANCHONDO 32B-20-692	T6S-R92W	20	Mamm Creek
05045176890000	BBC 42B-23-692	T6S-R92W	23	Mamm Creek
05045081340000	BRYNILDSON 14C-20-692	T6S-R92W	20	Mamm Creek
05045184930000	CIRCLE B. LAND 33A-35-692	T6S-R92W	35	Mamm Creek
05045068680000	DALEY # 1	T6S-R91W	29	Mamm Creek
05045075210000	GIBSON GULCH UNIT 15-30D	T6S-R91W	31	Mamm Creek
05045157380000	Jolley 31D-20-691	T6S-R91W	20	Mamm Creek
05045114020000	LAST DANCE 43C-3-792	T7S-R92W	3	Mamm Creek
05045160980000	Miller 24B-6-791	T7S-R91W	6	Mamm Creek
05045134160000	Nesbitt 13C-25-692	T6S-R92W	25	Mamm Creek
05045149230000	SCHIRER 14D-26-692	T6S-R92W	26	Mamm Creek
05045118440000	SPECIALTY 41A-28-692	T6S-R92W	28	Mamm Cree

Appendix A-1. The list of wells that have borehole-image log data was available in this study. UWI numbers, township and sector numbers, and field names are given.

Lithology	Code
Shale	0
Sandstone	1
Siltstone	2

Architectural Element	Code
Floodplain	0
Point Bar	1
Channel Bar	2
Crevasse Splay	3
Marine Sandstone	4
Marine Shale	5

Fracture Type	Code
Continuous Fracture	0
Partially Healed Fracture	1
Lithologically Bound Fracture	2
Resistive Fracture	3
Healed Continuous Fracture	4
Healed Lithologically Bound Fractures	5
Healed Fracture Terminated	6
Open Fracture Terminated	7

	Conductive Fracture
	Resistive Fracture

Appendix A-2. Lithology, architectural element, and fracture type codes used in spreadsheets. Each lithology, architectural element, and fracture type is represented by a number and a color code.

ANCHONDO 32B-20-692

UWI	MD	Dip Azimuth	Dip Angle	Fracture Type	Lithology	Architect. Element
05045106810000	4651	25	84	2	2	2
05045106810000	4661.75	40	72.5	2	2	2
05045106810000	4693.75	7	77.5	2	2	2
05045106810000	4926.3	185	75	2	1	2
05045106810000	4927.5	50	41	2	1	2
05045106810000	4944.4	20	79	2	1	3
05045106810000	5026.75	30	76	2	0	0
05045106810000	5029.9	40	75	2	2	3
05045106810000	5100	136	57.5	2	2	3
05045106810000	5108	338	40	3	1	3
05045106810000	5213.25	101	54	3	0	0
05045106810000	5214	302	30	3	0	0
05045106810000	5214.25	310	27	3	0	0
05045106810000	5214.5	132	39	3	0	0
05045106810000	5216.25	310	27	3	0	0
05045106810000	5217	281	40	3	0	0
05045106810000	5290.1	24	72.5	2	2	3
05045106810000	5311	31	70	2	2	3
05045106810000	5332	26	75	2	1	2
05045106810000	5345.75	38	72.5	2	2	2
05045106810000	5413.25	67	86	2	0	0
05045106810000	5470	48	74	1	0	0
05045106810000	5486.75	180	40	1	0	0
05045106810000	5552.75	63	84	1	2	3
05045106810000	5553.5	52	79	2	2	3
05045106810000	5586.75	347	32	3	1	2
05045106810000	5612.75	32	80	2	2	2
05045106810000	5614.25	35	85	2	2	2
05045106810000	5616.1	38	85	2	2	2
05045106810000	5627.5	38	75	2	0	0
05045106810000	5698.75	26	40	2	1	2
05045106810000	5703.7	12	78	2	1	2
05045106810000	5704	218	89	2	1	2
05045106810000	5704.5	41	79	2	1	2
05045106810000	5707.3	27	81	2	1	2
05045106810000	5721.5	29	72	2	1	2
05045106810000	5721.75	45	70	2	1	2

05045106810000	5725.5	66	80	2	1	2
05045106810000	5748.8	155	77	1	2	2
05045106810000	5749.4	4	62	2	2	2
05045106810000	5750.6	1	63	3	2	2
05045106810000	5751.25	183	70	3	2	2
05045106810000	5751.8	197	84	2	2	2
05045106810000	5760.2	69	65	2	1	2
05045106810000	5772	290	63	2	2	2
05045106810000	5772.75	53	71	2	1	2
05045106810000	5775.5	35	75	2	1	2
05045106810000	5777.25	31	77	2	1	2
05045106810000	5789.75	64	82	2	2	3
05045106810000	5864.75	241	75	3	0	0
05045106810000	5865	231	56	3	0	0
05045106810000	5868	72	74	3	0	0
05045106810000	5870.75	37	65	2	2	1
05045106810000	5877.75	62	83	2	1	1
05045106810000	5882.25	35	79	2	1	1
05045106810000	5902.25	38	74	2	0	0
05045106810000	5938	356	71	2	1	1
05045106810000	5958	33	82	2	1	1
05045106810000	5959	24	84	2	1	1
05045106810000	5992.75	39	82	2	1	1
05045106810000	6014.7	33	81	2	2	3
05045106810000	6064.5	28	64	2	2	3
05045106810000	6067	39	80	1	2	3
05045106810000	6097.95	118	59	3	2	3
05045106810000	6098.75	28	44	2	2	3
05045106810000	6111.75	330	51	3	2	3
05045106810000	6112.25	203	62	3	2	3
05045106810000	6112.75	231	55	3	2	3
05045106810000	6113	234	46	3	2	3
05045106810000	6113.15	62	53	3	1	3
05045106810000	6113.25	226	51	3	1	3
05045106810000	6113.65	223	50	3	1	3
05045106810000	6113.9	216	51	1	2	3
05045106810000	6114.1	217	47	1	2	3
05045106810000	6114.5	221	63	1	2	3
05045106810000	6122.75	40	85	2	2	1
05045106810000	6126.25	127	64	1	2	1
05045106810000	6147	186	42	1	1	1

05045106810000	6151.25	20	56	1	2	1
05045106810000	6159	35	83	2	0	0
05045106810000	6163.5	38	80	2	0	0
05045106810000	6177	38	80	2	2	3
05045106810000	6192.7	34	79	1	0	0
05045106810000	6202.25	33	80	1	2	1
05045106810000	6204.25	38	81	2	2	1
05045106810000	6207.9	28	82	2	2	1
05045106810000	6210.25	42	80	2	1	1
05045106810000	6210.5	40	85	2	1	1
05045106810000	6243.45	2	73	1	2	3
05045106810000	6249	26	68	2	2	3
05045106810000	6266.5	38	85	2	2	1
05045106810000	6278.25	40	81	2	1	1
05045106810000	6285.5	42	76	2	2	3
05045106810000	6288.75	26	66	2	1	3
05045106810000	6289.5	41	68	2	1	3
05045106810000	6290.25	34	73	2	1	3
05045106810000	6298.75	11	72	2	2	3
05045106810000	6301.75	41	81	2	2	3
05045106810000	6358.7	14	89	1	1	3
05045106810000	6418.45	213	63	2	1	1
05045106810000	6424.5	48	78	2	1	1
05045106810000	6433.8	46	82	2	2	1
05045106810000	6438.5	31	80	2	1	1
05045106810000	6452.5	41	80	2	1	1
05045106810000	6454.5	22	84	2	1	1
05045106810000	6467.5	45	85	2	1	1
05045106810000	6470.25	19	82	2	1	1
05045106810000	6581	12	59	1	2	3
05045106810000	6615	28	62	2	0	0
05045106810000	6617.25	46	83	2	1	1
05045106810000	6618.5	60	85	2	1	1
05045106810000	6629	25	77	1	2	1
05045106810000	6638.75	14	68	2	0	0
05045106810000	6669.95	48	81	2	2	1
05045106810000	6704.7	35	81	2	1	1
05045106810000	6730.5	207	80	3	2	3
05045106810000	6738.1	45	82	2	1	3
05045106810000	6759.5	38	84	2	1	1
05045106810000	6762.75	24	71	2	1	1

05045106810000	6766.5	51	86	2	1	1
05045106810000	6793.1	174	64	3	2	3
05045106810000	6810	48	70	2	2	3
05045106810000	6832.25	347	48	2	2	1
05045106810000	6837.4	34	53	2	1	1
05045106810000	6838.25	50	83	3	1	1
05045106810000	6844.5	39	75	2	2	1
05045106810000	6845.25	41	86	2	2	1
05045106810000	6897.1	65	55	2	2	1
05045106810000	7037.4	140	61	1	1	4
05045106810000	7037.6	129	65	2	1	4
05045106810000	7038	133	70	1	1	4
05045106810000	7038.5	139	33	0	1	4
05045106810000	7199	180	80	2	2	1
05045106810000	7271.9	30	74	2	2	3
05045106810000	7285.9	43	55	2	2	3
05045106810000	7322.4	33	78	2	1	1
05045106810000	7455.5	40	78	2	1	4
05045106810000	7461	184	80	2	2	4
05045106810000	7461.5	28	62	2	2	4
05045106810000	7463	181	58	1	2	4
05045106810000	7479.75	62	81	2	2	4
05045106810000	7481	62	82	2	1	4
05045106810000	7483.5	52	81	2	1	4
05045106810000	7488	200	79	2	1	4
05045106810000	7502	57	78	2	2	4
05045106810000	7533	44	54	2	2	4
05045106810000	7588.75	51	79	2	2	4
05045106810000	7593.25	159	75	2	2	4

Appendix A-3. Spreadsheet of natural fracture data in Anchondo 32B-20-692.

BBC 42B-23-692

UWI	MD	Dip Azimuth	Dip Angle	Fracture Type	Lithology	Arch. Elem.
05045176890000	4243.5	103	89	5	2	3
05045176890000	4474.25	185	57	5	0	0
05045176890000	4640	28	81	2	2	2
05045176890000	5390.5	105	66	5	0	0
05045176890000	5393.75	142	48	4	0	0
05045176890000	5410.5	132	85	5	0	0
05045176890000	5411	138	86	5	0	0
05045176890000	5411.25	262	79	5	0	0
05045176890000	5416	309	80	5	0	0
05045176890000	5751.7	42	81	1	1	1
05045176890000	5770	30	80	2	1	1
05045176890000	5772.35	28	75	2	1	1
05045176890000	5772.75	37	80	2	1	1
05045176890000	5788.75	48	71	2	1	1
05045176890000	5962.75	171	78	5	2	3
05045176890000	5963.25	347	48	5	2	3
05045176890000	6084.25	79	80	1	1	1
05045176890000	6142.5	47	80	2	2	3
05045176890000	6247.75	41	81	2	2	3
05045176890000	6352	181	43	5	0	0
05045176890000	6354.75	40	42	5	0	0
05045176890000	6355	26	43	5	0	0
05045176890000	6355.25	8	29	5	0	0
05045176890000	6415.75	165	63	4	2	1
05045176890000	6416.25	197	65	5	1	1
05045176890000	6417	207	43	5	1	1
05045176890000	6417.6	279	61	5	1	1
05045176890000	6481.5	359	55	5	1	3
05045176890000	6481.55	192	60	5	1	3
05045176890000	6639	192	77	5	2	3
05045176890000	6639.25	189	70	2	2	3
05045176890000	6641.25	194	78	5	2	3
05045176890000	6643.25	199	50	2	2	3
05045176890000	6647.75	275	60	5	1	3
05045176890000	6652.5	55	55	5	1	3
05045176890000	6652.75	56	64	5	1	3
05045176890000	6652.9	58	56	5	1	3

05045176890000	6653.25	57	55	5	1	3
05045176890000	6653.4	47	64	5	1	3
05045176890000	6653.5	54	59	5	1	3
05045176890000	6653.75	51	72	5	1	3
05045176890000	6654.5	263	85	5	1	3
05045176890000	6654.6	289	84	5	1	3
05045176890000	6654.75	289	82	5	1	3
05045176890000	6908.75	4	42	5	2	4
05045176890000	6933.5	103	35	5	2	1
05045176890000	6953.75	108	55	4	2	3
05045176890000	6957	183	75	5	2	1
05045176890000	7039.5	139	78	5	1	1
05045176890000	7039.55	106	61	2	1	1
05045176890000	7039.9	254	53	2	1	1
05045176890000	7040.05	288	56	5	1	1
05045176890000	7056.25	59	60	5	1	1
05045176890000	7073.25	273	75	2	1	1
05045176890000	7128.75	214	65	5	2	1
05045176890000	7183.3	61	27	4	2	3
05045176890000	7194.6	42	36	4	2	3
05045176890000	7195.75	39	61	5	0	0
05045176890000	7198.75	267	69	5	1	1
05045176890000	7209	205	80	2	2	1
05045176890000	7210	212	72	2	1	1
05045176890000	7210.9	213	72	2	1	1
05045176890000	7212.1	206	82	5	1	1
05045176890000	7213.9	183	80	4	1	1
05045176890000	7226.75	31	63	1	1	3
05045176890000	7227.9	18	58	5	2	3
05045176890000	7234	28	52	5	2	3
05045176890000	7261.25	72	39	5	1	1
05045176890000	7385.6	285	38	5	1	4
05045176890000	7386.5	283	48	5	1	4
05045176890000	7409.4	213	30	1	1	4
05045176890000	7482.3	39	86	2	1	4
05045176890000	7631	270	28	1	0	5
05045176890000	7739.75	115	44	4	0	5
05045176890000	7901.4	123	65	2	0	5
05045176890000	7906.75	143	45	5	0	5
05045176890000	7908.5	237	39	5	0	5
05045176890000	7909	128	62	1	0	5

05045176890000	7912.5	157	48	2	0	5
05045176890000	7956.25	25	79	5	0	5
05045176890000	7961.75	35	78	2	2	4
05045176890000	7962	38	79	2	2	4
05045176890000	7964	32	82	1	2	4
05045176890000	7980.5	28	79	2	1	4
05045176890000	7981	31	84	2	1	4
05045176890000	7981.75	27	81	2	1	4
05045176890000	7982	30	78	2	1	4
05045176890000	7984.1	220	80	5	2	4
05045176890000	8119	30	80	2	0	5
05045176890000	8119.25	28	81	2	0	5
05045176890000	8123.5	21	81	1	1	4
05045176890000	8132.9	29	81	5	0	5
05045176890000	8134.6	29	82	5	0	5
05045176890000	8135.75	212	73	5	0	5
05045176890000	8138.25	31	79	2	2	4
05045176890000	8150.75	30	80	1	1	4
05045176890000	8155	19	81	5	2	4
05045176890000	8161.25	359	81	1	1	4
05045176890000	8163	217	81	2	2	4
05045176890000	8163.5	11	82	1	2	4
05045176890000	8166	190	80	5	2	4
05045176890000	8173.2	47	86	1	2	4
05045176890000	8197.5	222	84	2	2	4
05045176890000	8203.25	36	85	1	2	4

Appendix A-4. Spreadsheet of natural fractures in BBC 42B-23-692.

BRYNILDSON 14C-20-692

UWI	MD	Dip Azimuth	Dip Angle	Fracture Type	Lithology	Architect. Element
05045081340000	5273.5	31	73	3	0	0
05045081340000	5283.5	18	79	2	0	0
05045081340000	5287	50	79	2	2	3
05045081340000	5291.5	33	79	2	2	3
05045081340000	5297	32	76	2	0	0
05045081340000	5299.5	22	76	2	0	0
05045081340000	5317.25	38	80	2	2	3
05045081340000	5322	204	57	2	2	2
05045081340000	5322.5	216	54	2	2	2
05045081340000	5322.5	215	49	2	2	2
05045081340000	5341	28	80	2	2	2
05045081340000	5366	120	50	1	0	0
05045081340000	5369.25	212	89	2	2	3
05045081340000	5370	282	65	3	1	3
05045081340000	5372.5	31	81	2	1	3
05045081340000	5376.5	39	83	2	2	3
05045081340000	5387	29	77	2	0	0
05045081340000	5436.75	32	82	2	2	3
05045081340000	5456	31	80	2	2	3
05045081340000	5464.75	16	83	2	1	4
05045081340000	5516.5	216	60	2	1	2
05045081340000	5523.75	64	66	2	1	2
05045081340000	5524	62	71	2	1	2
05045081340000	5524.5	64	72	2	1	2
05045081340000	5526	64	55	2	1	2
05045081340000	5526.5	52	57	2	1	2
05045081340000	5569.95	36	76	3	2	3
05045081340000	5572.25	36	79	3	2	3
05045081340000	5572.5	49	75	3	2	3
05045081340000	5583.5	31	82	3	2	3
05045081340000	5592	16	78	2	0	0
05045081340000	5596	25	80	2	1	2
05045081340000	5596.5	54	73	2	1	2
05045081340000	5597	62	72	2	1	2
05045081340000	5600.5	35	82	2	1	2
05045081340000	5605	25	61	2	1	2
05045081340000	5608	207	80	2	1	2

05045081340000	5609	8	73	2	1	2
05045081340000	5611	237	78	2	1	2
05045081340000	5613.5	43	75	2	1	2
05045081340000	5616	235	82	2	1	2
05045081340000	5630.5	33	80	1	1	2
05045081340000	5680	168	31	3	1	2
05045081340000	5681	192	39	2	1	2
05045081340000	5681.5	209	35	2	1	2
05045081340000	5694	23	83	2	2	4
05045081340000	5706.5	31	80	2	2	3
05045081340000	5719	36	72	2	2	3
05045081340000	5729	178	49	3	0	0
05045081340000	5751.5	8	73	2	0	0
05045081340000	5761	238	70	3	1	3
05045081340000	5782.75	31	84	2	2	3
05045081340000	5786	32	81	2	1	3
05045081340000	5795	34	80	2	2	3
05045081340000	5811	328	58	3	2	3
05045081340000	5813	210	76	3	0	0
05045081340000	5824	40	83	2	1	3
05045081340000	5824	40	73	2	1	3
05045081340000	5839	31	78	2	0	0
05045081340000	5841	57	80	3	0	0
05045081340000	5845	56	82	3	0	0
05045081340000	5848	56	84	3	2	1
05045081340000	5850	36	83	2	2	1
05045081340000	5858.5	36	79	2	1	1
05045081340000	5860.5	29	83	2	1	1
05045081340000	5864	35	79	2	2	3
05045081340000	5878	45	80	2	2	1
05045081340000	5882.5	36	76	3	0	0
05045081340000	5885	320	42	3	2	3
05045081340000	5890.75	41	75	2	2	3
05045081340000	5900.5	32	82	2	2	3
05045081340000	5901	39	80	2	2	3
05045081340000	5904.5	28	84	1	2	3
05045081340000	5928	76	64	2	2	3
05045081340000	5967.5	29	84	2	2	3
05045081340000	5981.5	26	85	1	2	3
05045081340000	5981.5	35	76	2	2	3
05045081340000	5982.75	37	84	2	2	3

05045081340000	5996.5	66	70	2	2	3
05045081340000	6001	33	84	2	1	3
05045081340000	6001.5	31	74	2	1	3
05045081340000	6002	36	69	2	1	3
05045081340000	6006.25	32	79	2	0	0
05045081340000	6008.75	36	80	2	0	0
05045081340000	6012	33	85	2	0	0
05045081340000	6014.25	39	82	2	2	3
05045081340000	6014.5	48	67	2	2	3
05045081340000	6019	45	78	3	0	0
05045081340000	6021	29	79	2	0	0
05045081340000	6028.5	35	79	2	2	3
05045081340000	6030	53	74	2	2	3
05045081340000	6036.25	14	72	3	2	1
05045081340000	6036.5	33	80	1	2	1
05045081340000	6036.5	39	83	2	2	1
05045081340000	6041	347	72	3	1	1
05045081340000	6059	44	83	2	2	3
05045081340000	6077.25	18	80	3	2	3
05045081340000	6111	40	84	2	2	3
05045081340000	6112.75	209	87	3	0	0
05045081340000	6115.5	44	81	2	2	1
05045081340000	6116	52	79	2	1	0
05045081340000	6129.5	41	47	3	0	0
05045081340000	6139	34	81	2	2	1
05045081340000	6170.5	37	82	3	2	3
05045081340000	6171.25	227	70	2	2	3
05045081340000	6220	37	82	3	2	3
05045081340000	6225	34	79	2	2	1
05045081340000	6231	208	69	3	1	1
05045081340000	6234	75	42	3	2	1
05045081340000	6241	124	48	3	2	3
05045081340000	6254.5	28	81	2	2	1
05045081340000	6257.5	51	79	2	2	1
05045081340000	6261	229	83	2	1	1
05045081340000	6298.75	35	84	1	2	3
05045081340000	6351	35	81	1	2	3
05045081340000	6371.5	17	83	2	2	3
05045081340000	6396.5	32	81	2	1	1
05045081340000	6413.5	240	40	3	0	0
05045081340000	6416	29	76	2	2	3

05045081340000	6419	65	78	2	2	3
05045081340000	6446	33	75	2	2	3
05045081340000	6446.75	358	76	3	2	3
05045081340000	6453	275	65	2	0	0
05045081340000	6458	44	79	2	2	3
05045081340000	6458.25	49	80	1	2	3
05045081340000	6458.75	327	73	3	2	3
05045081340000	6469	37	78	2	2	3
05045081340000	6475	36	76	2	2	3
05045081340000	6489.5	41	75	2	0	0
05045081340000	6492	36	76	1	0	0
05045081340000	6494.5	63	67	2	0	0
05045081340000	6498.5	41	72	2	0	0
05045081340000	6505	254	63	3	0	0
05045081340000	6507.75	256	67	3	2	1
05045081340000	6512	38	86	2	1	1
05045081340000	6513.5	54	81	3	1	1
05045081340000	6518	199	83	3	2	3
05045081340000	6525.5	104	69	3	1	3
05045081340000	6532	207	62	3	2	1
05045081340000	6534	35	46	3	2	1
05045081340000	6534.5	37	85	2	2	1
05045081340000	6535	318	60	3	2	1
05045081340000	6544.75	37	83	1	2	1
05045081340000	6547.5	15	84	2	1	1
05045081340000	6565.5	36	65	2	2	3
05045081340000	6570	42	75	2	2	3
05045081340000	6571	224	70	2	2	3
05045081340000	6599	50	37	3	1	3
05045081340000	6625	43	88	3	2	3
05045081340000	6637	33	80	2	2	1
05045081340000	6637	39	80	2	2	1
05045081340000	6638.5	36	84	2	1	1
05045081340000	6652	37	77	2	2	3
05045081340000	6656	42	70	2	0	0
05045081340000	6660.5	26	75	2	2	1
05045081340000	6662.5	40	82	1	1	1
05045081340000	6662.5	51	59	2	1	1
05045081340000	6663	43	58	2	1	1
05045081340000	6663.5	39	54	2	1	1
05045081340000	6663.75	51	63	2	1	1

05045081340000	6664	53	62	2	1	1
05045081340000	6666.5	56	80	2	1	1
05045081340000	6670	56	77	2	2	1
05045081340000	6672	24	79	1	1	1
05045081340000	6672.5	191	21	3	1	1
05045081340000	6680	218	40	3	2	1
05045081340000	6689.75	41	73	2	2	4
05045081340000	6691.25	41	77	2	2	3
05045081340000	6692.75	40	81	2	2	3
05045081340000	6725	183	64	3	0	0
05045081340000	6762.5	264	79	3	2	3
05045081340000	6762.75	29	83	3	2	3
05045081340000	6801	212	74	2	1	3
05045081340000	6807	39	79	2	2	1
05045081340000	6881.5	74	66	2	2	4
05045081340000	6884	35	72	2	2	4
05045081340000	6885.5	32	82	2	2	4
05045081340000	6889.1	48	66	2	2	4
05045081340000	6897	45	81	2	1	4
05045081340000	6897.5	50	77	2	1	4
05045081340000	6907	44	69	2	0	5
05045081340000	6911	37	68	1	2	4
05045081340000	6915.5	58	67	2	0	5
05045081340000	6917	48	67	1	0	5
05045081340000	6918	44	71	2	0	5
05045081340000	6925	183	84	3	2	4
05045081340000	6926	184	72	3	2	4
05045081340000	6929.5	132	75	3	2	4
05045081340000	6931	142	88	3	2	4
05045081340000	6931	212	86	3	2	4
05045081340000	6932	36	85	3	2	4
05045081340000	6936	41	80	2	2	4
05045081340000	6937.5	51	70	2	2	4
05045081340000	6939	42	65	2	2	4
05045081340000	6943.5	49	74	2	2	4
05045081340000	6959	298	55	3	2	4
05045081340000	6975	247	37	3	2	4
05045081340000	6997	320	46	3	1	3
05045081340000	7000	301	60	2	1	3
05045081340000	7000.5	146	84	2	1	3
05045081340000	7004.5	82	75	2	2	3

05045081340000	7005	296	73	2	2	3
05045081340000	7006.5	288	58	3	2	3
05045081340000	7011	290	78	3	0	0
05045081340000	7014	110	84	3	0	0
05045081340000	7018	66	72	2	1	3
05045081340000	7030	36	79	2	2	3
05045081340000	7046	51	69	2	2	1
05045081340000	7048	73	68	2	2	1
05045081340000	7050	221	63	2	2	1
05045081340000	7050.5	219	70	2	2	1
05045081340000	7051	221	80	2	2	1
05045081340000	7060.6	189	75	3	2	3
05045081340000	7068	337	34	3	1	1
05045081340000	7074	7	79	3	2	1
05045081340000	7076.35	198	74	3	2	1
05045081340000	7077	90	65	2	2	1
05045081340000	7078.25	127	80	3	2	1
05045081340000	7081.75	51	80	2	2	1
05045081340000	7086	61	69	3	1	1
05045081340000	7092	49	75	2	2	1
05045081340000	7096.5	315	80	2	1	1
05045081340000	7100	295	17	1	2	1
05045081340000	7100	233	63	3	2	1
05045081340000	7100.45	267	27	2	2	1
05045081340000	7108.75	70	59	3	0	0
05045081340000	7109	358	66	3	0	0
05045081340000	7109.1	249	73	3	0	0
05045081340000	7109.95	271	65	3	0	0
05045081340000	7114	199	60	1	0	0
05045081340000	7206.5	37	80	2	1	3
05045081340000	7207.5	68	64	2	2	3
05045081340000	7210.5	234	81	2	1	3
05045081340000	7232	53	76	2	1	4
05045081340000	7259	211	42	3	1	4
05045081340000	7271.5	27	69	1	1	4
05045081340000	7291	194	78	2	2	4
05045081340000	7303	52	67	3	1	4
05045081340000	7314	39	76	2	1	4
05045081340000	7316	58	80	2	1	4
05045081340000	7324	223	73	2	1	4
05045081340000	7324	245	48	3	1	4

05045081340000	7324.25	58	70	3	1	4
05045081340000	7324.5	217	75	2	1	4
05045081340000	7324.5	173	89	2	1	4
05045081340000	7324.5	70	54	3	1	4
05045081340000	7325	60	65	2	1	4
05045081340000	7325.5	49	64	3	1	4
05045081340000	7326	164	86	3	1	4
05045081340000	7326.5	202	53	3	1	4
05045081340000	7327	49	39	3	1	4
05045081340000	7327	285	72	3	1	4
05045081340000	7327.75	62	80	1	1	4
05045081340000	7327.75	222	59	3	1	4
05045081340000	7328.25	61	55	3	1	4
05045081340000	7328.5	74	49	3	1	4
05045081340000	7330	134	64	3	1	4
05045081340000	7330.5	33	76	3	1	4
05045081340000	7332.5	19	86	3	1	4
05045081340000	7333.5	44	77	1	1	4
05045081340000	7341	151	40	3	1	4
05045081340000	7346.5	201	87	2	0	5
05045081340000	7355.75	202	88	2	2	4
05045081340000	7359.25	57	72	2	2	4
05045081340000	7360.25	47	56	2	1	4
05045081340000	7361.25	242	66	2	1	4
05045081340000	7407	211	77	2	2	4
05045081340000	7408.5	258	72	2	2	4
05045081340000	7414	205	58	3	2	4
05045081340000	7443.5	74	70	2	2	4
05045081340000	7453.5	85	72	2	2	4
05045081340000	7459.5	44	75	3	1	4
05045081340000	7460.5	171	83	3	1	4
05045081340000	7467.25	327	62	3	2	4
05045081340000	7468	50	68	3	2	4
05045081340000	7470	49	77	2	2	4
05045081340000	7473	314	73	2	2	4
05045081340000	7475	108	68	2	2	4
05045081340000	7476.25	37	65	3	2	4
05045081340000	7516.75	253	68	3	2	4
05045081340000	7534	70	73	2	0	5
05045081340000	7796	149	44	1	0	5
05045081340000	7797	356	75	2	0	5

05045081340000	7825	4	50	2	1	4
05045081340000	7928.5	126	56	3	2	4
05045081340000	7929.5	129	42	3	1	4
05045081340000	8057	45	62	1	1	4
05045081340000	8059.5	67	43	2	1	4
05045081340000	8095	26	79	1	1	4
05045081340000	8100.5	256	59	1	2	4
05045081340000	8120	340	45	2	2	4
05045081340000	8125.5	51	38	3	0	5
05045081340000	8127.75	26	53	2	2	4
05045081340000	8128	230	29	3	2	4
05045081340000	8145	122	83	3	1	4
05045081340000	8146.5	209	54	3	1	4
05045081340000	8147.75	227	44	3	0	5
05045081340000	8151	223	35	3	0	5
05045081340000	8153	58	74	3	2	4
05045081340000	8153.75	220	74	3	2	4
05045081340000	8162	297	74	3	0	5
05045081340000	8164	97	49	2	1	4
05045081340000	8164.25	250	53	2	1	4
05045081340000	8165	288	48	2	1	4
05045081340000	8165.5	359	38	1	1	4
05045081340000	8165.5	138	64	2	1	4
05045081340000	8166.25	148	72	2	1	4
05045081340000	8166.5	330	62	2	1	4
05045081340000	8167	22	42	3	1	4
05045081340000	8168	208	56	2	2	4
05045081340000	8168.25	27	53	2	2	4
05045081340000	8168.5	226	59	2	2	4
05045081340000	8169.5	195	57	2	1	4
05045081340000	8170	206	58	2	1	4
05045081340000	8170.5	197	57	2	1	4
05045081340000	8171	16	50	2	1	4
05045081340000	8172	203	75	2	2	4
05045081340000	8172.5	56	73	2	2	4
05045081340000	8203.5	31	69	3	2	4
05045081340000	8221	34	63	2	2	4
05045081340000	8224	42	66	2	2	4
05045081340000	8228	81	28	1	2	4
05045081340000	8241.5	132	37	2	2	4
05045081340000	8331	16	21	3	0	5

05045081340000	8331	285	42	3	0	5
05045081340000	8331.5	34	25	3	0	5

Appendix A-5. Spreadsheet of natural fractures in BRYNILDSON 14C-20-692

Circle B. Land 33A-35-692

UWI	MD	Dip Azimuth	Dip Angle	Fracture Type	Lithology	Arch. Element
05045184930000	4245.7	220	79	1	2	2
05045184930000	4245.75	46	65	1	2	2
05045184930000	4245.75	47	68	1	2	2
05045184930000	4250.5	225	71	1	2	2
05045184930000	4251.9	32	65	1	2	2
05045184930000	4254.1	222	71	1	2	2
05045184930000	4514.25	30	87	1	0	0
05045184930000	4515	35	80	1	0	0
05045184930000	4543.5	26	63	1	2	2
05045184930000	4543.75	207	80	1	2	2
05045184930000	4545	233	87	1	2	2
05045184930000	4548.5	49	81	1	2	2
05045184930000	4566	47	87	1	2	3
05045184930000	4566.75	40	89	1	2	3
05045184930000	4571.1	47	78	1	0	0
05045184930000	4761	27	73	1	2	2
05045184930000	4761.25	18	67	1	2	2
05045184930000	4763.5	57	80	1	1	2
05045184930000	4764.1	210	87	1	1	2
05045184930000	4765	41	78	1	1	2
05045184930000	4765.75	31	80	1	1	2
05045184930000	4769.9	38	80	1	1	2
05045184930000	4770.75	38	81	1	1	2
05045184930000	4771	209	87	1	1	2
05045184930000	4774.75	29	87	1	1	2
05045184930000	4775.6	37	71	1	1	2
05045184930000	4775.75	358	87	1	1	2
05045184930000	4777.75	37	90	1	1	2
05045184930000	4777.9	37	73	1	1	2
05045184930000	4778.75	204	90	1	1	2
05045184930000	4782	212	90	1	1	2
05045184930000	4782.6	37	77	1	1	2
05045184930000	4785	38	74	1	1	2
05045184930000	4832.1	38	90	1	1	2
05045184930000	4834.5	37	89	1	1	2
05045184930000	4835.3	217	89	1	1	2
05045184930000	4842.25	36	80	1	1	2

05045184930000	4842.3	39	81	1	1	2
05045184930000	4848.5	37	79	1	1	2
05045184930000	5053	213	83	1	1	2
05045184930000	5053.7	220	89	1	1	2
05045184930000	5054	218	90	1	1	2
05045184930000	5054.75	45	79	1	1	2
05045184930000	5056.5	44	78	1	1	2
05045184930000	5056.75	37	80	1	1	2
05045184930000	5068.25	211	88	1	1	2
05045184930000	5068.75	27	89	1	1	2
05045184930000	5069.75	46	79	1	1	2
05045184930000	5071.5	19	79	1	1	2
05045184930000	5072	41	81	1	1	2
05045184930000	5169.5	217	89	1	1	2
05045184930000	5175	38	89	1	1	2
05045184930000	5175.25	44	88	1	1	2
05045184930000	5175.75	48	89	1	1	2
05045184930000	5178.75	46	89	1	1	2
05045184930000	5179	33	90	1	1	2
05045184930000	5179.25	28	81	1	1	2
05045184930000	5180.5	50	78	1	1	2
05045184930000	5184.25	41	80	1	1	2
05045184930000	5186.1	42	78	1	1	2
05045184930000	5282	224	88	1	2	1
05045184930000	5283.5	48	80	1	2	1
05045184930000	5285.5	215	81	1	1	1
05045184930000	5288.5	31	90	1	1	1
05045184930000	5288.5	34	90	1	1	1
05045184930000	5290	45	78	1	1	1
05045184930000	5292	35	82	1	1	1
05045184930000	5292	41	81	1	1	1
05045184930000	5295	37	89	1	1	1
05045184930000	5295	43	89	1	1	1
05045184930000	5297.5	44	89	1	1	1
05045184930000	5300.2	32	87	1	1	1
05045184930000	5310.75	226	88	1	2	1
05045184930000	5311.25	26	75	1	2	1
05045184930000	5313.9	50	81	1	2	1
05045184930000	5314.75	359	83	1	2	1
05045184930000	5556.25	209	90	1	1	1
05045184930000	5559.9	45	79	1	1	1

05045184930000	5559.9	34	90	1	1	1
05045184930000	5568.1	35	85	1	1	1
05045184930000	5569	40	85	1	1	1
05045184930000	5571	31	79	1	1	1
05045184930000	5573.5	38	79	1	1	1
05045184930000	5644.75	57	73	1	2	1
05045184930000	5646	45	88	1	2	1
05045184930000	5669.5	197	88	3	2	3
05045184930000	5670	22	88	3	2	3
05045184930000	5681.25	31	83	1	1	1
05045184930000	5725.75	229	85	1	2	1
05045184930000	5731.5	42	89	1	1	1
05045184930000	5754.5	233	76	1	1	1
05045184930000	5754.75	34	88	1	1	1
05045184930000	5755	42	89	1	1	1
05045184930000	5758.25	48	74	1	1	1
05045184930000	5758.75	51	77	1	1	1
05045184930000	5759.5	45	75	1	1	1
05045184930000	5767.25	47	75	1	1	1
05045184930000	5767.75	28	82	1	1	1
05045184930000	5770.5	221	89	1	1	1
05045184930000	5771	51	75	1	1	1
05045184930000	5776.25	41	85	1	1	1
05045184930000	5778.25	48	80	1	1	1
05045184930000	5780.2	248	83	1	1	1
05045184930000	5780.5	46	71	1	1	1
05045184930000	5781.2	233	85	1	1	1
05045184930000	5781.5	54	73	1	1	1
05045184930000	5787.75	24	75	1	1	1
05045184930000	5792.25	21	72	1	2	1
05045184930000	5793.25	21	71	1	1	1
05045184930000	5795.5	200	90	1	1	1
05045184930000	5817.5	42	70	1	2	1
05045184930000	5819.25	52	70	1	1	1
05045184930000	5823.25	34	81	1	2	1
05045184930000	5823.9	48	79	1	2	1
05045184930000	5860.75	204	71	3	1	3
05045184930000	5860.9	13	53	3	1	3
05045184930000	5861.25	201	80	1	1	3
05045184930000	5861.5	10	50	3	1	3
05045184930000	5861.75	207	79	1	1	3

05045184930000	5862.75	19	70	1	1	3
05045184930000	5864	205	85	1	2	3
05045184930000	5873	37	75	1	1	3
05045184930000	5874.5	33	89	1	1	3
05045184930000	5875.5	29	85	1	1	3
05045184930000	5962.75	356	81	3	1	4
05045184930000	5977.75	212	62	1	1	4
05045184930000	6026.25	53	77	1	1	4
05045184930000	6026.75	20	88	1	1	4
05045184930000	6028.25	40	87	1	1	4
05045184930000	6029	6	85	1	1	4
05045184930000	6111.1	41	89	1	1	4
05045184930000	6111.25	47	79	1	1	4
05045184930000	6131	47	80	1	1	1
05045184930000	6164.75	42	85	1	2	1
05045184930000	6168	41	86	1	1	1
05045184930000	6170.75	29	89	1	1	1
05045184930000	6171	30	79	1	1	1
05045184930000	6179	45	85	1	1	1
05045184930000	6180	213	86	1	1	1
05045184930000	6184	36	71	1	1	1
05045184930000	6185.9	37	89	1	1	1
05045184930000	6276	38	80	1	1	4
05045184930000	6276.75	38	79	1	1	4
05045184930000	6283.25	210	85	1	1	4
05045184930000	6284.5	44	80	1	1	4
05045184930000	6284.75	32	78	1	1	4
05045184930000	6287.25	37	77	1	2	4
05045184930000	6287.75	40	87	1	2	4
05045184930000	6288.25	43	83	1	2	4
05045184930000	6340.75	42	86	1	1	4
05045184930000	6348.25	38	87	1	1	4
05045184930000	6364.75	27	87	3	1	4
05045184930000	6367.5	33	86	1	1	4
05045184930000	6370.5	24	86	1	1	4
05045184930000	6415.75	332	87	3	2	3
05045184930000	6647	223	88	1	1	4
05045184930000	6647.25	37	74	1	1	4
05045184930000	6648	227	87	1	1	4
05045184930000	6648.75	48	71	1	1	4
05045184930000	6654.25	227	89	1	1	4

05045184930000	6807.15	42	79	1	1	4
05045184930000	6807.2	225	71	1	1	4
05045184930000	6807.25	215	81	1	1	4
05045184930000	7177.75	30	88	1	2	4
05045184930000	7179.75	21	87	1	2	4
05045184930000	7182.25	23	79	1	2	4
05045184930000	7183.85	22	79	1	2	4
05045184930000	7246.5	41	78	1	2	4
05045184930000	7253.5	27	90	1	2	4
05045184930000	7253.75	18	71	1	2	4
05045184930000	7255.5	24	86	1	2	4
05045184930000	7255.75	207	88	1	2	4
05045184930000	7258	24	87	1	1	4
05045184930000	7262.15	6	87	1	2	4
05045184930000	7270	11	86	1	2	4
05045184930000	7270.25	20	85	1	2	4
05045184930000	7270.6	20	84	1	2	4
05045184930000	7276.1	15	79	1	0	5
05045184930000	7278.5	19	79	1	0	5
05045184930000	7423.5	32	86	1	2	4
05045184930000	7424	35	88	1	2	4
05045184930000	7428.75	21	80	1	2	4
05045184930000	7429.75	26	88	1	1	4
05045184930000	7431.5	22	89	1	1	4
05045184930000	7431.75	25	79	1	1	4
05045184930000	7432	30	80	1	1	4
05045184930000	7438.75	29	90	1	1	4
05045184930000	7453.5	23	90	1	1	4
05045184930000	7454.75	22	75	1	1	4
05045184930000	7468.25	43	78	1	1	4
05045184930000	7480.25	27	83	1	1	4
05045184930000	7483.5	22	82	1	1	4
05045184930000	7485.25	21	88	1	2	4
05045184930000	7487.5	33	82	1	2	4
05045184930000	7498.75	46	78	1	2	4
05045184930000	7499.5	225	85	1	2	4
05045184930000	7500.5	59	79	1	2	4
05045184930000	7506.25	46	82	1	2	4
05045184930000	7509	27	81	1	2	4
05045184930000	7510	25	88	1	2	4
05045184930000	7513	203	85	1	2	4

05045184930000	7514.5	357	86	1	2	4
05045184930000	7521	24	81	1	2	4
05045184930000	7522.25	14	89	1	2	4
05045184930000	7538.25	25	84	1	1	4
05045184930000	7585	20	85	1	0	5
05045184930000	7585.75	23	85	1	0	5
05045184930000	7587	203	89	1	0	5
05045184930000	7587.9	34	83	1	0	5
05045184930000	7591.5	209	88	1	0	5
05045184930000	7593.75	196	88	1	0	5
05045184930000	7627.75	6	81	1	1	4
05045184930000	7692	208	85	1	2	4
05045184930000	7740	3	82	1	0	5
05045184930000	7741.9	24	75	3	0	5
05045184930000	7746	6	86	3	0	5
05045184930000	7754.75	22	79	3	0	5
05045184930000	7755	22	81	3	0	5
05045184930000	7764.25	359	90	3	0	5

Appendix A-6. Spreadsheet of natural fractures interpreted in Circle B. Land 33A-35-692.

DALEY 1-29

UWI	MD	Dip Azimuth	Dip Angle	Fracture Type	Lithology	Arch. Element
05045068680000	4012	132	63	3	0	0
05045068680000	4050.5	77	74	2	0	0
05045068680000	4251	254	50	3	2	2
05045068680000	4260.25	98	79	2	2	3
05045068680000	4272.4	28	79	2	0	0
05045068680000	4277	6	81	2	0	0
05045068680000	4308.5	39	85	1	2	3
05045068680000	4354	232	51	3	2	2
05045068680000	4366	65	63	1	2	2
05045068680000	4460	24	70	2	0	0
05045068680000	4502.5	27	83	2	2	3
05045068680000	4535	68	73	1	1	2
05045068680000	4557.75	48	78	2	2	2
05045068680000	4650	92	74	2	2	2
05045068680000	4654	9	82	2	2	2
05045068680000	4658	241	84	2	2	2
05045068680000	4659	13	75	2	2	2
05045068680000	4786	152	66	2	2	2
05045068680000	4787	226	52	2	2	2
05045068680000	4787	55	74	2	2	2
05045068680000	4819	61	76	2	1	2
05045068680000	4825	249	84	2	2	2
05045068680000	4838	11	69	2	0	0
05045068680000	4845	27	53	2	0	0
05045068680000	4941	28	81	2	2	3
05045068680000	4942.5	108	34	3	0	0
05045068680000	4943.5	46	33	3	0	0
05045068680000	4943.5	132	35	3	0	0
05045068680000	4987.5	6	69	2	2	2
05045068680000	4988	17	73	2	2	2
05045068680000	5192	59	66	1	2	2
05045068680000	5193.5	59	75	2	2	2
05045068680000	5196	80	61	2	2	2
05045068680000	5198.5	42	62	2	2	2
05045068680000	5199	43	80	2	2	2
05045068680000	5200	38	81	0	2	2
05045068680000	5202	33	81	2	2	2

05045068680000	5297	215	56	1	2	3
05045068680000	5313	4	69	1	2	2
05045068680000	5330.25	246	73	2	2	2
05045068680000	5342.5	219	79	2	1	2
05045068680000	5412.5	204	70	3	2	3
05045068680000	5413	207	76	3	2	3
05045068680000	5444	52	64	2	2	2
05045068680000	5460.5	210	53	3	0	0
05045068680000	5507	242	79	2	1	2
05045068680000	5553.5	67	72	1	1	2
05045068680000	5553.5	252	78	3	1	2
05045068680000	5595	72	75	2	1	3
05045068680000	5596.5	31	63	2	1	3
05045068680000	5626.75	53	80	3	2	3
05045068680000	5638	237	53	3	1	1
05045068680000	5640.5	241	73	2	1	1
05045068680000	5644	62	73	2	0	0
05045068680000	5666	227	84	2	2	1
05045068680000	5668	46	74	2	2	1
05045068680000	5668.5	43	70	2	2	1
05045068680000	5672	21	67	2	2	1
05045068680000	5683	237	78	2	2	1
05045068680000	5697.5	246	78	2	0	0
05045068680000	5701	237	74	2	2	1
05045068680000	5706	100	31	3	2	1
05045068680000	5710	249	74	2	1	3
05045068680000	5729.5	183	86	2	1	1
05045068680000	5734	353	62	1	1	1
05045068680000	5734.5	29	84	2	1	1
05045068680000	5757	16	64	2	0	0
05045068680000	5778.5	246	73	2	1	3
05045068680000	5783	211	52	2	0	0
05045068680000	5783.5	231	62	2	0	0
05045068680000	5785	195	72	1	0	0
05045068680000	5799.5	150	67	3	0	0
05045068680000	5827	24	76	2	2	3
05045068680000	5837	29	55	2	0	0
05045068680000	5862.5	56	62	1	2	3
05045068680000	5872	160	79	2	1	1
05045068680000	5914	55	65	2	1	1
05045068680000	5915	249	80	2	1	1

05045068680000	5934.25	196	76	2	2	3
05045068680000	5953	48	68	2	0	0
05045068680000	5954	281	67	1	0	0
05045068680000	5957	2	51	2	0	0
05045068680000	5991	219	83	2	2	1
05045068680000	6043	228	72	2	1	1
05045068680000	6043	218	45	2	1	1
05045068680000	6044	299	48	2	1	1
05045068680000	6053	251	65	2	1	1
05045068680000	6053.5	251	53	2	1	1
05045068680000	6054	270	79	2	1	1
05045068680000	6078	240	46	1	2	3
05045068680000	6123	55	41	3	1	4
05045068680000	6139	168	82	1	1	4
05045068680000	6140	180	74	1	1	4
05045068680000	6160	28	68	1	2	4
05045068680000	6167.5	52	52	2	2	4
05045068680000	6168	73	65	1	2	4
05045068680000	6168.5	262	57	2	2	4
05045068680000	6169	98	67	2	2	4
05045068680000	6170	99	75	1	2	4
05045068680000	6173	264	57	1	2	4
05045068680000	6174	266	59	3	2	4
05045068680000	6174.25	273	53	0	2	4
05045068680000	6174.25	90	62	1	2	4
05045068680000	6174.5	279	51	1	2	4
05045068680000	6174.5	118	68	1	2	4
05045068680000	6180	244	49	1	0	5
05045068680000	6190	274	61	1	2	4
05045068680000	6196.5	275	60	2	2	4
05045068680000	6209	291	47	1	1	4
05045068680000	6210	263	64	2	1	4
05045068680000	6212	234	58	1	1	4
05045068680000	6212.5	238	58	1	1	4
05045068680000	6215	268	50	1	1	4
05045068680000	6215.5	72	65	1	1	4
05045068680000	6215.75	248	55	1	1	4
05045068680000	6218	84	44	1	2	4
05045068680000	6218.5	74	74	1	2	4
05045068680000	6219.5	78	73	0	2	4
05045068680000	6220	73	68	0	2	4

05045068680000	6221	72	70	1	2	4
05045068680000	6263.5	199	67	3	2	1
05045068680000	6265	194	63	3	2	1
05045068680000	6265.5	197	63	3	2	1
05045068680000	6265.75	204	67	3	2	1
05045068680000	6266	201	63	3	2	1
05045068680000	6266.5	198	63	3	1	1
05045068680000	6267	200	63	3	1	1
05045068680000	6267.25	196	63	3	1	1
05045068680000	6267.5	198	63	3	1	1
05045068680000	6271.75	73	38	2	2	3
05045068680000	6274	102	53	3	0	0
05045068680000	6276.75	42	51	1	2	3
05045068680000	6277.75	37	50	1	2	3
05045068680000	6381.5	219	54	2	2	4
05045068680000	6382.5	207	44	1	2	4
05045068680000	6383	4	51	1	2	4
05045068680000	6400.5	77	56	2	1	4
05045068680000	6455	197	36	2	1	4
05045068680000	6455.5	209	39	2	1	4
05045068680000	6456	202	44	2	1	4
05045068680000	6456.25	213	43	2	1	4

Appendix A-7. Spreadsheet of natural fractures interpreted in Daley 1-29.

Jolley 31D-20-691

UWI	MD	Dip Azimuth	Dip Angle	Fracture Type	Lithology	Arch. Element
05045157380000	4326	177	59	1	2	3
05045157380000	4514.5	3	76	1	2	3
05045157380000	4515.5	200	68	1	2	3
05045157380000	4515.6	1	73	1	2	3
05045157380000	4517.25	187	69	1	2	2
05045157380000	4517.6	14	75	1	2	2
05045157380000	4519	206	68	1	2	2
05045157380000	5825.9	215	54	1	2	3
05045157380000	5826.4	201	57	1	2	3
05045157380000	6379.75	25	87	1	1	4
05045157380000	6380.25	236	73	1	1	4
05045157380000	6385.1	37	88	1	1	4
05045157380000	6385.5	223	76	1	1	4
05045157380000	6386	47	90	1	1	4
05045157380000	6562.6	151	35	3	0	0
05045157380000	6563	156	46	3	0	0
05045157380000	6563	332	53	3	0	0
05045157380000	6564.2	346	52	3	0	0
05045157380000	6713.5	200	71	3	1	1
05045157380000	6968.25	194	79	3	0	0
05045157380000	6969.5	189	75	3	0	0
05045157380000	6974	200	75	1	2	3
05045157380000	6974.25	194	74	3	2	3
05045157380000	6974.35	197	79	1	2	0
05045157380000	6977	194	80	3	0	0
05045157380000	6977.45	199	82	3	0	0
05045157380000	6979	192	79	3	0	0
05045157380000	6988.25	185	73	3	1	1
05045157380000	7004.9	204	78	3	0	0
05045157380000	7009.25	192	80	3	0	0

Appendix A-8. Spreadsheet of natural fractures interpreted in Jolley 31D-20-691.

Miller 24B-6-791

UWI	MD	Dip Azimuth	Dip Angle	Fracture Type	Lithology	Arch. Element
05045160980000	3810	13	33	1	2	2
05045160980000	3810	211	59	2	2	2
05045160980000	3810.5	214	58	2	2	2
05045160980000	3811	227	56	2	2	2
05045160980000	3811.5	244	59	2	2	2
05045160980000	3811.5	56	62	6	2	2
05045160980000	3814.5	51	51	6	1	2
05045160980000	3815	236	57	1	2	2
05045160980000	3879.5	272	61	5	0	0
05045160980000	3920.75	201	43	1	2	3
05045160980000	3921	172	52	2	2	3
05045160980000	3973	346	58	5	2	3
05045160980000	3974	340	54	5	2	3
05045160980000	3974	316	63	6	2	3
05045160980000	3974	176	69	6	2	3
05045160980000	3979.25	283	68	2	2	3
05045160980000	3989	242	69	5	0	0
05045160980000	3990.5	259	48	5	0	0
05045160980000	3992.5	191	89	5	2	3
05045160980000	3993	186	86	5	2	3
05045160980000	3993.25	221	86	5	2	3
05045160980000	3993.5	196	84	5	2	3
05045160980000	4051	224	80	5	2	3
05045160980000	4071.5	154	80	6	0	0
05045160980000	4072.5	156	73	6	0	0
05045160980000	4073	336	71	6	0	0
05045160980000	4074.5	325	74	6	0	0
05045160980000	4082	229	70	1	2	2
05045160980000	4093.5	59	54	5	2	2
05045160980000	4094	74	50	0	2	2
05045160980000	4098	235	67	1	2	2
05045160980000	4113.5	214	89	2	2	3
05045160980000	4143.5	214	80	2	0	0
05045160980000	4227	234	67	2	2	2
05045160980000	4227.5	41	57	1	2	2
05045160980000	4228	46	54	1	2	2
05045160980000	4228.5	247	68	2	2	2

05045160980000	4247.5	41	64	1	2	3
05045160980000	4253.5	314	80	5	1	2
05045160980000	4256	117	76	5	1	2
05045160980000	4260.5	206	54	1	1	2
05045160980000	4261	209	47	1	1	2
05045160980000	4327	163	57	1	2	2
05045160980000	4376.5	26	34	5	1	2
05045160980000	4377	17	33	5	1	2
05045160980000	4377	36	24	5	1	2
05045160980000	4379	208	65	5	0	0
05045160980000	4380	213	61	6	0	0
05045160980000	4380	31	63	6	0	0
05045160980000	4386	41	84	2	0	0
05045160980000	4469	357	68	1	0	0
05045160980000	4483	230	53	1	0	0
05045160980000	4484	358	62	1	0	0
05045160980000	4489.75	46	88	2	2	3
05045160980000	4514.5	169	77	1	2	2
05045160980000	4515.5	66	59	1	2	2
05045160980000	4520.5	72	69	1	2	2
05045160980000	4521	81	65	1	2	2
05045160980000	4521.5	78	66	1	2	2
05045160980000	4537	196	62	5	2	2
05045160980000	4544.5	34	76	5	0	0
05045160980000	4549.5	221	82	5	0	0
05045160980000	4557	18	42	5	2	3
05045160980000	4635.5	232	69	5	0	0
05045160980000	4639.5	191	45	5	0	0
05045160980000	4672.25	223	79	5	2	3
05045160980000	4673	219	68	5	1	3
05045160980000	4722	266	65	1	1	3
05045160980000	4722	111	54	5	1	3
05045160980000	4722	274	57	5	1	3
05045160980000	4722.5	86	32	5	1	3
05045160980000	4723	273	68	5	1	3
05045160980000	4732	25	63	5	0	0
05045160980000	4732.5	137	65	5	0	0
05045160980000	4737	39	82	2	2	3
05045160980000	4756	6	65	2	2	2
05045160980000	4774	198	55	5	0	0
05045160980000	4779	192	68	5	0	0

05045160980000	4781	339	61	5	0	0
05045160980000	4790.5	343	74	2	2	2
05045160980000	4792.5	209	84	2	1	2
05045160980000	4793	99	61	2	1	2
05045160980000	4794	79	57	2	1	2
05045160980000	4804.5	75	87	2	2	2
05045160980000	4808	37	86	2	2	2
05045160980000	4871	23	29	2	1	2
05045160980000	4871	39	86	2	1	2
05045160980000	4874	47	74	2	1	2
05045160980000	4875	239	83	2	1	2
05045160980000	4876	65	66	2	1	2
05045160980000	4876.5	55	64	2	1	2
05045160980000	4887	32	54	2	1	2
05045160980000	4887.5	47	58	0	1	2
05045160980000	4888.5	223	50	2	1	2
05045160980000	4911	310	27	5	0	0
05045160980000	4911.5	108	21	5	0	0
05045160980000	4913.5	45	77	2	2	3
05045160980000	4916.5	39	79	2	2	2
05045160980000	4919	49	81	2	2	2
05045160980000	4924.5	44	83	2	2	3
05045160980000	4935	356	76	6	0	0
05045160980000	4936	6	36	4	0	0
05045160980000	4940	175	86	6	0	0
05045160980000	4942	42	80	2	0	0
05045160980000	4943.5	301	76	2	2	2
05045160980000	4953	100	76	2	0	0
05045160980000	4954	82	70	2	0	0
05045160980000	4978	44	82	2	1	2
05045160980000	4980.75	236	78	2	1	2
05045160980000	4993.5	46	83	2	2	3
05045160980000	5000.5	38	77	2	2	2
05045160980000	5003	42	85	2	1	2
05045160980000	5009.5	56	67	2	2	3
05045160980000	5010	56	56	2	2	3
05045160980000	5018	2	55	2	2	3
05045160980000	5018	166	58	2	2	3
05045160980000	5022	42	86	2	2	3
05045160980000	5028.5	57	86	2	2	3
05045160980000	5040	158	68	2	0	0

05045160980000	5053.5	273	61	5	2	3
05045160980000	5061	23	78	5	1	2
05045160980000	5065	47	86	2	1	3
05045160980000	5081.75	235	80	5	2	3
05045160980000	5084.75	132	47	5	2	3
05045160980000	5094.5	340	36	2	2	3
05045160980000	5108.5	52	84	5	2	3
05045160980000	5125.5	2	58	5	1	2
05045160980000	5132	43	58	5	0	0
05045160980000	5132	130	33	5	0	0
05045160980000	5136	47	84	2	2	1
05045160980000	5138	46	88	2	2	1
05045160980000	5139	44	82	2	2	1
05045160980000	5139.5	46	78	2	2	1
05045160980000	5141.5	44	84	2	1	1
05045160980000	5151.5	225	87	2	1	1
05045160980000	5152	179	67	5	2	3
05045160980000	5152.5	59	84	2	2	3
05045160980000	5156.5	45	87	2	1	3
05045160980000	5157.5	102	82	5	1	3
05045160980000	5158	258	83	5	1	3
05045160980000	5160	116	83	5	2	3
05045160980000	5195.5	54	67	2	2	1
05045160980000	5197	39	68	5	2	1
05045160980000	5198	57	70	5	2	1
05045160980000	5200	54	77	1	2	1
05045160980000	5206	349	70	5	0	0
05045160980000	5207	14	63	5	0	0
05045160980000	5207.5	231	56	5	0	0
05045160980000	5208	352	64	2	0	0
05045160980000	5221	48	84	2	1	3
05045160980000	5229.75	45	86	2	2	3
05045160980000	5239.5	339	35	5	0	0
05045160980000	5254.5	48	84	2	1	3
05045160980000	5275	0	58	2	0	0
05045160980000	5304.5	293	67	5	1	1
05045160980000	5306	300	45	5	1	1
05045160980000	5317	12	73	5	0	0
05045160980000	5319.75	52	82	2	2	3
05045160980000	5336.75	229	38	1	2	3
05045160980000	5337.25	90	84	9	2	3

05045160980000	5338	256	73	6	2	3
05045160980000	5342.5	254	55	2	2	1
05045160980000	5384.5	31	81	2	1	3
05045160980000	5385	42	80	2	1	3
05045160980000	5395	47	83	2	2	3
05045160980000	5397.5	48	84	2	2	3
05045160980000	5403	42	85	2	1	3
05045160980000	5403.5	35	85	2	1	3
05045160980000	5442.5	163	46	5	0	0
05045160980000	5483.8	195	53	5	0	0
05045160980000	5486.5	199	58	5	2	3
05045160980000	5492	58	79	2	2	3
05045160980000	5520	45	86	2	2	3
05045160980000	5524.5	97	45	5	0	0
05045160980000	5526.5	284	49	1	0	0
05045160980000	5543.5	280	87	5	2	3
05045160980000	5558	48	63	5	0	0
05045160980000	5560.5	187	22	5	1	1
05045160980000	5561	194	21	5	1	1
05045160980000	5561.5	189	34	5	1	1
05045160980000	5562	259	21	5	1	1
05045160980000	5563.5	199	82	2	1	1
05045160980000	5565.5	2	79	1	2	1
05045160980000	5566.5	271	82	2	1	1
05045160980000	5567	341	44	5	1	1
05045160980000	5567.5	315	49	5	1	1
05045160980000	5570	175	46	5	2	1
05045160980000	5570.5	197	45	5	2	1
05045160980000	5588.5	338	53	0	2	3
05045160980000	5589	308	54	2	2	3
05045160980000	5591	21	70	2	2	3
05045160980000	5600	46	84	5	2	4
05045160980000	5602	60	79	5	1	4
05045160980000	5615.5	341	18	0	1	4
05045160980000	5666.5	58	87	2	1	4
05045160980000	5675.5	55	86	1	2	4
05045160980000	5676	53	81	5	2	4
05045160980000	5687.5	45	86	2	1	4
05045160980000	5693.5	37	85	2	1	4
05045160980000	5698	59	70	2	0	5
05045160980000	5713.5	54	86	5	2	4

05045160980000	5721.75	192	68	5	2	4
05045160980000	5721.8	349	40	5	2	4
05045160980000	5722.25	353	78	5	2	4
05045160980000	5762.5	83	63	5	2	1
05045160980000	5763.7	153	33	1	1	1
05045160980000	5793	234	85	2	2	3
05045160980000	5796.5	127	62	5	2	3
05045160980000	5802.5	232	86	2	1	1
05045160980000	5803.5	235	82	5	1	1
05045160980000	5804	42	85	2	1	1
05045160980000	5817	43	86	5	1	1
05045160980000	5821	348	35	1	1	1
05045160980000	5823.5	333	44	1	1	1
05045160980000	5829.5	111	41	1	1	1
05045160980000	5830.5	11	29	1	1	1
05045160980000	5835	207	24	5	1	1
05045160980000	5851	156	44	1	0	0
05045160980000	5852.5	173	75	4	0	0
05045160980000	5858.5	176	48	5	1	1
05045160980000	5899.75	261	87	2	1	3
05045160980000	5904.5	48	86	2	1	1
05045160980000	5905	45	85	2	1	1
05045160980000	5907.5	228	86	2	1	1
05045160980000	5908.5	232	74	2	1	1
05045160980000	5920.5	231	87	2	1	1
05045160980000	5938.5	221	84	2	2	3
05045160980000	5964	280	44	4	1	1
05045160980000	5972.5	153	77	5	1	1
05045160980000	5985.5	179	77	5	2	4
05045160980000	5986	180	75	5	2	4
05045160980000	5987.5	182	77	5	1	4
05045160980000	5992.25	113	85	2	1	4
05045160980000	5996.5	172	56	1	1	4
05045160980000	6031	219	35	2	1	4
05045160980000	6033	67	70	2	1	4
05045160980000	6050	231	82	5	1	4
05045160980000	6050.5	226	88	2	1	4
05045160980000	6050.5	3	78	5	1	4
05045160980000	6056	51	81	2	2	4
05045160980000	6082.5	238	88	2	1	4
05045160980000	6083.5	225	87	9	1	4

05045160980000	6086	227	87	2	1	4
05045160980000	6087.5	42	79	9	1	4
05045160980000	6113	206	56	5	2	4
05045160980000	6115	79	34	4	2	4
05045160980000	6123	220	87	2	2	4
05045160980000	6127.5	225	87	2	2	4
05045160980000	6136.5	14	77	2	1	4
05045160980000	6140.5	51	86	2	2	4
05045160980000	6158.5	241	86	2	2	4
05045160980000	6160	44	79	2	2	4
05045160980000	6160.5	24	70	5	2	4
05045160980000	6167.5	192	39	4	2	4
05045160980000	6172.5	130	38	1	2	4
05045160980000	6186.5	167	78	5	2	3
05045160980000	6189	205	83	5	0	0
05045160980000	6191	229	37	4	2	3
05045160980000	6206	21	44	4	0	0
05045160980000	6206.5	20	41	4	0	0
05045160980000	6207	13	34	4	0	0
05045160980000	6207.5	49	34	4	0	0
05045160980000	6221	35	84	2	2	1
05045160980000	6252.5	79	57	1	2	1
05045160980000	6252.5	290	75	5	2	1
05045160980000	6253.5	63	69	1	2	1
05045160980000	6266	42	86	2	1	1
05045160980000	6298	212	74	5	2	1
05045160980000	6299	223	34	4	2	1
05045160980000	6299	67	63	5	2	1
05045160980000	6348.5	98	77	5	2	1
05045160980000	6367	64	79	2	2	1
05045160980000	6414.5	128	60	1	1	1
05045160980000	6438	284	87	2	1	1
05045160980000	6442.5	111	63	1	1	1
05045160980000	6452	32	19	5	1	1
05045160980000	6459.75	104	55	5	2	3
05045160980000	6460.25	275	58	5	2	3
05045160980000	6461	56	81	5	2	3
05045160980000	6489	51	85	5	2	1
05045160980000	6493	49	78	5	1	1
05045160980000	6494	50	80	5	1	1
05045160980000	6511	217	64	5	1	4

05045160980000	6512.5	43	68	5	1	4
05045160980000	6513	189	67	5	1	4
05045160980000	6514.5	191	73	5	1	4
05045160980000	6514.5	198	80	5	1	4
05045160980000	6515	324	75	5	1	4
05045160980000	6517	248	27	5	1	4
05045160980000	6517.5	178	39	5	1	4
05045160980000	6518.5	162	68	5	2	4
05045160980000	6521.5	208	74	5	1	4
05045160980000	6522.5	262	72	5	1	4
05045160980000	6522.5	184	78	5	1	4
05045160980000	6522.5	54	68	5	1	4
05045160980000	6523	176	65	5	1	4
05045160980000	6524	239	70	4	1	4
05045160980000	6524.5	0	77	4	1	4
05045160980000	6525	195	69	4	1	4
05045160980000	6525.5	22	66	5	1	4
05045160980000	6525.5	192	58	5	1	4
05045160980000	6526	185	65	5	1	4
05045160980000	6526	17	74	5	1	4
05045160980000	6526.5	183	66	5	1	4
05045160980000	6529	287	35	2	1	4
05045160980000	6530.5	11	81	5	2	4
05045160980000	6531	335	82	5	2	4
05045160980000	6532	4	72	5	1	4
05045160980000	6535.5	47	60	2	1	4
05045160980000	6538.5	0	71	5	1	4
05045160980000	6542.5	51	86	2	1	4
05045160980000	6574.5	159	78	5	1	4
05045160980000	6577	350	87	5	2	4
05045160980000	6577.5	60	79	2	2	4
05045160980000	6590.5	44	67	1	2	4
05045160980000	6596	237	73	2	2	4
05045160980000	6605	217	70	2	2	4
05045160980000	6606	39	45	2	2	4
05045160980000	6606	222	77	2	2	4
05045160980000	6608	16	64	2	1	4
05045160980000	6609.5	194	59	5	2	4
05045160980000	6610	11	60	2	2	4
05045160980000	6616	57	82	2	1	4
05045160980000	6620.5	182	67	6	2	4

05045160980000	6622	165	74	2	0	5
05045160980000	6623.5	61	78	2	2	4
05045160980000	6641	44	51	2	2	4
05045160980000	6693	33	83	2	2	4
05045160980000	6698	50	64	2	2	4
05045160980000	6721	309	43	1	2	4
05045160980000	6763	124	38	5	0	5
05045160980000	6767	281	49	4	0	5
05045160980000	6767.5	94	28	4	0	5
05045160980000	6768	304	35	1	0	5
05045160980000	6807.5	251	59	5	0	5
05045160980000	6809	46	44	5	0	5
05045160980000	6821	341	33	2	0	5
05045160980000	6821.5	169	35	2	0	5

Appendix A-9. Spreadsheet of natural fractures interpreted in Miller 24B-6-791.

Nesbitt 13C-25-692

UWI	MD	Dip Azimuth	Dip Angle	Fracture Type	Lithology	Arch. Element
05045134160000	5219	49	45	2	0	0
05045134160000	5227.5	333	63	3	2	3
05045134160000	5228.5	34	76	2	2	3
05045134160000	5230	32	76	2	2	3
05045134160000	5257	48	74	3	2	3
05045134160000	5286.5	18	73	2	1	2
05045134160000	5293	24	79	2	0	0
05045134160000	5307	46	82	2	2	3
05045134160000	5327	42	74	3	1	3
05045134160000	5349	70	75	2	1	2
05045134160000	5351	41	80	2	1	2
05045134160000	5357.5	46	80	2	1	2
05045134160000	5367	25	76	2	2	2
05045134160000	5373.5	44	75	2	2	3
05045134160000	5414	339	68	2	2	3
05045134160000	5419	79	74	2	0	0
05045134160000	5431	62	68	2	0	0
05045134160000	5463	47	64	2	1	2
05045134160000	5506	39	74	2	2	2
05045134160000	5509	44	80	2	1	2
05045134160000	5518	54	77	2	1	2
05045134160000	5550	45	82	2	1	2
05045134160000	5561	130	69	2	1	2
05045134160000	5563	142	57	2	1	2
05045134160000	5601	43	81	2	2	3
05045134160000	5602	44	79	2	2	3
05045134160000	5615	46	78	2	1	2
05045134160000	5667	47	84	2	2	3
05045134160000	5702.75	58	79	2	2	3
05045134160000	5705	49	78	2	2	3
05045134160000	5706.5	57	69	2	2	3
05045134160000	5752.25	41	74	2	2	3
05045134160000	5754	39	79	2	2	3
05045134160000	5763.5	51	82	2	1	2
05045134160000	5773.5	62	78	0	1	2
05045134160000	5776.5	46	82	2	1	2
05045134160000	5776.5	77	73	2	1	2

05045134160000	5836	68	82	2	1	1
05045134160000	5837	70	85	2	1	1
05045134160000	5839	87	72	2	1	1
05045134160000	5842	47	80	2	1	1
05045134160000	5843.5	38	79	2	1	1
05045134160000	5844.5	47	78	2	1	1
05045134160000	5869	52	82	2	1	1
05045134160000	5887.5	49	76	2	2	1
05045134160000	5891	52	84	2	1	1
05045134160000	5907	52	79	2	1	1
05045134160000	5927	52	81	2	2	3
05045134160000	5970.5	46	81	1	2	3
05045134160000	5972.5	52	84	2	1	3
05045134160000	6008.5	72	83	2	2	1
05045134160000	6015	65	78	2	1	1
05045134160000	6017.5	51	78	2	1	1
05045134160000	6027.5	48	78	2	2	3
05045134160000	6223	59	75	2	2	4
05045134160000	6242	59	80	2	2	4
05045134160000	6247	60	82	1	1	4
05045134160000	6251	51	76	2	1	4
05045134160000	6256	333	55	3	0	5
05045134160000	6279	42	85	2	2	4
05045134160000	6284	51	83	2	2	4
05045134160000	6291	69	85	1	1	4
05045134160000	6307.5	31	84	2	2	4
05045134160000	6322	44	84	0	1	4
05045134160000	6326	42	78	2	1	4
05045134160000	6341.5	312	29	3	1	4
05045134160000	6399	248	27	1	1	3
05045134160000	6417.25	68	76	2	2	1
05045134160000	6439.5	51	64	2	2	1
05045134160000	6550.5	54	80	2	1	1
05045134160000	6555	61	81	2	1	1
05045134160000	6615.5	57	75	2	1	4
05045134160000	6642	51	80	2	1	4
05045134160000	6646.5	49	80	2	1	4
05045134160000	6738	308	34	3	2	4
05045134160000	6739	131	27	3	2	4
05045134160000	6747	58	81	2	1	4
05045134160000	6760	54	82	2	1	4

05045134160000	6784.5	117	70	2	1	4
05045134160000	6785	56	71	2	1	4
05045134160000	6840.5	9	32	3	0	5
05045134160000	6945.75	67	67	2	2	1
05045134160000	6949	145	79	2	1	1
05045134160000	6958	84	73	2	0	0
05045134160000	6960.5	66	70	2	0	0
05045134160000	6997	66	76	2	0	0
05045134160000	7004.5	70	85	3	2	1
05045134160000	7014	77	76	3	2	1
05045134160000	7064	57	60	2	2	4
05045134160000	7116.5	55	85	2	1	4
05045134160000	7159	4	69	2	2	4
05045134160000	7275	134	86	3	2	4
05045134160000	7276.5	292	74	3	2	4
05045134160000	7278	119	80	3	1	4
05045134160000	7666	267	60	1	0	5
05045134160000	7668	49	60	2	0	5
05045134160000	7708.5	29	82	2	1	4
05045134160000	7723	18	74	0	1	4
05045134160000	7745	27	80	2	1	4
05045134160000	7750	39	86	2	1	4
05045134160000	7752.5	28	83	0	1	4
05045134160000	7896	43	88	2	2	4
05045134160000	7901	208	74	2	0	5
05045134160000	7905.5	31	87	2	2	4
05045134160000	7914	34	84	2	2	4
05045134160000	7917	55	83	2	1	4
05045134160000	7927	40	85	2	1	4
05045134160000	7966.5	82	41	1	2	4
05045134160000	7975	31	84	2	1	4
05045134160000	7994	37	82	2	2	4
05045134160000	7998.8	269	52	3	2	4
05045134160000	8030.5	13	74	2	2	4
05045134160000	8067	246	89	2	2	4
05045134160000	8076.5	24	80	2	2	4
05045134160000	8078	14	78	3	2	4
05045134160000	8089.5	49	75	2	2	4

Appendix A-10. Spreadsheet of natural fractures interpreted in Nesbitt 13C-25-692.

Schirer 14D-26-692

UWI	MD	Dip Azimuth	Dip Angle	Fracture Type	Lithology	Arch. Element
05045149230000	4115	44	78	2	0	0
05045149230000	4122.25	46	71	2	0	0
05045149230000	4122.5	276	80	2	0	0
05045149230000	4124.5	44	75	2	2	3
05045149230000	4125.95	226	81	2	2	3
05045149230000	4306.1	308	58	5	0	0
05045149230000	4335.5	39	65	1	1	2
05045149230000	4402	332	40	1	1	2
05045149230000	4470.25	75	70	4	0	0
05045149230000	4476	57	70	2	2	3
05045149230000	4476.75	228	71	0	2	3
05045149230000	4496.25	111	29	1	2	3
05045149230000	4500.5	303	89	5	0	0
05045149230000	4517	292	59	5	0	0
05045149230000	4518.75	282	73	5	0	0
05045149230000	4521.1	316	71	5	0	0
05045149230000	4608.5	100	69	2	2	3
05045149230000	4626.5	117	82	2	0	0
05045149230000	4652	306	52	1	1	2
05045149230000	4686.5	312	38	1	1	2
05045149230000	4686.5	141	66	1	1	2
05045149230000	4909	136	76	5	2	2
05045149230000	4909.75	154	82	5	2	2
05045149230000	4952.75	339	37	4	2	3
05045149230000	4961	134	84	5	1	2
05045149230000	5174.25	43	88	2	1	2
05045149230000	5175	235	89	2	1	2
05045149230000	5221.5	230	80	2	1	2
05045149230000	5222.4	28	68	2	1	2
05045149230000	5307	227	90	2	1	2
05045149230000	5309.25	39	85	2	1	2
05045149230000	5309.5	241	72	2	1	2
05045149230000	5311.5	41	84	1	1	2
05045149230000	5314.35	215	87	9	1	2
05045149230000	5317.25	41	74	2	1	2
05045149230000	5326.75	35	86	2	1	2
05045149230000	5337.25	39	87	2	1	2

05045149230000	5364.5	43	88	2	1	2
05045149230000	5366.75	32	88	2	1	2
05045149230000	5370	46	78	2	1	2
05045149230000	5393	225	90	2	2	3
05045149230000	5397.75	259	62	2	1	3
05045149230000	5407.5	224	90	2	2	2
05045149230000	5421.25	207	65	2	2	3
05045149230000	5421.75	41	88	2	2	3
05045149230000	5431.4	61	68	2	2	3
05045149230000	5431.75	52	80	2	2	3
05045149230000	5449	225	88	2	2	2
05045149230000	5454.75	51	90	2	2	2
05045149230000	5459.5	43	86	2	2	2
05045149230000	5469.5	236	66	4	2	3
05045149230000	5470	236	66	4	2	3
05045149230000	5470.75	246	65	4	2	3
05045149230000	5471.25	237	66	4	2	3
05045149230000	5475.5	59	81	2	2	3
05045149230000	5476	44	76	2	2	3
05045149230000	5476.35	44	83	2	2	3
05045149230000	5486.25	228	41	4	3	3
05045149230000	5492.75	208	60	4	1	3
05045149230000	5602.25	80	41	4	1	1
05045149230000	5631.25	42	88	2	1	3
05045149230000	5632.5	41	80	2	1	3
05045149230000	5634.5	45	81	2	2	3
05045149230000	5689.5	189	48	5	2	3
05045149230000	5738.7	49	83	2	1	1
05045149230000	5745.4	49	84	2	1	1
05045149230000	5804.5	200	63	1	1	1
05045149230000	5805.5	353	45	1	1	1
05045149230000	5954	46	84	5	1	1
05045149230000	5984	196	68	2	2	1
05045149230000	5987.5	201	70	2	1	1
05045149230000	5994.6	188	63	2	1	1
05045149230000	5999.2	214	70	2	1	1
05045149230000	5999.75	206	58	2	1	1
05045149230000	6000.5	57	53	1	1	1
05045149230000	6002	46	60	2	1	1
05045149230000	6002.8	58	62	2	1	1
05045149230000	6040.25	48	88	2	1	1

05045149230000	6060.8	319	82	5	2	4
05045149230000	6075.75	103	48	5	2	4
05045149230000	6078.6	47	83	2	1	4
05045149230000	6122.75	110	43	1	1	4
05045149230000	6156.25	208	82	5	1	4
05045149230000	6157	206	80	5	1	4
05045149230000	6157.8	212	78	5	1	4
05045149230000	6183.25	205	78	2	0	0
05045149230000	6184.5	196	75	2	0	0
05045149230000	6185.5	195	68	2	0	0
05045149230000	6198.75	58	83	2	1	1
05045149230000	6277.5	55	82	2	1	3
05045149230000	6381.5	65	87	2	2	1
05045149230000	6442	50	85	2	1	4
05045149230000	6450.75	61	87	2	1	4
05045149230000	6454	51	80	2	1	4
05045149230000	6455	30	89	2	1	4
05045149230000	6473	47	86	2	1	4
05045149230000	6480.75	54	82	2	2	4
05045149230000	6481.2	57	81	2	2	4
05045149230000	6481.75	49	81	2	2	4
05045149230000	6482.25	53	82	2	2	4
05045149230000	6487.75	61	80	2	1	4
05045149230000	6490.1	49	81	2	2	4
05045149230000	6493.75	46	81	2	1	4
05045149230000	6505.75	207	39	1	1	4
05045149230000	6511	51	82	2	1	4
05045149230000	6513.5	55	82	2	1	4
05045149230000	6554.3	56	82	2	1	4
05045149230000	6556.8	42	82	0	1	4
05045149230000	6618.1	88	71	5	0	0
05045149230000	6619.1	88	68	5	2	3
05045149230000	6619.55	144	78	5	2	3
05045149230000	6620.25	113	78	5	2	3
05045149230000	6620.25	266	51	5	2	3
05045149230000	6621	268	63	5	2	3
05045149230000	6621.25	265	58	5	2	3
05045149230000	6621.6	256	61	5	2	3
05045149230000	6627.5	132	31	4	0	0
05045149230000	6638.5	324	60	4	2	3
05045149230000	6639.75	135	63	4	2	3

05045149230000	6642.1	295	52	4	0	0
05045149230000	6661.5	53	58	5	2	1
05045149230000	6705.25	56	73	2	2	1
05045149230000	6764	162	70	5	1	1
05045149230000	6765.3	271	63	5	2	3
05045149230000	6766	84	45	5	2	3
05045149230000	6766.1	287	56	5	2	3
05045149230000	6766.15	75	37	5	2	3
05045149230000	6766.3	30	73	2	2	3
05045149230000	6766.3	283	56	5	2	3
05045149230000	6766.7	283	56	5	2	3
05045149230000	6767.25	303	70	5	2	3
05045149230000	6772.8	42	77	5	2	1
05045149230000	6774	44	83	5	2	1
05045149230000	6774.5	39	81	5	2	1
05045149230000	6850	56	75	2	2	4
05045149230000	6851.75	253	74	2	1	4
05045149230000	6852.35	38	68	2	1	4
05045149230000	6860.75	51	83	1	2	4
05045149230000	6894.75	292	85	2	1	4
05045149230000	6914.25	70	83	2	1	4
05045149230000	6925.5	48	85	2	1	4
05045149230000	6942.5	46	89	2	1	4
05045149230000	6950.5	44	72	2	1	4
05045149230000	6950.6	57	82	2	1	4
05045149230000	6958.5	54	80	2	2	4
05045149230000	6963.25	56	86	2	1	4
05045149230000	6963.75	215	84	2	1	4
05045149230000	6981.55	48	69	2	2	4
05045149230000	6981.75	62	64	2	2	4
05045149230000	6983.25	65	74	2	2	4
05045149230000	6987.5	224	80	2	2	4
05045149230000	6997.45	25	70	2	2	4
05045149230000	7000.75	54	80	2	2	4
05045149230000	7003.75	55	82	2	2	4
05045149230000	7005.5	221	64	2	2	4

Appendix A-11. Spreadsheet of natural fracture data interpreted in Schirer 14D-26-692.

SPECIALITY 41A-28-692

UWI	MD	Dip Azimuth	Dip Angle	Fracture Type	Lithology	Architect. Element
05045118440000	4786	358	33	3	0	0
05045118440000	4870.75	64	42	1	0	0
05045118440000	4953	40	60	1	2	3
05045118440000	5124	216	83	2	2	2
05045118440000	5126	238	89	2	2	2
05045118440000	5128	208	85	2	2	2
05045118440000	5210.9	255	78	1	1	2
05045118440000	5211.1	252	76	1	1	2
05045118440000	5263.75	181	55	2	2	2
05045118440000	5265.25	35	80	2	2	2
05045118440000	5454.25	37	81	2	2	3
05045118440000	5484.15	37	84	2	2	3
05045118440000	5575	39	80	2	2	3
05045118440000	5660.25	33	81	1	1	2
05045118440000	5704.1	227	67	1	1	3
05045118440000	5731.5	50	75	2	2	3
05045118440000	5787	37	79	2	1	2
05045118440000	5788.75	43	82	2	1	2
05045118440000	5789.25	40	83	2	1	2
05045118440000	5811.75	38	83	1	2	3
05045118440000	5816.75	54	85	2	2	3
05045118440000	5829.5	45	90	1	2	3
05045118440000	5830.75	43	84	2	2	3
05045118440000	5863.5	48	82	1	2	1
05045118440000	5956.25	42	86	1	1	3
05045118440000	6047.5	271	53	1	1	1
05045118440000	6049	225	89	3	1	1
05045118440000	6050	33	83	1	1	1
05045118440000	6063	232	51	3	2	3
05045118440000	6086.5	36	80	1	2	3
05045118440000	6105.75	39	84	2	2	3
05045118440000	6150	37	83	2	2	1
05045118440000	6152	47	83	2	1	1
05045118440000	6158.5	48	85	2	1	1
05045118440000	6164.75	53	83	2	1	1
05045118440000	6175.25	57	58	3	2	3
05045118440000	6175.75	32	46	3	2	3

05045118440000	6178.5	37	85	1	1	3
05045118440000	6207.75	221	50	3	0	0
05045118440000	6368.25	43	80	2	1	3
05045118440000	6434.25	56	84	2	2	4
05045118440000	6449.2	238	20	3	1	4
05045118440000	6487.9	103	32	1	1	4
05045118440000	6539.5	60	47	3	0	0
05045118440000	6540.5	47	50	3	0	0
05045118440000	6710.25	59	80	2	1	1
05045118440000	6738.75	39	81	2	1	4
05045118440000	6750.5	54	81	2	1	4
05045118440000	6769.5	43	82	2	1	4
05045118440000	6770.75	42	84	2	1	4
05045118440000	6772.5	40	85	2	1	4
05045118440000	6839	43	89	2	1	4
05045118440000	6891.25	290	47	1	0	5
05045118440000	7009.5	64	82	2	1	1
05045118440000	7182.5	44	81	2	1	4
05045118440000	7183.25	243	85	2	1	4
05045118440000	7202	44	84	2	1	4
05045118440000	7202.25	36	84	2	1	4
05045118440000	7789.5	39	83	2	1	4
05045118440000	7858.5	32	82	2	2	4
05045118440000	7946.25	211	55	3	1	4
05045118440000	7946.5	37	40	3	1	4
05045118440000	8017.5	42	82	2	2	4
05045118440000	8031.25	51	85	2	1	4

Appendix A-12. Spreadsheet of natural fractures interpreted in SPECIALITY 41A-28-692.

APPENDIX B

Appendix B contains statistics of natural fractures. For each well, the number of natural fractures is given with respect to architectural element and lithology where natural fractures were observed. Architectural element and lithology logs were generated using the criteria given in “Controls on Fracture Distribution” section in Chapter 3 Fracture Analysis. The discrimination of fractures are also made by using a color code—conductive versus resistive fractures.

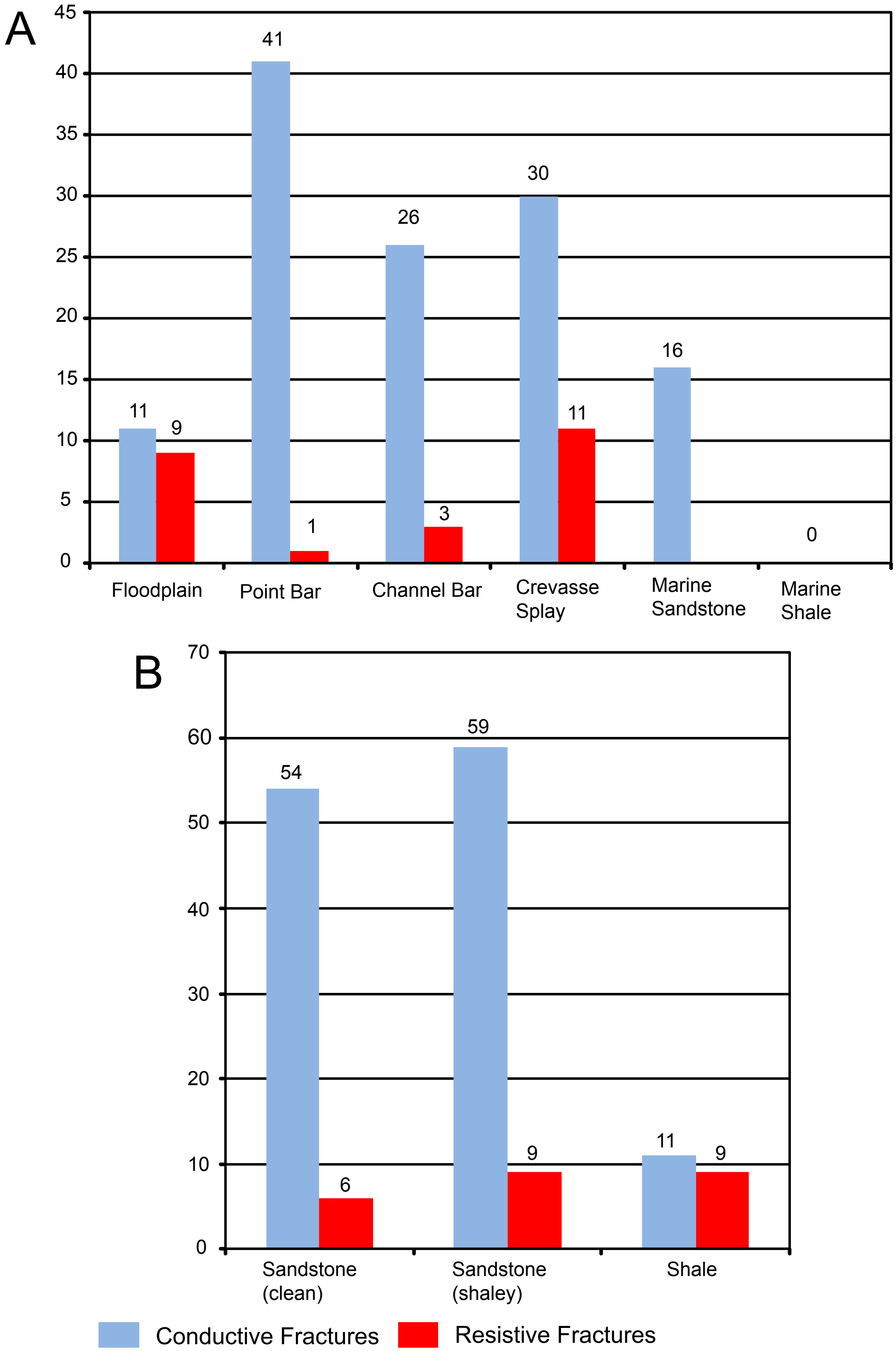

Appendix B-1. Fracture statistics for Anchondo 32B-20-692. A) the number of natural fractures observed in each architectural element. B) the number of natural fractures observed in each lithology type.

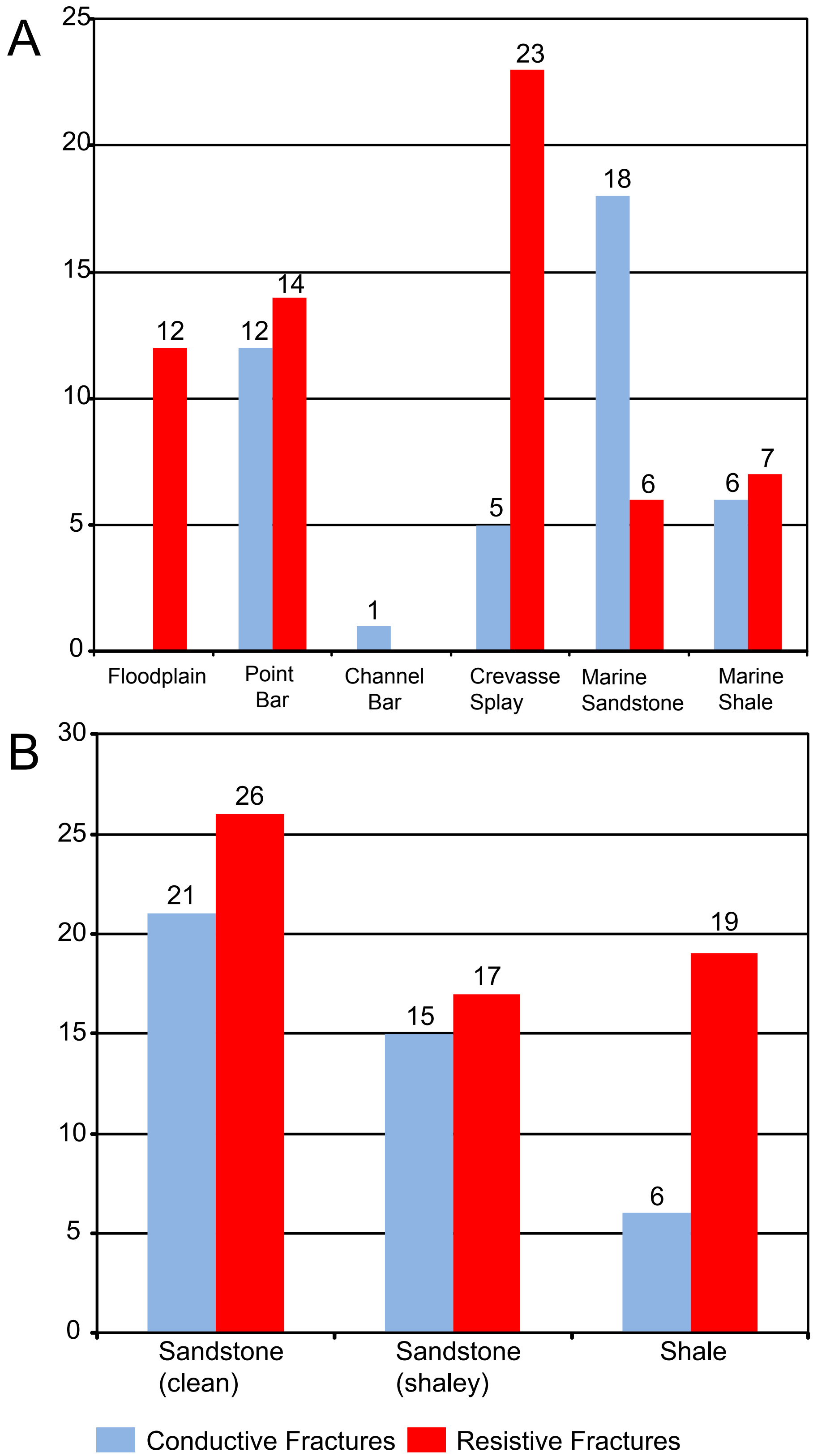

Appendix B-2. Fracture statistics for BBC 42B-23-692. A) the number of natural fractures observed in each architectural element in this well. B) the number of natural fractures observed in each lithology type.

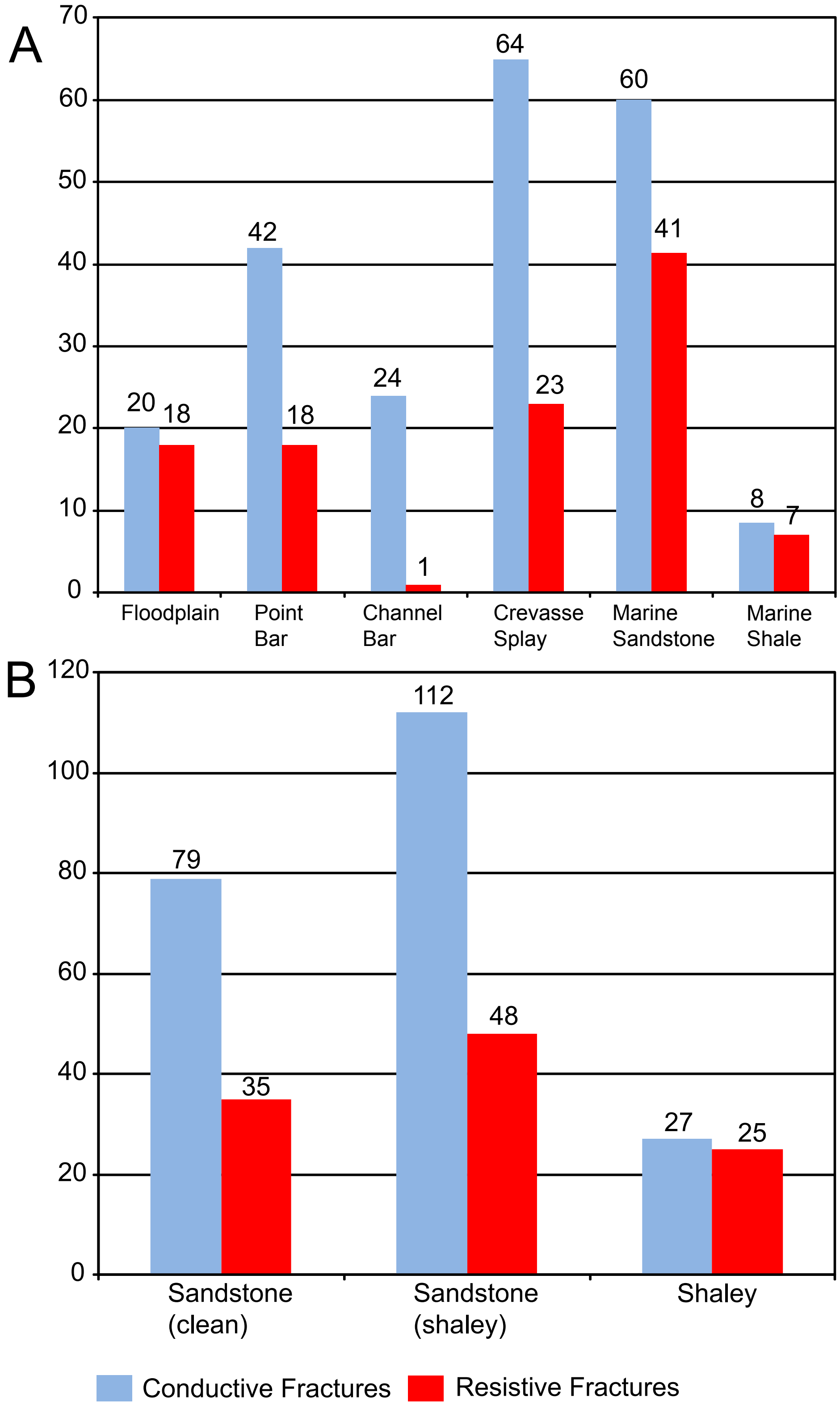

Appendix B-3. Fracture statistics for Brynildson 14C-20-692. A) the number of natural fractures observed in each architectural element in this well. B) the number of natural fractures observed in each lithology type.

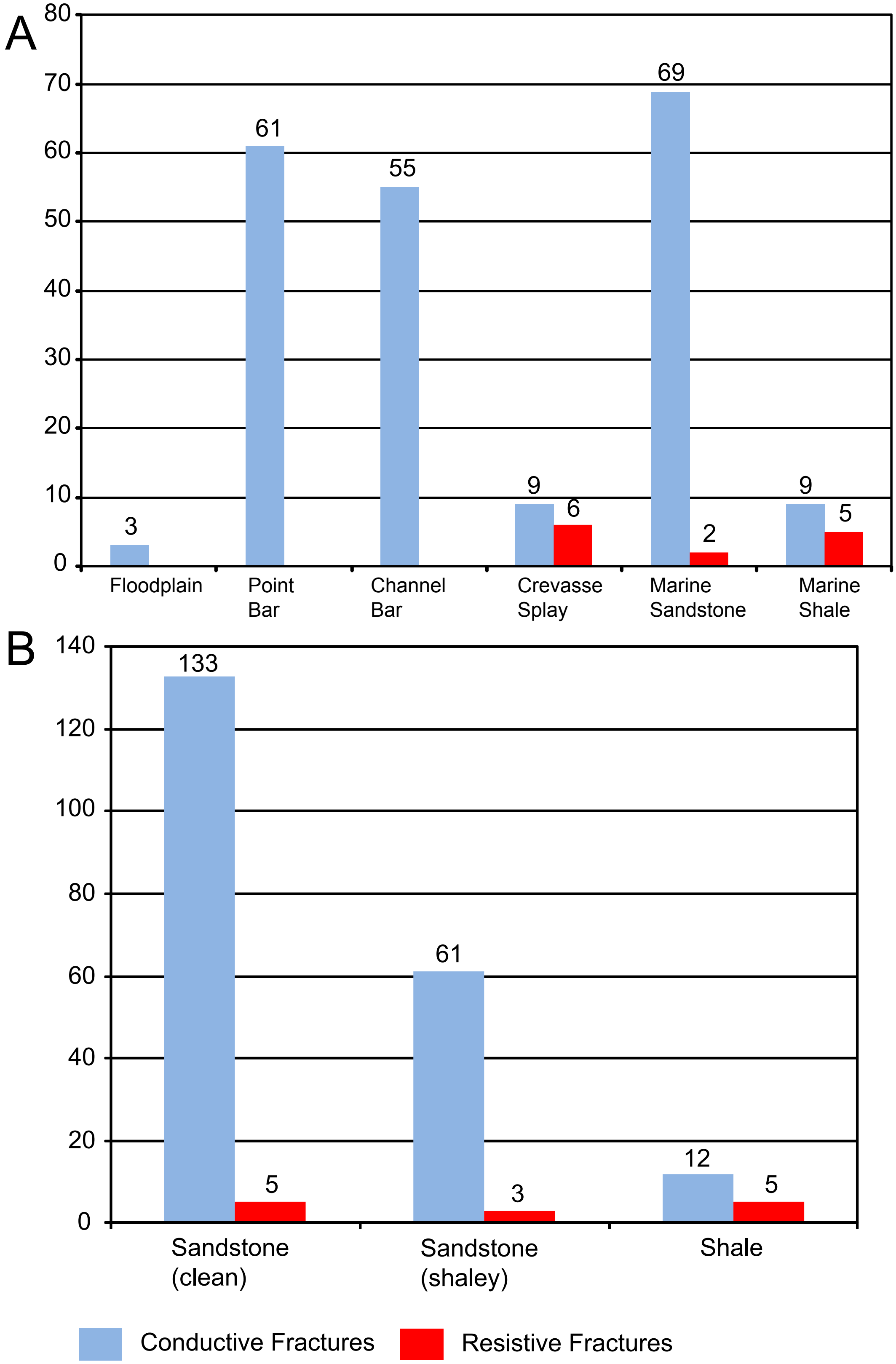

Appendix B-4. Fracture statistics for Circle B. Land 33A-35-692. A) the number of natural fractures observed in each architectural element in this well. B) the number of natural fractures observed in each lithology type.

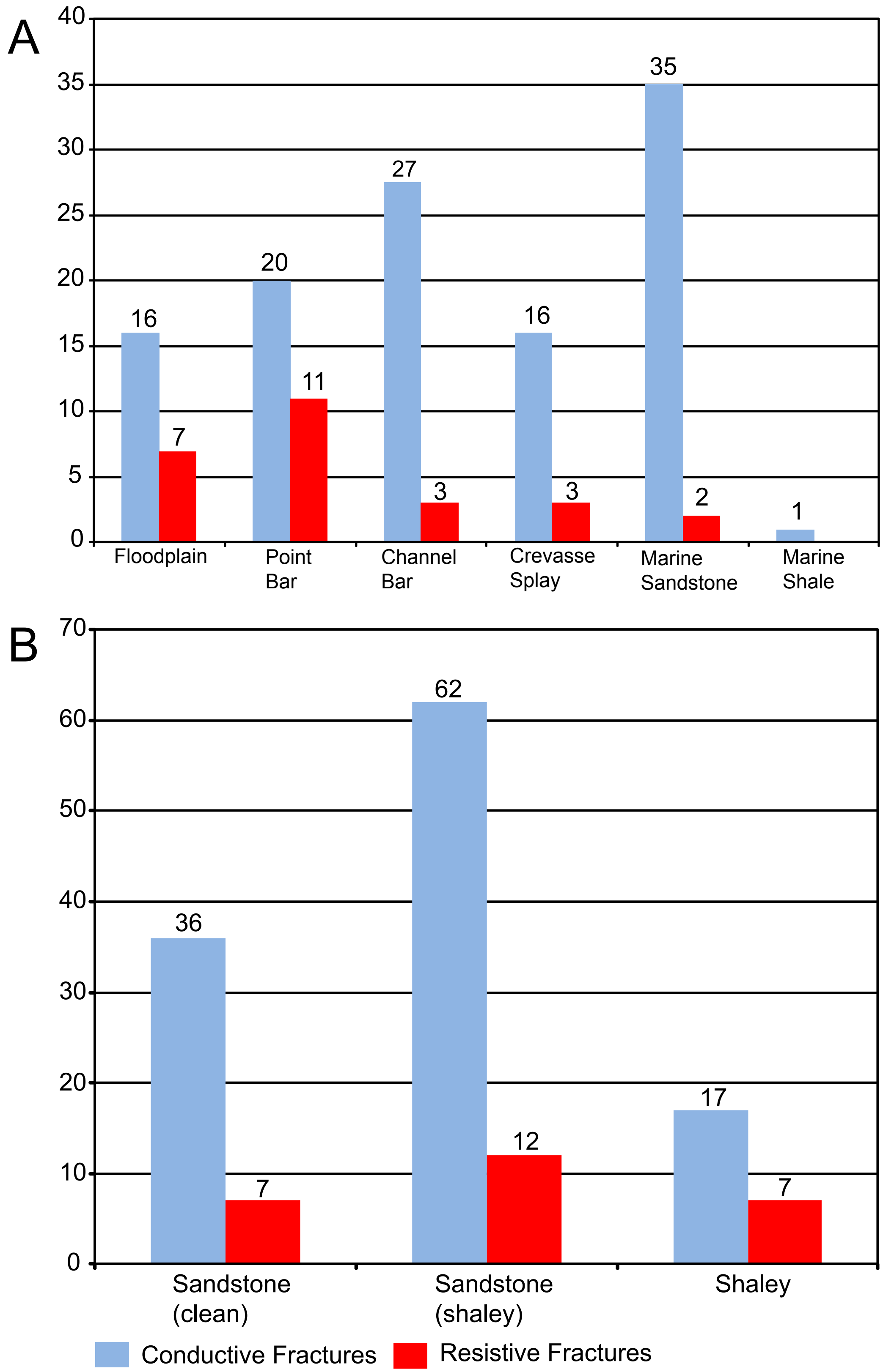

Appendix B-5. Fracture statistics for Daley 1-29. A) the number of natural fractures observed in each architectural element in this well. B) the number of natural fractures observed in each lithology type.

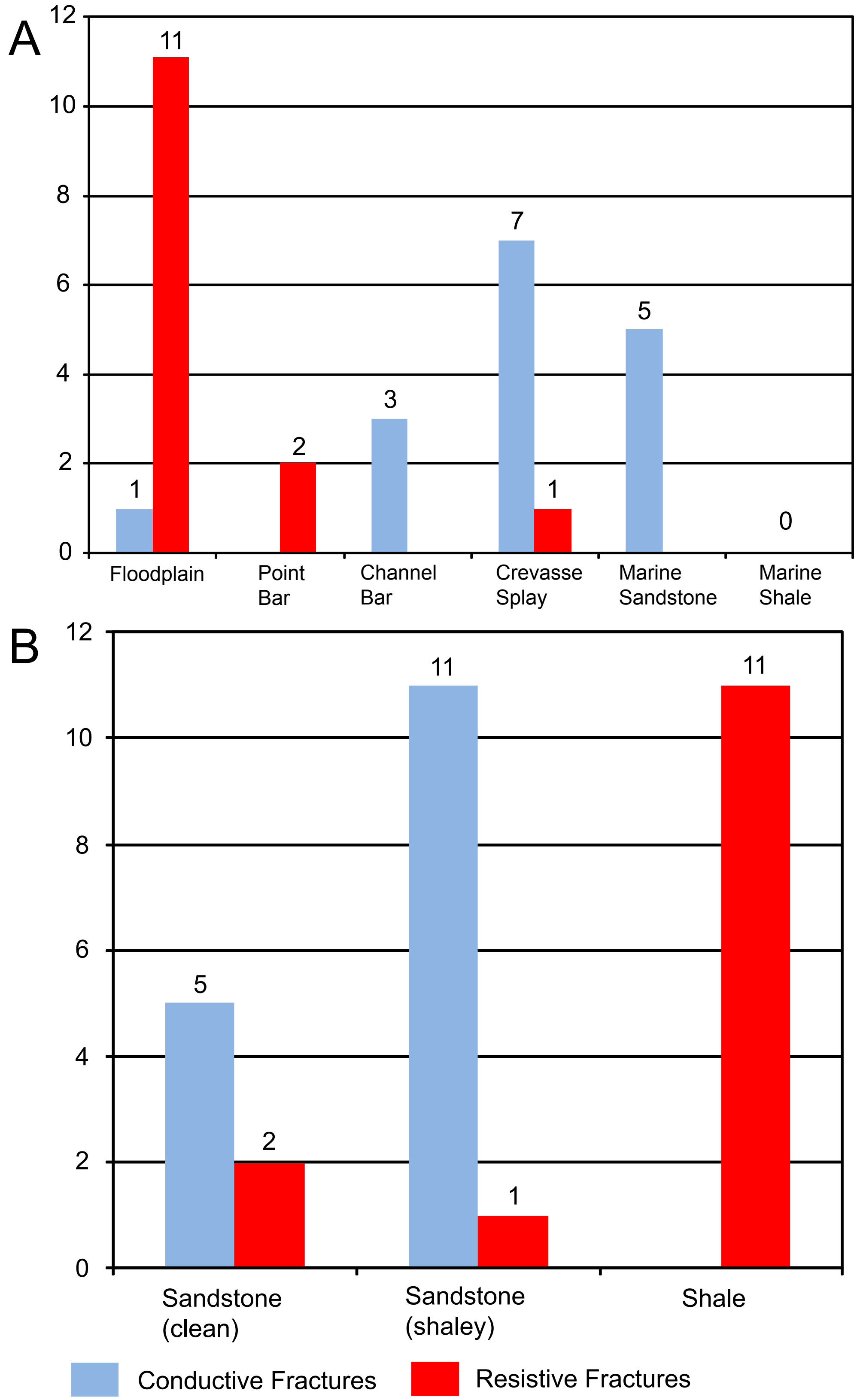

Appendix B-6. Fracture statistics for Jolley 31D-20-691. A) the number of natural fractures observed in each architectural element in this well. B) the number of natural fractures observed in each lithology type.

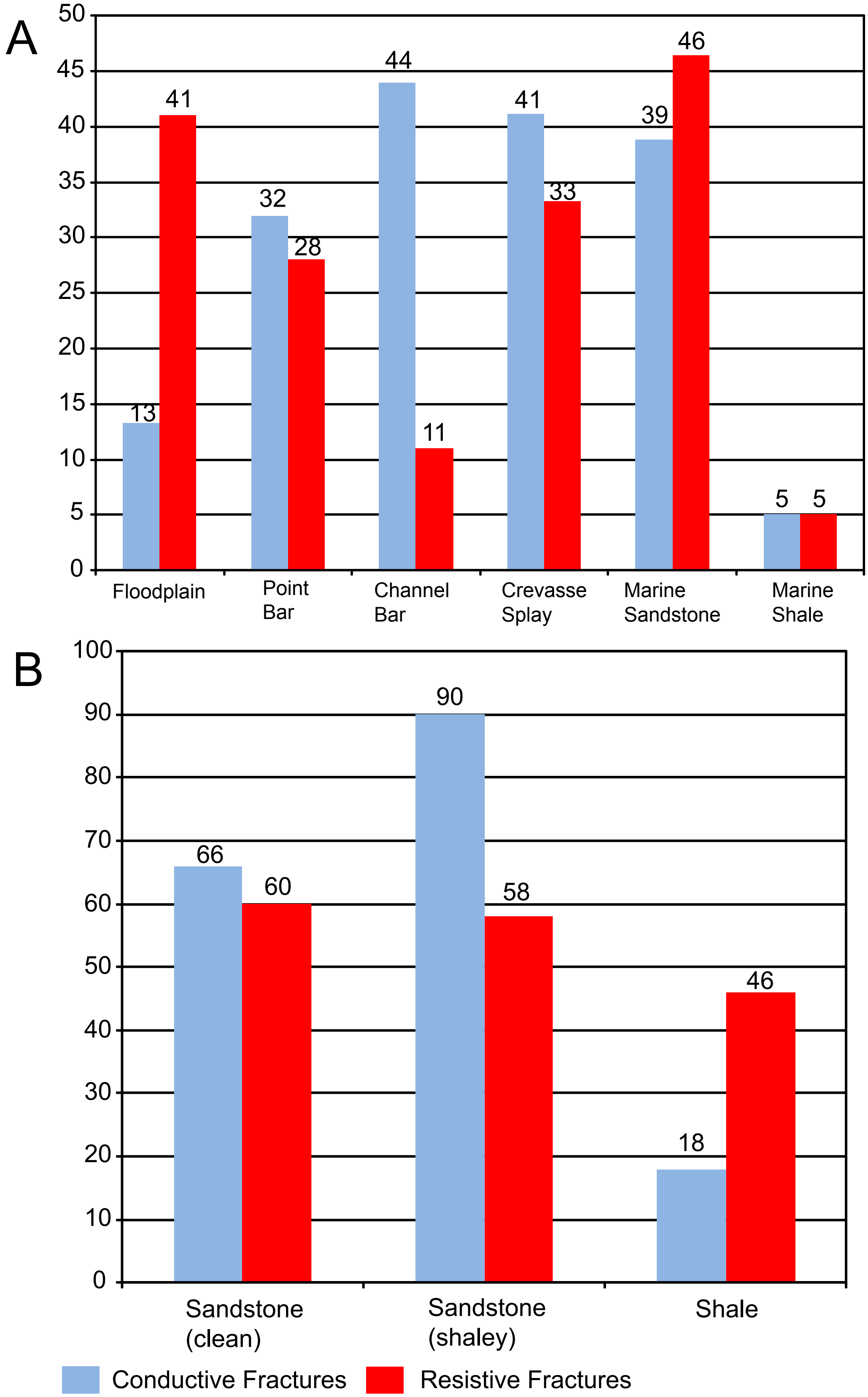

Appendix B-7. Fracture statistics for Miller 24B-6-791. A) the number of natural fractures observed in each architectural element in this well. B) the number of natural fractures observed in each lithology type.

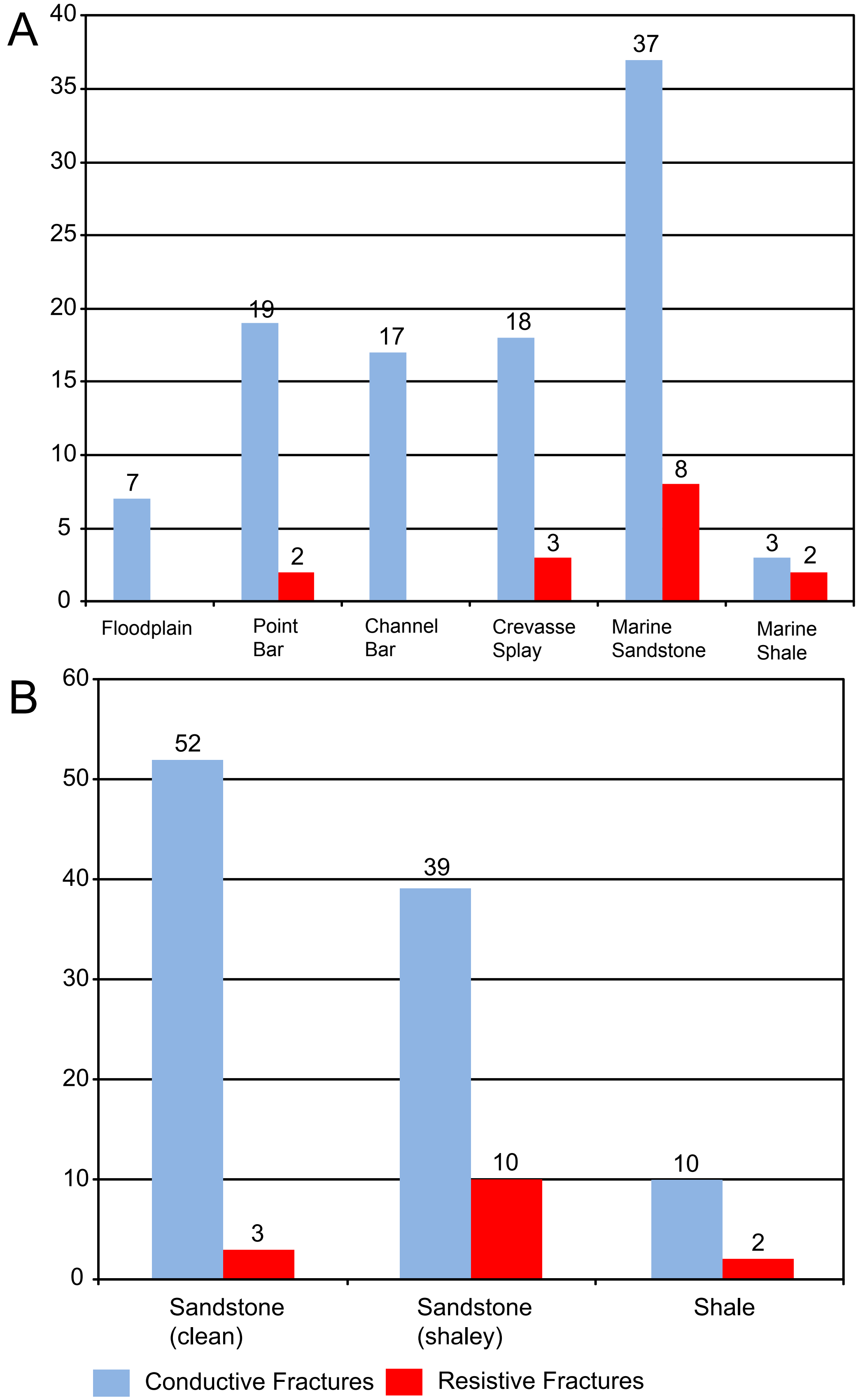

Appendix B-8. Fracture statistics for Nesbitt 13C-25-692. A) the number of natural fractures observed in each architectural element in this well. B) the number of natural fractures observed in each lithology type.

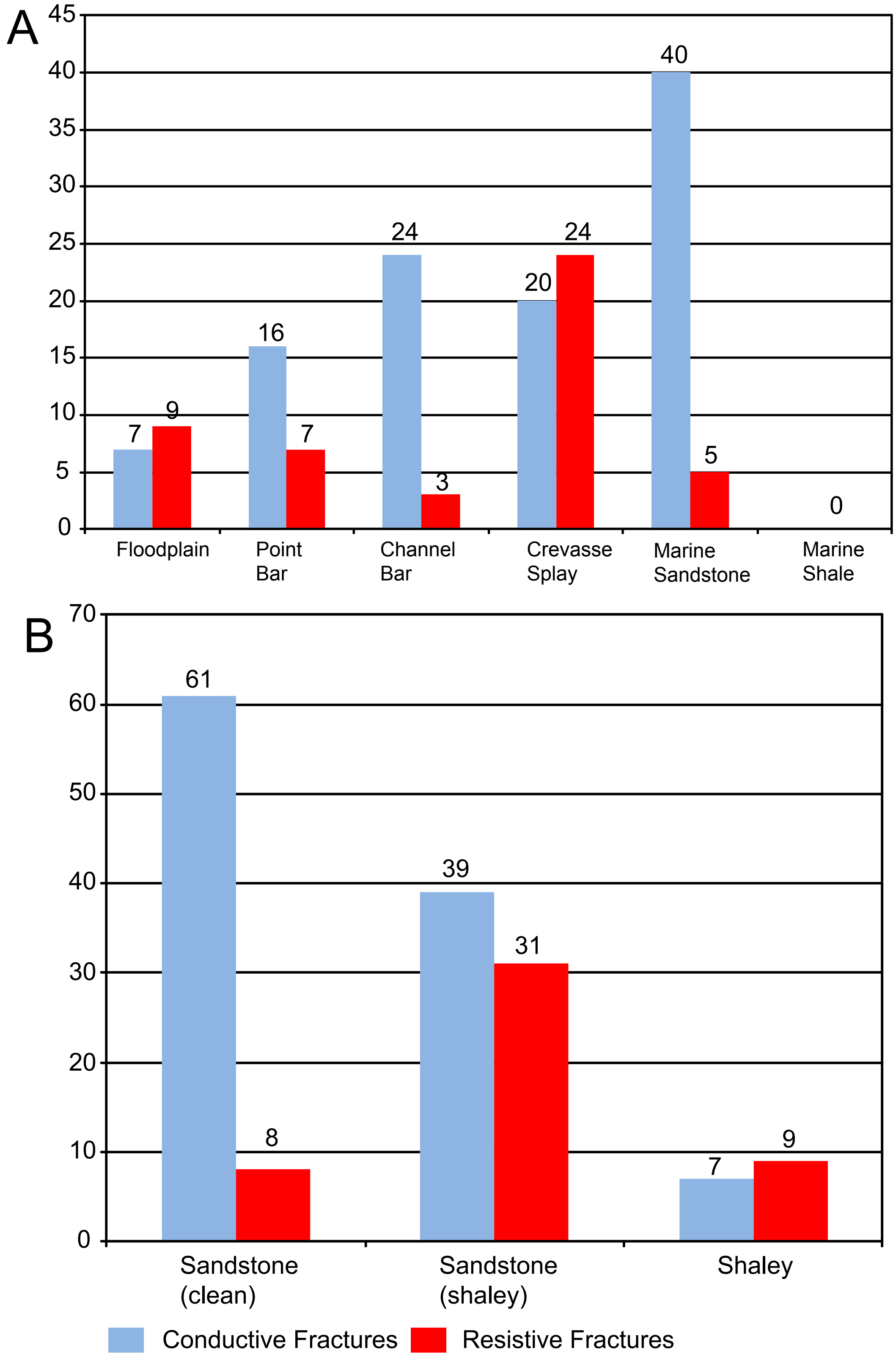

Appendix B-9. Fracture statistics for Schirer 14D-26-692. A) the number of natural fractures observed in each architectural element in this well. B) the number of natural fractures observed in each lithology type.

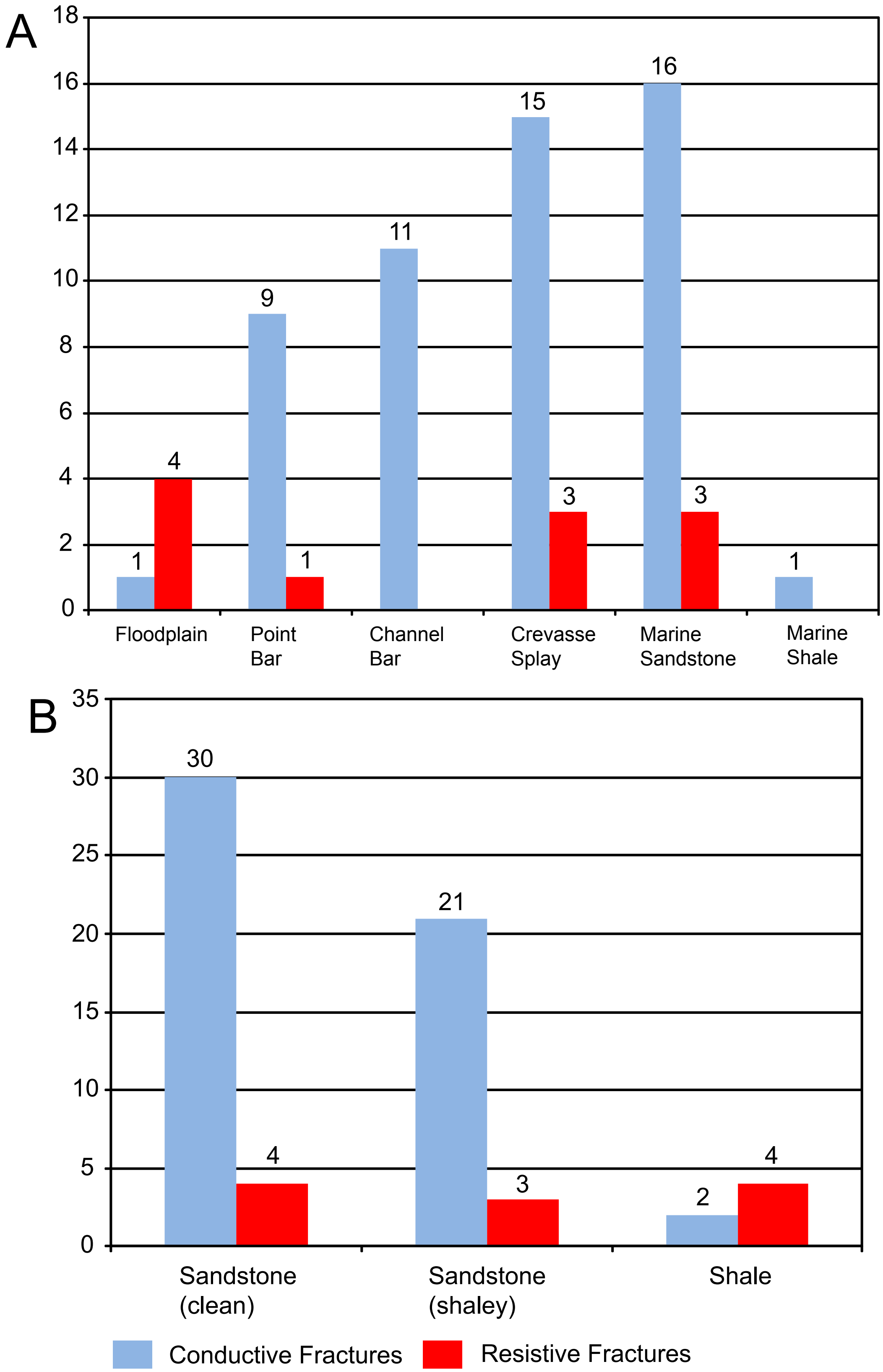

Appendix B-10. Fracture statistics for Speciality 41A-28-692. A) the number of natural fractures observed in each architectural element in this well. B) the number of natural fractures observed in each lithology type.

APPENDIX C

Appendix C contains fracture-intensity logs generated for each borehole-image log. Fracture-intensity logs were generated using a sampling rate of 1 ft (0.3 m) and a window length of 5 ft (1.5 m). In the fracture analysis part of this study, the window length was set to 100 ft (30 m).

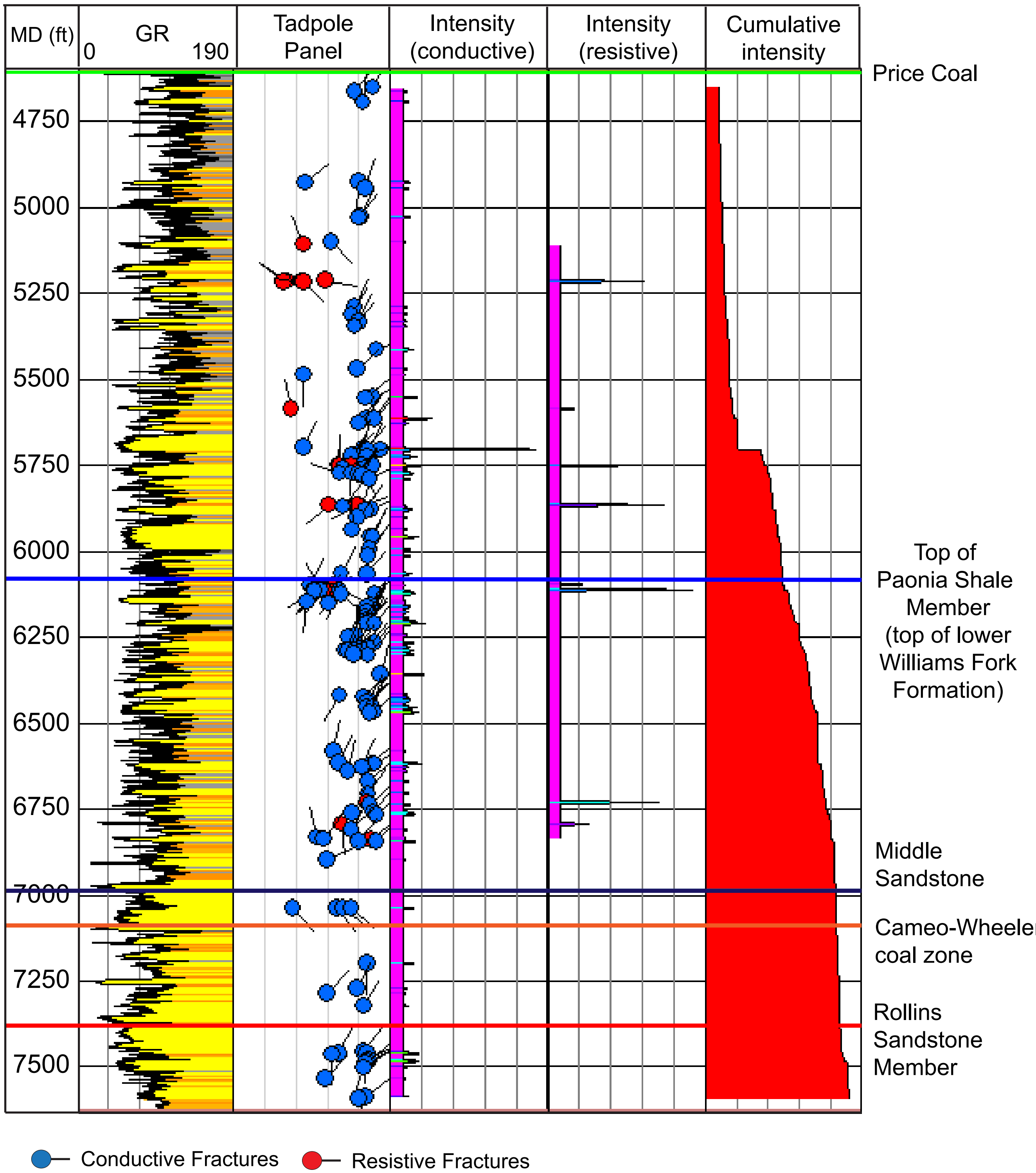

Appendix C-1. Type log for Anchondo 32B-20-692. Gamma ray log, fracture tadpoles, fracture-intensity log for conductive fractures, fracture-intensity log for resistivefractures, and cumulative fracture intensity log are given.

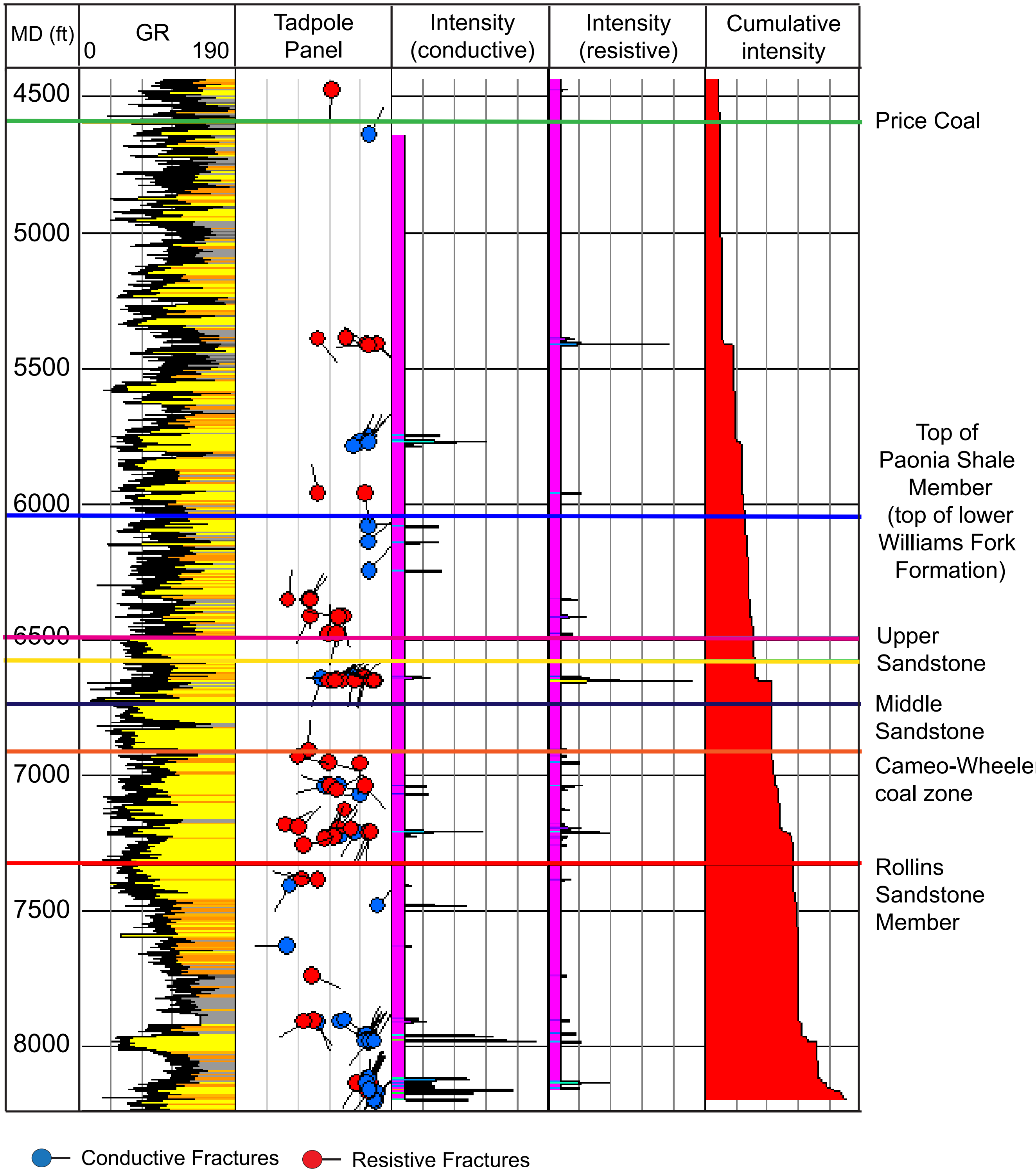

Appendix C-2. Type log for BBC 42B-23-692. Gamma ray log, fracture tadpoles, fracture-intensity log for conductive fractures, fracture-intensity log for resistivefractures, and cumulative fracture intensity log are given.

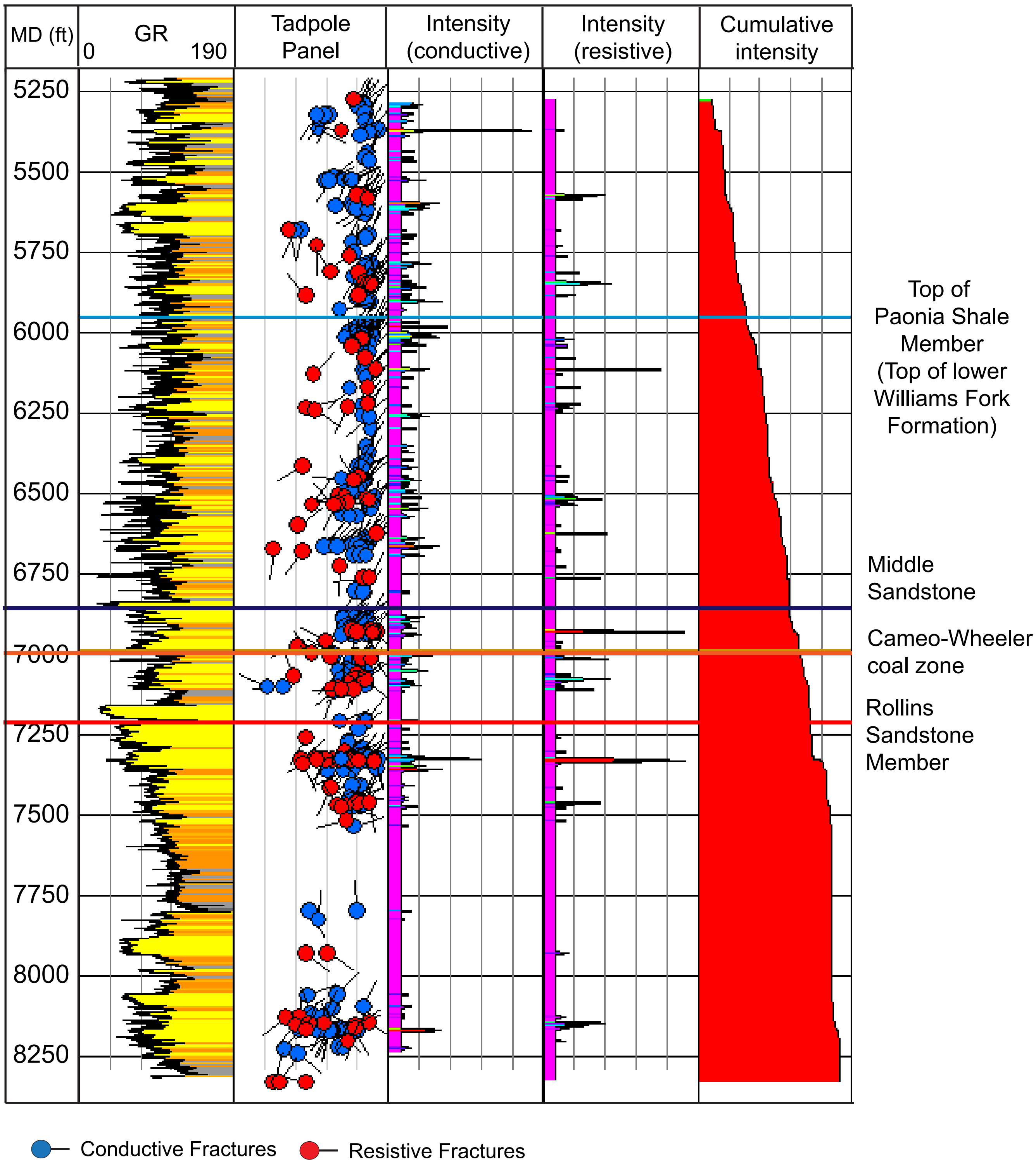

Appendix C-3. Type log for Brynildson 14C-20-692. Gamma ray log, fracture tadpoles, fracture-intensity log for conductive fractures, fracture-intensity log for resistivefractures, and cumulative fracture intensity log are given.

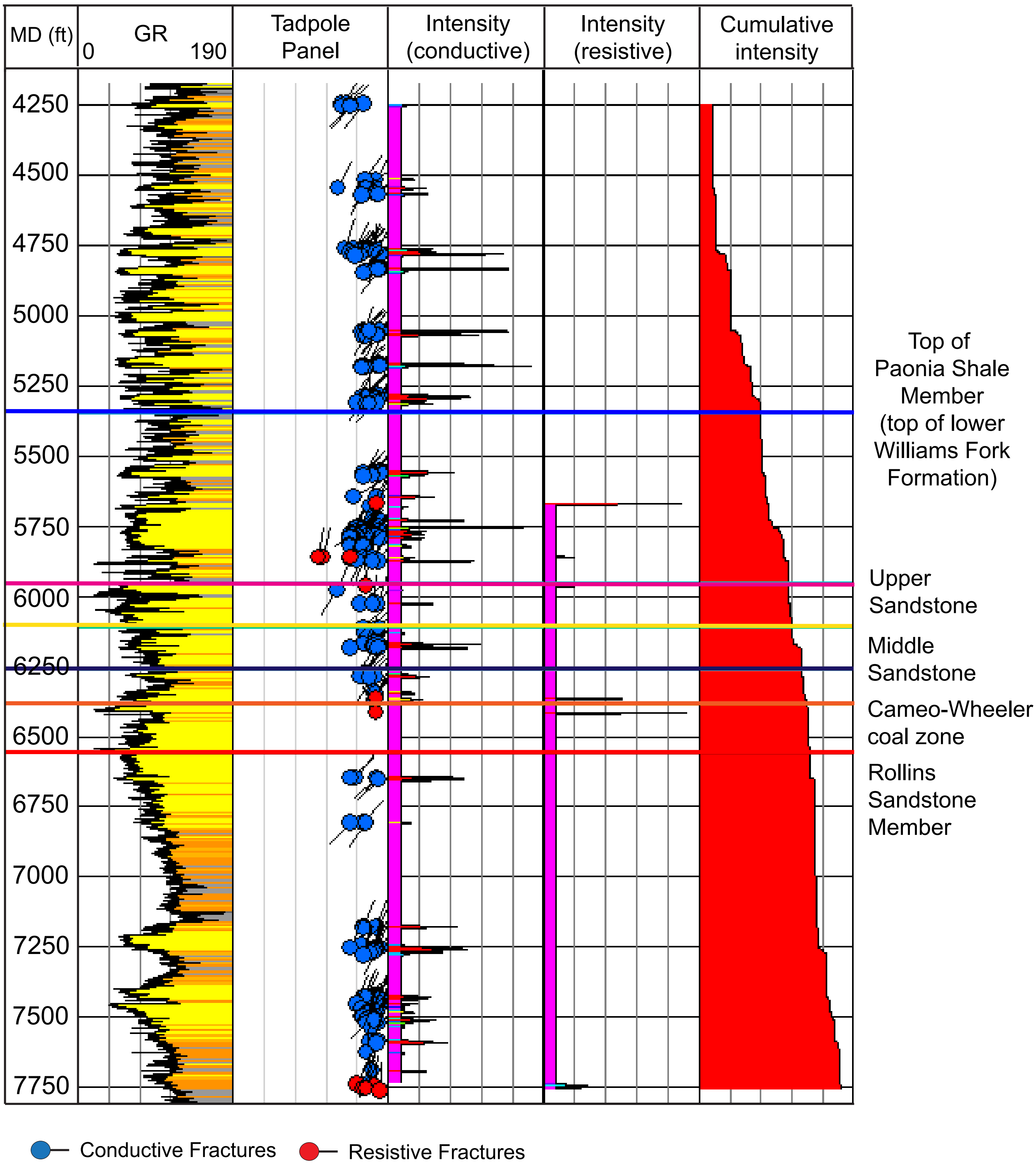

Appendix C-4. Type log for Circle B. Land 33A-35-692. Gamma ray log, fracture tadpoles, fracture-intensity log for conductive fractures, fracture-intensity log for resistivefractures, and cumulative fracture intensity log are given.

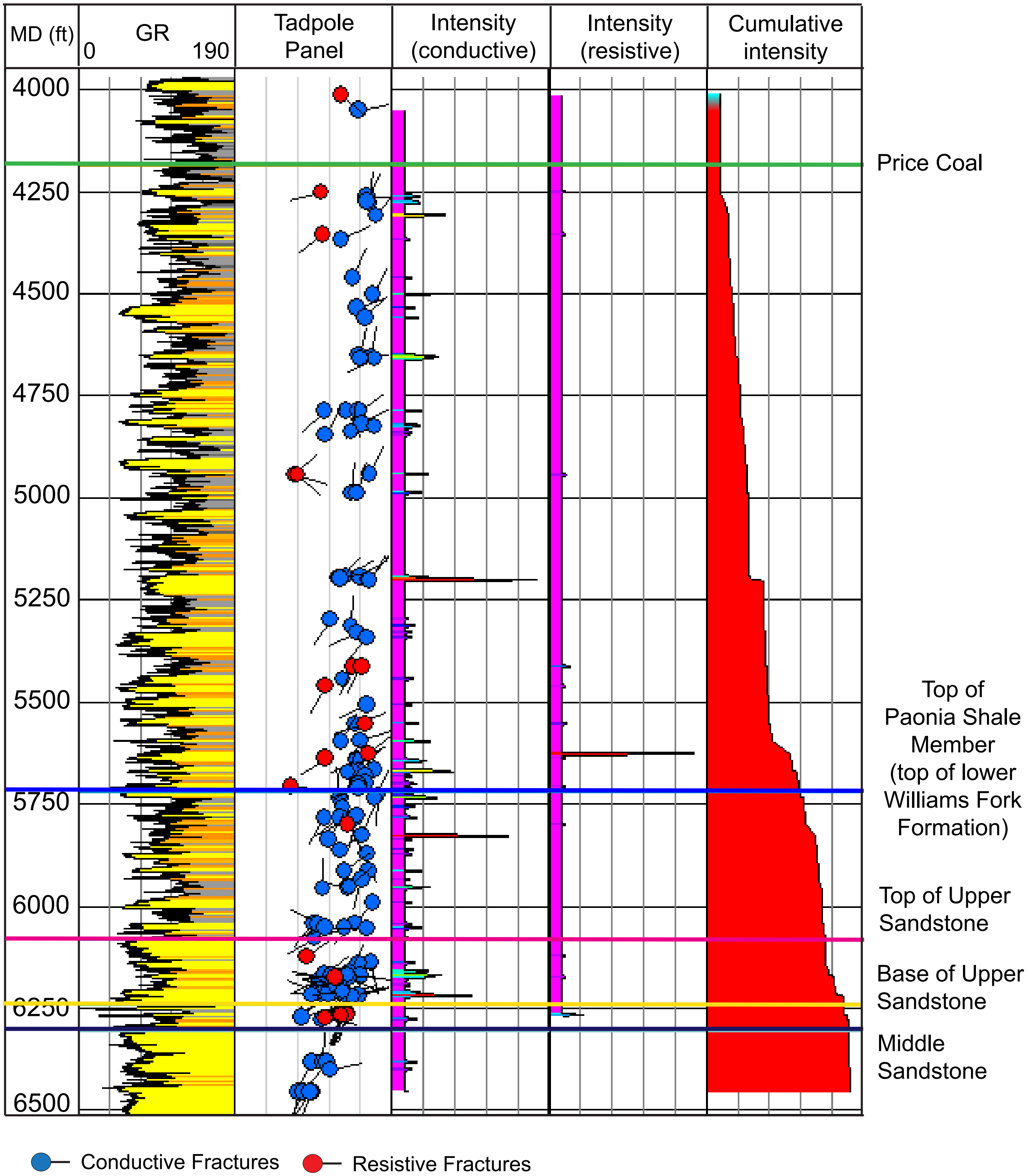

Appendix C-5. Type log for Daley 1-29. Gamma ray log, fracture tadpoles, fracture-intensity log for conductive fractures, fracture-intensity log for resistivefractures, and cumulative fracture intensity log are given.

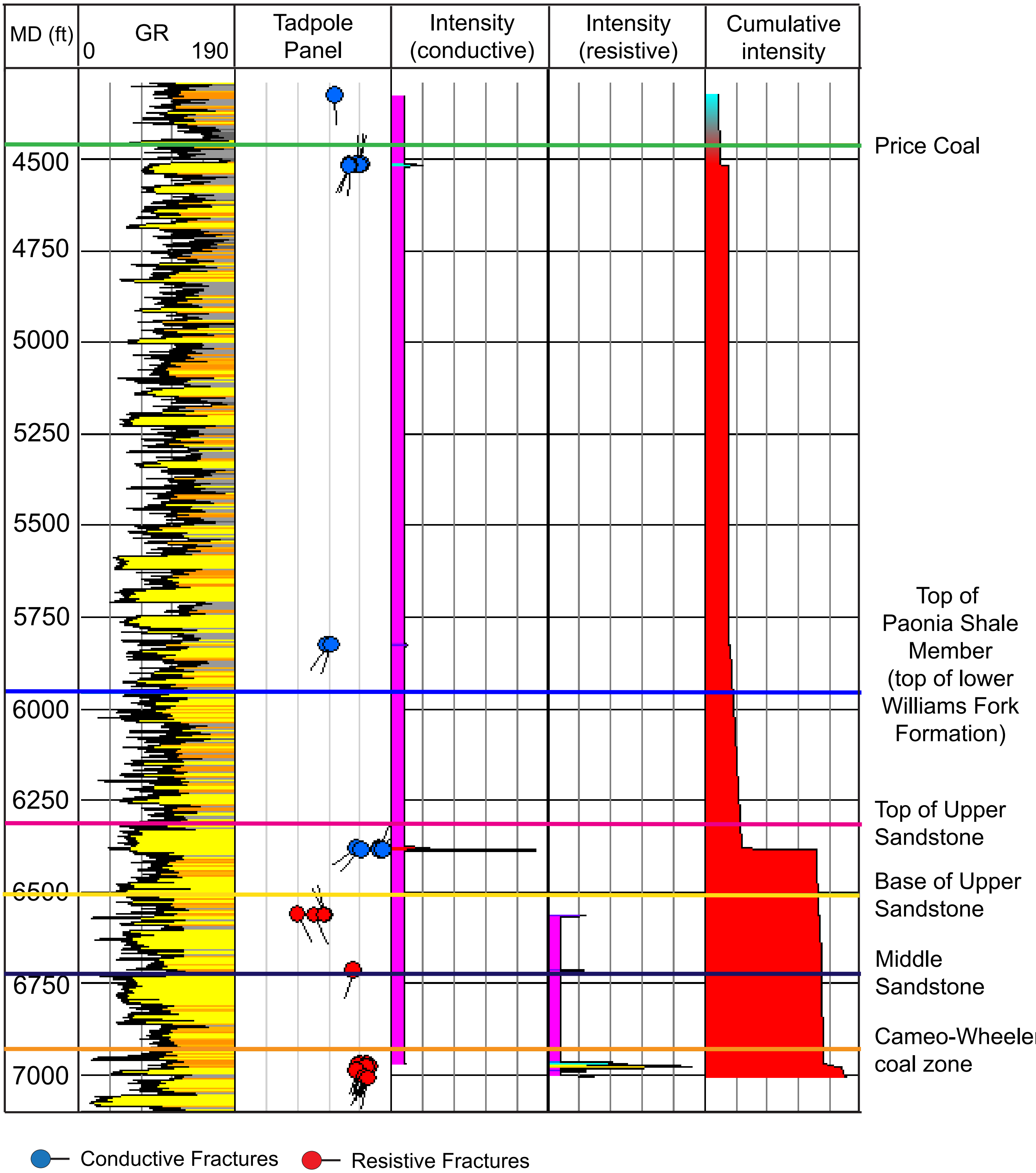

Appendix C-6. Type log for Jolley 31D-20-691. Gamma ray log, fracture tadpoles, fracture-intensity log for conductive fractures, fracture-intensity log for resistivefractures, and cumulative fracture intensity log are given.

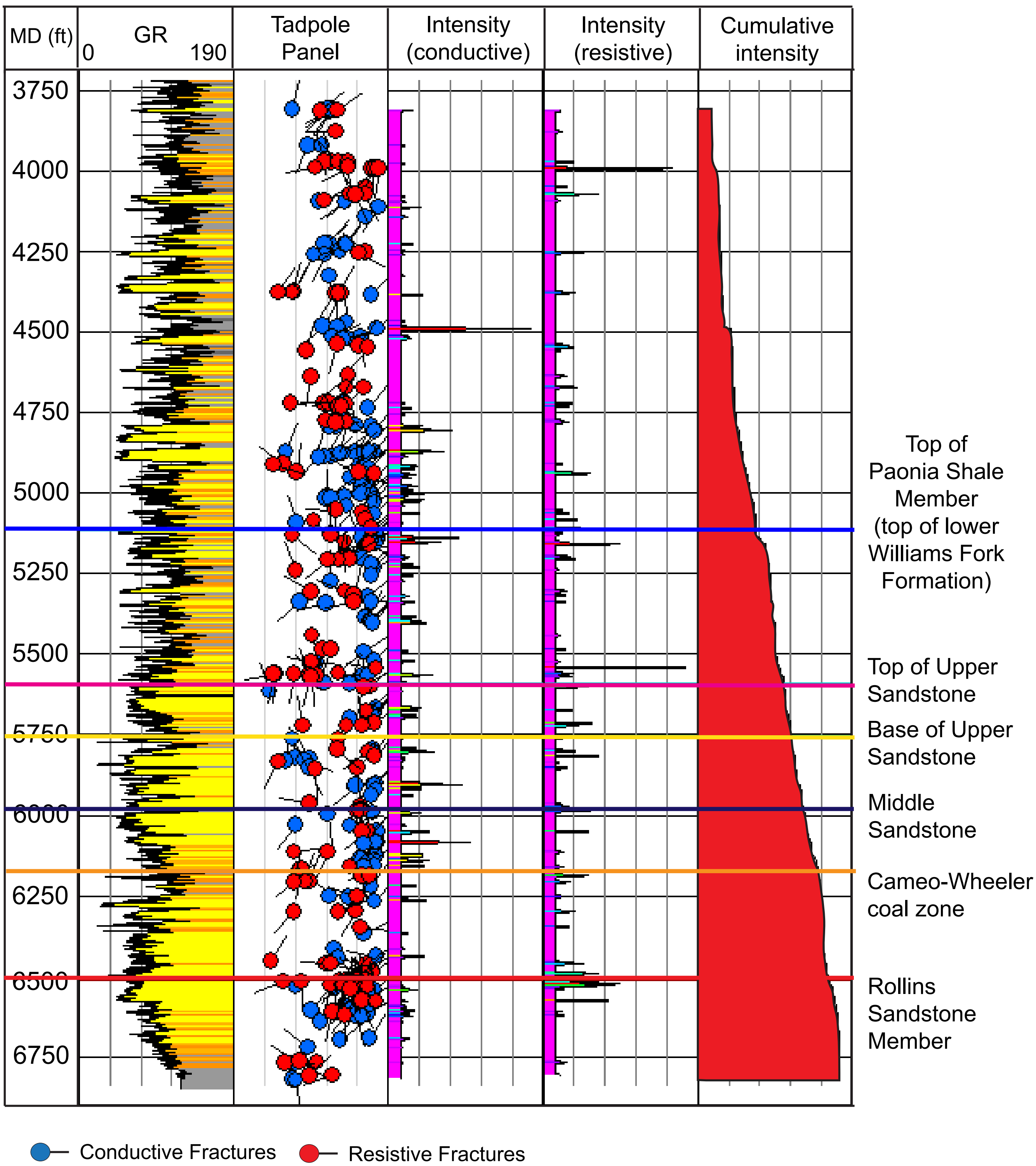

Appendix C-7. Type log for Miller 24B-6-791. Gamma ray log, fracture tadpoles, fracture-intensity log for conductive fractures, fracture-intensity log for resistivefractures, and cumulative fracture intensity log are given.

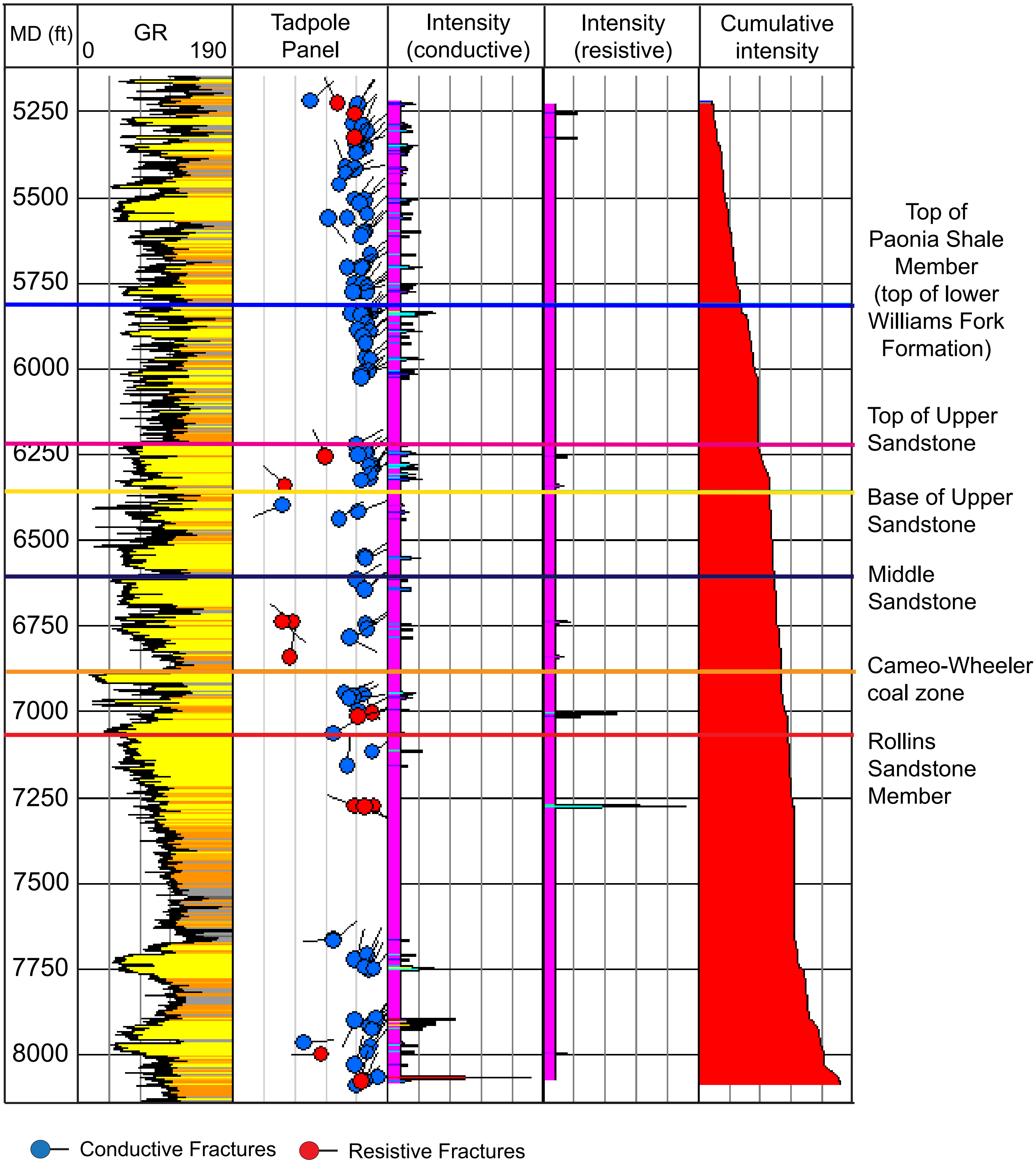

Appendix C-8. Type log for Nesbitt 13C-25-692. Gamma ray log, fracture tadpoles, fracture-intensity log for conductive fractures, fracture-intensity log for resistivefractures, and cumulative fracture intensity log are given.

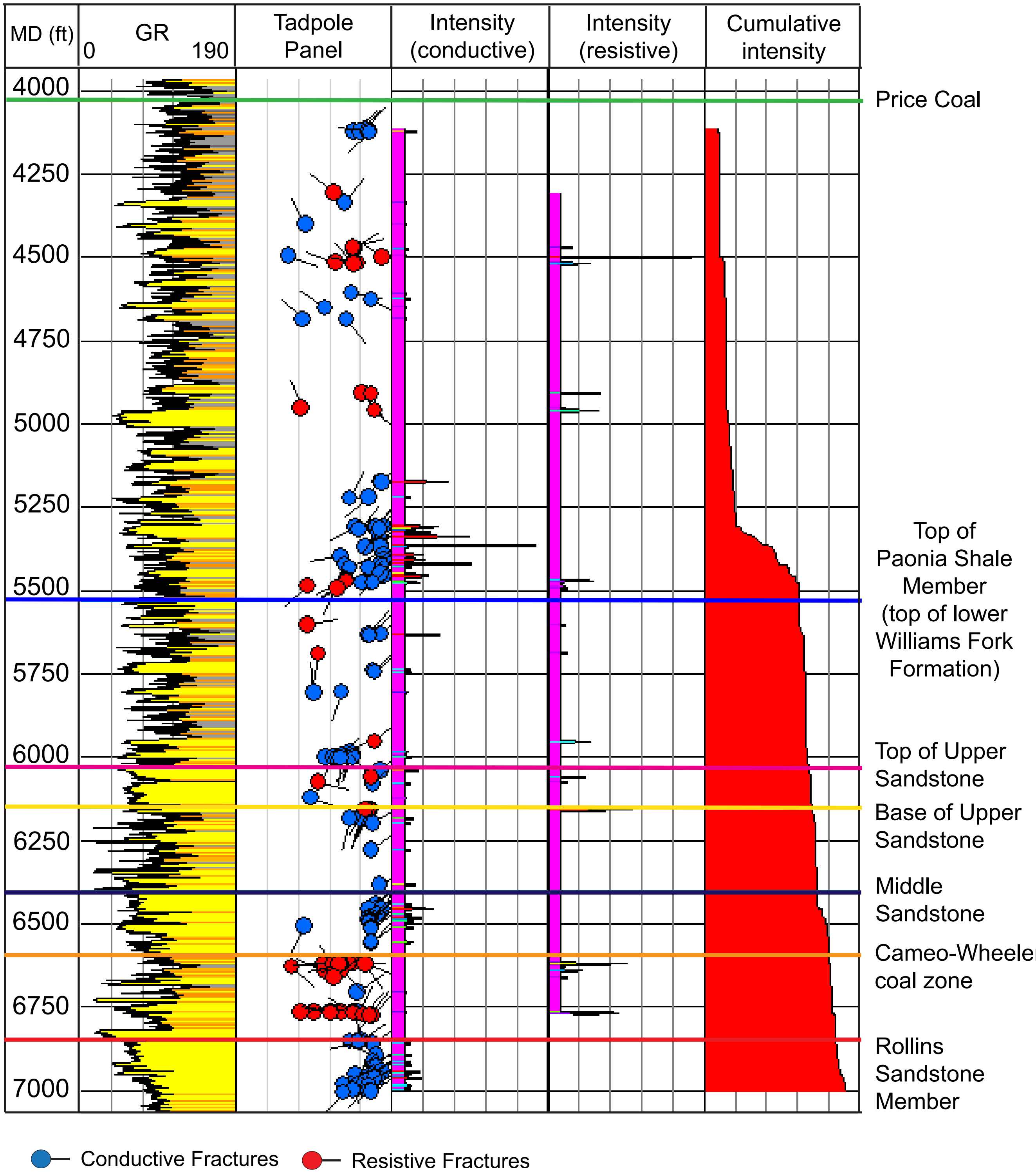

Appendix C-9. Type log for Schirer 14D-26-692. Gamma ray log, fracture tadpoles, fracture-intensity log for conductive fractures, fracture-intensity log for resistivefractures, and cumulative fracture intensity log are given.

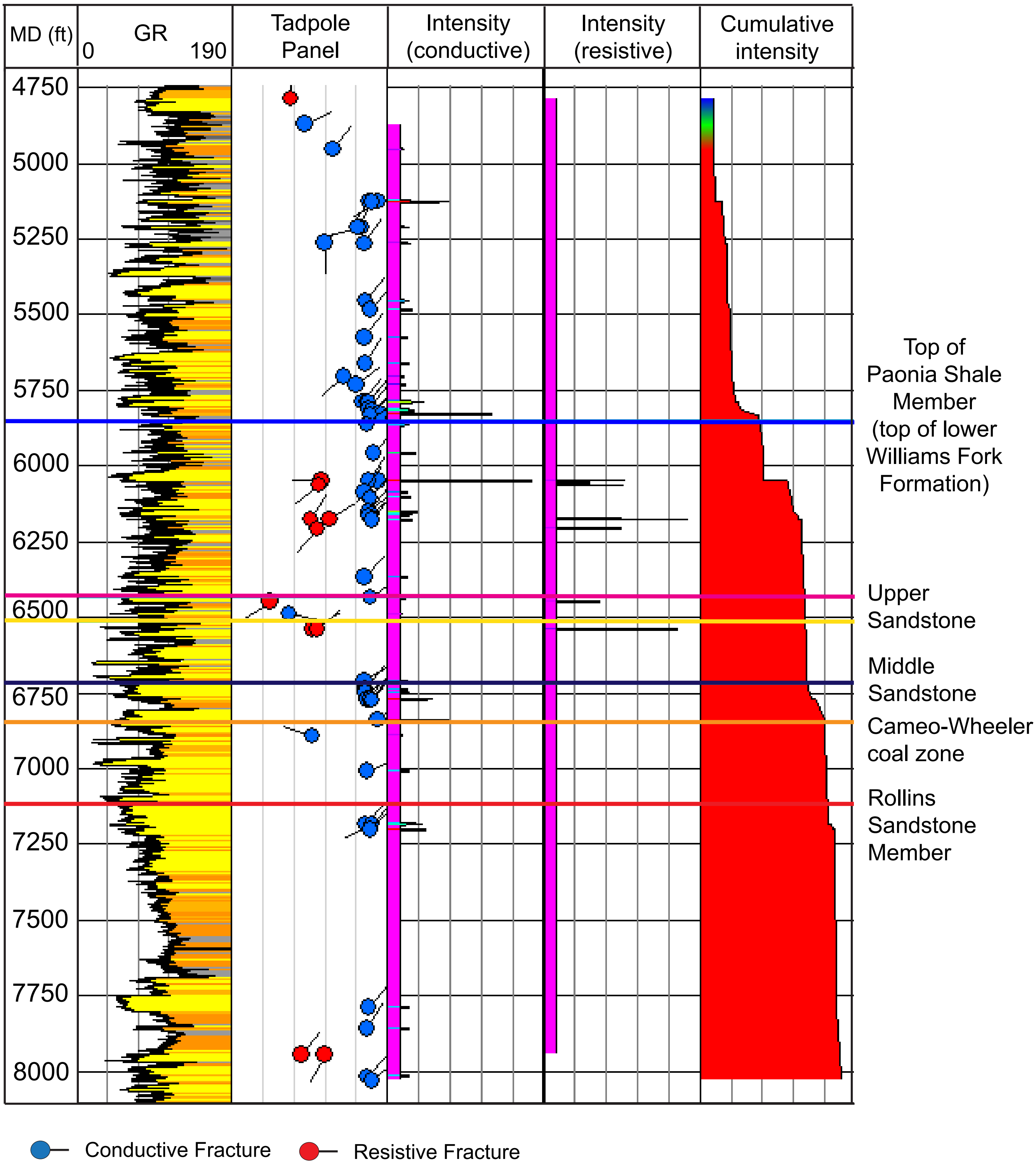

Appendix C-10. Type log for Speciality 41A-28-692. Gamma ray log, fracture tadpoles, fracture-intensity log for conductive fractures, fracture-intensity log for resistivefractures, and cumulative fracture intensity log are given.

APPENDIX D

Appendix D contains rose diagrams generated for each interval at 10 wells with respect to formation tops. Rose diagrams shows dip azimuth point data with strike presentation. Formation tops used to generate rose diagrams include (from top to bottom) Price Coal, base of middle Williams Fork Formation (also referred to as top of Paonia Shale Member and top lower Williams Fork Formation), top of Upper Sandstone (also referred to as top of Bowie Shale Member), base of Upper Sandstone, top of Middle Sandstone, top of Cameo-Wheeler coal zone, and top of Rollins Sandstone Member.

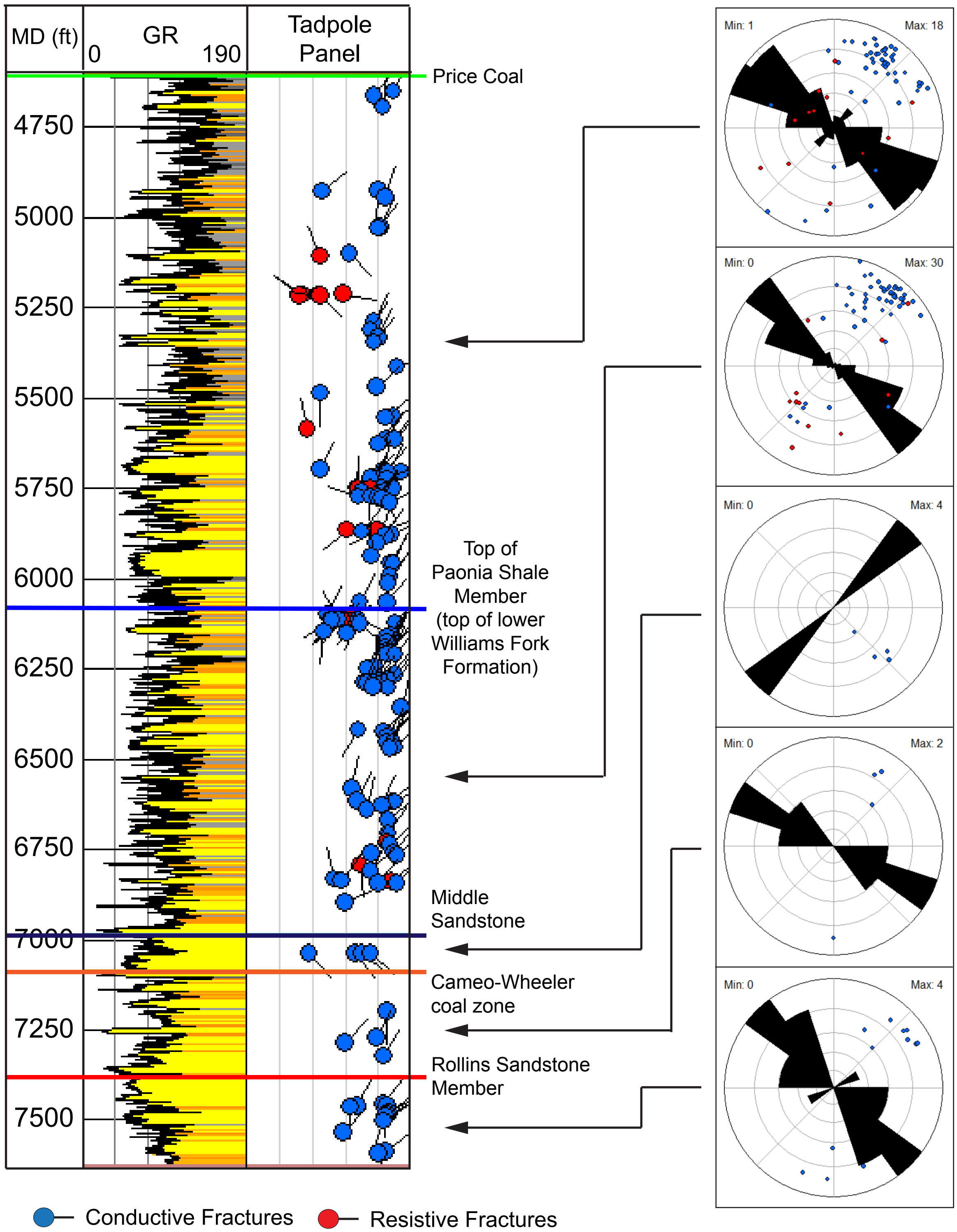

Appendix D-1. Type log for Anchondo 32B-20-692 and rose diagrams for each interval with respect to formation tops. Rose diagrams show dip azimuth point data for each fracture and strike orientation represents.

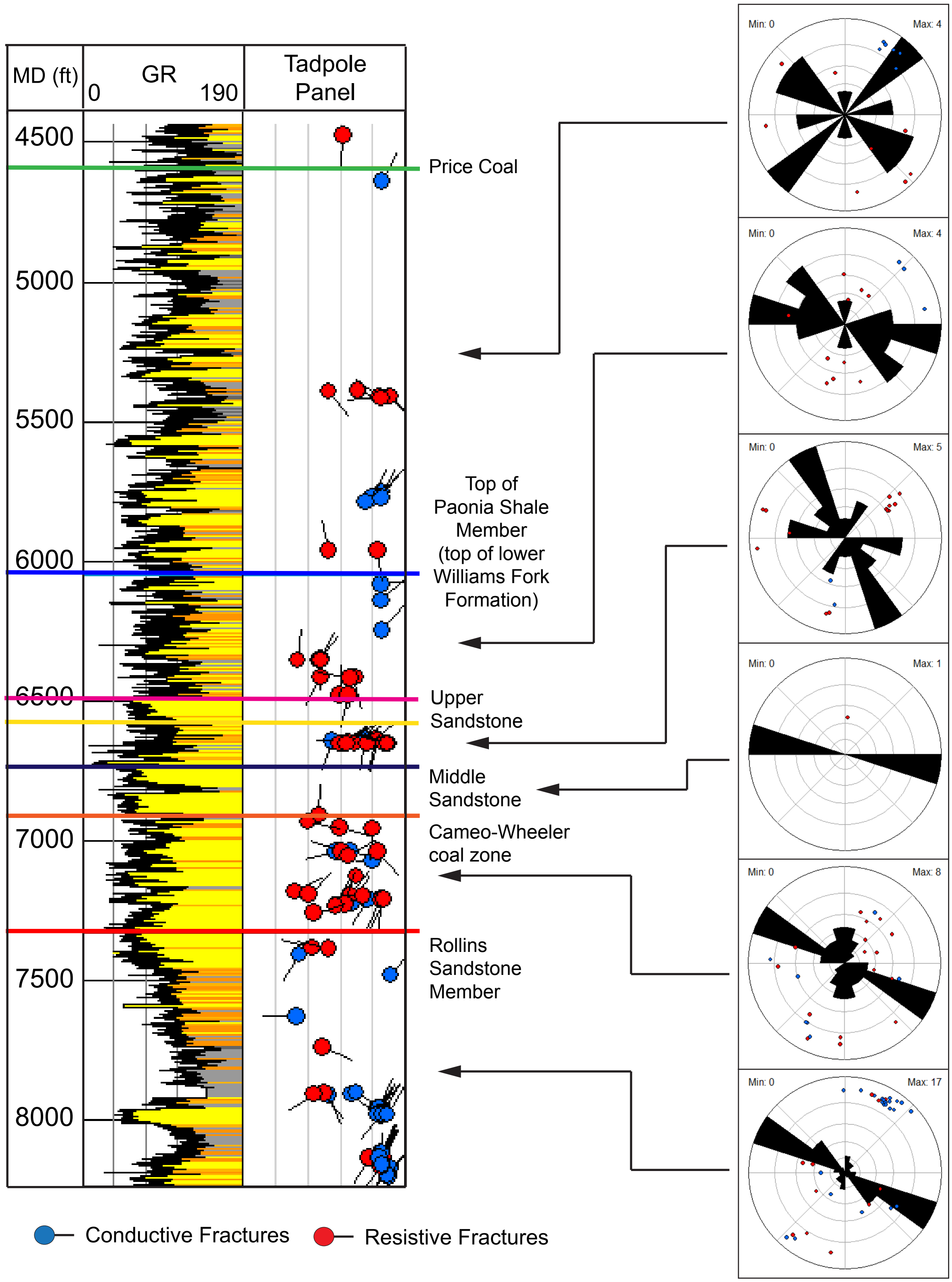

Appendix D-2. Type log for BBC 42B-23-692 and rose diagrams for each interval with respect to formation tops. Rose diagrams show dip azimuth point data for each fracture and strike orientation represents.

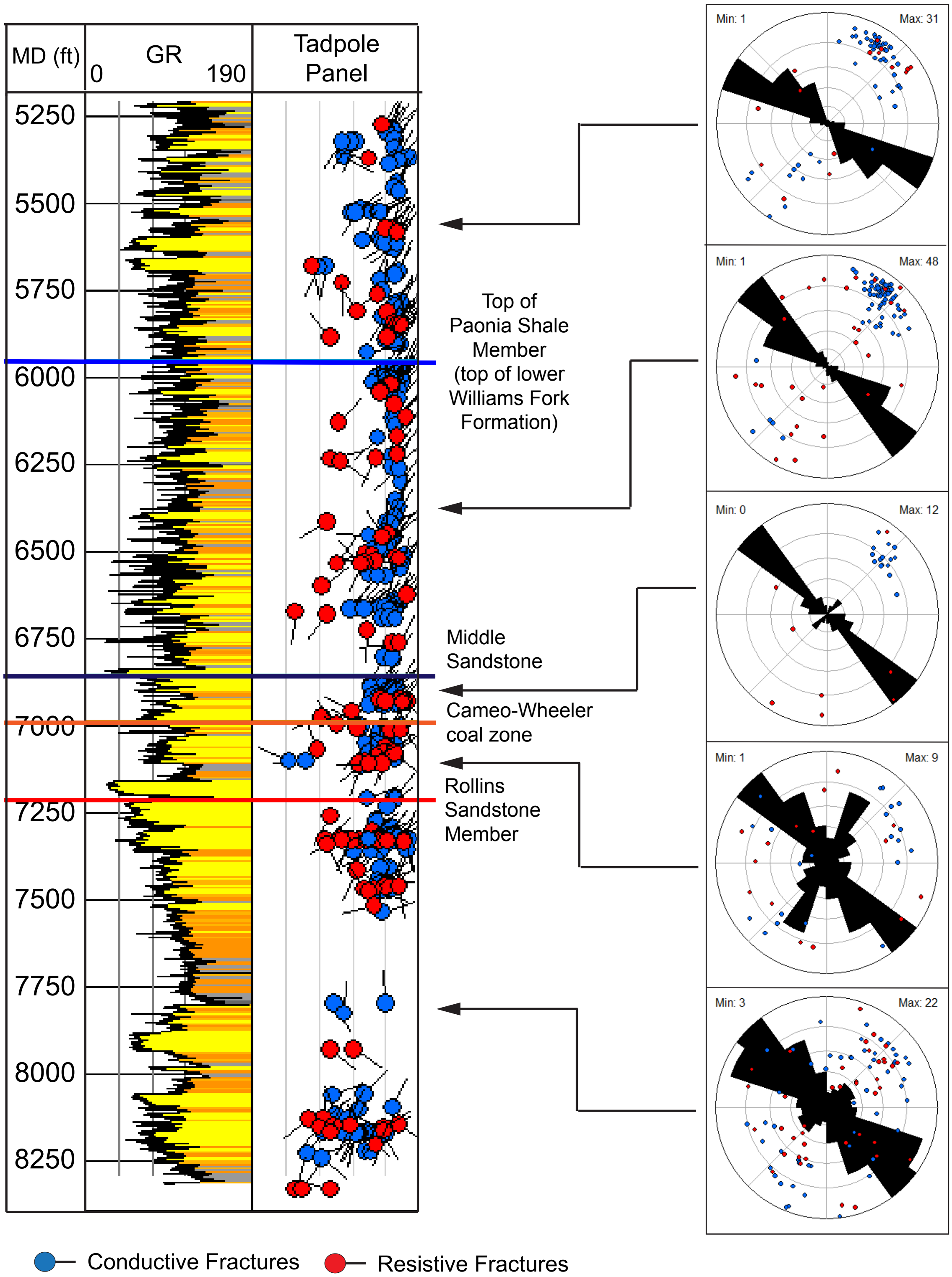

Appendix D-3. Type log for Brynildson 14C-20-692 and rose diagrams for each interval with respect to formation tops. Rose diagrams show dip azimuth point data for each fracture and strike orientation represents.

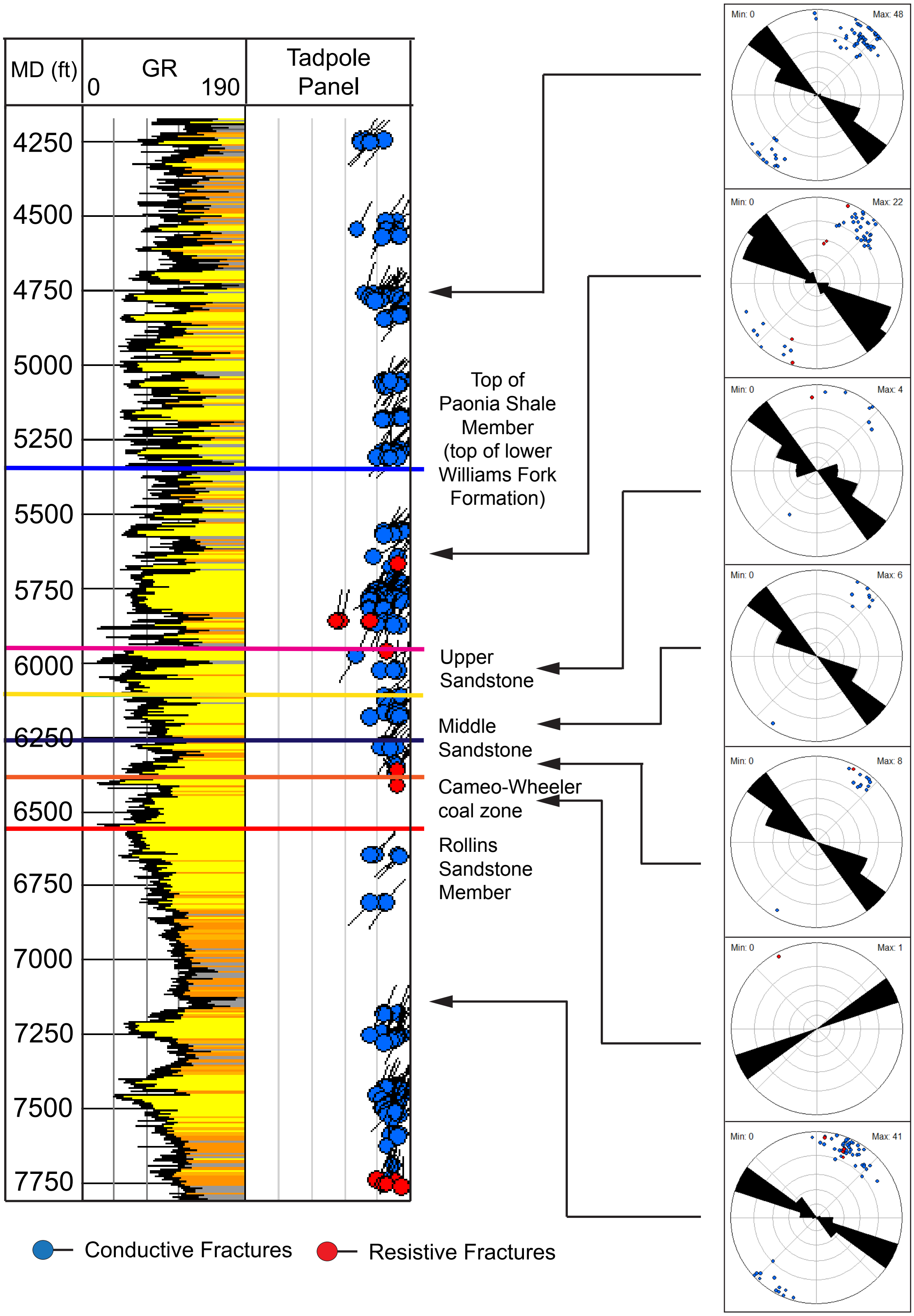

Appendix D-4. Type log for Circle B. Land 33A-35-692 and rose diagrams for each interval with respect to formation tops. Rose diagrams show dip azimuth point data for each fracture and strike orientation represents.

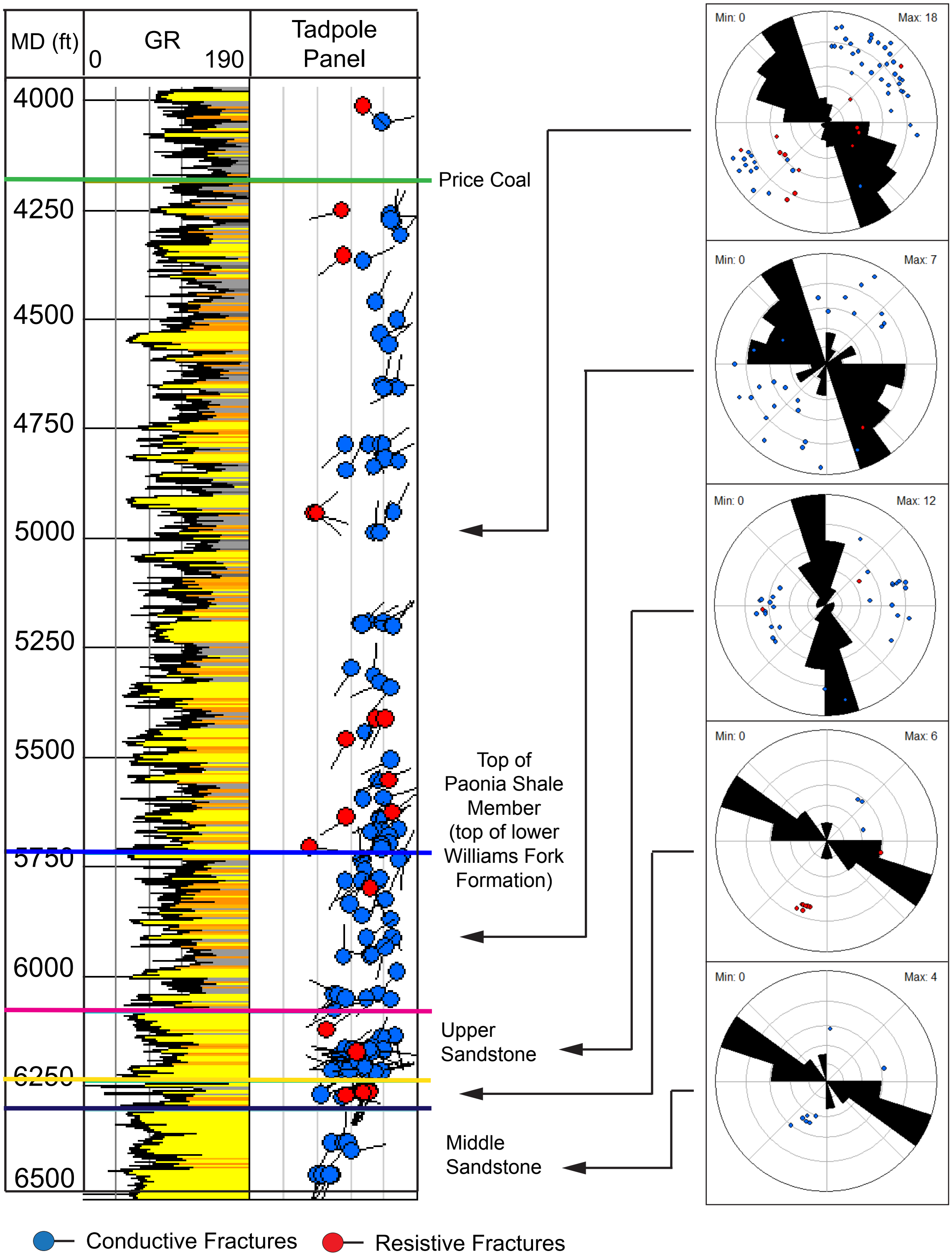

Appendix D-5. Type log for Daley 1-29 and rose diagrams for each interval with respect to formation tops. Rose diagrams show dip azimuth point data for each fracture and strike orientation represents.

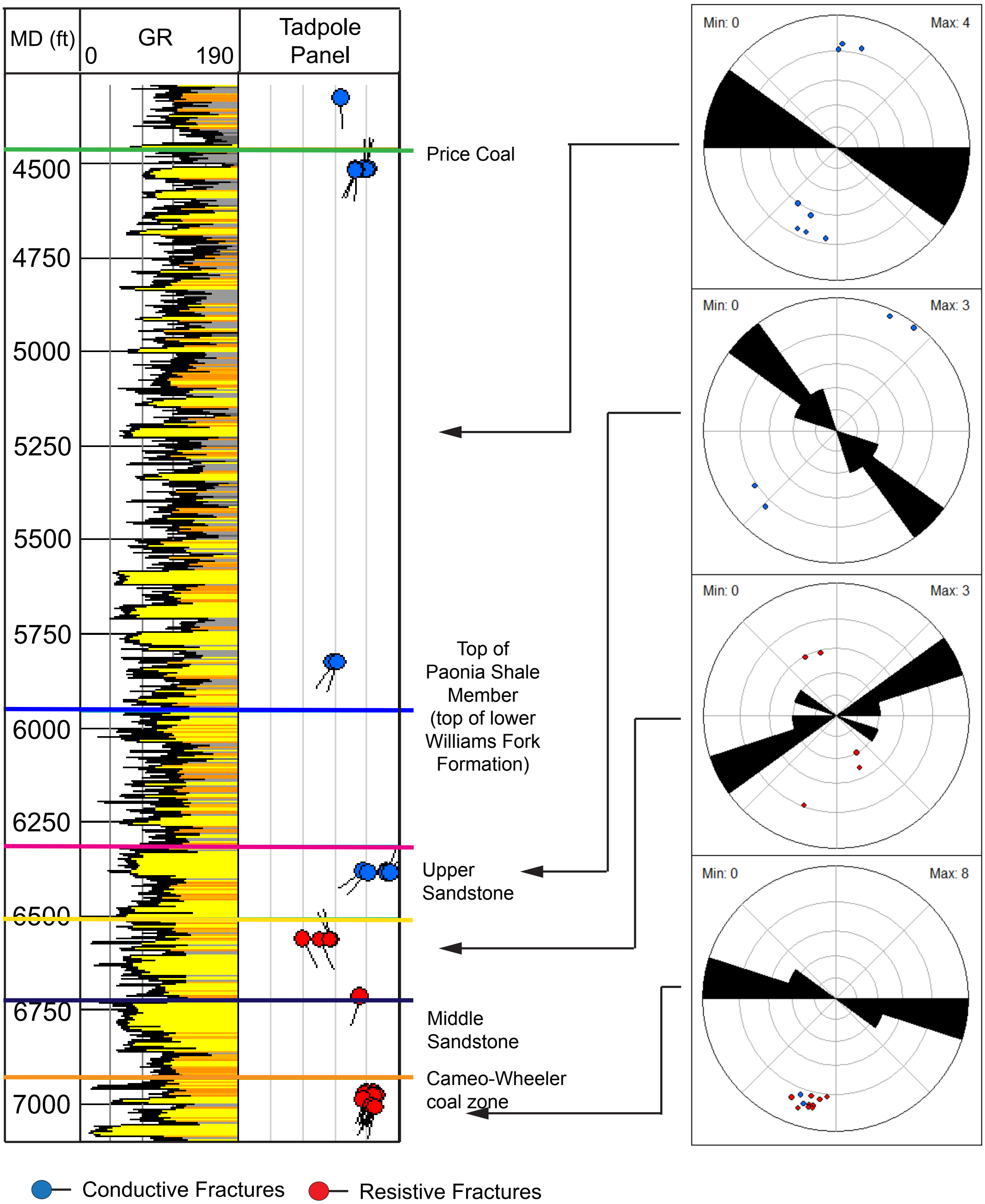

Appendix D-6. Type log for Jolley 31D-20-691 and rose diagrams for each interval with respect to formation tops. Rose diagrams show dip azimuth point data for each fracture and strike orientation represents.

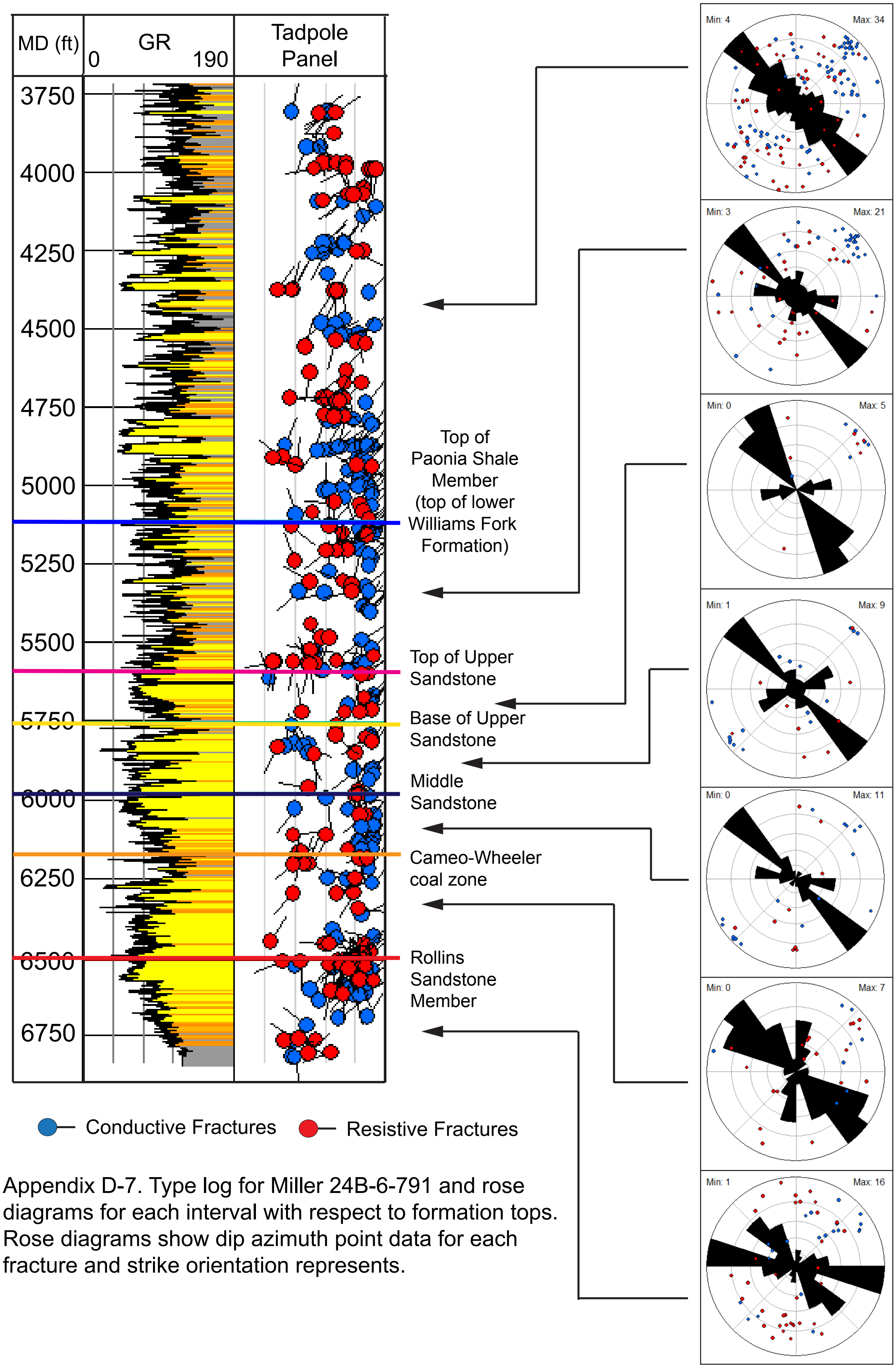

Appendix D-7. Type log for Miller 24B-6-791 and rose diagrams for each interval with respect to formation tops. Rose diagrams show dip azimuth point data for each fracture and strike orientation represents.

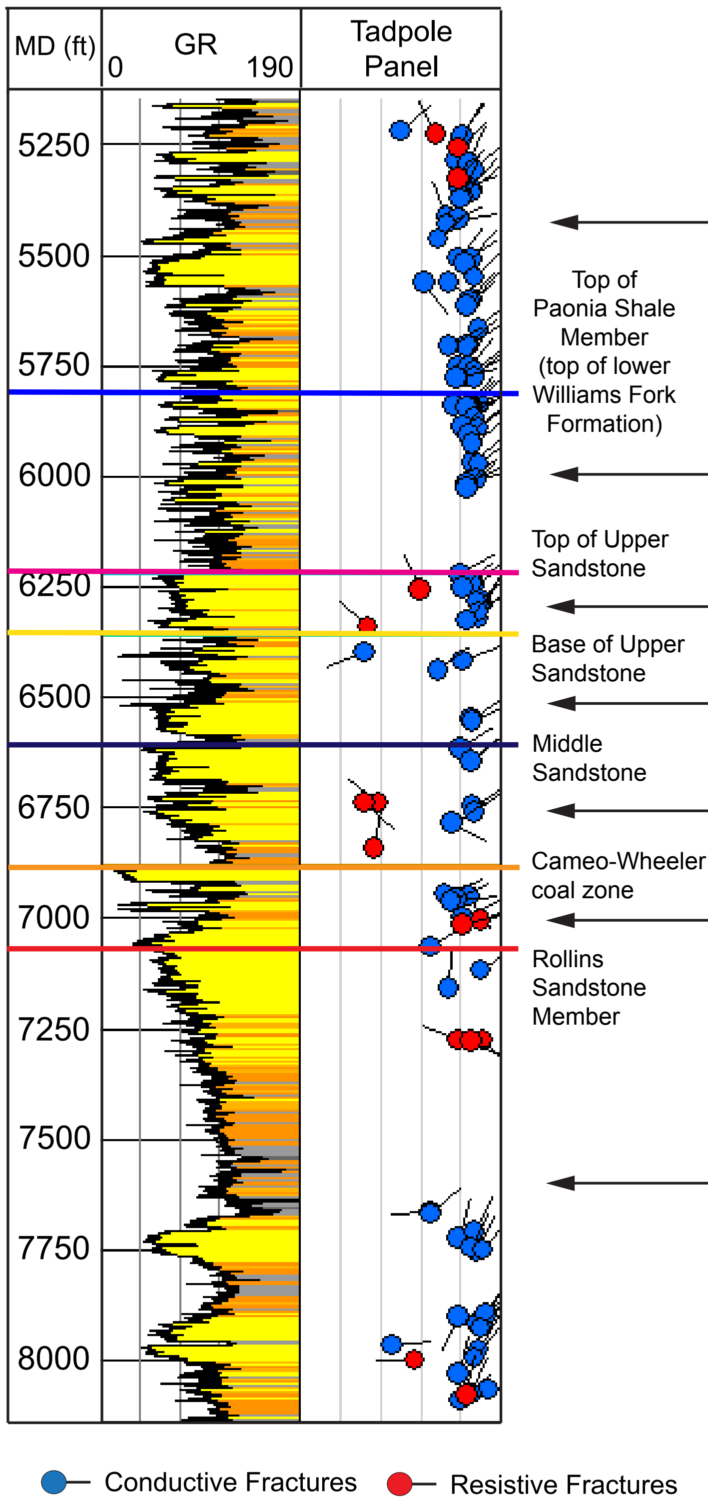

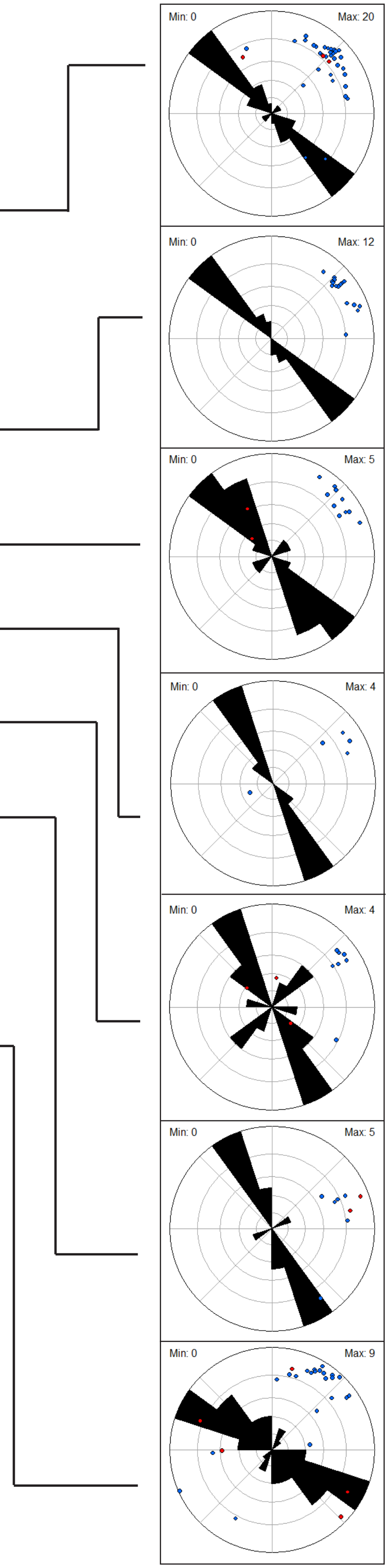

Appendix D-8. Type log for Nesbitt 13C-25-692 and rose diagrams for each interval with respect to formation tops. Rose diagrams show dip azimuth point data for each fracture and strike orientation represents.

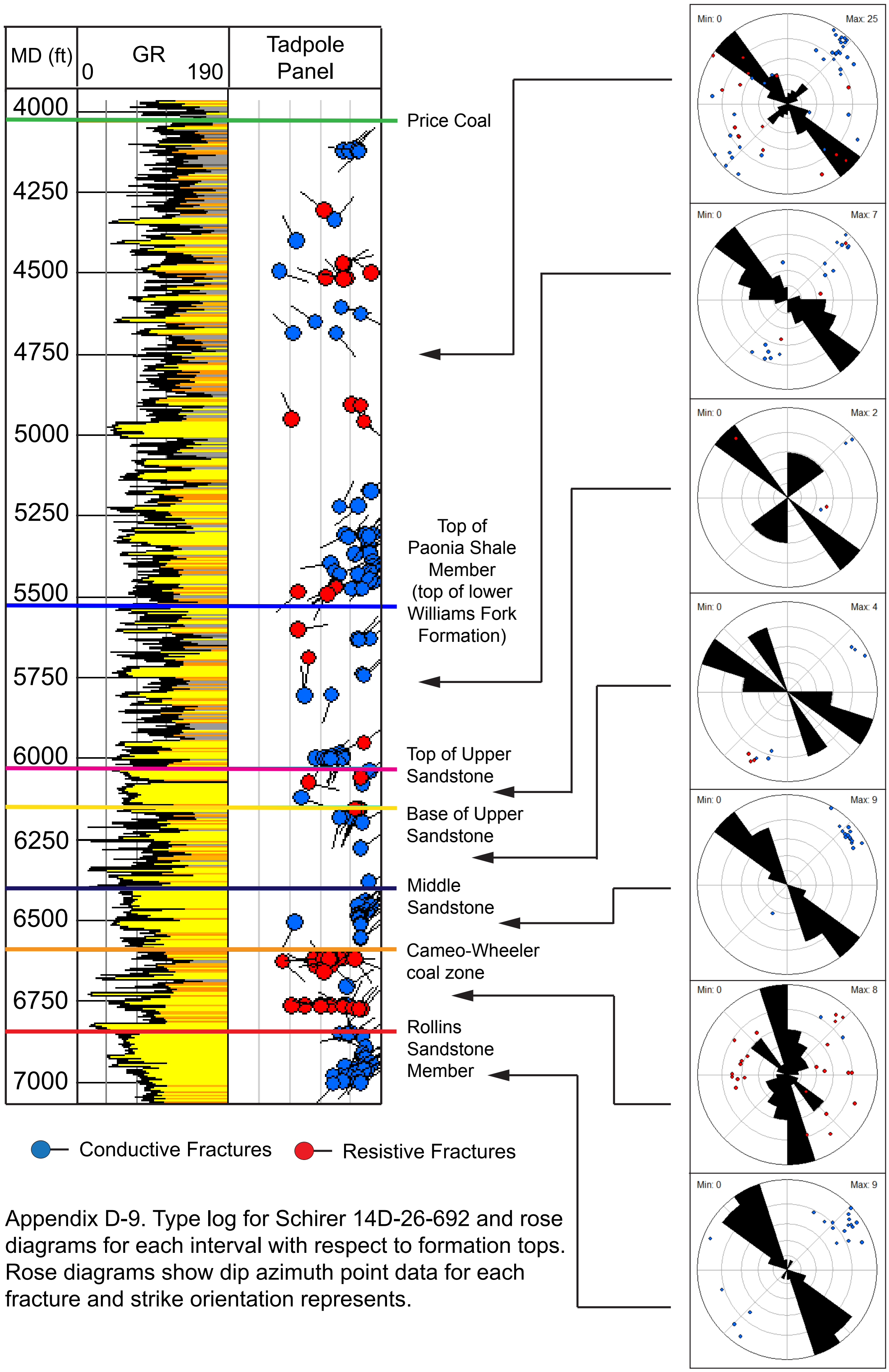

Appendix D-9. Type log for Schirer 14D-26-692 and rose diagrams for each interval with respect to formation tops. Rose diagrams show dip azimuth point data for each fracture and strike orientation represents.

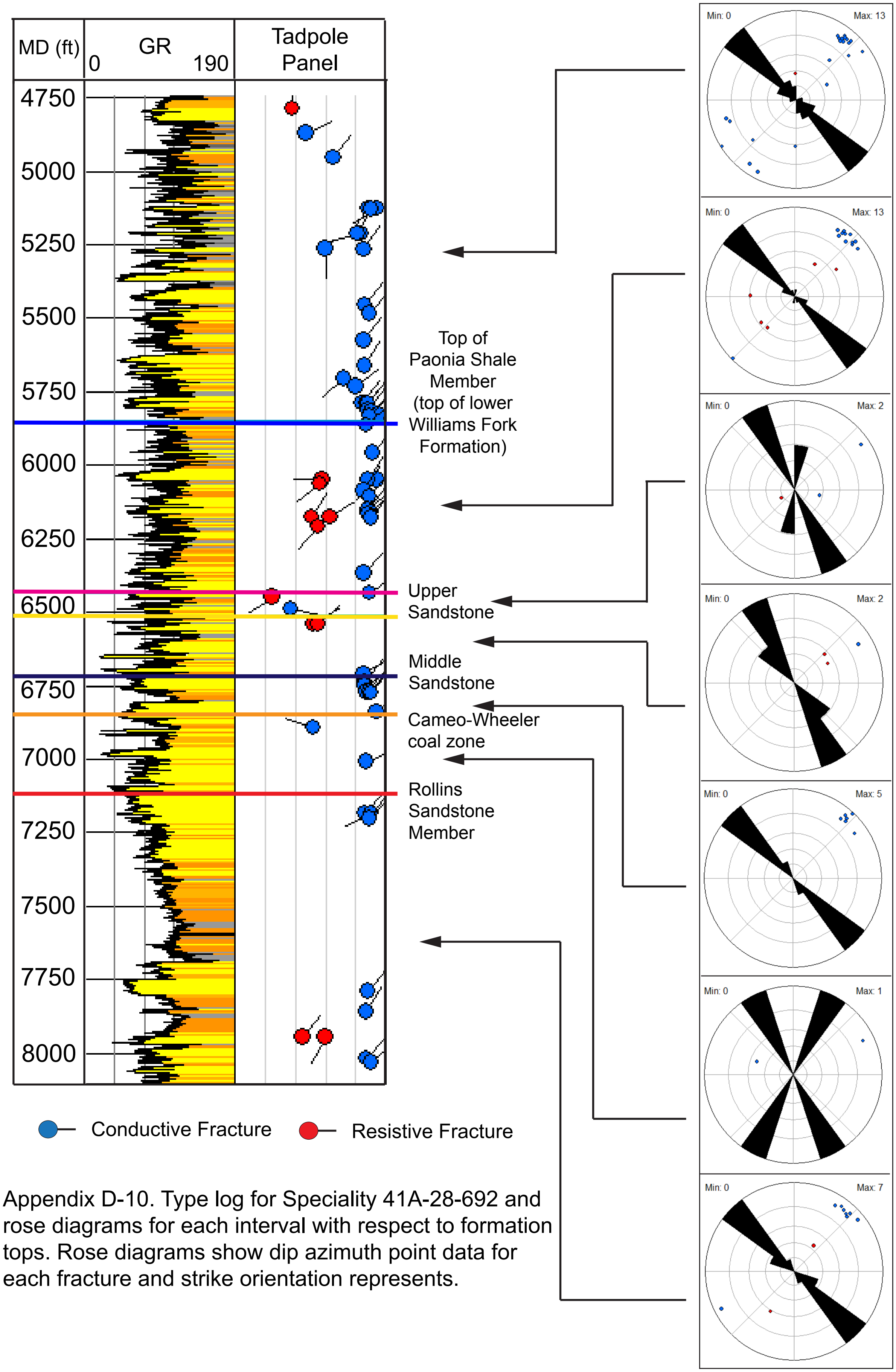

Appendix D-10. Type log for Speciality 41A-28-692 and rose diagrams for each interval with respect to formation tops. Rose diagrams show dip azimuth point data for each fracture and strike orientation represents.

APPENDIX E

Appendix E contains production data of estimated ultimate recovery (EUR) values for each well and 3-D screen captures of seismic volumes, fault interpretation, and structure contour maps for seven key stratigraphic surfaces in the study area.

WELL NAME	UWI	EUR (MMcf)	WELL NAME	UWI	EUR (MMcf)
Jolley	05045158720000	85	CIRCLE_B-LAND	05045151250000	1022
OKAGAWA_FED	05045112270000	390	OKAGAWA_FED	05045112260000	1025
GG_VanOrdstrand	05045150740000	396	BRYNILSON	05045169590000	1025
CIRCLE_B_LAND	05045125010000	417	GGU_JOLLEY_FED	05045177500000	1028
GGU_Barge	05045159220000	442	SCOTT	05045146510000	1037
MCLAUGHLIN	05045145950000	484	Snyder	05045149080000	1037
Schirer+	05045149200000	506	SNYDER	05045149160000	1042
CIRCLE_B-LAND	05045125020000	514	JCJ	05045168680000	1042
GGU_JOLLEY	05045163720000	528	GEISKE	05045143220000	1043
GGU_Roderick	05045157360000	552	MCLAUGHLIN	05045145960000	1046
BRYNILSON	05045171480000	561	SPECIALTY	05045126450000	1049
CIRCLE_B-LAND	05045156380000	562	SPECIALTY	05045155670000	1053
Jolley	05045158730000	563	GGU_JOLLEY_FED	05045177510000	1058
Miller (FMI)	05045160980000	566	JCJ	05045168590000	1059
GGU_MILLER	05045143120000	568	CIRCLE_B-LAND	05045143010000	1061
GEISKE	05045170080000	586	GGU_JOLLEY	05045163750000	1062
SCOTT	05045146500000	601	GGU_JOLLEY_FED	05045177540000	1064
Miller	05045160950000	601	BRYNILSON	05045105130000	1068
MCLAUGHLIN	05045118850000	602	GUCCINI	05045108120000	1070
GG_VanOrdstrand	05045150760000	605	JOLLEY+	05045136740000	1075
LAST_DANCE	05045129840000	606	SPECIALTY	05045157590000	1087
CIRCLE_B_LAND	05045126050000	613	GGU-FEDERAL	05045108000000	1089
Schirer	05045149180000	618	Schirer	05045149210000	1092
Snyder	05045149100000	625	LAST_DANCE	05045129990000	1096
MCLAUGHLIN	05045145970000	626	GGU_JOLLEY_FED	05045177520000	1098
GEISKE	05045170070000	629	SPECIALTY	05045126440000	1100
MCLAUGHLIN	05045118870000	646	SPECIALTY	05045157540000	1103
GGU_MILLER	05045143110000	646	SPECIALTY	05045157520000	1112
PLATZER_FED	05045129960000	656	SPECIALTY	05045145990000	1113
Schirer	05045149190000	656	GGU_JOLLEY	05045163760000	1116
GGU_Roderick	05045157330000	657	GUCCINI	05045140520000	1125
MCLAUGHLIN	05045118860000	665	CIRCLE_B_LAND	05045126080000	1134
MCLAUGHLIN	05045118880000	665	BRYNILSON	05045169550000	1141
CIRCLE_B-LAND	05045143020000	666	MILLER	05045132890000	1143
GGU_JOLLEY	05045163570000	689	BRYNILSON	05045169530000	1150
SPECIALTY	05045157560000	694	CIRCLE_B_LAND	05045120590000	1159
Schirer	05045149220000	698	JOLLEY	05045136730000	1160
BRYNILSON	05045104260000	703	GUCCINI	05045140500000	1163
JCJ	05045163820000	704	Jolley	05045158750000	1163
SPECIALTY	05045157600000	719	SCOTT	05045146530000	1165

TRANT	05045118450000	724	JCJ	05045168670000	1172
GG_VanOrdstrand	05045150720000	726	JCJ	05045168620000	1174
JCJ	05045168640000	737	MILLER	05045125600000	1177
JCJ	05045168650000	740	CIRCLE_B-LAND	05045126060000	1177
GGU_MILLER	05045143090000	741	Jolley	05045158740000	1177
SPECIALTY	05045145980000	745	ANCHONDO	05045141040000	1178
Schirer (FMI)	05045149230000	745	BRYNILDSON	05045171450000	1178
JCJ	05045168660000	748	GGU_JOLLEY_FED	05045177530000	1180
SCOTT	05045103910000	762	CIRCLE_B-LAND	05045122590000	1183
GGU_Roderick	05045157350000	763	MILLER	05045125610000	1187
BRYNILSON	05045104880000	765	BRYNILSON	05045169540000	1192
SPECIALTY	05045157550000	767	SPECIALTY	05045148250000	1199
JCJ	05045168610000	777	SPECIALTY	05045143880000	1200
SPECIALTY	05045157500000	782	ANCHONDO	05045141010000	1201
PLATZER_FED	05045129950000	798	MILLER	05045140970000	1210
GGU_Roderick	05045157340000	800	SPECIALTY_FEDERAL	05045111090000	1225
JCJ	05045168550000	811	GGU_JOLLEY_FED	05045177560000	1240
CIRCLE_B-LAND	05045156390000	813	JCJ	05045168570000	1244
PLATZER	05045129980000	815	BRYNILDSON	05045171470000	1248
GEISKE	05045143250000	815	SPECIALTY	05045126420000	1249
CIRCLE_B-LAND	05045123850000	823	JCJ	05045168540000	1252
CIRCLE_B-LAND	05045151180000	831	Snyder	05045149130000	1264
JCJ	05045168600000	833	GGU_JOLLEY_FED	05045177550000	1267
OKAGAWA_FED	05045112240000	835	SPECIALTY	05045143310000	1270
GEISKE	05045170090000	836	SPECIALTY	05045142630000	1275
Miller	05045160940000	839	GGU_Barge	05045159240000	1283
CIRCLE_B-LAND	05045126100000	840	SPECIALTY	05045155630000	1288
BRYNILSON	05045169570000	841	GGU-SWANSON	05045131870000	1294
Miller	05045161000000	845	SPECIALTY	05045126430000	1316
GGU_Barge	05045159180000	851	GGU_Barge	05045159210000	1316
SPECIALTY	05045157610000	858	GGU_DALEY	05045131840000	1330
SPECIALTY	05045157510000	860	GGU_DALEY	05045131880000	1336
CIRCLE_B-LAND	05045151170000	861	BRYNILSON	05045169580000	1337
GGU_Barge	05045159190000	863	SCOTT	05045114340000	1338
SPECIALTY	05045157580000	864	SCOTT	05045154330000	1339
GEISKE	05045143300000	871	Specialty	05045148200000	1341
SPECIALTY	05045148220000	874	JCJ	05045168580000	1353
CIRCLE_B-LAND	05045143000000	875	SHIDELER_FEDERAL	05045123600000	1364
Schirer	05045149170000	875	GGU_VanOrdstrand	05045150730000	1384
GGU_Barge	05045159170000	886	CIRCLE_B_LAND	05045123830000	1388
Snyder	05045149120000	887	SPECIALTY	05045143870000	1398

GEISKE	05045170100000	888	GGU-SWANSON	05045131860000	1399
SNYDER	05045149150000	890	CIRCLE_B_LAND	05045124990000	1400
MILLER	05045140990000	892	CIRCLE_B-LAND	05045125030000	1409
CIRCLE_B-LAND	05045120630000	896	SPECIALTY	05045146000000	1419
GEISKE	05045170050000	898	MILLER	05045125580000	1421
GGU_JOLLEY	05045163730000	902	SCOTT	05045146520000	1423
CIRCLE_B-LAND	05045143030000	905	GG_VanOrdstrand	05045150710000	1432
CIRCLE_B_LAND	05045126070000	907	SPECIALTY	05045143840000	1444
GG_VanOrdstrand	05045150750000	908	MILLER	05045132870000	1453
CIRCLE_B-LAND	05045151160000	910	SPECIALTY	05045155680000	1453
Snyder	05045149110000	911	Specialty	05045155130000	1458
SPECIALTY	05045143850000	916	MILLER	05045140980000	1468
GGU_Barge	05045159230000	916	TRANT	05045118460000	1473
Specialty	05045148230000	917	SPECIALTY	05045155140000	1477
BRYNILDSON	05045171460000	917	MILLER	05045125620000	1495
SPECIALTY	05045157570000	921	SHIDELER_FEDERAL	05045123590000	1506
JCJ	05045168560000	930	GUCCINI	05045140510000	1515
TRANT	05045144460000	932	TRANT	05045144470000	1521
CIRCLE_B_LAND	05045126090000	934	SPECIALTY	05045143860000	1524
ANCHONDO	05045141020000	935	GUCCINI	05045140530000	1525
GEISKE	05045143230000	936	GGU_MILLER	05045143130000	1548
CIRCLE_B_LAND	05045119930000	937	Miller_Federal	05045160920000	1563
GGU_DALEY	05045131850000	938	SCOTT	05045114360000	1565
JCJ	05045168630000	943	MILLER	05045132930000	1565
TRANT	05045118480000	951	SPECIALTY	05045155650000	1582
BRYNILDSON	05045104280000	955	CIRCLE_B-LAND	05045125000000	1584
GGU_Roderick	05045157300000	955	SPECIALTY	05045141970000	1594
BRYNILDSON	05045171440000	955	SPECIALTY	05045143820000	1597
CIRCLE_B-LAND	05045151200000	960	GGU_JOLLEY	05045137710000	1599
MILLER	05045140960000	961	CIRCLE_B_LAND	05045122120000	1600
ANCHONDO	05045141030000	961	CIRCLE_B-LAND	05045120640000	1621
BRYNILSON	05045169560000	962	GGU_Barge	05045159200000	1656
SPECIALTY	05045155640000	965	SPECIALTY	05045142640000	1658
SPECIALTY	05045155660000	966	MILLER	05045132880000	1659
GEISKE	05045170060000	972	MILLER	05045125590000	1673
BRYNILSON	05045169520000	975	SPECIALTY_FEDERAL	05045111080000	1682
GGU_JOLLEY	05045138810000	977	GGU_JOLLEY	05045137720000	1695
CIRCLE_B-LAND	05045151190000	978	GGU_MILLER	05045143140000	1699
Miller	05045160930000	981	SPECIALTY	05045148190000	1772
PLATZER	05045129970000	982	GGU_MILLER	05045143100000	1787
SPECIALTY	05045157530000	982	CIRCLE_B_LAND	05045123780000	1794

GGU_JOLLEY	05045163710000	982	GGU_DALEY	05045122180000	1824
CIRCLE_B-LAND	05045123840000	993	SHIDELER_FEDERAL	05045123610000	1850
GGU_JOLLEY	05045138800000	1000	CIRCLE_B-LAND	05045122840000	1904
SNYDER	05045149140000	1000	GGU_DALEY	05045122170000	1911
GGU_JOLLEY	05045163700000	1000	MILLER	05045125570000	1968
GGU_JOLLEY_FED	05045177490000	1002	MILLER	05045132950000	2013
GGU_JOLLEY	05045163740000	1009	Miller	05045160960000	2199
BBC (FMI)	05045176890000	1009	SHIDELER_FEDERAL	05045143170000	2210
GEISKE	05045170040000	1011	SPECIALTY	05045148210000	2263
Miller	05045160990000	1016	CIRCLE_B_LAND	05045123800000	2488
SPECIALTY	05045148240000	1018	GGU-FEDERAL	05045108030000	2531
Miller	05045160970000	1018	CIRCLE_B-LAND	05045123790000	2633

Appendix E-1. List of Estimated Ultimate Recovery (EUR) values for wells in the study area. This is the production data used to generate production bubble map in Figure 31.

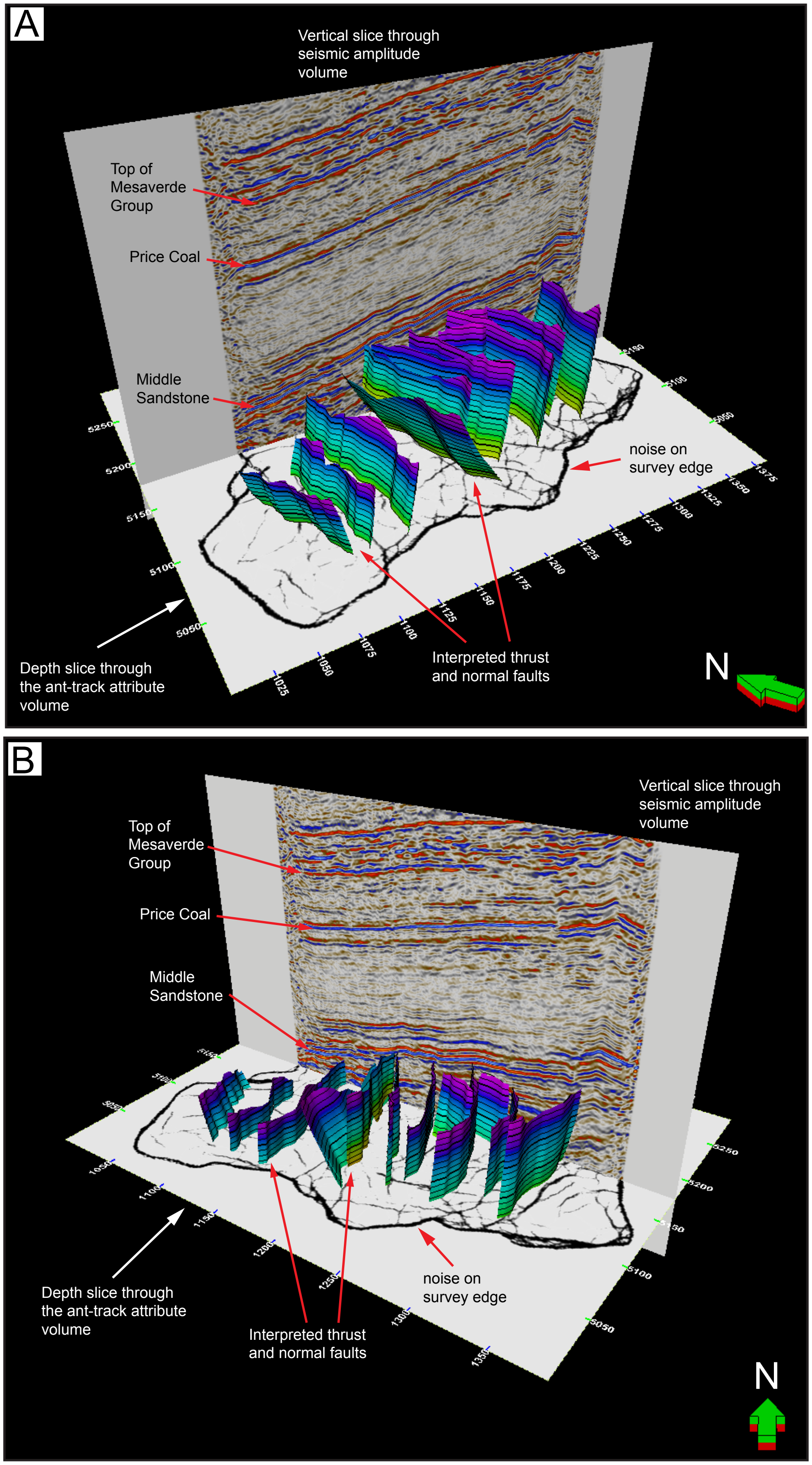

Appendix E-2. Two screen captures through the seismic data. Three dimensional view of interpreted basement-involved thrust and normal faults are shown.

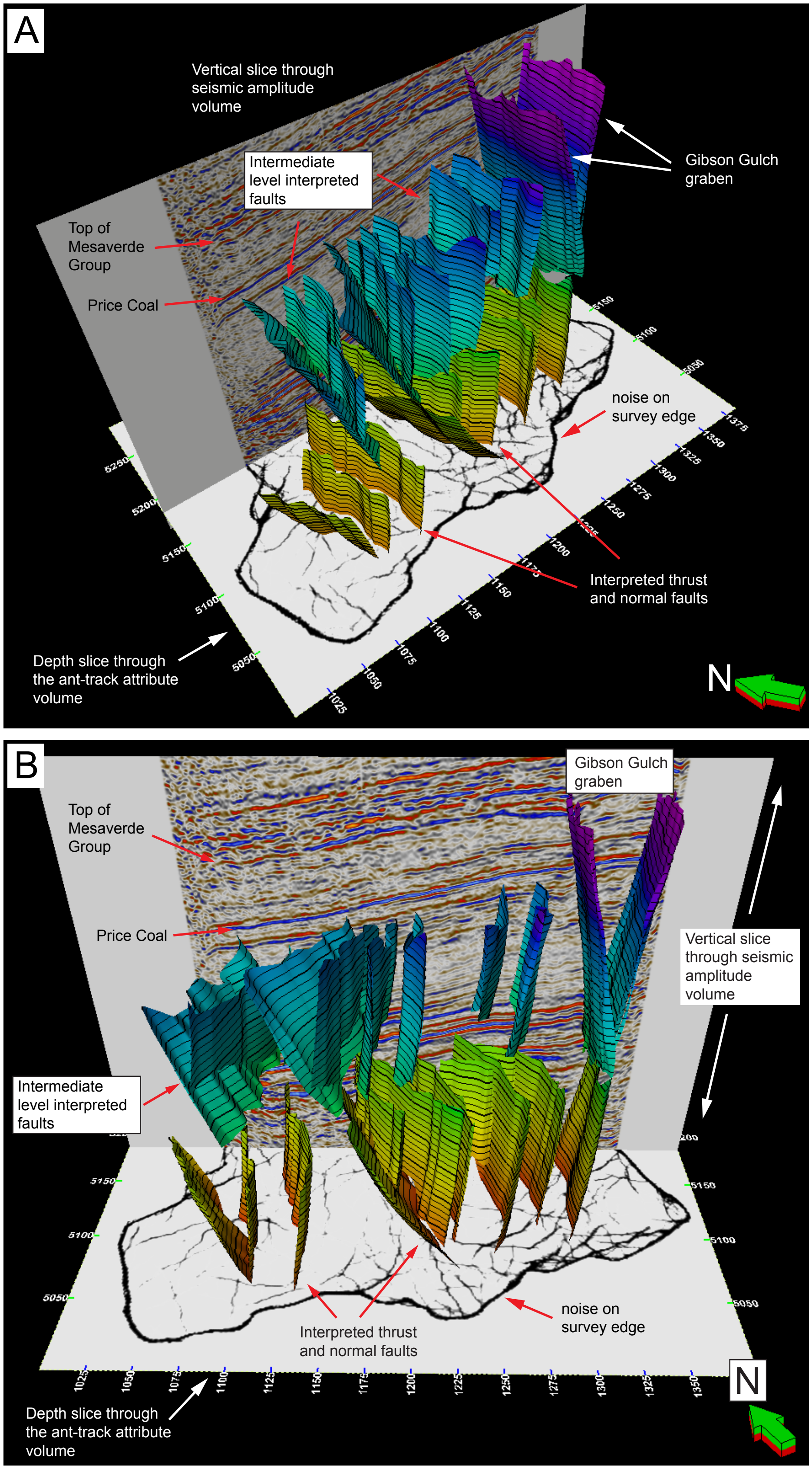

Appendix E-3. Two screen captures through the seismic data. Three dimensional view of interpreted basement-involved thrust and normal faults, intermediate level interpreted faults, and Gibson Gulch graben area are shown.

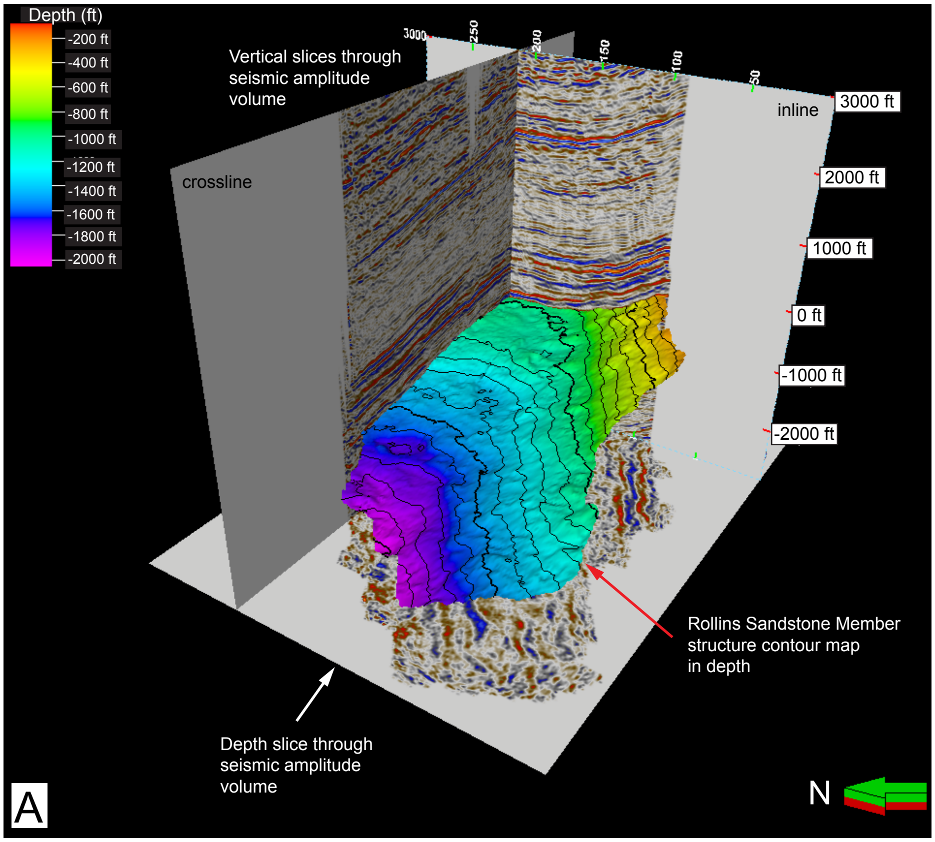

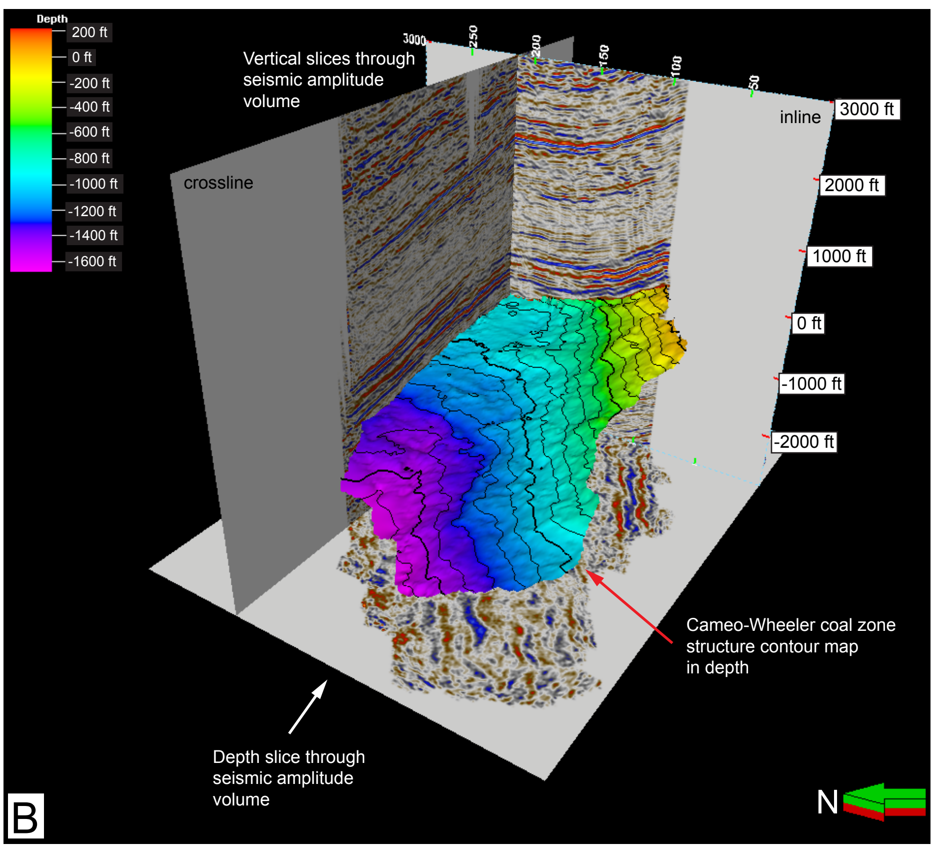

Appendix E-4. A) Depth structure contour map of the Rollins Sandstone Member. B) depth structure contour map of the Cameo-Wheeler coal zone in the study area.

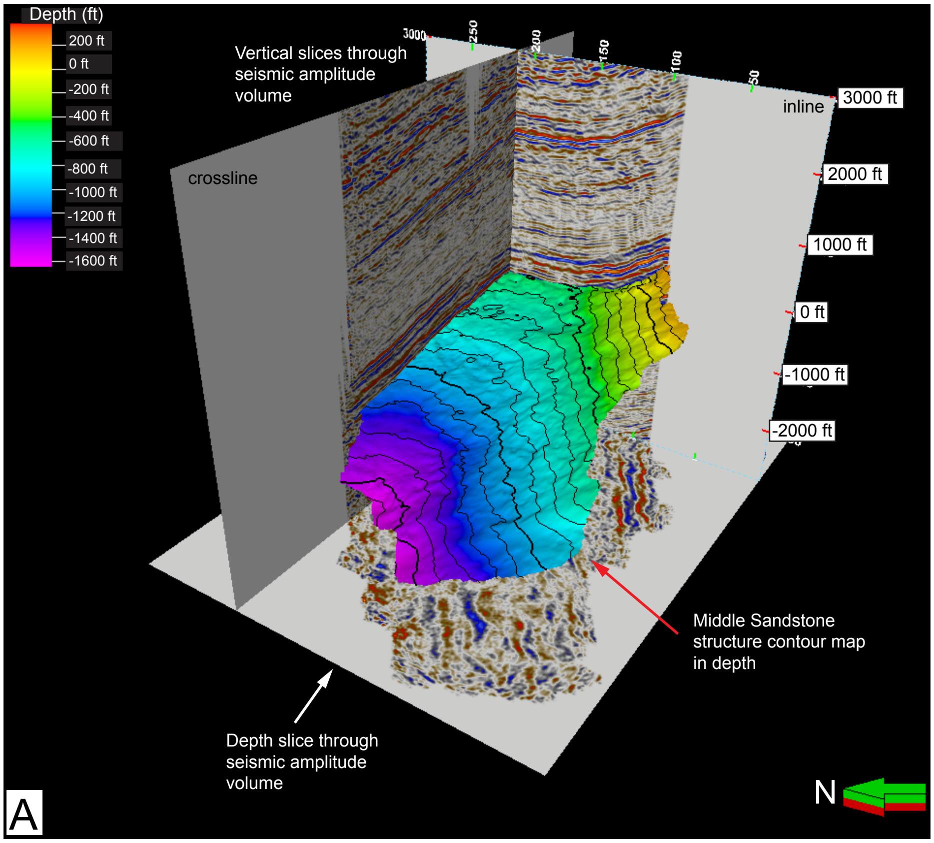

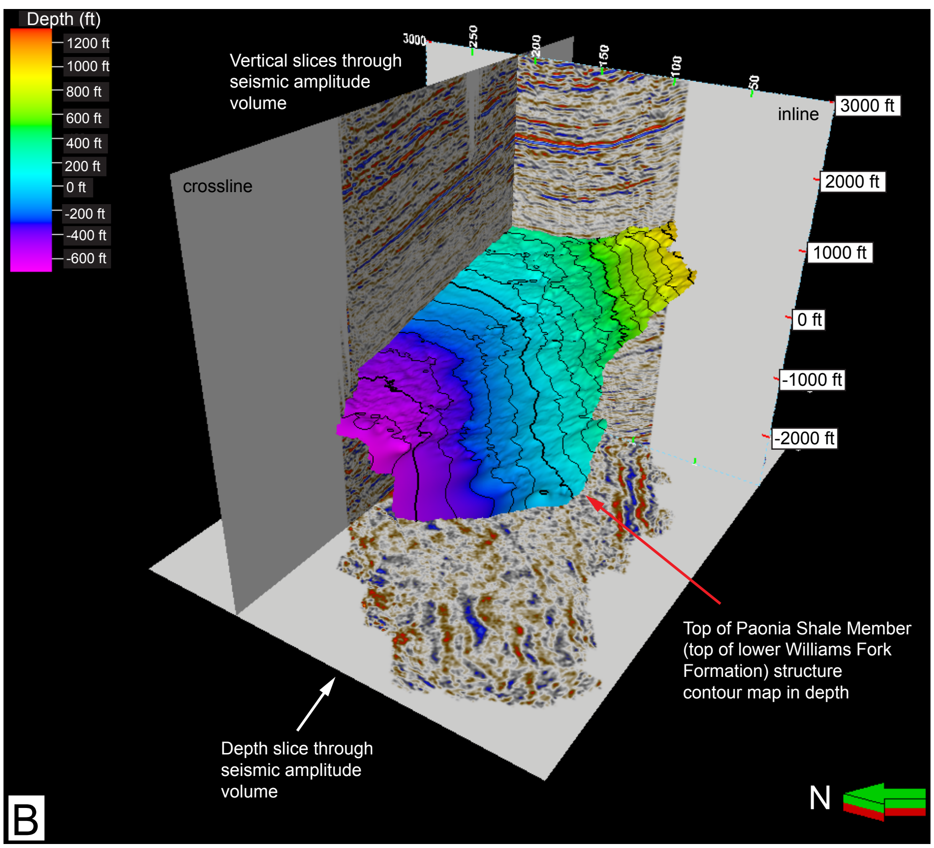

Appendix E-5. A) Depth structure contour map of Middle Sandstone. B) depth structure contour map of the top of Paonia Shale Member (also referred to as top of lower Williams Fork Formation) the study area.

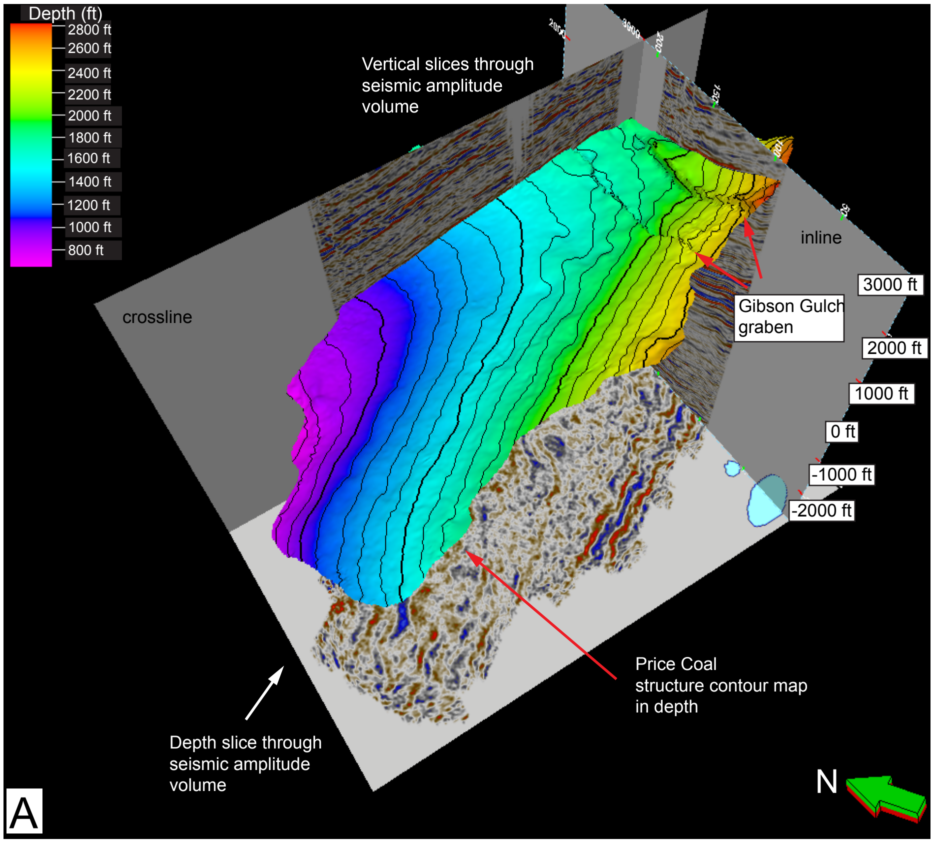

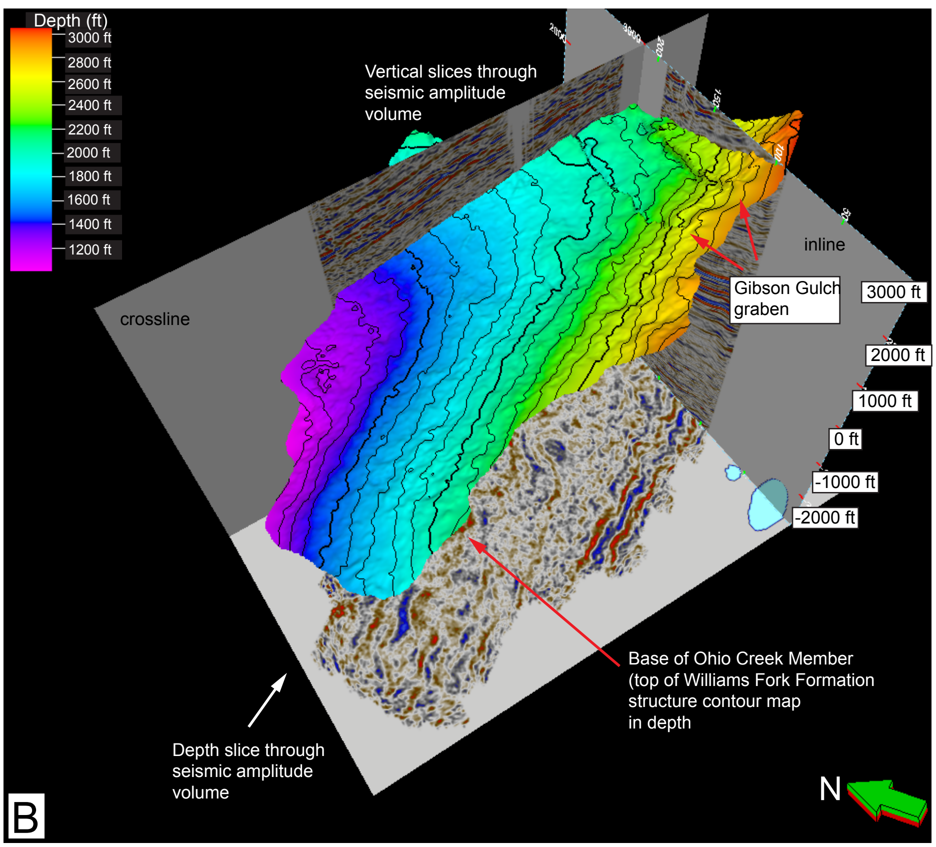

Appendix E-6. A) Depth structure contour map of Price Coal. B) depth structure contour map of base of the Ohio Creek Member of the Mesaverde Group (also referred to as top of the Williams Fork Formation) in the study area.

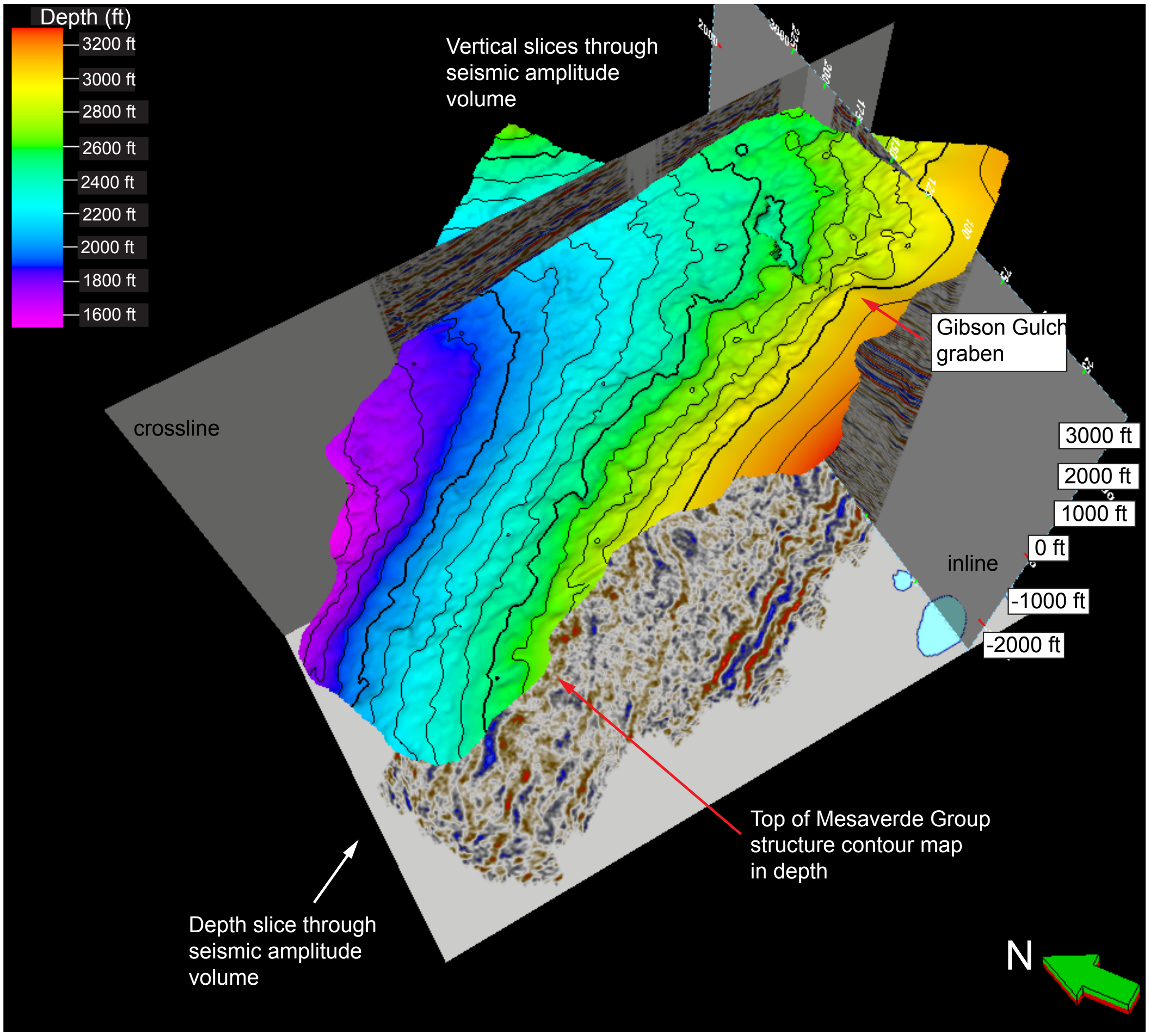

Appendix E-7. Depth structure contour map of top of Mesaverde Group (also referred to as top of the Ohio Creek Member of the Mesaverde Group.